UNIVERSITY OF ROCHESTER
LABORATORY FOR LASER ENERGETICS

Volume 141
October–December 2014
DOE/NA/1944-1210

LLE Review

Quarterly Report

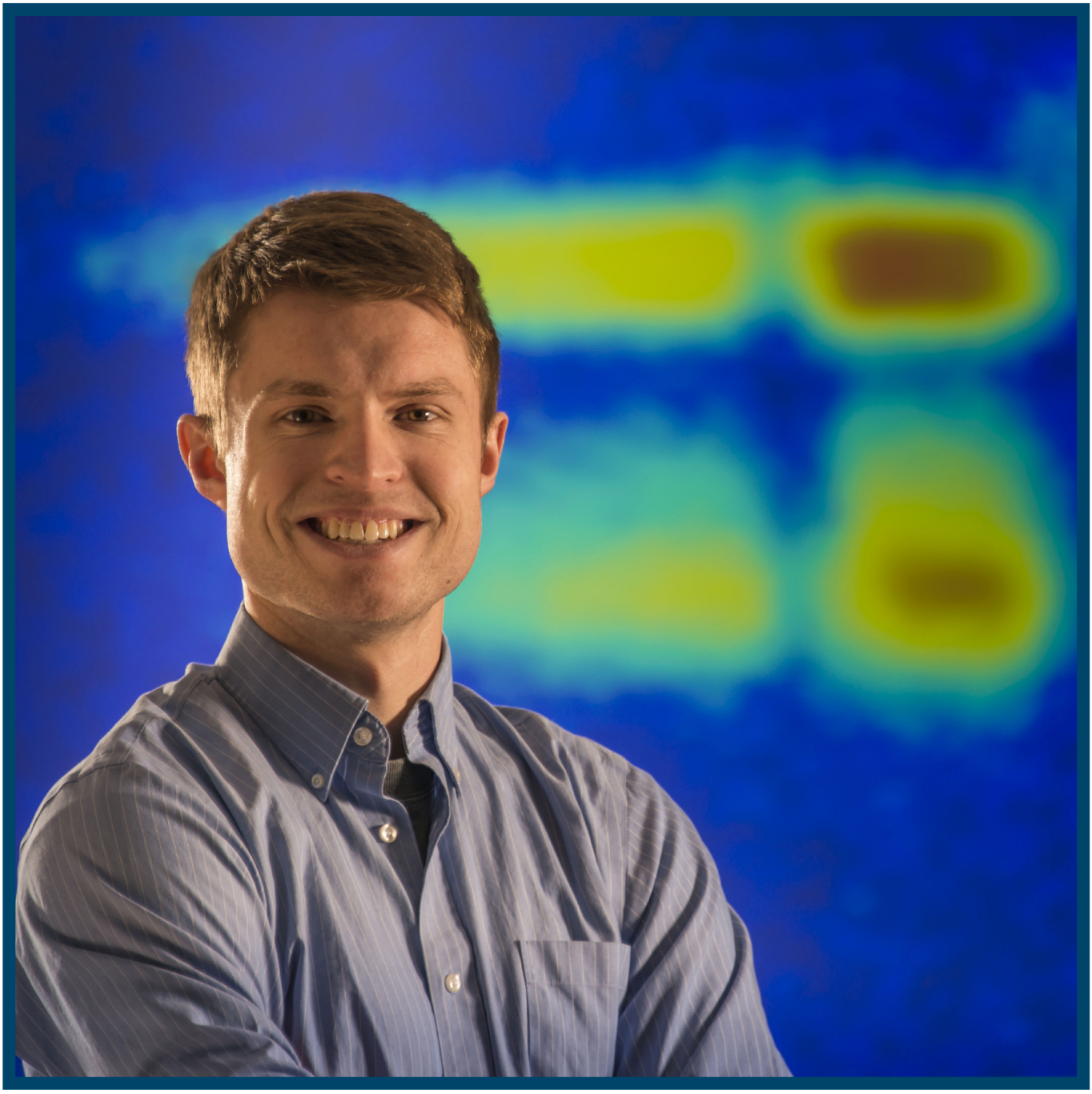

About the Cover:

The photo on the cover shows Physics and Astronomy graduate student R. K. Follett who reports on the direct observation of electron plasma waves driven by multibeam two-plasmon decay (TPD) using ultraviolet Thomson scattering. In inertial confinement fusion experiments, the TPD instability has the potential to generate large-amplitude electron plasma waves that accelerate electrons to high energies. In these experiments, Thomson scattering provides a measure of the electron plasma wave amplitudes responsible for accelerating the electrons. Simulated Thomson-scattering spectra from 3-D numerical solutions of the extended Zakharov equations of TPD are in excellent agreement with the experimental spectra. The cover background is Thomson-scattering spectra from an experiment, where five laser beams were focused onto a planar target.

Recent theories and modeling have suggested that when multiple laser beams are used, their interactions with electron plasma waves can be synchronized by phase coupling to common decay waves. The figure shown here illustrates a longer-wavelength feature that is the direct observation of TPD waves driven by multiple laser beams. The shorter-wavelength peak corresponds to electron plasma waves generated by the Langmuir decay of backscattered TPD waves. The numerical Thomson-scattering spectra (blue curve) calculated by the 3-D fluid code *LPSE* show excellent quantitative agreement with the measured spectra (red curve). This is an encouraging result, demonstrating that *LPSE* includes the relevant physics to capture the TPD-driven electron plasma wave amplitudes. *LPSE* has recently been extended to use these wave amplitudes to calculate the hot-electron spectrum.

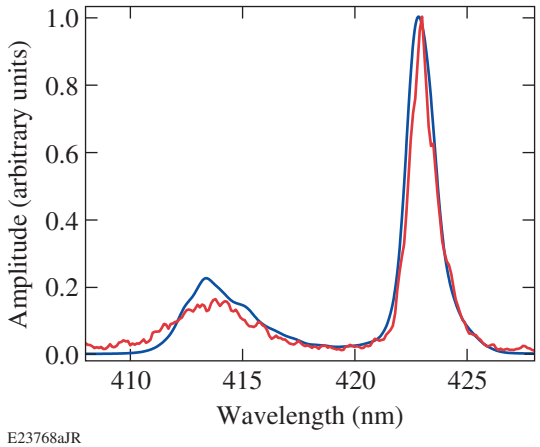

E23768aJR

The work described in this volume includes current research at the Laboratory for Laser Energetics, which is supported by New York State Energy Research and Development Authority, the University of Rochester, the U.S. Department of Energy Office of Inertial Confinement Fusion under Cooperative Agreement No. DE-NA0001944, and other agencies.

Printed in the United States of America
Available from
National Technical Information Services
U.S. Department of Commerce
5285 Port Royal Road
Springfield, VA 22161
www.ntis.gov

For questions or comments, contact Dustin H. Froula, Editor, Laboratory for Laser Energetics, 250 East River Road, Rochester, NY 14623-1299, (585) 273-3686.

Worldwide-Web Home Page: http://www.lle.rochester.edu/
(Color online)

UNIVERSITY OF ROCHESTER
LABORATORY FOR LASER ENERGETICS

Volume 141
October–December 2014
DE-NA0001944-1210

LLE Review

Quarterly Report

UR LLE

Contents

In Brief

This volume of the LLE Review, covering October–December 2014, features "Direct Observation of the Two-Plasmon–Decay Common Plasma Wave Using Ultraviolet Thomson Scattering" by R. K. Follett and D. H. Froula (LLE and the Department of Physics and Astronomy, University of Rochester) and D. H. Edgell, R. J. Henchen, S. X. Hu, J. Katz, D. T. Michel, J. F. Myatt, and J. Shaw (LLE). This article (p. 1) reports on the use of a 263-nm Thomson-scattering beam to directly probe common two-plasmon–decay (TPD) electron plasma waves (EPW's) driven by between two and five 351-nm laser beams. When probing quarter-critical densities $\left(n_c/4\right)$ for 351-nm light, a narrow high-intensity scattering feature was observed at a wavelength consistent with the maximum growth rate given by the linear TPD theory. Electron plasma waves corresponding to the Langmuir decay of backscattered TPD EPW's were observed, suggesting the Langmuir decay instability as a TPD saturation mechanism. Simulated Thomson-scattering spectra from three-dimensional (3-D) numerical solutions of the extended Zakharov equations of TPD are in excellent agreement with the experimental spectra and verify the presence of the Langmuir-decay instability.

Additional highlights of research presented in this issue include the following:

- D. T. Michel, A. K. Davis, V. N. Goncharov, T. C. Sangster, S. X. Hu, I. V. Igumenshchev, D. D. Meyerhofer, W. Seka, and D. H. Froula (LLE) use the measurements of the conduction zone length (110 ± 20 μm at $t = 2.8$ ns), the averaged mass ablation rate of the CD (7.95 ± 0.3 μg/ns), shell trajectory, and laser absorption to quantify the electron thermal transport through the conduction zone in direct-drive cryogenic implosions (p. 7). Hydrodynamic simulations that use nonlocal thermal transport and cross-beam energy transfer models reproduce these experimental observables. Hydrodynamic simulations that use a time-dependent flux-limited model reproduce the measured shell trajectory and the laser absorption, but they overestimate the mass ablation rate by ~10% and underestimate the length of the conduction zone by nearly a factor of 2.

- M. Hohenberger, P. B. Radha, J. F. Myatt, J. A. Marozas, F. J. Marshall, D. T. Michel, S. P. Regan, W. Seka, A. Shvydky, T. C. Sangster, T. R. Boehly, M. J. Bonino, T. J. B. Collins, R. S. Craxton, J. A. Delettrez, D. H. Edgell, R. Epstein, G. Fiksel, D. H. Froula, V. N. Goncharov, D. R. Harding, T. J. Kessler, J. P. Knauer, M. Lafon, P. W. McKenty, M. J. Rosenberg, S. Skupsky, A. A. Solodov, C. Stoeckl, B. Yaakobi, and J. D. Zuegel (LLE); R. Betti, R. L. McCrory, and D. D. Meyerhofer (LLE and Departments of Physics and Astronomy and Mechanical Engineering, University of Rochester); S. LePape, D. T. Casey, D. H. Kalantar, K. N. LaFortune, B. J. MacGowan, A. J. Mackinnon, A. G. MacPhee, J. F. Meeker, S. R. Nagel, R. J. Wallace, and C. Widmayer (LLNL); J. W. Bates, M. Karasik, S. Obenschain, J. E. Ralph, A. J. Schmitt, and J. Weaver (U.S. Naval Research Laboratory); P. Fitzsimmons, J. D. Kilkenny, C. Kurz, and A. Nikroo (General Atomics); and J. A. Frenje, R. D. Petrasso, and H. G. Rinderknecht (MIT) propose a concept to support direct-drive inertial confinement fusion experiments at the National Ignition Facility (NIF) in its indirect-drive beam configuration—polar direct drive (PDD). Ignition in PDD geometry requires direct-drive–specific beam smoothing, phase plates, and repointing the NIF beams toward the equator to ensure symmetric target irradiation (p. 13). First experiments to study the energetics and preheat in PDD implosions utilize the NIF in its current configuration, including beam geometry, phase plates, and beam smoothing. Results from these initial experiments are presented, including measurements of shell trajectory, implosion symmetry, and the level of hot-electron preheat in plastic and Si ablators. Experiments are simulated with the 2-D hydrodynamics code *DRACO* including a full 3-D ray trace to model oblique beams and models for nonlocal electron transport and cross-beam energy transport.

- S. X. Hu, V. N. Goncharov, T. R. Boehly, and S. Skupsky (LLE); R. L. McCrory (LLE and Departments of Physics and Astronomy and Mechanical Engineering, University of Rochester); L. A. Collins and J. D. Kress (LANL); and B. Militzer (University of California, Berkeley) discuss the comprehensive knowledge of the properties of high-energy-density plasmas that is crucial to understanding and designing low-adiabat, inertial confinement fusion (ICF) implosions through hydrodynamic simulations (p. 29). The warm-dense-matter (WDM) properties used in hydrocodes of deuterium–tritium (DT) mixtures and ablator materials, such as the equation of state (EOS), thermal conductivity, opacity, and stopping power, were usually estimated by models where many-body and quantum effects were approximately taken into account in the WDM regime. To examine the accuracy of these models, the static, transport, and optical properties of warm dense DT plasmas were systematically calculated using first-principles (FP) methods over a wide range of densities and temperatures that cover the ICF "path" to ignition. This research shows that the lower the adiabat of DT capsules, the more variations in hydro simulations. The FP-based properties of DT are essential to design ICF ignition targets. Future work on FP studies of ICF ablator materials is discussed.

- W. Theobald, W. Seka, M. Lafon, K. S. Anderson, M. Hohenberger, F. J. Marshall, D. T. Michel, A. A. Solodov, C. Stoeckl, D. H. Edgell, B. Yaakobi, and A. Shvydky (LLE); R. Nora and R. Betti (LLE and Departments of Physics and Astronomy and Mechanical Engineering, University of Rochester); A. Casner and C. Reverdin (CEA); X. Ribeyre and A. Vallet (Centre Lasers Intenses et Applications, University of Bordeaux, France); J. Peebles and F. N. Beg (University of California, San Diego); and M. S. Wei (General Atomics) present recent experiments that were carried out on the OMEGA laser to produce strong shocks in solid spherical targets with direct laser illumination (p. 48). The shocks are launched at pressures of several hundred Mbars and reach Gbar pressures upon convergence. The results are relevant to the validation of the shock-ignition scheme and to the development of an OMEGA experimental platform to study material properties at Gbar pressures. The experiments investigate the strength of the ablation pressure and the hot-electron production at incident laser intensities of ~2 to 6×10^{15} W/cm^2 and demonstrate ablation pressures exceeding 300 Mbar, which is crucial to developing a shock-ignition target design for the National Ignition Facility.

- M. Sharpe (LLE and Departments of Chemistry and Physics, University of Rochester); W. T. Shmayda (LLE); and W. U. Schröder (Departments of Chemistry and Physics, University of Rochester) study the migration of tritium to the surfaces of aluminum 6061, oxygen-free, high-conductivity copper, and stainless-steel 316 from the bulk metal using low-pressure Tonks–Langmuir argon plasma (p. 62). The plasma is shown to be effective at removing tritium from metal surfaces in a controlled manner. Tritium is removed in decreasing quantities with successive plasma exposures, which suggests a depletion of the surface and near-surface tritium inventories. A diffusion model was developed to predict tritium migration from the bulk and its accumulation in the water layers present on the metal surface. This model reproduces the rate of tritium regrowth on the surface for all three metals and can be used to calculate the triton solubility in the water layers present on metal surfaces. The ratio of surface to bulk solubilities at the water layer/bulk metal interface uniquely determines the concentration ratio between these two media. Removing the tritium-rich water layers induces tritium to migrate from the bulk to the surface. This process is driven by a concentration gradient that develops in the bulk because of the perturbation on the surface.

Dustin H. Froula
Editor

Direct Observation of the Two-Plasmon–Decay Common Plasma Wave Using Ultraviolet Thomson Scattering

The self-organization of nonlinearly interacting dynamic systems into coherent synchronized states has attracted a broad interest across a range of subject areas in the biological and physical sciences.[1] Within plasma physics, multibeam laser facilities present the opportunity for synchronization of parametric instabilities driven by intense laser beams propagating through a long-scale-length plasma. Two-plasmon decay (TPD) is a three-wave parametric instability in which an electromagnetic wave decays into two electron plasma waves (EPW's),[2] and when multiple laser beams are used, their interactions with EPW's can be synchronized by phase coupling to common decay waves. This leads to a reduction in the single-beam intensity required to drive the TPD instability above the linear threshold.[3]

Numerical simulations predict that once the TPD instability is driven above the linear threshold, EPW's rapidly reach amplitudes where secondary processes such as the Langmuir decay instability (LDI)[4] and cavitation lead to a broad EPW spectrum.[5,6] This broad EPW spectrum can stochastically accelerate electrons from the bulk velocity distribution to high energies (>30 keV) (Refs. 7 and 8).

Early multibeam experiments showed evidence of TPD-generated hot electrons when the single-beam growth rates were significantly below threshold. These studies showed that TPD hot-electron generation was governed by the overlapped drive intensity;[9] subsequent experiments showed that hot-electron generation scaled with the maximum multibeam growth rate.[10] These studies used indirect measurements of TPD that were dependent on nonlinear processes associated with TPD saturation, which challenges the validity of comparing to linear TPD theory. Thomson scattering of the drive laser beams (self-Thomson scattering) provides a more-direct signature of TPD-driven EPW's,[11] and the spectral features have been discussed in theoretical studies of TPD-driven LDI.[12] Quantitative comparison has been limited by the difficulty in defining the EPW's that are probed when using large numbers of drive beams.[13,14] Very early laser-plasma experiments made the most-direct experimental observations of TPD by using a Thomson-scattering probe to observe the amplitude, which is proportional to the square root of the scattered power and the frequency of EPW's driven by a single CO_2 laser.[15,16]

This article presents the direct observation of TPD waves and associated Langmuir decay daughter waves driven by multiple laser beams. An ultraviolet Thomson-scattering probe beam was used to isolate EPW's driven by multibeam TPD, which allowed for a quantitative comparison of the results with three-dimensional (3-D) numerical simulations that account for the nonlinear nature of the instability and the multibeam geometry used in the experiments. The narrow width [1.6±0.1-nm full width at half maximum (FWHM)] and peak wavelength (423.1±0.2 nm) of the common-wave scattering feature show that the EPW's are driven near the region of maximum common-wave growth. When a fixed overlapped intensity was maintained, the plasma-wave amplitudes were nearly independent of the number of drive beams, demonstrating that these EPW's are driven by multiple laser beams. A broad (3.1±0.5-nm FWHM) Thomson-scattering feature driven by TPD was observed while probing a range of wave vectors that did not include primary common EPW's. A second peak, corresponding to Langmuir decay of primary TPD EPW's, was observed in the Thomson-scattering spectra, suggesting that LDI is responsible for the observed broad range of driven EPW's. The measured Thomson-scattering spectra were well reproduced by 3-D numerical simulations, suggesting that the simulations accurately model the EPW amplitudes in this highly nonlinear system.

The experiments were conducted on the OMEGA Laser System[17] and used two to five $\lambda_{3\omega}$ = 351-nm laser beams to drive common EPW's. The beams were incident on a planar target with an angle of 23° with respect to the target normal. Phase plates[18] were used on each beam to define the 300-μm FWHM flattop laser spots. Prior to being focused by an *f*/6.7 lens, the beams propagated through a birefringent polarization smoothing crystal that separated the incident linearly polarized laser beam into two overlapped beams with orthogonal polarizations propagating at a slight angle (~40 μrad). The laser beams used

1-ns- or 2-ns-long square pulses with the same energy in each beam. When the number of beams and pulse lengths were varied, the laser energies were adjusted to maintain a constant vacuum overlapped intensity ($\sim 10^{15}$ W/cm^2), resulting in the same hydrodynamic conditions for all experiments. The planar targets were 3-mm × 3-mm squares consisting of 30-μm-thick CH layers coated on 30-μm-thick Mo. The CH-layer thickness was chosen such that the burnthrough time was much longer than the laser pulse.[19]

The Thomson-scattering diagnostic consisted of a $\lambda_{4\omega}$ = 263.25-nm f/6.7 probe beam with a best-focus diameter of ~50 μm (Ref. 20). The Thomson-scattered light was collected by a reflective f/10 collection system coupled to two spectrometer/streak cameras, used to simultaneously observe the EPW and ion-acoustic wave (IAW) scattering features.[21] The spectral resolutions of the IAW and EPW systems are 0.05 nm and 0.5 nm, respectively. Scattered light was collected from an ~50 × 50 × 50-μm^3 volume located either 150 μm $\left(n_e/n_c \approx 0.18 \text{ to } 0.21\right)$ or 100 μm $\left(n_e/n_c \approx 0.21 \text{ to } 0.25\right)$ from the target surface (where n_e is the electron density and n_c is the critical density for 351-nm light). The angle between the collection optic and probe beam was 120°. Two Thomson-scattering geometries were used to probe plasma wave vectors near the region of maximum common-wave growth (common-wave configuration) and a region where there was no linear common-wave coupling (non-common-wave configuration). The range of wave vectors probed in the two configurations [Fig. 141.1(a)] was calculated by ray tracing through density profiles generated using the two-dimensional (2-D) hydrodynamic code *DRACO*, where the electron heat flux was limited to 6% of the free-streaming flux.[22] Refraction reduced the scattering angle in the plasma to $\theta_s^{cw} \approx 32^\circ$ and $\theta_s^{ncw} \approx 55^\circ$ in the common-wave and non-common-wave configurations, respectively.

The TPD linear theory with multiple laser beams predicts a maximum growth rate along the axis of symmetry defined by the laser beams [the z axis in Fig. 141.1(a)].[3] The frequency ($\omega_0 = \omega_1 + \omega_2$) and wave vector $\left(\mathbf{k}_0 = \mathbf{k}_1 + \mathbf{k}_2\right)$ matching conditions and linear EPW dispersion relation $\left(\omega_{1,2}^2 = \omega_{pe}^2 + 3k_{1,2}^2 v_{te}^2\right)$ can be satisfied for multiple beams sharing a common daughter wave only when they share a common angle relative to the driven wave [where ($\omega_{1,2}$, $\mathbf{k}_{1,2}$) are the daughter EPW frequencies and wave vectors, (ω_0, $\mathbf{k}_0$) are the drive-beam frequency and wave vector, $\omega_{pe} = \omega_0\sqrt{n_e/n_c}$ is the electron plasma frequency, and $v_{te} = \sqrt{T_e/m_e}$ is the electron thermal velocity (m_e is the electron mass)].

In experiments where multiple beams share a common azimuthal angle, the maximum linear growth rate occurs at the

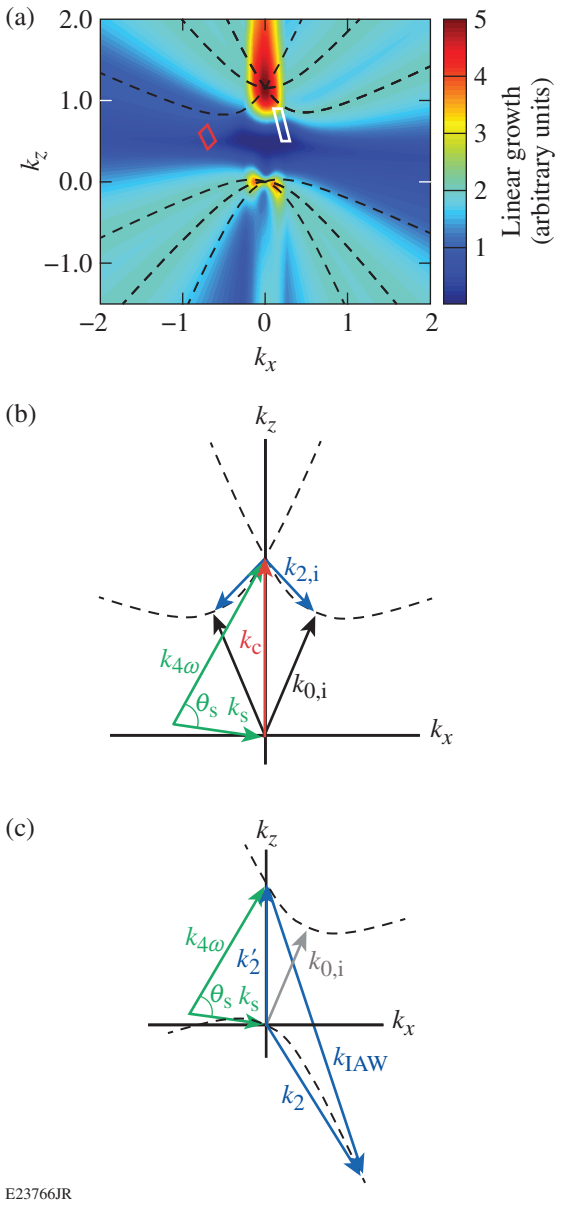

Figure 141.1
(a) The normalized five-beam common-wave growth rate (color scale) in the Thomson-scattering plane [defined by $\hat{y} \parallel \left(\hat{k}_{4\omega} \times \hat{k}_s\right)$ with the target normal in the $-\hat{z}$ direction]. The dashed curves show the linear two-plasmon–decay (TPD) theory maximum growth for each drive beam. The white (red) box shows the range of wave vectors probed by the Thomson-scattering diagnostic in the common-wave (non-common-wave) configuration. (b) Wave-matching conditions for Thomson scattering $\left(\mathbf{k}_c = \mathbf{k}_{4\omega} - \mathbf{k}_s\right)$ from common TPD electron plasma waves (EPW's); (c) daughter EPW's from Langmuir decay of backscattered TPD EPW's $\left(\mathbf{k}_2' = \mathbf{k}_2 - \mathbf{k}_{IAW} = \mathbf{k}_{4\omega} - \mathbf{k}_s\right)$.

intersection of the single-beam maximum growth rates, which lies along hyperboloids $\left[k_\perp = k_\parallel\left(k_\parallel - k_0\right)\right]$ (where $k_\perp$ and $k_\parallel$ are the components of the plasma-wave vector perpendicular and parallel to the drive-beam wave vector, respectively).[10] Electron plasma waves corresponding to distinct branches of a hyperboloid are categorized as forward scattered $\left(\omega_1 > \omega_0/2, \mathbf{k}_1 \cdot \mathbf{k}_0 > 0\right)$ or backscattered $\left(\omega_2 > \omega_0/2, \mathbf{k}_2 \cdot \mathbf{k}_0 > 0\right)$. Figure 141.1(b) shows the wave-vector–matching condition for Thomson scattering from forward-scattered common TPD EPW's $\mathbf{k}_c = \mathbf{k}_{4\omega} - \mathbf{k}_s$ (where $\mathbf{k}_{4\omega}$, $\mathbf{k}_s$, and $\mathbf{k}_c$ are the wave vectors of the probe beam, Thomson-scattered light, and common EPW, respectively). The associated matching conditions and dispersion relations predict a Thomson-scattered peak wavelength of $\lambda_{s,c} = 423 \pm 0.5$ nm.

Figure 141.2(a) shows a broad (9.1±1.1-nm FWHM) EPW Thomson-scattering spectrum measured 150 μm from the initial target surface. The scattering feature has a single spectral peak with a shape consistent with the intensity distribution of the probe beam, indicating that thermal EPW's of roughly equal amplitudes are present throughout the (physical) scattering volume. The observed peak corresponds to Thomson scattering from EPW's from a range of densities $n_e/n_c \approx 0.18$ to 0.21. The IAW spectrum was fit to the collisionless dynamic structure factor, giving a measure of the electron temperature ($T_e = 2.0 \pm 0.2$ keV at 1 ns) and plasma flow velocity along the target normal ($v_f = 5.5 \pm 0.5 \times 10^7$ cm/s) (Ref. 23). The simulated values of $T_e = 1.9$ keV and $v_f = 5 \times 10^7$ cm/s from *DRACO* agree with the measurements.

Figure 141.2(b) shows a narrow (1.6±0.1-nm FWHM) high-intensity feature that appears at a wavelength (λ_s = 423.1±0.2 nm) consistent with the common-wave model ($\lambda_{s,c}$ = 423±0.5 nm). The peak is an order of magnitude more intense and ~10× narrower than the thermal peak [presumably below the detection level in Fig. 141.2(b)], showing the driven nature of the waves. The wavelength range corresponds to Thomson scattering from densities between $n_e/n_c \approx 0.246$ and 0.247. This is much narrower than the range of densities in the scattering volume $\left(n_e/n_c \approx 0.21 \text{ to } 0.25\right)$, indicating that the peak corresponds to locally driven EPW's.

The integrated Thomson-scattered power in the common-wave configuration (proportional to the square root of the wave amplitude) was nearly independent of the number of drive beams when maintaining a constant overlapped intensity. For two-, three-, and five-beam experiments, the relative Thomson-scattered power scaled by 1, 0.7, and 0.5, respectively. The same scaling (within ~10%) was observed in simultaneous hard x-ray measurements, consistent with the expected correlation between hard x-ray generation and TPD-driven EPW amplitudes.[13] The small amplitude variation with the number of beams at a fixed overlapped intensity and the narrow spectral width shows that the observed peak corresponds to Thomson scattering from common TPD EPW's.

The shorter-wavelength peak (λ_s = 413.7±0.2 nm) shown in Fig. 141.2(b) corresponds to Thomson scattering from

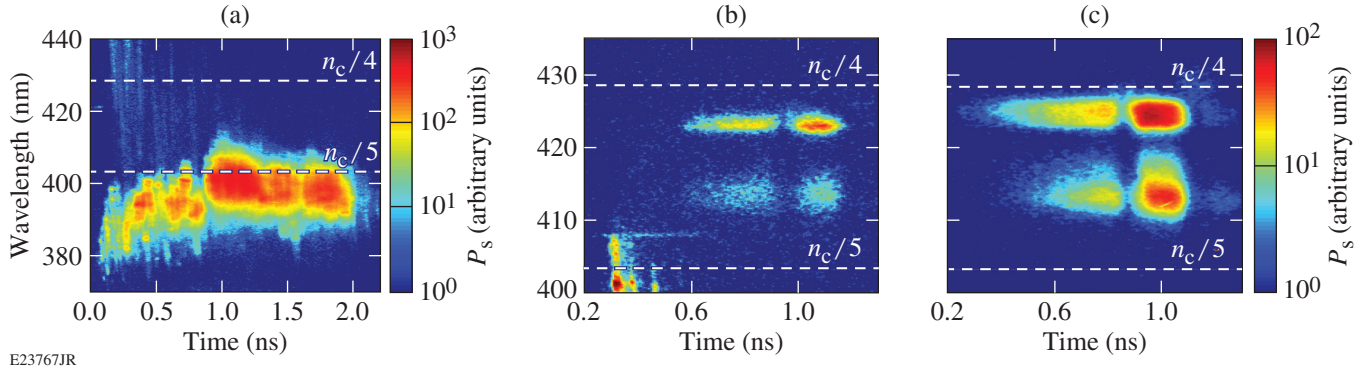

Figure 141.2
Thomson-scattering spectra for scattering from EPW's with dashed lines at wavelengths corresponding to the quarter $\left(n_c/4\right)$- and fifth $\left(n_c/5\right)$-critical surfaces. (a) Scattering from thermal EPW's (150 μm from target surface) generates a broad spectrum corresponding to the range of densities within the Thomson-scattering volume. (b) Scattering spectra from common EPW's (100 μm from target surface) show narrow peaks corresponding to locally driven TPD EPW's. (c) Off-hyperbola scattering (100 μm from target surface) results in a broad spectrum of TPD-driven EPW's. The dip in scattering amplitude at 0.9 ns in all three spectra is caused by a shock, reflected from the Mo layer, traveling through the Thomson-scattering volume.

EPW's driven by Langmuir decay of backscattered TPD EPW's. Figure 141.1(c) shows the wave-matching condition for Thomson scattering from secondary backscattered EPW's $(\mathbf{k}_2')$, where the blue triangle satisfies the LDI-matching conditions $(\mathbf{k}_2 = \mathbf{k}_2' + \mathbf{k}_{\mathrm{IAW}}', \omega_2 = \omega_2 + \omega_{\mathrm{IAW}})$. Assuming that the observed EPW's correspond to direct LDI backscatter $(k_2 = k_{\mathrm{IAW}} - k_2')$, the matching conditions and dispersion relations give λ_s = 413.8±0.3 nm for Thomson scattering from secondary backscattered EPW's, in agreement with the observed peak.

Figure 141.3(a) compares the measured [Fig. 141.2(b)] and simulated Thomson-scattering spectra from the five-beam common-wave geometry. The simulated peak widths and amplitude ratio are in excellent agreement with the experiment. The simulation parameters were taken from *DRACO* profiles: T_e = 1.9 keV, $\left(In_c/4 = 6 \times 10^{14}\ \mathrm{W/cm^2}\right)$, L_n = 190 μm (density scale length), T_i = 1 keV, $v_{\mathrm{flow}} = 5.15 \times 10^7$ cm/s, and

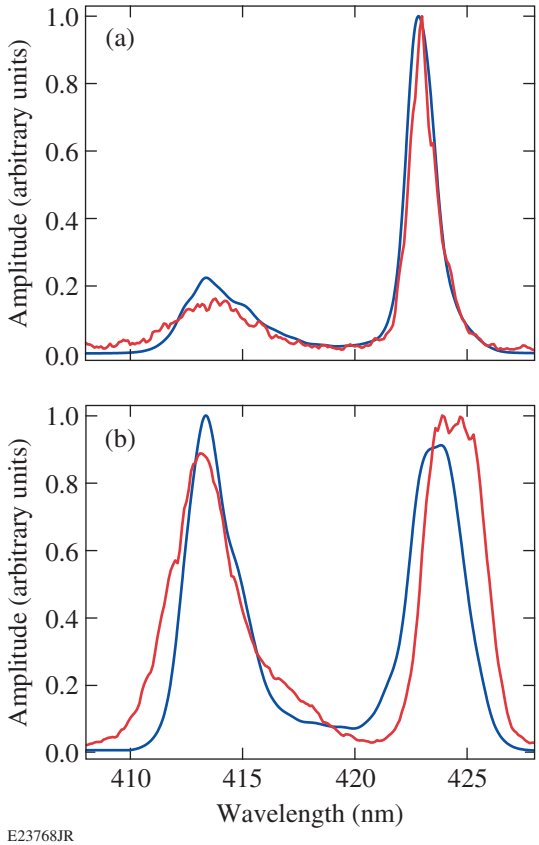

Figure 141.3
Thomson-scattering spectrum measured (red curve) at ~1 ns and simulated (blue curve) in the (a) common-wave and (b) non-common-wave Thomson-scattering configurations.

$n_e(z) = n_0\left[1 - (z/L_n)^{1.12}\right]$, where $n_e(z)$ is a power law fit to the unperturbed electron density profile near $(n_c/4)$ and n_0 = 0.27 n_c is the peak electron density in the simulation box.

The spectra were simulated using a 3-D numerical plasma fluid code (*LPSE*[24]) that solves the extended Zakharov equations of TPD[12,25] for the low-frequency IAW's and high-frequency (enveloped) EPW's. The Zakharov equations are used to model the nonlinear coupling between EPW's and IAW's.[8] Phase plates with polarization smoothing were modeled by splitting each incident beam cone into two sets of 100 cross-polarized plane-wave beamlets with a 40-μrad angular divergence and random phase. The simulation box was 66 × 13 × 13 μm^3 on a uniform 1300 × 256 × 256 Cartesian grid. Thomson-scattering spectra are generated using a numerical structure factor obtained from simulated time series.

In *LPSE* simulations, the shorter-wavelength Thomson-scattering peak was correlated to the Langmuir decay of backward-propagating TPD EPW's by comparing the temporal evolution of the Thomson-scattering spectrum and the low-frequency density perturbations (IAW's). Figure 141.4(a) shows the simulated EPW spectrum at 1 ps, when the TPD instability was in the linear growth stage; large-amplitude EPW's corresponding to the maximum five-beam common-wave growth rate are the dominant spectral feature. At this time, the corresponding IAW spectrum has no driven waves, and only the peak corresponding to forward-scattered TPD EPW's is observed in the simulated Thomson-scattering spectrum. When the ponderomotive force associated with the electric field of counter-propagating EPW's is sufficient to overcome IAW damping, a series of Langmuir decays generate large-amplitude IAW's, leading to broad IAW and EPW spectra [Fig. 141.4(b)]. At this time (~2 ps), the simulated EPW Thomson-scattering spectrum shows two spectral peaks at wavelengths corresponding to forward- and backscattered TPD EPW's.

In simulations where the intensity was just above the threshold for the onset of the TPD instability $\left(In_c/4 = 2 \times 10^{14}\ \mathrm{W/cm^2}\right)$, the EPW amplitudes did not reach sufficient amplitudes to drive large-amplitude IAW's, and the EPW spectrum looks similar to Fig. 141.4(a) at all times. The spectral peak corresponding to backscattered TPD EPW's never appears in the low-intensity simulated Thomson-scattering spectra, consistent with these EPW's being generated by LDI.

Figure 141.2(c) shows a Thomson-scattering spectrum measured in the non-common-wave geometry [red box in Fig. 141.1(a)], which was chosen such that the Thomson-

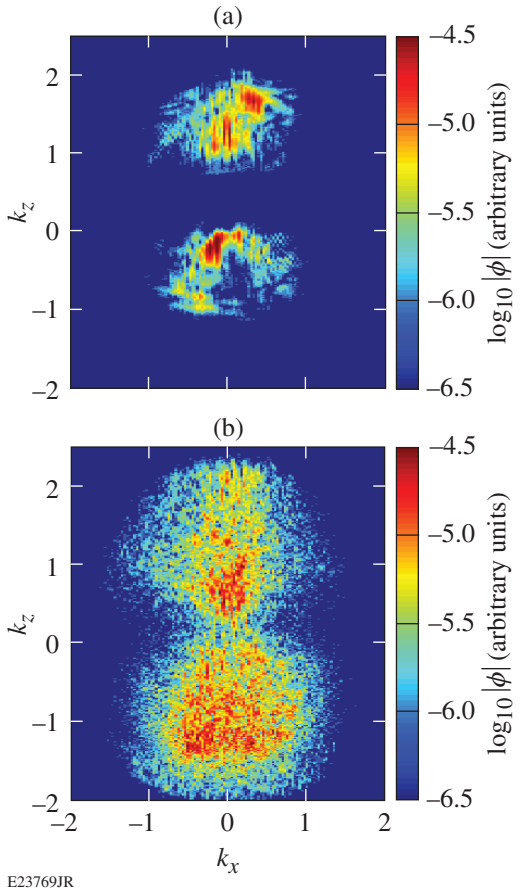

Figure 141.4
Simulated EPW spectra for five drive beams (a) during linear TPD growth (1 ps) and (b) after saturation (2 ps), where ϕ is the high-frequency (enveloped) potential.

scattering diagnostic probes wave vectors that do not satisfy the common-wave matching conditions but is measuring light scattered from a range of densities $\left(n_e/n_c \approx 0.21 \text{ to } 0.25\right)$, where TPD is active. The simulated spectrum [Fig. 141.3(b)] is in good agreement with the measured peak widths and relative amplitudes. The small discrepancy observed between the simulated and measured peak wavelengths could be a result of an ~10% underestimation of the electron temperature or an overestimation of the effects of refraction. For a given scattering geometry (i.e., fixed θ_s), the location of the peaks is determined by the electron temperature and their separation is approximately linear in electron temperature.

In summary, common TPD EPW's were observed using ultraviolet Thomson scattering. The common-wave Thomson-scattering feature is characterized by its narrow width (1.6 nm) and weak amplitude scaling with overlapped drive-beam intensity. The observation of EPW's driven by LDI experimentally shows the nonlinear state of the TPD instability and suggests that LDI is responsible for generating a broad EPW spectrum. These results are supported by 3-D *LPSE* simulations that quantitatively reproduce the experimental scattering spectra.

ACKNOWLEDGMENT

This material is based upon work supported by the Department of Energy National Nuclear Security Administration under Award Number DE-NA0001944, the University of Rochester, and the New York State Energy Research and Development Authority. The support of DOE does not constitute an endorsement by DOE of the views expressed in this article.

REFERENCES

1. A. Pikovsky, M. Rosenblum, and J. Kurths, *Synchronization: A Universal Concept in Nonlinear Sciences* (Cambridge University Press, Cambridge, 2001).
2. E. A. Jackson, Phys. Rev. **153**, 235 (1967).
3. D. T. Michel, A. V. Maximov, R. W. Short, S. X. Hu, J. F. Myatt, W. Seka, A. A. Solodov, B. Yaakobi, and D. H. Froula, Phys. Rev. Lett. **109**, 155007 (2012).
4. D. F. DuBois and M. V. Goldman, Phys. Rev. **164**, 207 (1967).
5. H. X. Vu, D. F. DuBois, D. A. Russell, and J. F. Myatt, Phys. Plasmas **17**, 072701 (2010).
6. J. Meyer and Y. Zhu, Phys. Rev. Lett. **71**, 2915 (1993).
7. R. Yan, C. Ren, J. Li, A. V. Maximov, W. B. Mori, Z.-M. Sheng, and F. S. Tsung, Phys. Rev. Lett. **108**, 175002 (2012).
8. J. F. Myatt, H. X. Vu, D. F. DuBois, D. A. Russell, J. Zhang, R. W. Short, and A. V. Maximov, Phys. Plasmas **20**, 052705 (2013).
9. C. Stoeckl, R. E. Bahr, B. Yaakobi, W. Seka, S. P. Regan, R. S. Craxton, J. A. Delettrez, R. W. Short, J. Myatt, A. V. Maximov, and H. Baldis, Phys. Rev. Lett. **90**, 235002 (2003).
10. D. T. Michel, A. V. Maximov, R. W. Short, J. A. Delettrez, D. Edgell, S. X. Hu, I. V. Igumenshchev, J. F. Myatt, A. A. Solodov, C. Stoeckl, B. Yaakobi, and D. H. Froula, Phys. Plasmas **20**, 055703 (2013).
11. W. Seka, J. F. Myatt, R. W. Short, D. H. Froula, J. Katz, V. N. Goncharov, and I. V. Igumenshchev, Phys. Rev. Lett. **112**, 145001 (2014).
12. D. A. Russell and D. F. DuBois, Phys. Rev. Lett. **86**, 428 (2001).
13. W. Seka, D. H. Edgell, J. F. Myatt, A. V. Maximov, R. W. Short, V. N. Goncharov, and H. A. Baldis, Phys. Plasmas **16**, 052701 (2009).
14. R. L. Berger and L. V. Powers, Phys. Fluids **28**, 2895 (1985).
15. J. J. Schuss, T. K. Chu, and L. C. Johnson, Phys. Rev. Lett. **40**, 27 (1978).
16. H. A. Baldis, J. C. Samson, and P. B. Corkum, Phys. Rev. Lett. **41**, 1719 (1978).

17. T. R. Boehly, R. S. Craxton, T. H. Hinterman, J. H. Kelly, T. J. Kessler, S. A. Kumpan, S. A. Letzring, R. L. McCrory, S. F. B. Morse, W. Seka, S. Skupsky, J. M. Soures, and C. P. Verdon, Rev. Sci. Instrum. **66**, 508 (1995).

18. T. J. Kessler, Y. Lin, J. J. Armstrong, and B. Velazquez, in *Laser Coherence Control: Technology and Applications*, edited by H. T. Powell and T. J. Kessler (SPIE, Bellingham, WA, 1993), Vol. 1870, pp. 95–104.

19. B. Yaakobi, P.-Y. Chang, A. A. Solodov, C. Stoeckl, D. H. Edgell, R. S. Craxton, S. X. Hu, J. F. Myatt, F. J. Marshall, W. Seka, and D. H. Froula, Phys. Plasmas **19**, 012704 (2012).

20. A. J. Mackinnon, S. Shiromizu, G. Antonini, J. Auerbach, K. Haney, D. H. Froula, J. Moody, G. Gregori, C. Constantin, C. Sorce, L. Divol, R. L. Griffith, S. Glenzer, J. Satariano, P. K. Whitman, S. N. Locke, E. L. Miller, R. Huff, K. Thorp, W. Armstrong, W. Bahr, W. Seka, G. Pien, J. Mathers, S. Morse, S. Loucks, and S. Stagnitto, Rev. Sci. Instrum. **75**, 3906 (2004).

21. J. Katz, R. Boni, C. Sorce, R. Follett, M. J. Shoup III, and D. H. Froula, Rev. Sci. Instrum. **83**, 10E349 (2012).

22. P. B. Radha, V. N. Goncharov, T. J. B. Collins, J. A. Delettrez, Y. Elbaz, V. Yu. Glebov, R. L. Keck, D. E. Keller, J. P. Knauer, J. A. Marozas, F. J. Marshall, P. W. McKenty, D. D. Meyerhofer, S. P. Regan, T. C. Sangster, D. Shvarts, S. Skupsky, Y. Srebro, R. P. J. Town, and C. Stoeckl, Phys. Plasmas **12**, 032702 (2005).

23. D. H. Froula, S. H. Glenzer, N. C. Luhmann, and J. Sheffield, *Plasma Scattering of Electromagnetic Radiation: Theory and Measurement Techniques*, 2nd ed. (Academic Press, Burlington, MA, 2011).

24. J. F. Myatt, J. Shaw, J. Zhang, A. V. Maximov, R. W. Short, W. Seka, D. H. Edgell, D. F. Dubois, D. A. Russell, and H. X. Vu, Bull. Am. Phys. Soc. **59**, 241 (2014).

25. D. F. DuBois, D. A. Russell, and H. A. Rose, Phys. Rev. Lett. **74**, 3983 (1995).

Measurements of the Conduction Zone Length and Mass Ablation Rate in Cryogenic Direct-Drive Implosions on OMEGA

Electron thermal transport of energy through a plasma plays an important role in many areas of plasma physics.[1] In laser–matter experiments, the laser energy is absorbed near the critical surface and transported through the conduction zone by electrons to the ablation surface. This electron thermal transport governs the energy flow through the conduction zone, which determines the length of the conduction zone, the mass ablation rate, and ultimately the energy coupled to the target through the rocket effect. In inertial confinement fusion, where laser beams are used to drive a spherical capsule,[2] the mass ablation rate and the length of the conduction zone play a critical role in mitigating hydrodynamic instabilities that could limit the ultimate implosion performance.[3] The conduction zone provides a buffer between the high-intensity modulations in the laser beam (speckles) and the ablation surface where these modulations seed the Rayleigh–Taylor (RT) instability,[4] while the mass ablation reduces the growth of this instability by etching away the target material.[2,5,6]

A complete description of electron thermal transport requires an understanding of both the laser–plasma interactions (e.g., inverse-bremsstrahlung, laser–plasma instabilities) and the conduction process. Laser–plasma interactions depend strongly on the plasma properties and the plasma properties depend on the laser–plasma interactions and the thermal transport, so a complete model must resolve both the laser wavelength scales and the kinetic motion of the plasma over large spatial scales. Historically, large hydrodynamic simulations have been limited to laser absorption by inverse-bremsstrahlung and Spitzer–Härm heat-transport models[7] that use the local plasma conditions to calculate the laser absorption and heat flux. To account for the physics neglected in these simulations (e.g., laser–plasma instabilities, magnetic fields, and non-Maxwellian distribution functions), the flux was typically limited to a fraction of the free-streaming flux [$q_{fs} = n_e T_e \left(T_e / m_e\right)^{1/2}$, where n_e, T_e, and m_e are the electron density, temperature, and mass, respectively].[8] Early experiments indicated that limiting the flux to 6% of the free-streaming flux reproduced time-integrated observables,[8] but to replicate the target trajectories, a time-dependent flux limiter was required.[9–11]

To more accurately calculate the heat flux, nonlocal thermal-transport models have been developed.[12–15] These models account for high-energy electrons that deposit their energy over a large distance, which tends to increase the mass ablation rate and the size of the conduction zone, but direct measurements of these effects are limited. Nonlocal thermal-transport models were required to accurately calculate the heat-wave propagation in relatively simple single-beam gas–target experiments[16] and to simultaneously reproduce the shock timing and perturbation growth in more-sophisticated planar-target experiments.[15,17] Recent implosion experiments have shown that nonlocal thermal transport[15] and cross-beam energy transfer (CBET) models[18] must be used to reproduce the coronal plasma conditions and the absorbed laser power.[19] The mass ablation rates in spherical targets were measured using spectroscopic techniques,[20,21] but these measurements were not able to constrain the thermal-transport models and the ablation pressure in imploding targets, in part because of the sensitivity to perturbations at the ablation surface and the lack of trajectory measurements.

This article presents measurements of the conduction-zone length and the mass ablation rate in a direct-drive implosion. The spherical target was constructed with a thin CD ablator containing a thick cryogenic DT ice layer that enabled the use of a novel technique to measure the average mass ablation rate of the CD (7.95 ± 0.3 μg/ns) and the conduction-zone length (110 ± 20 μm) at the time when the laser light begins to be deposited in the ice layer. These measurements coupled with the simultaneous measurements of the absorbed laser power and ablation-front trajectory fully constrain the electron thermal transport. Hydrodynamic simulations that use nonlocal thermal transport and CBET models reproduce the experimental observables, while hydrodynamic simulations that use a time-dependent flux-limited model reproduce the shell trajectory

and the absorbed laser power, but underestimate the mass ablation rate by ~10% and the length of the conduction zone by nearly a factor of 2. These results highlight the importance of developing multidimensional hydrodynamic codes that include CBET and nonlocal thermal-transport models for studying hydrodynamic instabilities to accurately calculate the mass ablation rate and the conduction zone length.

The experiments employed 60 ultraviolet (λ_0 = 351 nm) laser beams at the Omega Laser Facility.[22] The laser beams uniformly illuminated the target and were smoothed by polarization smoothing,[23] smoothing by spectral dispersion,[24] and distributed phase plates[25] (fourth-order super-Gaussian with 95% of the energy contained within the initial target diameter). Two 100-ps-long pickets were used to set the target implosion onto a low adiabat (α = 2.8) (Ref. 26) followed by a 2-ns pulse that drove the target to its final velocity [Fig. 141.5(a)]. The total energy of the laser was 24.4±0.2 kJ, which resulted in a maximum on-target overlapped intensity of 1×10^{15} W/cm^2. The target had an 868-μm outer diameter with a 7.2-μm-thick CD ablator (18.6±0.6 μg) containing a 62.8-μm-thick cryogenic DT ice layer (28.3±0.6 μg).

The total unabsorbed laser energy was measured by five calorimeters located around the target chamber with an absolute uncertainty of 5%. The scattered-light spectra were measured at four locations by multiplexing the signal into a 1.5-m spectrometer with a high-dynamic-range streak camera. The system has a 100-ps full width at half maximum (FWHM) temporal resolution and a 0.3-Å FWHM spectral resolution.

The recently developed self-emission x-ray imaging technique[28] was used to simultaneously measure the CD/DT interface and the ablation-surface trajectories [Fig. 141.5(b)]. The soft x rays emitted by the imploding target were integrated over 40 ps and imaged with an array of 20-μm-diam pinholes onto a four-strip fast x-ray framing camera (XRFC),[29] with a 6× magnification. The absolute timing of the measurements was known to an accuracy of 30 ps and the interstrip timing was determined within 5 ps (Ref. 30).

Figure 141.5(c) shows the calculated x-ray self-emission profile after the laser has burned through the outer CD layer (black curve). The outer peak in this profile corresponds to the radius of the CD/DT interface. The flux at the detector increases with decreasing radius as a result of the increasing integration length along the line of sight of the diagnostic [orange region in Fig. 141.5(b)]. This line-integrated flux begins to decrease at the CD/DT interface because the DT x-ray emission is reduced relative to the CD emission. The flux increases between the CD/DT interface and the ablation surface [blue region of Fig. 141.5(b)] because of the radially increasing density. When the electron temperature drops below 100 eV (ablation surface), the emission of >1-keV x rays approaches zero and the x rays emitted on the opposite side of the target from the detector are absorbed. This results in a rapid decrease in the line-integrated flux over a few microns, providing an excellent measure of the ablation surface's location.[28]

Figure 141.6 shows the emission profiles that were azimuthally averaged over 360° and were determined from the self-

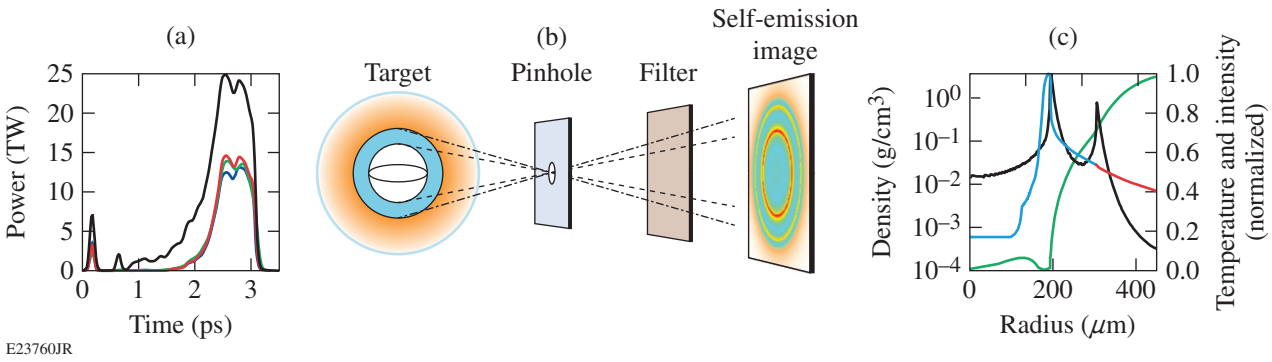

Figure 141.5

(a) The laser pulse shape (black curve) is shown along with a comparison of the measured time-resolved scattered-light power (green curve), calculated with hydrodynamic simulation using the nonlocal thermal transport and cross-beam energy transfer (CBET) models (red curve) and using the time-dependent flux-limiter model (blue curve). (b) Self-emission x-ray image calculated after the laser has burned through the outer CD layer. The image contains two rings: the inner ring correspon2ds to the emission at the ablation surface (dashed lines) and the outer ring corresponds to the emission at the CD/DT interface (dotted–dashed line). (c) Comparison of the density profile (the blue curve corresponds to DT and the orange curve corresponds to CD), normalized temperature profile (green curve), and normalized self-emission lineout (black curve) calculated 460 ps after the laser has burned through the outer CD layer. In (b) and (c), the x-ray self-emission was calculated by post-processing the hydrodynamic simulation with *Spect3D*.[27]

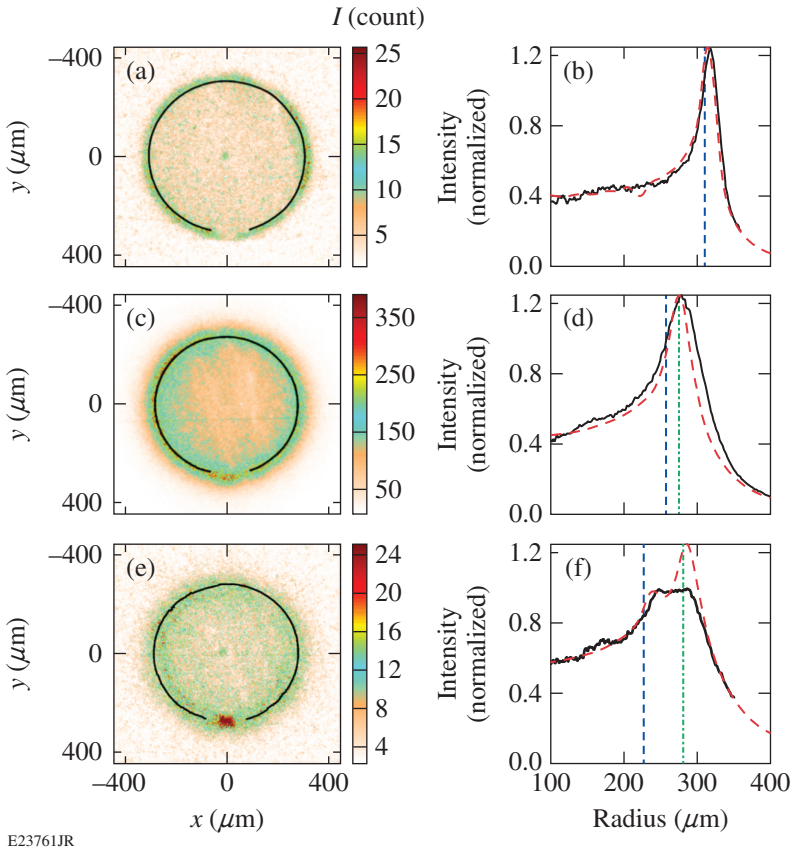

Figure 141.6
[(a),(c),(e)] Self-emission images and [(b),(d),(f)] profiles azimuthally averaged over 360° (black line) measured at [(a),(b)] $t = 2.2$ ns, [(c),(d)] $t = 2.5$ ns, and [(e),(f)] $t = 2.6$ ns. [(a),(c),(e)] The positions of the radial shifts added to the peak intensity determined in the 360°-averaged profile are plotted (black line). [(b),(d),(f)] The self-emission profiles (dashed red lines), the position of the ablation front (dashed blue line), and the position of the CD/DT interface (dashed–dotted green line) calculated with the hydrodynamic simulations using the nonlocal thermal transport and CBET models. The calculated profiles were convolved using the point-spread function of the diagnostic.[28,31]

emission images. The center of each image was determined iteratively. Intensity profiles were taken along chords through the center of the image and azimuthally averaged over 20°. The radial shifts between the 360°-averaged emission profile and each 20°-averaged emission profile were determined by χ^2 analysis. A contour was defined by adding the radial shifts to the radius of the peak intensity determined from the 360°-averaged profile. A new center was calculated by comparing this contour to a circle using a χ^2 analysis. This process was repeated until the center changed by no more than 0.1 μm. A standard deviation <3 μm was obtained in the position of each 20°-averaged emission profile relative to the 360°-averaged emission profile [black line in Figs. 141.6(a), 141.6(c), and 141.6(e)]. This resulted in a negligible spatial convolution to the 360°-averaged emission profiles (about the size of this measured standard deviation).

Figure 141.7 shows the measured CD/DT interface and ablation-front trajectories. At $t = 2.34 \pm 0.05$ ns, the CD begins to expand from the ablation surface, indicating that the initial 18.6 ± 0.6 μg of CD has been ablated. This results in an averaged mass ablation rate of 7.95 ± 0.3 μg/ns. At this time, the mass of the shell corresponds to the difference in the initial mass of the DT layer (28.3 ± 0.6 μg) and the DT that has been released into

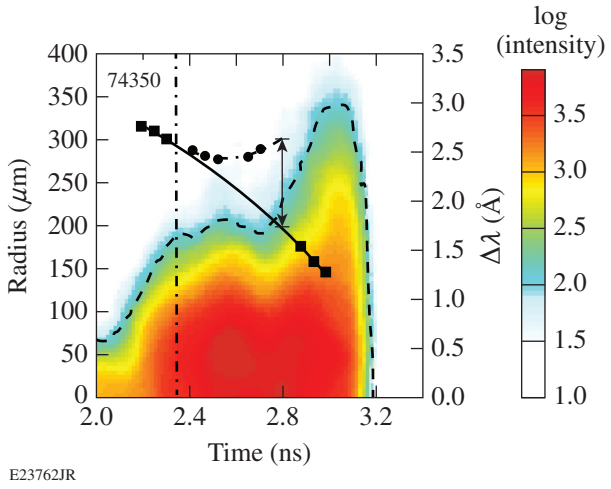

Figure 141.7
Measured ablation front (squares) and CD/DT interface (diamond) trajectories are plotted (left axis) on top of the measured scattered-light spectrum (right axis). Third-order polynomials are fit to the ablation front (solid curve) and to the CD/DT interface (dashed curve). The CD is ablated at 2.34 ns when the CD/DT interface separates from the ablation surface (dashed–dotted line). The 5% intensity contour is used to determine the maximum wavelength shift (dashed curve). The rapid increase in wavelength shift at 2.8 ns is a result of the CD/DT interface crossing the critical-density surface. The length of the conduction zone is determined from the distance between the ablation surface and CD/DT interface at the time when the interface crosses the critical-density surface (black double arrow).

the hot spot (simulations indicate ~0.4 μg). The ablation front and CD/DT interface trajectories were determined following the method described in Ref. 31, where a detailed analysis of the instrument function and opacities quantify the positions of the ablation front and the material interface. The ablation front is located 3 μm inward from the inner peak [Fig. 141.6(b)]. Through most of the implosion, the CD/DT interface is best tracked by the peak [Fig. 141.6(d)], but when the intensities of the inner and outer peaks are comparable [Fig. 141.6(f)], the outer peak becomes an edge, so a robust criterion was developed to determine the position of the interface. The maximum slope averaged over 30 μm along the outer edge of the profile is determined, extended beyond the interface radius and the interface position corresponds to the point where the measured intensity deviates from the extended line by 10% (Ref. 31).

The CD burnthrough time is confirmed by the scattered-light spectra, where a flattening of the maximum shifted scatter light (Fig. 141.7) is observed at $t \sim 2.35 \pm 0.1$ ns, indicating that the acceleration of the critical-density surface is reduced. This is a consequence of the increased length of the conduction zone that occurs when the DT begins to ablate. At this time the mass ablation rate increases because of an increase in $\langle A \rangle / \langle Z \rangle$, where $\langle A \rangle$ is the averaged atomic mass and $\langle Z \rangle$ is the averaged atomic number near the ablation surface.[32]

The distance between the CD/DT interface and the ablation surface at the time when the CD/DT interface reaches the critical surface (absorption region) provides a measure of the length of the conduction zone. The unabsorbed light with the maximum red-shifted wavelength (dashed curve in Fig. 141.7) results from rays with their turning point near the critical surface. The jump in the maximum red-shifted wavelength from 1.7 Å to 3 Å (Fig. 141.7) observed at $t = 2.87$ ns (half-intensity point in the rise of the shift) corresponds to the time when the CD/DT interface reaches the turning point of the unabsorbed light. It is a result of a jump in the radial position of the critical density between the CD and the DT (the difference in $\langle A \rangle / \langle Z \rangle$, combined with the continuity of the mass flux results in a jump in the electron density). Because the turning point in DT is closer to the ablation surface than in CD, the inward velocity of the turning point is larger in DT, leading to a larger frequency shift.[32] When accounting for the distance between the critical surface and this turning point (simulations show ~70 ps), the CD/DT interface is determined to reach the critical surface at $t = 2.8 \pm 0.05$ ns. At this time the length of the conduction zone is 110 ± 20 μm. The error bar corresponds to the simulated variation of the distance between the ablation front and the CD/DT interface over the 50-ps uncertainty in the measurement.

Figure 141.8(a) shows an excellent agreement between the measured and the simulated trajectories when the *LILAC*[33] simulation uses nonlocal thermal transport and CBET models. This is consistent with the good agreement observed in the self-emission profiles (Fig. 141.6). The small differences in the profiles observed in Figs. 141.6(d) and 141.6(f) are likely a

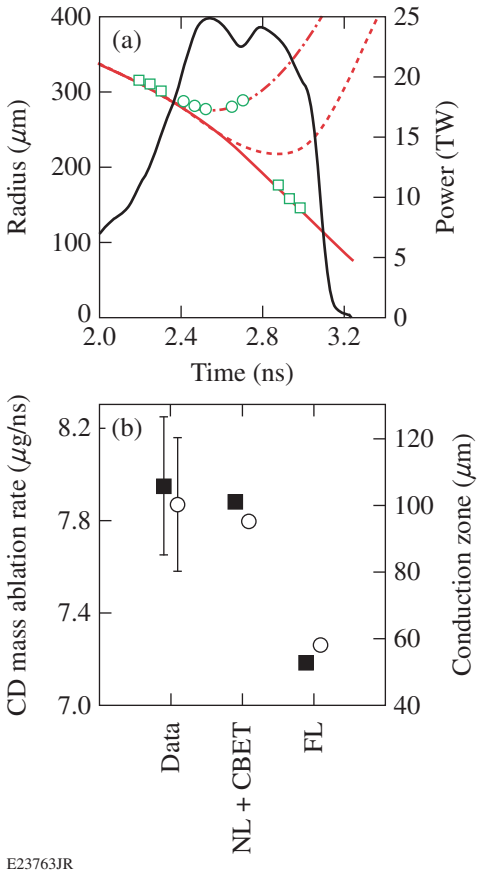

Figure 141.8
(a) Comparison of the measured ablation front (squares) and CD/DT interface (circles) trajectories with ablation front (solid red curve) and the CD/DT interface (dashed–dotted red curve) calculated using a simulation that includes nonlocal thermal transport and cross-beam energy transfer models (NL + CBET) and the CD/DT interface trajectory calculated using a simulation with a time-dependent, flux-limited (FL) thermal-transport model (dashed red curve). The flux limiter was adapted to have the ablation-front radius match the measured ablation front at each time. The laser pulse (black curve) corresponds to the right axis. (b) Comparison of the averaged mass ablation rate of the CD (solid squares) and the size of the conduction zone (open circles) measured at $t = 2.8$ ns with simulations that use nonlocal thermal transport and CBET models and a time-dependent flux-limiter model.

result of perturbation growth at the CD/DT interface, but this has a negligible effect on measuring the interface trajectories.[31] Excellent agreement between the measured and simulated CD burnthrough times indicates that the averaged mass ablation rate of the CD is well modeled. These measurements of the averaged mass ablation rate, the shell trajectory, and the laser absorption significantly constrain the hydrodynamic modeling, as evident by the simulation performed using a Spitzer–Härm heat-transport model [Fig. 141.8(a)]. In this simulation, the flux limiter was varied at each time step to match the measured shell trajectory. With this model, the laser burns through the outer CD layer 250 ps later than in the measurements, indicating that the averaged mass ablation rate is underestimated by 10% [Fig. 141.8(b)]. This results in a more-massive shell and an overestimate of the shell's kinetic energy by 10%. At maximum compression, the mass of the shell calculated by the two models differs by 26%. These results show that time-dependent flux-limiter simulations cannot reproduce simultaneously the shell mass and trajectory.

The measured and calculated sizes of the conduction zone at $t = 2.8$ ns are compared in Fig. 141.8(b). Excellent agreement is obtained when the simulation uses nonlocal thermal transport and CBET models. When using a time-dependent flux limiter, the lower thermal flux reduces the conduction zone to 58 μm, which corresponds to nearly a factor of 2 smaller than measured.

In summary, the size of the conduction zone, the mass ablation rate, the shell trajectory, and the absorbed laser power were measured in direct-drive cryogenic experiments. These measurements quantify the electron thermal transport from the laser-absorption region to the ablation front. Hydrodynamic simulations that include nonlocal thermal transport and CBET models accurately reproduce these experimental observables. When a time-dependent flux limiter was used to match the measured shell trajectory, the laser absorption was well reproduced, but the mass ablation rate was underestimated by ~10% and the conduction-zone length by nearly a factor of 2. These results highlight the importance of developing multidimensional hydrodynamic codes that include CBET and nonlocal thermal-transport models to accurately determine the energy flow between the laser-absorption region and the ablation surface, particularly when studying effects that depend on the mass ablation rate. For example, when studying the effects of the RT instability on target performance using hydrodynamic simulations that use Spitzer–Härm thermal transport with a time-dependent flux limiter adjusted to match the shell trajectory, the mass ablation rate is underestimated, leading to a shorter conduction zone. The shorter conduction zone produces a higher level of laser imprint, which seeds the RT instability, while the lower mass ablation rate underestimates the reduction in the perturbation growth at the ablation surface. Both of these errors overestimate the effects of the RT instability on target performance.

ACKNOWLEDGMENT

This material is based upon work supported by the Department of Energy National Nuclear Security Administration under Award Number DE-NA0001944, the University of Rochester, and the New York State Energy Research and Development Authority. The support of DOE does not constitute an endorsement by DOE of the views expressed in this article.

REFERENCES

1. R. P. Drake, *High-Energy-Density Physics: Fundamentals, Inertial Fusion, and Experimental Astrophysics, Shock Wave and High Pressure Phenomena* (Springer, Berlin, 2006).
2. J. Nuckolls *et al*., Nature **239**, 139 (1972).
3. S. X. Hu, V. N. Goncharov, P. B. Radha, J. A. Marozas, S. Skupsky, T. R. Boehly, T. C. Sangster, D. D. Meyerhofer, and R. L. McCrory, Phys. Plasmas **17**, 102706 (2010).
4. M. H. Emery *et al*., Phys. Rev. Lett. **48**, 253 (1982).
5. S. E. Bodner, Phys. Rev. Lett. **33**, 761 (1974).
6. R. Betti, V. N. Goncharov, R. L. McCrory, and C. P. Verdon, Phys. Plasmas **5**, 1446 (1998).
7. R. C. Malone, R. L. McCrory, and R. L. Morse, Phys. Rev. Lett. **34**, 721 (1975).
8. R. L. McCrory, J. M. Soures, C. P. Verdon, P. Audebert, D. Bradley, J. Delettrez, R. Hutchison, S. D. Jacobs, P. Jaanimagi, R. Keck, H. Kim, T. Kessler, J. Knauer, R. Kremens, S. Letzring, F. Marshall, P. McKenty, M. C. Richardson, A. Simon, R. Short, S. Skupsky, and B. Yaakobi, in *High Intensity Laser-Matter Interactions*, edited by E. M. Campbell and H. Baldis (SPIE, Bellingham, WA, 1988), Vol. 913, pp. 40–58.
9. A. Sunahara, J. A. Delettrez, C. Stoeckl, R. W. Short, and S. Skupsky, Phys. Rev. Lett. **91**, 095003 (2003).
10. S. X. Hu, V. Smalyuk, V. N. Goncharov, S. Skupsky, T. C. Sangster, D. D. Meyerhofer, and D. Shvarts, Phys. Rev. Lett. **101**, 055002 (2008).
11. I. V . Igumenshchev, V. N. Goncharov, W. T. Shmayda, D. R. Harding, T. C. Sangster, and D. D. Meyerhofer, Phys. Plasmas **20**, 082703 (2013).
12. J. F. Luciani, P. Mora, and J. Virmont, Phys. Rev. Lett. **51**, 1664 (1983).
13. E. M. Epperlein and R. W. Short, Phys. Fluids B **3**, 3092 (1991).

14. G. P. Schurtz, Ph. D. Nicolaï, and M. Busquet, Phys. Plasmas **7**, 4238 (2000).

15. V. N. Goncharov, O. V. Gotchev, E. Vianello, T. R. Boehly, J. P. Knauer, P. W. McKenty, P. B. Radha, S. P. Regan, T. C. Sangster, S. Skupsky, V. A. Smalyuk, R. Betti, R. L. McCrory, D. D. Meyerhofer, and C. Cherfils-Clérouin, Phys. Plasmas **13**, 012702 (2006).

16. G. Gregori, S. H. Glenzer, J. Knight, C. Niemann, D. Price, D. H. Froula, M. J. Edwards, R. P. J. Town, A. Brantov, W. Rozmus, and V. Yu. Bychenkov, Phys. Rev. Lett. **92**, 205006 (2004).

17. O. Gotchev, V. N. Goncharov, J. P. Knauer, T. R. Boehly, T. J. B. Collins, R. Epstein, P. A. Jaanimagi, and D. D. Meyerhofer, Phys. Rev. Lett. **96**, 115005 (2006).

18. I. V. Igumenshchev, D. H. Edgell, V. N. Goncharov, J. A. Delettrez, A. V. Maximov, J. F. Myatt, W. Seka, A. Shvydky, S. Skupsky, and C. Stoeckl, Phys. Plasmas **17**, 122708 (2010).

19. D. H. Froula, I. V. Igumenshchev, D. T. Michel, D. H. Edgell, R. Follett, V. Yu. Glebov, V. N. Goncharov, J. Kwiatkowski, F. J. Marshall, P. B. Radha, W. Seka, C. Sorce, S. Stagnitto, C. Stoeckl, and T. C. Sangster, Phys. Rev. Lett. **108**, 125003 (2012).

20. D. K. Bradley, J. A. Delettrez, and C. P. Verdon, Phys. Rev. Lett. **68**, 2774 (1992).

21. S. P. Regan, R. Epstein, V. N. Goncharov, I. V. Igumenshchev, D. Li, P. B. Radha, H. Sawada, W. Seka, T. R. Boehly, J. A. Delettrez, O. V. Gotchev, J. P. Knauer, J. A. Marozas, F. J. Marshall, R. L. McCrory, P. W. McKenty, D. D. Meyerhofer, T. C. Sangster, D. Shvarts, S. Skupsky, V. A. Smalyuk, B. Yaakobi, and R. C. Mancini, Phys. Plasmas **14**, 056305 (2007).

22. T. R. Boehly, D. L. Brown, R. S. Craxton, R. L. Keck, J. P. Knauer, J. H. Kelly, T. J. Kessler, S. A. Kumpan, S. J. Loucks, S. A. Letzring, F. J. Marshall, R. L. McCrory, S. F. B. Morse, W. Seka, J. M. Soures, and C. P. Verdon, Opt. Commun. **133**, 495 (1997).

23. T. R. Boehly, V. A. Smalyuk, D. D. Meyerhofer, J. P. Knauer, D. K. Bradley, R. S. Craxton, M. J. Guardalben, S. Skupsky, and T. J. Kessler, J. Appl. Phys. **85**, 3444 (1999).

24. S. Skupsky, R. W. Short, T. Kessler, R. S. Craxton, S. Letzring, and J. M. Soures, J. Appl. Phys. **66**, 3456 (1989).

25. T. J. Kessler, Y. Lin, J. J. Armstrong, and B. Velazquez, in *Laser Coherence Control: Technology and Applications*, edited by H. T. Powell and T. J. Kessler (SPIE, Bellingham, WA, 1993), Vol. 1870, pp. 95–104.

26. V. N. Goncharov, T. C. Sangster, T. R. Boehly, S. X. Hu, I. V. Igumenshchev, F. J. Marshall, R. L. McCrory, D. D. Meyerhofer, P. B. Radha, W. Seka, S. Skupsky, C. Stoeckl, D. T. Casey, J. A. Frenje, and R. D. Petrasso, Phys. Rev. Lett. **104**, 165001 (2010).

27. J. J. MacFarlane *et al*., High Energy Density Phys. **3**, 181 (2007).

28. D. T. Michel, C. Sorce, R. Epstein, N. Whiting, I. V. Igumenshchev, R. Jungquist, and D. H. Froula, Rev. Sci. Instrum. **83**, 10E530 (2012).

29. D. K. Bradley, P. M. Bell, J. D. Kilkenny, R. Hanks, O. Landen, P. A. Jaanimagi, P. W. McKenty, and C. P. Verdon, Rev. Sci. Instrum. **63**, 4813 (1992).

30. D. T. Michel, V. N. Goncharov, I. V. Igumenshchev, R. Epstein, and D. H. Froula, Phys. Rev. Lett. **111**, 245005 (2013).

31. A. K. Davis, D. T. Michel, S. X. Hu, R. S. Craxton, R. Epstein, V. N. Goncharov, I. V. Igumenshchev, T. C. Sangster, and D. H. Froula, Rev. Sci. Instrum. **85**, 11D616 (2014).

32. V. N. Goncharov, T. C. Sangster, R. Betti, T. R. Boehly, M. J. Bonino, T. J. B. Collins, R. S. Craxton, J. A. Delettrez, D. H. Edgell, R. Epstein, R. K. Follet, C. J. Forrest, D. H. Froula, V. Yu. Glebov, D. R. Harding, R. J. Henchen, S. X. Hu, I. V. Igumenshchev, R. Janezic, J. H. Kelly, T. J. Kessler, T. Z. Kosc, S. J. Loucks, J. A. Marozas, F. J. Marshall, A. V. Maximov, R. L. McCrory, P. W. McKenty, D. D. Meyerhofer, D. T. Michel, J. F. Myatt, R. Nora, P. B. Radha, S. P. Regan, W. Seka, W. T. Shmayda, R. W. Short, A. Shvydky, S. Skupsky, C. Stoeckl, B. Yaakobi, J. A. Frenje, M. Gatu-Johnson, R. D. Petrasso, and D. T. Casey, Phys. Plasmas **21**, 056315 (2014).

33. J. Delettrez, Can. J. Phys. **64**, 932 (1986).

Polar-Direct-Drive Experiments at the National Ignition Facility

Introduction

In inertial confinement fusion (ICF), a capsule containing cryogenic deuterium–tritium (DT) fusion fuel is rapidly compressed to high temperatures and areal densities that are sufficient for thermonuclear fusion.[1–3] In laser-driven ICF, the compression drive is provided by coupling laser energy into an ablator surrounding a spherical fuel capsule, either directly via symmetric irradiation of the fusion target[4] or indirectly via a thermal x-ray bath generated from laser illumination of the inner walls of a cavity (hohlraum).[2] If the compressed central hot spot of an imploded capsule reaches a temperature of 5 keV or above and an areal density of at least 0.3 g/cm^2, the α particles generated via the D–T fusion reactions deposit their energy in the compressed core and the capsule can ignite.[5] Provided the confinement time determined by the inertia of the fuel mass is sufficiently long, the energy released via the fusion burn can exceed the incident driver energy and the energy gain exceeds unity. The demonstration of this concept is the primary mission of the National Ignition Facility (NIF),[6] a 192-beam laser delivering up to 1.8 MJ at a wavelength of 351 nm.

The current beam layout on the NIF is optimized for x-ray drive geometry where beams enter a cylindrical hohlraum through laser entrance holes along the polar axis, with no beams located around the equator. Figure 141.9(a) shows the NIF target chamber configured for x-ray drive with beam entry ports highlighted in blue. The optimum beam configuration for direct-drive target illumination is, however, spherically symmetric. The NIF target chamber was originally designed to support both the x-ray drive beam geometry and a symmetric beam layout by rearranging half of the beamlines to locations closer to the equator.[7,8] This is shown in Fig. 141.9(b) with the direct-drive ports highlighted in blue. Reconfiguring the NIF for a symmetric beam layout, however, poses a significant impact on NIF operations; therefore, the polar-direct-drive (PDD)[9] scheme was proposed to accommodate direct-drive experiments on the NIF using the indirect-drive beam configuration. Symmetric target irradiation is achieved by repointing beams increasingly toward the equator the farther they are located from the poles. This departure from

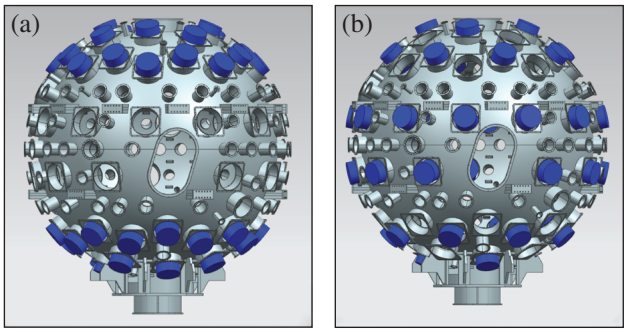

E23750JR

Figure 141.9
The National Ignition Facility (NIF) target chamber with beam ports highlighted. (a) The configuration for x-ray drive with beams clustered around the poles and (b) the symmetric configuration ideal for direct-drive inertial confinement fusion (ICF) experiments, with beams distributed uniformly around the chamber.

normal-incidence irradiation near the target equator leads to a drop in hydrodynamic efficiency and a reduction of kinetic energy imparted onto the shell.[10,11] To compensate for this effect, polar-direct-drive–ignition designs use increased drive energy toward the equator, beam profiles that include a skewed ellipse for the most-oblique beams, and DT ice layers of varying thickness (contoured shells) with lower mass around the equatorial region.[10,11]

This article presents results from PDD experiments on the NIF, designed to understand the effect of two-plasmon decay on preheat and cross-beam energy transfer on implosion energetics and symmetry.[11] This campaign is based on polar and symmetric direct-drive experiments on the OMEGA laser,[12] which provide a solid foundation for the PDD campaign on the NIF.[13,14] The experiments described here utilize the NIF in its indirect-drive configuration, including beam geometry, phase plates,[15] and beam smoothing by spectral dispersion (SSD).[16,17] Since the indirect-drive phase-plate spots are too small for direct-drive targets, they are operated out of best focus.[18] While this configuration is not suitable for full-scale, PDD-ignition experiments, it is highly valuable for initial studies of laser coupling, symmetry tuning, and laser–plasma

interactions. The goals of these early NIF experiments are (1) to develop a stable, room-temperature implosion platform to investigate laser deposition and laser–plasma instabilities at ignition-relevant plasma conditions and (2) to develop and validate ignition-relevant models of laser deposition and energy transport. Room-temperature, 2.2-mm-diam plastic shells were imploded with total drive energies ranging from approximately 500 to 750 kJ with peak powers of 120 to 180 TW and peak on-target intensities from 8×10^{14} to 1.2×10^{15} W/cm^2. Measurements of the shell-mass trajectory obtained via x-ray radiography agree reasonably well with 2-D *DRACO*[19] simulations when including the effect of cross-beam energy transfer (CBET)[20] in the calculations, while the ablation-surface trajectory inferred from self-emission images[21] is slower than simulations predict and increasingly deviates from the simulations at later times. Symmetry measurements are reproduced qualitatively by 2-D simulations, but it is expected that a 3-D treatment is required to fully capture the measured implosion shape. Modest hot-electron levels were inferred via hard x-ray emission[22] and are indicative of the two-plasmon–decay (TPD) instability.[23–25]

This article provides a description of laser–plasma interactions relevant to PDD and direct-drive ignition; presents the experimental setup and target parameters for the shots discussed herein; discusses shell trajectory and symmetry data obtained on PDD implosion experiments, followed by an examination of evidence for the TPD instability and the hot-electron population; presents future experimental plans and a brief overview of additional NIF capabilities required for a full-scale PDD ignition experiment; and summarizes our conclusions.

Laser–Plasma Interactions

Understanding and controlling the impact of parametric instabilities from intense laser–plasma interactions (LPI's) is a key requirement in ICF research. These can act as energy sinks and reduce the implosion velocity or give rise to hot electrons that can preheat the target and reduce target performance.[11] In the context of PDD, two instabilities are of particular importance: CBET[20] and the TPD instability.

In a direct-drive platform, CBET can arise when light rays in the wings of incident laser beams propagate past the target horizon and, on their outward trajectory, interact with incoming laser light. In an expanding plasma, this can result in energy transfer from the high-intensity region of the incoming beam to the low-intensity seed, thereby taking away energy from the capsule drive.[24] In polar-direct-drive geometry, this predominantly affects the equatorial region around $\theta = 90°$. This can be seen in Fig. 141.10, which shows calculated, instantaneous

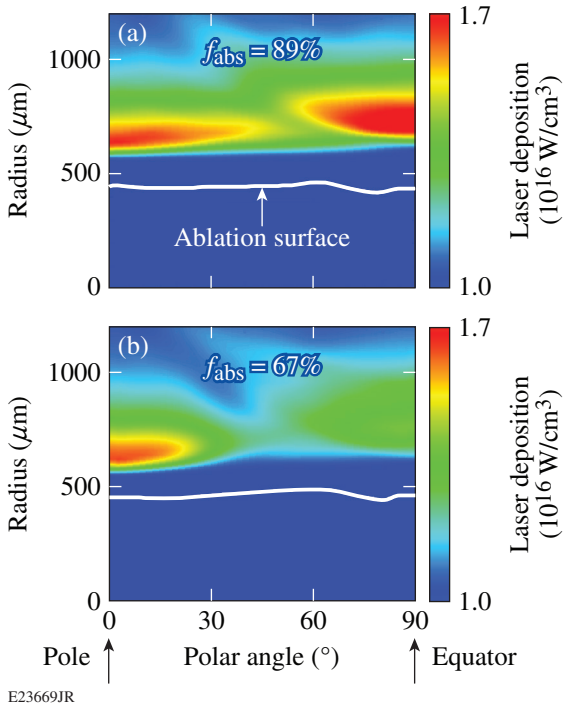

Figure 141.10
Calculated, instantaneous deposited laser power for polar-direct-drive (PDD) shot N130128 at 6.5 ns using the 2-D code *DRACO*: (a) collisional absorption only and (b) including cross-beam energy transfer (CBET). The integrated absorption in the presence of CBET is reduced by ~20%.

deposited laser power for a NIF PDD implosion experiment.[26] The simulations were performed using the 2-D hydrocode *DRACO*,[19] including a full 3-D laser ray trace,[27] a flux-limited heat-conduction model (with a flux limiter $f = 0.06$), and multigroup diffusive radiation transport with opacity tables from the Los Alamos astrophysical opacity library.[28] Figure 141.10(a) shows the calculated absorption without CBET, whereas Fig. 141.10(b) includes CBET. These calculations show a drop in deposited laser power near the equator ($\theta \sim 90°$) in the presence of CBET, with the instantaneous absorption fraction integrated over the entire deposition region dropping by more than 20% from $f_{abs} = 89\%$ to $f_{abs}^{CBET} = 67\%$.

Two-plasmon decay is an instability in which the electromagnetic (EM) wave of the incident laser light parametrically decays into two longitudinal electron plasma waves.[24] The requirement for matching wave number and frequency of the combined decay products and the incident EM wave along with the plasmon dispersion relation limits this process to regions close to the quarter-critical density $(n_c/4)$ in the coronal plasma.[24] Characteristic signatures of the TPD instability are the emission of scattered light at odd half-integer harmonics of

the incident laser frequency $\left(\omega_L/2 \text{ and } 3/2\omega_L\right)$ (Ref. 24) and a component of several tens of keV in the x-ray emission.[29,30] The hard x rays are a result of energetic electrons being accelerated in the presence of the TPD. Two-plasmon decay is relevant in direct-drive research because of its potential to result in anomalous absorption of laser light in the coronal region below the quarter-critical density and the acceleration of hot electrons to energies above 20 keV (Refs. 29 and 31). Hot electrons can penetrate the ignition target and prematurely heat the fuel, raising the fuel adiabat and resulting in lower compression and reduced target performance. The mechanism and magnitude of hot-electron production can change during the implosion, and the acceptable level of hot-electron preheat increases as the capsule is compressed and as the areal density and the electron stopping power of the imploded shell grow.

Experimental Setup

Figure 141.11(a) shows a typical target used for the first series of PDD experiments on the NIF. The targets were room-temperature, 2.2-mm-diam plastic shells with a wall thickness of 100 μm, typically filled with ~20 atm of D_2 gas. The target is placed at the NIF's target chamber center and irradiated with 192 laser beams. The 192 beams are divided into 48 groups of four beams (quads), arranged in four cones per hemisphere sharing the same polar angle at 23.5° and 30° (inners) and 44.5° and 50° (outers), respectively. The drive and implosion symmetry were tuned by repointing both quads and individual beams and also through separate pulse shapes defined for each cone of quads. The beam-pointing scheme is illustrated in Fig. 141.11(b), with circles denoting original quad-port locations, and the other symbols indicating repointed beam or quad positions on the initial target surface at r = 1.1 mm. The arrows show pointing shifts for each cone. The quads located in the 23.5° cone are not repointed and remain at their original orientation; all other quads are increasingly pointed toward the equator with decreasing latitude. The quads originating at 30° are shifted 5° toward the equator at the nominal target surface. Quads in the outer cones are split, and the beams in cones 3 and 4 are repointed in both polar and azimuthal angles. All four beams in 44.5° quads are pointed to individual locations, as indicated by the four arrows starting from a 44.5° quad location in Fig. 141.11(b). Beams in the 50° cone are used to illuminate the equatorial region of the target. These beams experience the largest repointing at ~33° toward the equator, with two beams per quad sharing the same focus point.

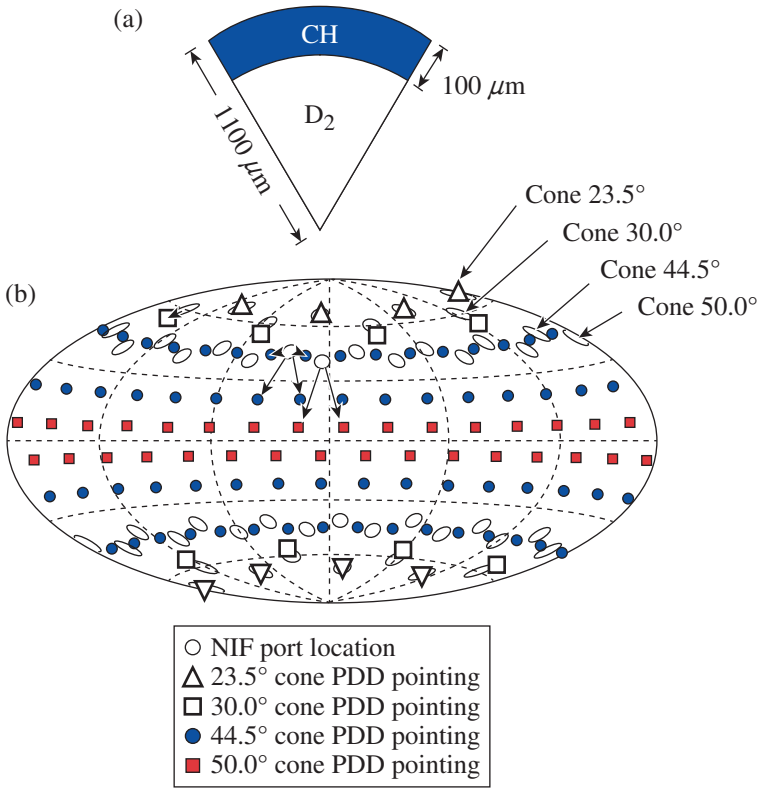

E23751JR

Figure 141.11
(a) Typical target used for the first series of PDD experiments on the NIF. (b) Beam pointing in PDD experiments, illustrated with respect to the initial target surface. Open circles denote original port locations.

Typical pulse shapes for each cone are shown in Fig. 141.12(a) (Ref. 11). The pulse comprises a flat foot, setting the shell to a low adiabat of $\alpha \sim 3$ (ratio of pressure to the Thomas–Fermi pressure at peak density), followed by a continuous rise to the main drive that lasts for ~3 ns. The pulse shapes between individual cones differ slightly for improved implosion symmetry. The total requested power for this shot (N131210) peaks at 124 TW and is shown in Fig. 141.12(b) as the dashed line. This corresponds to an overlapped intensity at the nominal target radius of $r = 1.1$ mm of 8×10^{14} W/cm^2. The total delivered laser power on this shot is shown as the solid line in Fig. 141.12(b), containing a total energy of 609 kJ. Figure 141.12(c) shows a hard-sphere projection of the normalized on-target intensity distribution at the nominal capsule radius of 1.1 mm. It can be seen that the intensity along the equator at $\theta \sim 90°$ is enhanced to offset the reduced hydroefficiency of the non-normal incidence beams driving the equatorial shell acceleration. The achievable target performance is limited since the experiments are performed with indirect-drive phase plates and beam smoothing. Direct-drive experiments require better beam smoothing than x-ray drive,[10] and the currently available NIF beam smoothing limits PDD experiments to modest laser intensities and low-convergence implosions to maintain shell integrity during the implosion. Furthermore, the achievable drive uniformity determined by the use of indirect-drive phase plates is expected to be limited even with an optimized pointing on the capsule (see also **Shell Trajectory and Symmetry**, p. 17).

The shell trajectory and symmetry were measured by imaging the imploding capsule from both the equatorial and polar directions using gated x-ray diagnostics (GXD's).[32,33] These record multiple x-ray images of the target evolution over the course of one experiment by using a high-voltage pulse (gate) that propagates the length of a stripline, i.e., the active region of the camera. Individual images are integrated over ~100 ps, as set by the gate width. The imaging system typically used a pinhole array with a pinhole diameter between 20 and 40 μm and beryllium filtration to reject optical and x-ray emission below ~1 keV. Spectrally and temporally resolved backscattered light between 450 and 750 nm is recorded using the full-aperture backscatter station (FABS).[34] The time-resolved hot-electron distribution is inferred by measuring the hard x-ray emission using the filter-fluorescer x-ray diagnostic (FFLEX).[22] FFLEX is an absolutely calibrated, time-resolved ten-channel spectrometer operating in the 20- to 500-keV range. Lastly, a suite of nuclear diagnostics measures the absolute neutron yield and temperature using neutron time-of-flight (nTOF) detectors,[35] the time of peak neutron emission using the particle time-of-flight (PTOF) diagnostic,[36] and the total areal densities using wedge-range-filter (WRF) proton spectrometers.[37]

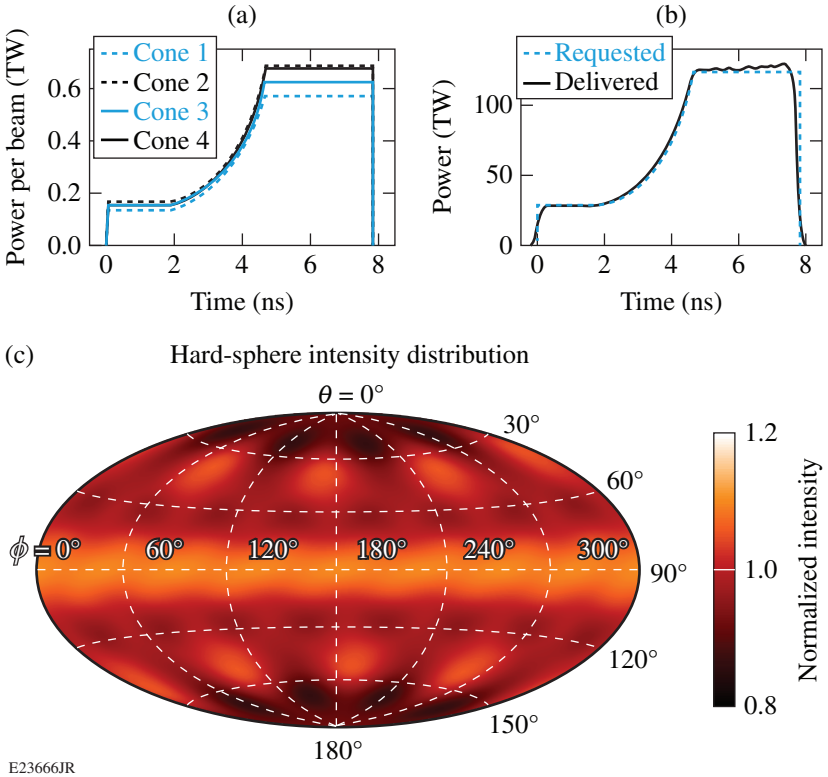

Figure 141.12
(a) Pulse shapes in each cone for shot N131210 comprising a low foot to set the shell adiabat followed by a slow rise to peak intensity. (b) Comparison between requested and delivered total pulse shapes. (c) Hard-sphere projection of the intensity distribution at the initial target radius. The intensity is increased near the equator to compensate for the reduced hydroefficiency of the energy deposited there.

Shell Trajectory and Symmetry

The shell trajectory is an important measure of how efficiently the incident laser energy is coupled to the imploding targets. Based on the work described in Ref. 38, an x-ray radiography platform using an areal backlighter was developed to image the shell position in an imploding capsule from the equatorial direction. In this technique, two of the NIF's 48 quads were redirected from the capsule to an iron backlighter foil located 5 mm from capsule center in the equatorial plane. The backlighter was irradiated with ~25 kJ using a 2-ns square pulse, generating Fe He_α emission at 6.7 keV over an ~1.5-mm-diam spot. Of the remaining 184 beams driving the capsule implosion, 16 beams were repointed and increased in energy by 50% to compensate for the missing drive from the backlighter beams. Radiography data were recorded with GXD's. Individual images of the framing-camera data were matched to the pinhole layout in the imaging setup, providing an accurate measurement of the image magnification and size. The gate velocity, i.e., the time between individual images, and interstrip delays were measured in offline calibrations, which, in conjunction with a measurement of the trigger time of the first strip on the camera, determined the timing of each recorded frame to within 50 ps. An example of a backlit image from shot N140612-001 at a radius of ~350 μm is shown in Fig. 141.13(a). In the image, the bright outer feature is the backlighter, with the central darker ring corresponding to the shell mass that has partially absorbed the backlighter emission. This made it possible to track the point of peak absorption as a function of polar angle, as highlighted by the white line in Fig. 141.13(a). Figures 141.13(b) and 141.13(c) are synthetic backlit images from 2-D *DRACO* simulations. The shape of the compressing shell is better modeled with the inclusion of CBET in the simulation [Fig. 141.13(c)] compared to the simulation without CBET [Fig. 141.13(b)]. This is discussed in detail later.

Performing the same analysis on multiple images over a single experiment provides a portion of the shell trajectory. Figure 141.14 shows the extracted radius of an imploding shell, given by the peak absorption, as a function of time (diamonds). These data represent the accumulated trajectory data over two NIF shots (N140612-001 and N140816) with nominally identical experimental parameters such as target size and incident laser power, with high reproducibility of the experimental results. Temporal overlap in the measurements ensures that, within the measurement uncertainty, the same trajectory is observed for both shots. To generate synthetic radiography data, *DRACO* simulations of the implosion experiment are post-processed with the code *Spect3D*,[39] which transports x rays through the *DRACO* profiles, accounting for absorption using opacities generated by the PRISM group.[39] The detector resolution and the time window over which the images are integrated in the experiment are included in the post-processing. Examples of simulated radiography images are shown in Fig. 141.13 for a calculation without CBET [Fig. 141.13(b)] and with CBET [Fig. 141.13(c)]. In addition to the experimental data, Fig. 141.14

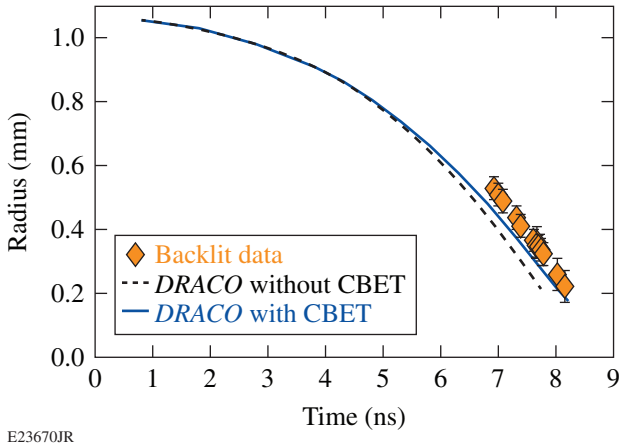

Figure 141.14
Two-dimensional *DRACO* simulations without CBET (dashed line) do not match the experimental shell trajectory extracted from radiography data (diamonds). By including CBET, the agreement improves (solid blue line).

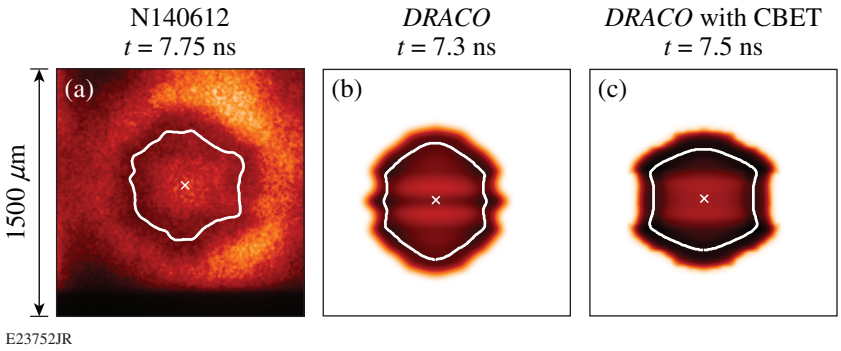

Figure 141.13
(a) Two-dimensional radiography data using 6.7-keV x rays to backlight the imploding PDD shell on shot N140612-001. The white line corresponds to the peak x-ray absorption. [(b),(c)] Synthetic radiography data from 2-D *DRACO* simulations without and with CBET, respectively.

also shows trajectory calculations with (solid blue line) and without CBET (dashed black line). Noticeably, the simulation result without CBET predicts an earlier capsule implosion, with the experimental trajectory data delayed by ~500 ps at the end of the observation window (~8 ns), and with the experimental trajectory converging by a factor of ~3 compared to ~5 in the simulation. When including CBET in the trajectory calculation, the discrepancy between experimental data and simulation reduces to ~200 ps. Between 7 and 8 ns, the shell exhibits a velocity of $v = 238 \pm 20$ km/s with an error of the shell radius of ~20 μm in the radiography data and ~50-ps timing uncertainty. The radial error is obtained by performing the trajectory analysis separately over each half of the radiography image. While the measured velocity agrees with the simulated value of 221 km/s of the CBET calculation over the same time interval (to within the error bars), the discrepancy in radial position of ~50 μm or 200 ps exceeds the uncertainty in the measurement. The delayed trajectory in the experiment compared to the calculation may indicate missing information in the simulations. A plausible hypothesis is that nonuniformities from laser imprint or initial shell-surface perturbations can grow via the Rayleigh–Taylor instability.[40,41]

A key requirement for an ICF platform is a high degree of spherical symmetry of the implosion to achieve maximum compression of the fuel and hot spot. Any deviations from spherical symmetry will result in transverse fuel motion and reduced conversion efficiency of the shell's kinetic energy into thermal hot-spot energy. In the case of PDD, the energy deposition is particularly compromised along the equator because of the indirect-drive beam geometry. Shell symmetry is extracted from the radiography data by fitting a superposition of low-mode Legendre polynomials from zeroth to tenth order to the shape of the measured peak-of-emission lineout [white line in Fig. 141.13(a)]. In Fig. 141.15, the amplitudes of modes 2, 4, and 6 extracted from the backlit equatorial images of a single shot are plotted as a function of shell radius (diamonds). Amplitudes are displayed in units normalized to the shell radius $\left(P_n/P_0\right)$. In this case, time is going from right to left as the capsule is compressed.

An alternative technique for extracting the modal evolution from radiography data is to image the soft x-ray self-emission of the coronal plasma at ~1 keV (Ref. 21). The combination of the limb effect and the optically thick shell results in a ring of soft x-ray emission in the image plane. The steep inner gradient of this image has been demonstrated to track with the ablation surface in directly driven implosions on OMEGA.[42,43] From these data, the shell symmetry is extracted from each frame by tracking the midpoint of the inner intensity gradient as a function of polar angle, followed by a Legendre-polynomial analysis as with the radiography data discussed above. Imaging the self-emission rather than backlighting the shell has the advantage of not requiring dedicated backlighter beams. The backlighter beams are not available for irradiation of the implosion target, which compromises the symmetry and hydrodynamic performance of the implosion. Additionally, the high signal-to-background ratio of the self-emission data results in an intrinsically lower uncertainty in extracting the inner-gradient midpoint for shape analysis compared to using the point of peak absorption in the radiography data. Because of its reliance on sufficient coronal plasma emission, self-emission imaging is limited to times during which the laser is incident onto the target since the coronal temperature quickly drops without laser illumination. This is in contrast to backlit imaging, which requires low self-emission. The opacity of the compressed shell in current

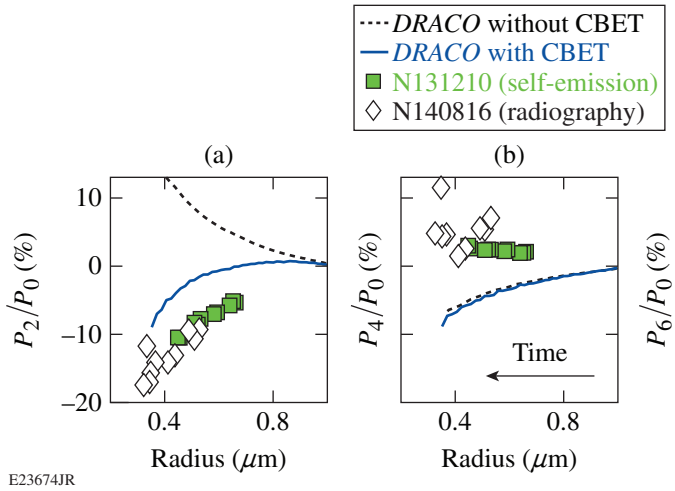

Figure 141.15
Equatorial shape evolution of an imploding PDD capsule. Modal amplitudes normalized to the shell radius are shown for (a) P_2, (b) P_4, and (c) P_6. Data are plotted as a function of shell radius, with time going from right to left. Diamonds are extracted from radiography data of shot N140816; squares are extracted from self-emission images on shot N131210. Lines show 2-D *DRACO* simulation results for shot N131210 with (solid) and without (dashed) CBET in the calculations.

PDD implosion experiments requires backlighter x rays in the range of 6 to 8 keV for optimal image contrast. At that photon energy, the coronal emission of a driven capsule is still bright enough to reduce the achievable signal-to-background ratio and to compromise a radiography measurement. Radiography imaging performs best in the absence of capsule drive, and radiography data were obtained with truncated laser pulses. The two techniques should be considered complementary since they can probe different times in a given implosion.

Two examples of self-emission data are displayed in Fig. 141.16. These data were acquired on the same shot and at roughly the same time at a convergence ratio of CR ~ 2.5, with Fig. 141.16(a) being taken from the polar direction, looking down onto the target, and Fig. 141.16(b) from the equatorial direction at $\theta = 90°$ using port (90,78). The elongated feature visible on the left in Fig. 141.16(a) is the stalk holding the target, which is located behind the capsule in Fig. 141.16(b) and is not visible in the equatorial data. In the case of the equatorial image, the implosion shape exhibits visible low-mode asymmetry, with, e.g., a noticeable P_6 mode of $P_6/P_0 \approx 2.5\%$. In contrast, the polar image is far more symmetric and the Legendre analysis gives $P_6/P_0 \approx 0.2\%$. This difference in asymmetry is a result of the NIF beam geometry for x-ray drive; it impacts the target illumination as seen from the equator. This is compounded by the use of indirect-drive phase plates that are not optimized for PDD illumination. The polar image is significantly more symmetric because the beams are arranged azimuthally symmetric around the target.

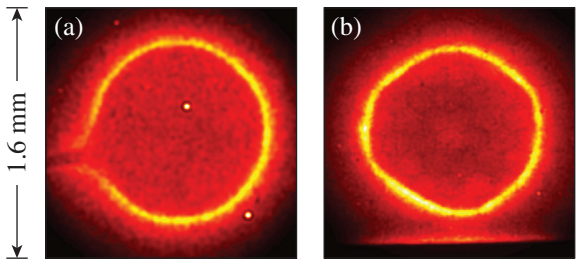

E23672JR

Figure 141.16
Self-emission images of an imploding PDD capsule on shot N131210 as seen from (a) the polar direction at 7.0 ns and (b) the equator at 7.3 ns.

Symmetry data extracted from equatorial self-emission images such as Fig. 141.16(b) are shown in Fig. 141.15 as the square data points. It should be noted that these data were not acquired on the same shot as the radiography images (diamonds). For both experiments, the target parameters such as target size, shell thickness, and gas fill, as well as the incident laser power and beam pointing, were nearly identical. The two measurement techniques—radiography and self-emission imaging—probe different surfaces of the target, which do not necessarily exhibit the same low-mode asymmetry. Since the shell is relatively thin compared to the wavelengths of the modes plotted in Fig. 141.15, it is not surprising that the data generally show comparable modal amplitudes with excellent reproducibility between shots. The self-emission data show considerably less scatter because of the intrinsically higher resolution of the well-defined inner-gradient feature in the self-emission images. This validates using self-emission imaging as a tool for tracking low-mode asymmetries in PDD implosion experiments.

Also shown in Fig. 141.15 are results of the simulated mode evolution from 2-D *DRACO* simulations for shot N131210 [self-emission data (squares)]. Similar to the trajectory data in Fig. 141.14, calculations with (blue solid line) and without (black dashed line) CBET are shown. The biggest difference is observed for the P_2 mode, which evolves in the no-CBET case with a positive P_2 amplitude (prolate) with the equator slightly overdriven with respect to the pole. In contrast, the CBET calculation predicts a negative P_2 (oblate) with an underdriven equatorial region [see also Figs. 141.13(b) and 141.13(c)]. For modes P_4 and P_6, the differences between the two simulations are small, further underlining the importance of CBET on the equatorial energy deposition in PDD geometry. The negative P_2 observed in the CBET calculation qualitatively matches the experimentally observed P_2 evolution, although the calculation underpredicts the P_2 amplitude by ~50%. The same trend is seen for the P_6 evolution, although the no-CBET calculation is slightly closer to the experiment than the CBET calculation. The biggest discrepancy between simulations and experiment is observed for the P_4 amplitudes, with simulations predicting a distinctly negative P_4, whereas the experimental data exhibit a marginally positive P_4 at a few percent. This discrepancy may be caused by 3-D effects that are not modeled with 2-D *DRACO*. The intensity distribution on the target is inherently three dimensional, and a 2-D calculation is not expected to fully capture these details. Three-dimensional simulations with the hydrodynamic code *HYDRA*[44] are being planned to investigate these effects.

A primary goal of the early NIF PDD experiments was to demonstrate tunability of the implosion symmetry. Figures 141.17(a) and 141.17(b) show equatorial self-emission images from two separate shots, both recorded at a CR ~ 2. The first shot [Fig. 141.17(a)] exhibited a pronounced P_6, and a subsequent shot [Fig. 141.17(b)] was tuned specifically to reduce the P_6 amplitude by adjusting the beam pointing and

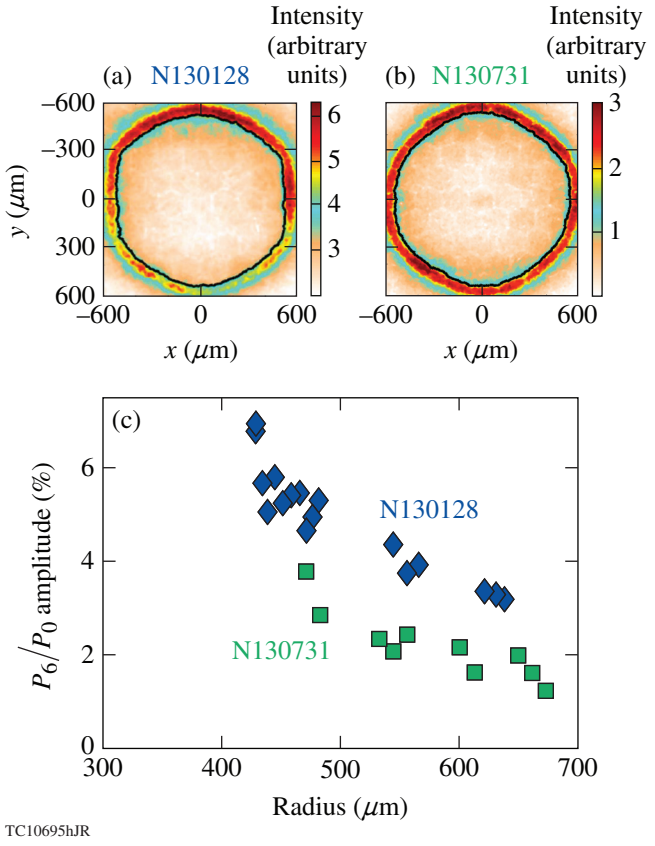

Figure 141.17
Demonstration that improved symmetry can be obtained by tuning beam pointing and the power balance between NIF cones. [(a),(b)] Equatorial self-emission images of shots N130128 (before retuning) and N130731 (after retuning), both at a convergence ratio (CR) ~ 2. (c) P_6 amplitude normalized to the shell radius as a function of the shell radius, with time going from right to left. Shot N130128 [(a) and diamonds in (c)] exhibits a pronounced P_6 amplitude, which was reduced by ~50% in N130731 [(b) and squares in (c)].

power balance. The respective P_6/P_0 evolution is shown in Fig. 141.17(c). The P_6 amplitude was reduced by ~50% between the two experiments, consistent with amplitudes observed in subsequent implosions [see, e.g., Fig. 141.15(c)], but is still non-negligible. Given the currently available NIF hardware optimized for x-ray drive platforms, there are limitations to the level of achievable symmetry. To improve on the uniformity achievable with the current indirect-drive phase plates, PDD phase plates are currently in production to optimize the irradiation profile and generate more-symmetric implosions.[10] The phase plates will correct the reduced hydroefficiency near the equator with a focal-spot profile containing a secondary ellipse. First experiments with these phase plates are anticipated in 2017. It should be noted that the currently available phase plates and achievable symmetry are adequate for the initial primary goals of the PDD campaign, i.e., to study laser coupling, symmetry tunability, and LPI's under NIF-relevant conditions.

The primary purpose of the self-emission imaging is to extract symmetry information, but it is also possible to track the implosion trajectory via the ablation surface. Figure 141.18 shows trajectory data extracted from self-emission images (squares) obtained on shot N140612-001, one of the two shots for which the radiography data are shown in Fig. 141.14. Figure 141.18 also shows 2-D *DRACO* simulations of the ablation-surface trajectory (solid line). In this case, only the calculation including CBET is shown. As with the x-ray radiography, simulated self-emission images were generated by post-processing *DRACO* simulations with *Spect3D*.[39] It can be seen that, as the implosion progresses, the self-emission data increasingly lag the simulation results, with a delay of nearly 700 ps for the latest measurements at ~7 ns. This is in contrast to the trajectory extracted from radiography data (Fig. 141.14), which agrees reasonably well with the simulations. This effect may be partially explained by nonuniformity growth on the ablation surface or preheat from the corona, both of which can result in decoupling the ablation surface from the shell. The outer-surface root-mean-square (rms) roughness of these targets is nearly a factor of 4 higher than the NIF standard (55-nm rms between modes 51 to 1000 compared to 14-nm rms). In addition, the indirect-drive beam smoothing is lower than that required for high-convergence direct-drive implosions,[10] and instability growth from laser-seeded imprint may be significant in these experiments.

This expectation is corroborated by measurements of the areal density (ρR), which typically range from 120 to 150 mg/cm^2, while simulations predict 120 to 280 mg/cm^2, depending on the time of measurement. The areal density is measured at the time of peak fusion yield via the downshifted proton spectrum,[37] and

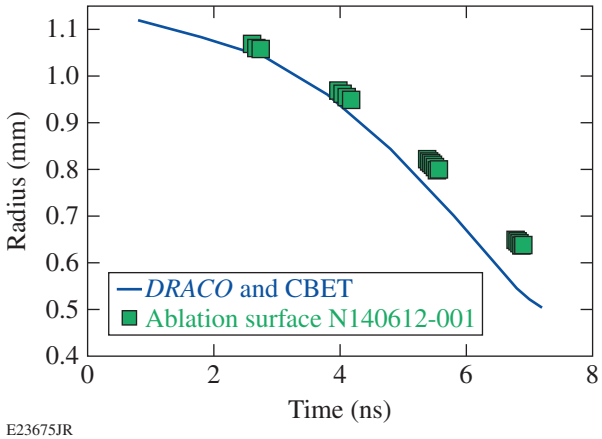

Figure 141.18
Comparison of trajectory data extracted from self-emission images (squares) and 2-D *DRACO* simulations with CBET (solid line).

it is possible that this is not equivalent to the time of peak ρR in the simulations. Uncertainties in the shell trajectory and the time of peak emission result in a range of possible values for areal density from the simulations. For example, instability growth on the inside of the ablator may penetrate into the hot spot and quench the fusion reactions early compared with simulations, as has been observed in OMEGA implosions.[45] Future experiments will investigate Rayleigh–Taylor growth from laser imprint and shell nonuniformities in PDD geometry.[46] Improved beam smoothing is a required capability for full-scale, PDD-ignition experiments (see also **Future Experiments and Additional NIF Capabilities**, p. 24). In conclusion, while the agreement between simulation results and the measured shell trajectory (as given by the radiography data) provides some confidence in the modeling of laser-energy coupling to shell kinetic energy, the mismatch with the self-emission data and the role of nonuniformity growth must be better understood.

Two-Plasmon Decay in Polar Direct Drive

Both planar[31,47] and spherical implosion experiments[48,49] on the OMEGA Laser System[12] have demonstrated the production of a hot tail on the electron distribution function that has been associated with the TPD instability.[48] This association has been determined on the basis of the temporal coincidence between half- and three-halves-harmonic emission and hard x-ray production.[48] For long-scale-length (~350-μm) targets irradiated at the highest overlapped (vacuum) laser intensities (~7×10^{14} W/cm^2), this tail was shown to exhibit a slope temperature of 60 to 80 keV (Refs. 47 and 50) and contain a few percent of the total incident laser energy.

In direct-drive experiments, TPD is a multibeam instability that requires several laser beams to cooperate (by sharing decay waves) in order to overcome the instability threshold[51] that is assumed to arise primarily because of density inhomogeneity (characterized by the scale length L_n). Expressions for the threshold of multibeam TPD were obtained by *ad hoc* use of the Simon *et al*. threshold,[48,52] by computing the maximum convective gain for common waves,[53] or by numerical solution of the TPD equations in three dimensions.[54] In all cases the threshold for the onset of the TPD instability is seen to depend on the quantity $I_L L_n / T_e$, where I_L is the overlapped intensity *resulting from a subset of the incident beams* (determined by a symmetry condition), L_n is the density scale length, and T_e is the electron temperature. Additional factors modifying the threshold arise as a result of beam polarization and beam-incidence angles.[55] A simple extrapolation of OMEGA/OMEGA EP data to the NIF (i.e., by computing $I_L L_n / T_e$ with the total overlapped intensity) would suggest that similar, or greater, levels of hot electrons are to be expected in PDD-ignition targets, mainly because of the larger scale length but partially mitigated by higher coronal temperatures. These levels would lead to an unacceptable amount of preheat. However, significant differences exist between experiments on OMEGA and the NIF that may result in different TPD behavior—these motivate, in part, the present experiments. In NIF PDD experiments many more beams are overlapped. The beam symmetry and incidence angles also differ, leading to uncertainties in which beams are to be included when computing the overlapped intensity. It is speculated that because of the characteristics of the beam overlap on the target, the TPD instability will be able to share decay waves most effectively along the polar axis and around the equatorial region.

The TPD instability can be identified via the energetic electrons and hard x rays that it produces. Hard x-ray spectra are measured in NIF PDD experiments with the FFLEX diagnostic,[22] measuring the temporal history of the bremsstrahlung spectrum in the 20- to 500-keV range using ten individually filtered, time-resolved detectors. It provides the basis for extracting the characteristics of the hard x-ray spectrum and consequently the energetic electron distribution.[56,57] FFLEX integrates the x-ray emission over a field of view of ~100 mm at target chamber center without spatial resolution.

A typical hot-electron spectrum produced in a NIF PDD experiment (shot N131210) is shown in Fig. 141.19. For this shot, a total laser energy of E_L = 609 kJ was incident on the target, corresponding to a nominal overlapped intensity at the target surface (r = 1.1 mm) of 8×10^{14} W/cm^2. *DRACO*

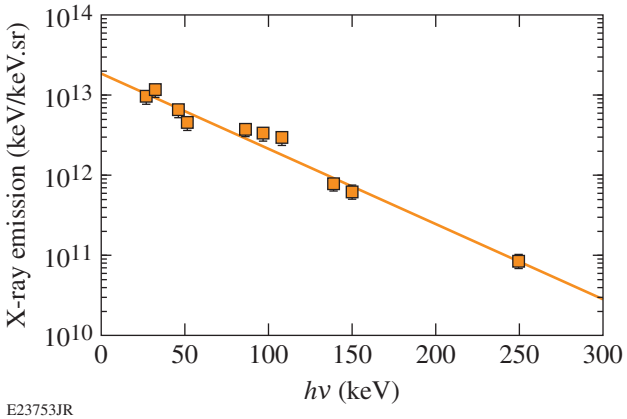

Figure 141.19
Time-integrated FFLEX analysis for shot N131210. The squares denote total emission as measured by the FFLEX detector; the solid line is the fitted x-ray spectrum giving a hot-electron component in the experiment at a temperature of 46±2 keV and with a total energy content of 2.5±0.3 kJ.

simulations (including CBET) suggest that, at the time of strong hot-electron production (t = 6 ns), the peak intensity (polar angle averaged) at the quarter-critical density surface was ~3.5 × 10^{14} W/cm^2, with a density scale length of ~360 μm and a coronal temperature of ~3.2 keV (Table 141.I). For later times (t = 7 ns) the quarter-critical intensity, density scale length, and electron temperature increase slightly (by ~10%, ~5%, and 10%, respectively). In Fig. 141.19 the squares show the measured, time-integrated x-ray emission for the ten FFLEX channels, and the solid line represents the one-temperature, x-ray emission fit through the data. The standard fit to the FFLEX data yields a time-averaged temperature of T_e ~ 46±2 keV, with a total energy content in the hot electrons of E_{hot} ~ 2.5±0.3 kJ. This temperature is consistent with recent experiments on the OMEGA Laser System,[49] where TPD is known with some certainty to be the origin. For this analysis it was assumed that hot electrons deposit their energy in the plastic ablator, with negligible attenuation of the x-ray emission in the shell material or the coronal plasma. In contrast to typical two-temperature distributions for indirect-drive ICF platforms,[58] NIF PDD experiments are typically well fit by a one-temperature distribution.

The hot electrons observed here are attributed to TPD rather than stimulated Raman scattering (SRS). SRS hot electrons are typically expected to be of somewhat lower temperatures (i.e., as observed by Döppner *et al.*[58] in indirect-drive experiments). The scattered-light spectrum (Fig. 141.20) collected in the FABS diagnostic located in beam 315, quad Q31B, indicates that SRS is excited, but the low measured SRS reflectivity <0.1% is not consistent with a 0.4% energetic electron fraction (as deduced from FFLEX data). This conclusion does not take into account illumination nonuniformities that may drive SRS in places not observable by the FABS (i.e., at the target equator, beam 315 irradiates the mid-latitudes of the southern

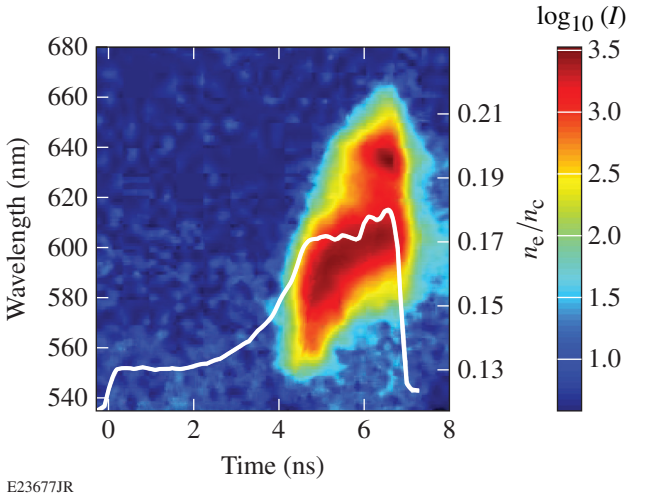

Figure 141.20
Stimulated Raman scattering spectrum obtained on shot N140816 using the full-aperture backscatter station (FABS) in quad Q31B at a polar angle of θ = 152°. The white line is the incident laser power in the experiment.

hemisphere of the target at a polar angle of θ ~ 152°). Figure 141.20 shows that the SRS spectrum increases in time from wavelengths of 550 nm to 650 nm, corresponding to a shift in the maximum electron density of the SRS active region from 0.13 n_c to 0.22 n_c, where n_c is the critical density. It is speculated that the SRS region moves to higher densities with time because of the $I_L L_n / T_e$ dependence of the SRS convective gain.

A time-resolved FFLEX analysis of the same shot (N131210) is shown in Figs. 141.21(a) and 141.21(b). In both plots the squares are experimental data and the dashed lines denote the incident total laser power in the experiment as a temporal reference. The temperature history [Fig. 141.21(a)] shows T_e ~ 47 keV during the peak intensity portion of the incident laser pulse, with no hard x-ray emission observed during the foot up to ~4 ns. The time-resolved, total cumulative conver-

Table 141.I: Representative parameters for the PDD experiments shown in Fig. 141.22. The laser intensity, density scale length L_n, and electron temperature T_e are evaluated from *DRACO* calculations (averaged over polar angle θ), including CBET (except where noted), at the quarter-critical density surface for t = 6 ns. The threshold parameter η is described in the text.

Ablator material	Nominal laser intensity (W/cm^2)	Energy on target E_L (kJ)	I_L (W/cm^2)	L_n (μm)	T_e (keV)	η
CH	8 × 10^{14}	490 to 660	3.5 × 10^{14} 5.5 × 10^{14} (no CBET)	360	3.2	1.7
CH	1.2 × 10^{15}	645	4.6 × 10^{14} 6.1 × 10^{14} (no CBET)	360	3.5	2.0
CH + Si	1.2 × 10^{15}	760	4.6 × 10^{14} 6.7 × 10^{14} (no CBET)	310	4.5	1.4

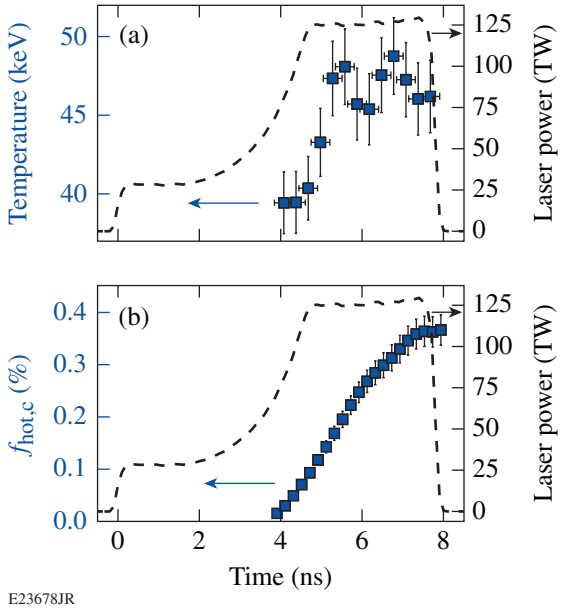

Figure 141.21
Time-resolved FFLEX analysis for shot N131210 (compare Fig. 141.20). The dashed line is the total incident laser power. (a) The hot-electron temperature and (b) the time-resolved, total conversion efficiency of incident laser energy into hot electrons. At the end of the laser pulse, ~0.4% of the incident energy has been converted into energetic electrons.

sion efficiency of incident laser energy into hot electrons $f_{\mathrm{hot,c}}(t)$ [Fig. 141.21(b)] is a guide to target preheat. This efficiency is defined by

$$f_{\mathrm{hot,c}}(t) = \int_0^t E_{\mathrm{hot}}(t')\mathrm{d}t' \Big/ \int_0^t E_{\mathrm{L}}(t')\mathrm{d}t',$$

where $E_{\mathrm{hot}}(t)$ and $E_{\mathrm{L}}(t)$ are the instantaneous energy converted into hot electrons and the incident laser energy, at time t, respectively. The sharp rise, starting at $t \sim 4$ ns, is followed by a roll-over and saturation near the end of the laser pulse, leading to a total conversion efficiency of $f_{\mathrm{hot}} \sim 0.4\%$.

The total hot-electron fraction $f_{\mathrm{hot}} = E_{\mathrm{hot}}/E_{\mathrm{L}}$ is shown in Fig. 141.22 for six PDD shots. Data obtained at nominal overlapped intensities of ~8×10^{14} W/cm^2 with various pulse durations (6.8 to 8.5 ns, E_{L} = 490 to 660 kJ) are marked as the open circles. These data exhibit hot-electron fractions of $f_{\mathrm{hot}} \sim 0.4\%$ characterized by a temperature of $T_{\mathrm{e}} \sim$ 50 keV.

It is estimated that if more than ~0.15% of the laser energy is coupled into a direct-drive–ignition target in the form of hot electrons, the target performance will be negatively affected.[59] To compute the preheat resulting from a given hot-electron source, several factors must be taken into account.[49] Based on the results of Yaakobi *et al.*,[49] it is estimated that ~25% of the hot electrons produced will intersect the target and result in preheat. This leads to an estimated upper limit of ~0.6% for the tolerable hot-electron production in PDD-ignition experiments. The observed hot-electron generation in current NIF PDD experiments with nominal intensities of 8×10^{14} W/cm^2 falls below this limit and is therefore a promising result. Nonetheless, the current experiments are not full scale, and CBET is expected to have lowered the intensity at $n_{\mathrm{c}}/4$ (Table 141.I). It is therefore essential that mitigation schemes be investigated and experiments be performed at a higher laser intensity and longer scale length (at the $n_{\mathrm{c}}/4$ surface).

It has been observed in experiments on OMEGA,[47,60] and discussed in Refs. 48 and 61, that higher-Z coronal plasmas lead to a reduction in TPD hot electrons and increase the threshold intensity for its onset. The addition of an outer 13.5-μm Si layer to the plastic ablator has been investigated as a possible miti-

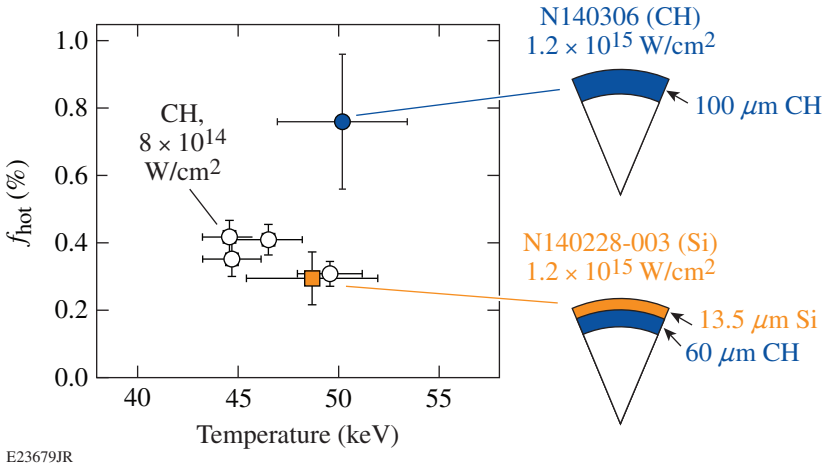

Figure 141.22
Hot-electron fraction from six PDD targets, mostly CH, irradiated with nominal peak intensity of 8×10^{14} W/cm^2 (open circles). Two shots were taken at 1.2×10^{15} W/cm^2; one with a CH ablator (solid circle), the other with a Si ablator (solid square).

gation strategy on NIF shot N140228-003. This is compared in Fig. 141.22 with a standard CH target (shot N140306), both of which were driven with a higher peak laser power of ~180 TW, corresponding to a nominal overlapped peak intensity of 1.2×10^{15} W/cm^2. The same foot intensity of ~30 TW was used as for the experiments with a nominal intensity of 8×10^{14} W/cm^2. The pulse driving the Si-layer target implosion was slightly longer by 0.5 ns, corresponding to a total incident energy of 760 kJ, compared to 645 kJ incident onto the pure-CH ablator target (Table 141.I). The hot-electron data for these two experiments are displayed as the blue solid circle (CH ablator) and the orange solid square (Si ablator) in Fig. 141.22. The hot-electron fraction for the $I_L = 1.2 \times 10^{15}$ W/cm^2, plastic-ablator experiment approximately doubled to $f_{hot} \sim 0.8\%$, while the Si-ablator experiment saw a reduction in the hot-electron fraction to $f_{hot} \sim 0.3\%$ (both relative to the 8×10^{14} W/cm^2 CH experiments). Since FFLEX does not identify the origin of the x rays, an assumption must be made about the material in which hot electrons lose their energy via bremsstrahlung emission. For the analysis of the Si-layer capsule displayed in Fig. 141.22, it was assumed that the Si was fully ablated and the electrons deposited their energy solely in the unablated plastic shell, with no attenuation of the x-ray emission by the coronal plasma. Since the thick-target bremsstrahlung equation (relating x-ray emission to hot-electron population) scales linearly with the effective Z of the target material, assuming electrons deposit their energy in both CH and Si, would necessarily further reduce the inferred energy in the hot-electron population. The analysis of the Si-ablator shot displayed in Fig. 141.22 is therefore a pessimistic interpretation. The actual hot-electron fraction may be lower and the mitigating effect greater than indicated in Fig. 141.22.

The lower observed hot-electron fraction in the Si-ablator target is consistent with an increased TPD threshold based on the simple $I_L L_n / T_e$ scaling. In previous OMEGA experiments TPD signatures were observed when the parameter $\eta = I_L L_n / 233 T_e$ exceeded unity. In this expression, I_L is in units of 10^{14} W/cm^2, L_n is in μm, and T_e is in keV. This empirical scaling is based on the Simon threshold for the absolute instability of a single plane wave.[52] It was generalized by Seka *et al.*[48] in an *ad hoc* way by substituting the total overlapped laser intensity at the $n_c/4$ surface in place of the single-plane wave intensity assumed by the theory. When this was done, the onset of TPD was well modeled over a range of different experiments on OMEGA. Table 141. I shows that, for the $I_L = 8 \times 10^{14}$ W/cm^2 reference case, $\eta = 1.7$ and TPD is expected (and observed) to be above threshold. The increase in hot electrons for the high-intensity CH ablator is consistent with the larger value of $\eta = 2.0$. This increase in η is a result of a combination of larger scale length and higher laser intensity. In contrast, the Si-ablator experiment is predicted to have a reduced scale length, and a significantly higher electron temperature. As a result, the η parameter is lower ($\eta = 1.4$) than the reference experiment (marginally above threshold) and the hot-electron fraction behaves accordingly. The total overlapped intensity has been used here in the expression for the threshold parameter η. No account is made for beam symmetry requirements that are known to play a role in multibeam TPD.[54,62] These requirements would lead to a lower effective overlapped intensity.

Higher-Z ablator materials have disadvantages, such as a lower hydrodynamic efficiency, reduced heat conduction, and potential radiation preheat of the target core. Pure-Si ablators are, therefore, not an attractive solution for TPD mitigation. Therefore, current PDD-ignition target designs utilize multiple layers for an optimized coronal plasma[63] that include a thin mid-Z layer (e.g., Si) for LPI mitigation inside lower-Z material with better hydrodynamic performance.

Future Experiments and Additional NIF Capabilities

The PDD campaign on the NIF has started to investigate direct drive in integrated implosion experiments. It is clear that a detailed understanding of the physics governing implosion performance at NIF conditions and ignition scales will require dedicated platforms to decouple individual aspects of the implosion. In particular, hydrodynamic instability growth has been identified as an important factor in understanding the discrepancy between the simulated and measured shell trajectories (see **Shell Trajectory and Symmetry**, p. 17). Future experiments will investigate Rayleigh–Taylor growth[41] from shell surface perturbations and laser imprint in a spherical-implosion PDD platform on the NIF using cone-in-shell targets. Similar experiments have been used successfully to measure Rayleigh–Taylor growth in spherical convergent geometry for indirect drive on the NIF[64] and direct drive on OMEGA.[65]

It has been suggested that CBET is responsible for a significant reduction in absorption efficiency of the incident laser power, particularly near the equator (see **Shell Trajectory and Symmetry**, p. 17), and mitigating CBET is of key importance for developing a robust PDD-ignition platform for the NIF. A viable mitigation strategy for CBET is to introduce a wavelength separation between interacting beams.[63,66] To mitigate CBET in PDD experiments on the NIF, a hemispheric laser wavelength separation in excess of ±5 Å at $\lambda = 351$ nm has been proposed,[67,68] such that beams incident on the equa-

tor from the upper and lower hemispheres are separated in wavelength by >10 Å. This is expected to reduce the volume over which efficient CBET gain can occur at the equator and to recover a significant fraction of the CBET-incurred losses. The current NIF front end supports tunable wavelengths of up to approximately ±2.5 Å for each of the inner beam cones at 23.5° and 30° and for both outer cones combined (44.5° and 50°). This is insufficient for optimized CBET mitigation in NIF PDD implosions but is expected to be adequate to test this mitigation scheme. Using the nominal PDD pointing, only the outer-cone beams are incident near the equator of the target and wavelength separation at the equator is currently not supported. However, to test this CBET mitigation scheme, a hemispheric $\Delta\lambda$ shift can be achieved by repointing beams in one hemisphere such that inner-cone beams drive the equator from one hemisphere and overlap with outer-cone beams from the opposite side. With different wavelengths for inner and outer cones, this results in a nonzero, equatorial wavelength separation. The currently achievable wavelength detuning of ±2.5 Å between inner and outer cones is anticipated to increase the absorption fraction by ~5%, corresponding to ~25% of the total CBET-incurred losses.

It is important to understand hot-electron generation in NIF PDD implosions, and it is expected that successful CBET mitigation will result in an increase of the effective laser intensity at quarter-critical density and therefore an increase in the TPD gain, as discussed in **Two-Plasmon Decay in Polar Direct Drive** (p. 21). The TPD instability is believed to be strongest along the polar axis and around the equator, but it is difficult to decouple the contributions of these two locations in integrated implosion experiments. Future experiments will use planar targets to approximate the laser–target interactions and coronal conditions at the pole and the equator of a PDD target. This will be used to investigate the effect of the beam angle of incidence on the TPD instability and hot-electron production at NIF-relevant scale lengths and temperatures. Importantly, since planar targets exhibit a very high absorption efficiency, CBET seeded by backscattered light is not expected to be a significant source of laser-energy losses in these experiments.

In addition to a hemispheric wavelength separation capability with $\Delta\lambda > 5$ Å for CBET mitigation, additional NIF capabilities and hardware are required to support ignition-scale, cryogenic PDD experiments on the NIF. These are being implemented by the NIF PDD Laser Path Forward working group. The achievable uniformity in current direct-drive experiments is limited by the use of defocused indirect-drive phase plates; dedicated PDD phase plates are required for high-convergence implosions. These are in production and first experiments with these phase plates are anticipated for 2017.

High beam-smoothing rates are required to limit the imprint of laser nonuniformities that can disrupt the implosion. Some instability mitigation is provided by the SSD system currently installed on the NIF,[16,17] but this is less than that required for PDD-ignition experiments.[10] One-dimensional SSD with multiple phase-modulation frequencies (multi-FM 1-D SSD)[69] has been developed at LLE to provide the smoothing level required for the current NIF polar-direct-drive–ignition point design. It is compatible with the existing NIF Laser System, and modifications required to implement multi-FM 1-D SSD on the NIF are limited to fiber-based systems in the Master Oscillator Room, in addition to a new diffraction grating in the preamplifier module.[10]

Polarization smoothing overlaps beams or beamlets of orthogonal polarization, to suppress interference between speckle patterns from different beamlets.[70] This provides instantaneous smoothing in addition to the SSD system.[71] The polarization smoothing currently used on the NIF employs a polarization rotation of two beams per quad to smooth out interference modulations between beams within a quad. This provides smoothing only of micron-scale speckle, however, which does not affect direct-drive uniformity,[10] and relies on beam overlap within a quad. Polarization smoothing based on glancing angle deposited (GLAD) film is being explored for PDD on the NIF.[72] The proposed polarization smoothing for PDD will be applied to each beam individually to generate two overlapping and noninterfering speckle patterns of orthogonal polarizations per beam.

Finally, modifications to the NIF's Target Handling and Positioning Systems are required to support the fielding of cryogenically cooled, layered direct-drive targets.

Conclusions

Results from a first series of PDD experiments on the NIF have been presented. The campaign is based on polar and symmetric direct-drive experiments performed on the OMEGA laser, which provide a solid foundation for the PDD campaign on the NIF. Room-temperature, 2.2-mm-diam plastic shells were imploded with total drive energies of ~500 to 750 kJ with peak powers of 120 to 180 TW and peak on-target intensities from 8×10^{14} to 1.2×10^{15} W/cm^2. The trajectory and low-mode asymmetry evolution of the imploding shell were measured with x-ray radiography to track the dense shell and with self-emission imaging of the coronal plasma to measure

the ablation surface. Agreement with 2-D *DRACO* simulations was found to improve when the effect of CBET was included in the calculations. These simulations reproduce the radiography data reasonably well, but the ablation surface trajectory is delayed, when compared with simulations, by several hundred picoseconds. Both radiography and self-emission images are reproduced qualitatively by the 2-D *DRACO* simulations, but it is expected that a 3-D treatment is required to fully capture the measured implosion shape.

Evidence of the TPD instability was found by the emission of hard x rays associated with energetic electrons. The hot-electron population for experiments with a nominal intensity of 8×10^{14} W/cm^2 was found to exhibit temperatures of ~45 to 50 keV with a total conversion efficiency of laser energy to hot electrons of ~0.4%. At higher intensities of 1.2×10^{15} W/cm^2, this increased to ~0.8%, while a high-intensity experiment using a Si ablator exhibited only ~0.3% conversion efficiency.

Future dedicated experiments will investigate Rayleigh–Taylor growth from shell surface perturbations and laser imprint in a spherical-implosion PDD platform on the NIF using cone-in-shell targets, CBET mitigation via a hemispheric $\Delta\lambda$ shift, and TPD scaling with plasma scale length and coronal temperature in planar targets.

Additional capabilities and hardware are required to support ignition-scale, cryogenic PDD experiments on the NIF. These capabilities include hemispheric $\Delta\lambda$, improved beam smoothing, dedicated PDD phase plates, and a direct-drive cryogenic target positioner system for direct-drive targets.

ACKNOWLEDGMENT

We gratefully acknowledge support by S. Ayers and I. E. Scott (Lawrence Livermore National Laboratory) as well as C. Robillard and M. J. Shoup III (Laboratory for Laser Energetics) for providing the figure of the NIF target chamber (Fig. 141.9).

This material is based upon work supported by the Department of Energy National Nuclear Security Administration under Award Number DE-NA0001944, the University of Rochester, the New York State Energy Research and Development Authority, and Lawrence Livermore National Laboratory (LLNL-JRNL-664443). The support of DOE does not constitute an endorsement by DOE of the views expressed in this article.

REFERENCES

1. J. Nuckolls *et al*., Nature **239**, 139 (1972).
2. J. D. Lindl, *Inertial Confinement Fusion: The Quest for Ignition and Energy Gain Using Indirect Drive* (Springer-Verlag, New York, 1998).
3. S. Atzeni and J. Meyer-ter-Vehn, *The Physics of Inertial Fusion: Beam Plasma Interaction, Hydrodynamics, Hot Dense Matter, International Series of Monographs on Physics* (Clarendon Press, Oxford, 2004).
4. R. L. McCrory, D. D. Meyerhofer, R. Betti, R. S. Craxton, J. A. Delettrez, D. H. Edgell, V. Yu. Glebov, V. N. Goncharov, D. R. Harding, D. W. Jacobs-Perkins, J. P. Knauer, F. J. Marshall, P. W. McKenty, P. B. Radha, S. P. Regan, T. C. Sangster, W. Seka, R. W. Short, S. Skupsky, V. A. Smalyuk, J. M. Soures, C. Stoeckl, B. Yaakobi, D. Shvarts, J. A. Frenje, C. K. Li, R. D. Petrasso, and F. H. Séguin, Phys. Plasmas **15**, 055503 (2008).
5. S. W. Haan, J. D. Lindl, D. A. Callahan, D. S. Clark, J. D. Salmonson, B. A. Hammel, L. J. Atherton, R. C. Cook, M. J. Edwards, S. Glenzer, A. V. Hamza, S. P. Hatchett, M. C. Herrmann, D. E. Hinkel, D. D. Ho, H. Huang, O. S. Jones, J. Kline, G. Kyrala, O. L. Landen, B. J. MacGowan, M. M. Marinak, D. D. Meyerhofer, J. L. Milovich, K. A. Moreno, E. I. Moses, D. H. Munro, A. Nikroo, R. E. Olson, K. Peterson, S. M. Pollaine, J. E. Ralph, H. F. Robey, B. K. Spears, P. T. Springer, L. J. Suter, C. A. Thomas, R. P. Town, R. Vesey, S. V. Weber, H. L. Wilkens, and D. C. Wilson, Phys. Plasmas **18**, 051001 (2011).
6. G. H. Miller, E. I. Moses, and C. R. Wuest, Opt. Eng. **43**, 2841 (2004).
7. S. W. Haan *et al*., Phys. Plasmas **2**, 2480 (1995).
8. D. Eimerl, ed., Lawrence Livermore National Laboratory, Livermore, CA, Report UCRL-ID-120758 (1995).
9. S. Skupsky, J. A. Marozas, R. S. Craxton, R. Betti, T. J. B. Collins, J. A. Delettrez, V. N. Goncharov, P. W. McKenty, P. B. Radha, T. R. Boehly, J. P. Knauer, F. J. Marshall, D. R. Harding, J. D. Kilkenny, D. D. Meyerhofer, T. C. Sangster, and R. L. McCrory, Phys. Plasmas **11**, 2763 (2004).
10. T. J. B. Collins, J. A. Marozas, K. S. Anderson, R. Betti, R. S. Craxton, J. A. Delettrez, V. N. Goncharov, D. R. Harding, F. J. Marshall, R. L. McCrory, D. D. Meyerhofer, P. W. McKenty, P. B. Radha, A. Shvydky, S. Skupsky, and J. D. Zuegel, Phys. Plasmas **19**, 056308 (2012).
11. P. B. Radha, F. J. Marshall, J. A. Marozas, A. Shvydky, I. Gabalski, T. R. Boehly, T. J. B. Collins, R. S. Craxton, D. H. Edgell, R. Epstein, J. A. Frenje, D. H. Froula, V. N. Goncharov, M. Hohenberger, R. L. McCrory, P. W. McKenty, D. D. Meyerhofer, R. D. Petrasso, T. C. Sangster, and S. Skupsky, Phys. Plasmas **20**, 056306 (2013).
12. T. R. Boehly, D. L. Brown, R. S. Craxton, R. L. Keck, J. P. Knauer, J. H. Kelly, T. J. Kessler, S. A. Kumpan, S. J. Loucks, S. A. Letzring, F. J. Marshall, R. L. McCrory, S. F. B. Morse, W. Seka, J. M. Soures, and C. P. Verdon, Opt. Commun. **133**, 495 (1997).
13. V. N. Goncharov, T. C. Sangster, T. R. Boehly, S. X. Hu, I. V. Igumenshchev, F. J. Marshall, R. L. McCrory, D. D. Meyerhofer, P. B. Radha, W. Seka, S. Skupsky, C. Stoeckl, D. T. Casey, J. A. Frenje, and R. D. Petrasso, Phys. Rev. Lett. **104**, 165001 (2010).
14. T. C. Sangster, V. N. Goncharov, R. Betti, P. B. Radha, T. R. Boehly, D. T. Casey, T. J. B. Collins, R. S. Craxton, J. A. Delettrez, D. H. Edgell, R. Epstein, C. J. Forrest, J. A. Frenje, D. H. Froula, M. Gatu-Johnson, V. Yu. Glebov, D. R. Harding, M. Hohenberger, S. X. Hu, I. V. Igumenshchev, R. Janezic, J. H. Kelly, T. J. Kessler, C. Kingsley,

T. Z. Kosc, J. P. Knauer, S. J. Loucks, J. A. Marozas, F. J. Marshall, A. V. Maximov, R. L. McCrory, P. W. McKenty, D. D. Meyerhofer, D. T. Michel, J. F. Myatt, R. D. Petrasso, S. P. Regan, W. Seka, W. T. Shmayda, R. W. Short, A. Shvydky, S. Skupsky, J. M. Soures, C. Stoeckl, W. Theobald, V. Versteeg, B. Yaakobi, and J. D. Zuegel, Phys. Plasmas **20**, 056317 (2013).

15. P. J. Wegner *et al*., in *Optical Engineering at the Lawrence Livermore National Laboratory II: The National Ignition Facility*, edited by M. A. Lane and C. R. Wuest (SPIE, Bellingham, WA, 2004), Vol. 5341, pp. 180–189.

16. B. J. MacGowan *et al*., Phys. Plasmas **3**, 2029 (1996).

17. C. A. Haynam *et al*., Appl. Opt. **46**, 3276 (2007).

18. A. M. Cok, R. S. Craxton, and P. W. McKenty, Phys. Plasmas **15**, 082705 (2008).

19. P. B. Radha, V. N. Goncharov, T. J. B. Collins, J. A. Delettrez, Y. Elbaz, V. Yu. Glebov, R. L. Keck, D. E. Keller, J. P. Knauer, J. A. Marozas, F. J. Marshall, P. W. McKenty, D. D. Meyerhofer, S. P. Regan, T. C. Sangster, D. Shvarts, S. Skupsky, Y. Srebro, R. P. J. Town, and C. Stoeckl, Phys. Plasmas **12**, 032702 (2005).

20. C. J. Randall, J. R. Albritton, and J. J. Thomson, Phys. Fluids **24**, 1474 (1981).

21. D. T. Michel, C. Sorce, R. Epstein, N. Whiting, I. V. Igumenshchev, R. Jungquist, and D. H. Froula, Rev. Sci. Instrum. **83**, 10E530 (2012).

22. M. Hohenberger, F. Albert, N. E. Palmer, J. J. Lee, T. Döppner, L. Divol, E. L. Dewald, B. Bachmann, A. G. MacPhee, G. LaCaille, D. K. Bradley, and C. Stoeckl, Rev. Sci. Instrum. **85**, 11D501 (2014).

23. M. N. Rosenbluth, R. B. White, and C. S. Liu, Phys. Rev. Lett. **31**, 1190 (1973).

24. J. F. Myatt, J. Zhang, R. W. Short, A. V. Maximov, W. Seka, D. H. Froula, D. H. Edgell, D. T. Michel, I. V. Igumenshchev, D. E. Hinkel, P. Michel, and J. D. Moody, Phys. Plasmas **21**, 055501 (2014).

25. M. V. Goldman, Ann. Phys. **38**, 117 (1966).

26. P. B. Radha, V. N. Goncharov, M. Hohenberger, T. C. Sangster, R. Betti, R. S. Craxton, D. H. Edgell, R. Epstein, D. H. Froula, J. A. Marozas, F. J. Marshall, R. L. McCrory, P. W. McKenty, D. D. Meyerhofer, D. T. Michel, S. X. Hu, W. Seka, A. Shvydky, S. Skupsky, J. A. Frenje, M. Gatu Johnson, R. D. Petrasso, T. Ma, S. Le Pape, and A. J. Mackinnon, "Direct-Drive Implosion Physics: Results from OMEGA and the National Ignition Facility," to be published in the Journal of Physics: Conference Series.

27. J. A. Marozas, F. J. Marshall, R. S. Craxton, I. V. Igumenshchev, S. Skupsky, M. J. Bonino, T. J. B. Collins, R. Epstein, V. Yu. Glebov, D. Jacobs-Perkins, J. P. Knauer, R. L. McCrory, P. W. McKenty, D. D. Meyerhofer, S. G. Noyes, P. B. Radha, T. C. Sangster, W. Seka, and V. A. Smalyuk, Phys. Plasmas **13**, 056311 (2006).

28. W. F. Huebner *et al*., Los Alamos National Laboratory, Los Alamos, NM, Report LA-6760-M (1977).

29. N. A. Ebrahim *et al*., Phys. Rev. Lett. **45**, 1179 (1980).

30. J. F. Myatt, J. Zhang, J. A. Delettrez, A. V. Maximov, R. W. Short, W. Seka, D. H. Edgell, D. F. DuBois, D. A. Russell, and H. X. Vu, Phys. Plasmas **19**, 022707 (2012).

31. B. Yaakobi, P.-Y. Chang, A. A. Solodov, C. Stoeckl, D. H. Edgell, R. S. Craxton, S. X. Hu, J. F. Myatt, F. J. Marshall, W. Seka, and D. H. Froula, Phys. Plasmas **19**, 012704 (2012).

32. J. A. Oertel *et al*., Rev. Sci. Instrum. **77**, 10E308 (2006).

33. G. A. Kyrala *et al*., Rev. Sci. Instrum. **81**, 10E316 (2010).

34. J. D. Moody *et al*., Rev. Sci. Instrum. **81**, 10D921 (2010).

35. V. Yu. Glebov, T. C. Sangster, C. Stoeckl, J. P. Knauer, W. Theobald, K. L. Marshall, M. J. Shoup III, T. Buczek, M. Cruz, T. Duffy, M. Romanofsky, M. Fox, A. Pruyne, M. J. Moran, R. A. Lerche, J. McNaney, J. D. Kilkenny, M. J. Eckart, D. Schneider, D. Munro, W. Stoeffl, R. Zacharias, J. J. Haslam, T. Clancy, M. Yeoman, D. Warwas, C. J. Horsfield, J.-L. Bourgade, O. Landoas, L. Disdier, G. A. Chandler, and R. J. Leeper, Rev. Sci. Instrum. **81**, 10D325 (2010).

36. H. G. Rinderknecht, M. Gatu Johnson, A. B. Zylstra, N. Sinenian, M. J. Rosenberg, J. A. Frenje, C. J. Waugh, C. K. Li, F. H. Séguin, R. D. Petrasso, J. R. Rygg, J. R. Kimbrough, A. MacPhee, G. W. Collins, D. Hicks, A. Mackinnon, P. Bell, R. Bionta, T. Clancy, R. Zacharias, T. Döppner, H. S. Park, S. LePape, O. Landen, N. Meezan, E. I. Moses, V. Yu. Glebov, C. Stoeckl, T. C. Sangster, R. Olson, J. Kline, and J. Kilkenny, Rev. Sci. Instrum. **83**, 10D902 (2012).

37. A. B. Zylstra, J. A. Frenje, F. H. Séguin, M. J. Rosenberg, H. G. Rinderknecht, M. Gatu Johnson, D. T. Casey, N. Sinenian, M. J. E. Manuel, C. J. Waugh, H. W. Sio, C. K. Li, R. D. Petrasso, S. Friedrich, K. Knittel, R. Bionta, M. McKernan, D. Callahan, G. W. Collins, E. Dewald, T. Doppner, M. J. Edwards, S. Glenzer, D. G. Hicks, O. L. Landen, R. London, A. Mackinnon, N. Meezan, R. R. Prasad, J. Ralph, M. Richardson, J. R. Rygg, S. Sepke, S. Weber, R. Zacharias, E. Moses, J. Kilkenny, A. Nikroo, T. C. Sangster, V. Glebov, C. Stoeckl, R. Olson, R. J. Leeper, J. Kline, G. Kyrala, and D. Wilson, Rev. Sci. Instrum. **83**, 10D901 (2012).

38. M. J. Schmitt, P. A. Bradley, J. A. Cobble, J. R. Fincke, P. Hakel, S. C. Hsu, N. S. Krasheninnikova, G. A. Kyrala, G. R. Magelssen, D. S. Montgomery, T. J. Murphy, K. A. Obrey, R. C. Shah, I. L. Tregillis, J. A. Baumgaertel, F. J. Wysocki, S. H. Batha, R. S. Craxton, P. W. McKenty, P. Fitzsimmons, A. Nikroo, and R. Wallace, Phys. Plasmas **20**, 056310 (2013).

39. J. J. MacFarlane *et al*., High Energy Density Phys. **3**, 181 (2007).

40. S. E. Bodner, Phys. Rev. Lett. **33**, 761 (1974).

41. S. Chandrasekhar, in *Hydrodynamic and Hydromagnetic Stability*, International Series of Monographs on Physics (Clarendon Press, Oxford, 1961).

42. D. H. Froula, I. V. Igumenshchev, D. T. Michel, D. H. Edgell, R. Follett, V. Yu. Glebov, V. N. Goncharov, J. Kwiatkowski, F. J. Marshall, P. B.

Radha, W. Seka, C. Sorce, S. Stagnitto, C. Stoeckl, and T. C. Sangster, Phys. Rev. Lett. **108**, 125003 (2012).

43. D. T. Michel, V. N. Goncharov, I. V. Igumenshchev, R. Epstein, and D. H. Froula, Phys. Rev. Lett. **111**, 245005 (2013).

44. M. M. Marinak *et al*., Phys. Plasmas **8**, 2275 (2001).

45. P. B. Radha, C. Stoeckl, V. N. Goncharov, J. A. Delettrez, D. H. Edgell, J. A. Frenje, I. V. Igumenshchev, J. P. Knauer, J. A. Marozas, R. L. McCrory, D. D. Meyerhofer, R. D. Petrasso, S. P. Regan, T. C. Sangster, W. Seka, and S. Skupsky, Phys. Plasmas **18**, 012705 (2011).

46. A. Shvydky, M. Hohenberger, P. B. Radha, R. S. Craxton, V. N. Goncharov, J. A. Marozas, F. J. Marshall, P. W. McKenty, and T. C. Sangster, Bull. Am. Phys. Soc. **59**, 330 (2014).

47. D. H. Froula, D. T. Michel, I. V. Igumenshchev, S. X. Hu, B. Yaakobi, J. F. Myatt, D. H. Edgell, R. Follett, V. Yu. Glebov, V. N. Goncharov, T. J. Kessler, A. V. Maximov, P. B. Radha, T. C. Sangster, W. Seka, R. W. Short, A. A. Solodov, C. Sorce, and C. Stoeckl, Plasma Phys. Control. Fusion **54**, 124016 (2012).

48. W. Seka, D. H. Edgell, J. F. Myatt, A. V. Maximov, R. W. Short, V. N. Goncharov, and H. A. Baldis, Phys. Plasmas **16**, 052701 (2009).

49. B. Yaakobi, A. A. Solodov, J. F. Myatt, J. A. Delettrez, C. Stoeckl, and D. H. Froula, Phys. Plasmas **20**, 092706 (2013).

50. D. H. Froula, B. Yaakobi, S. X. Hu, P.-Y. Chang, R. S. Craxton, D. H. Edgell, R. Follett, D. T. Michel, J. F. Myatt, W. Seka, R. W. Short, A. Solodov, and C. Stoeckl, Phys. Rev. Lett. **108**, 165003 (2012).

51. C. Stoeckl, R. E. Bahr, B. Yaakobi, W. Seka, S. P. Regan, R. S. Craxton, J. A. Delettrez, R. W. Short, J. Myatt, A. V. Maximov, and H. Baldis, Phys. Rev. Lett. **90**, 235002 (2003).

52. A. Simon, R. W. Short, E. A. Williams, and T. Dewandre, Phys. Fluids **26**, 3107 (1983).

53. D. T. Michel, A. V. Maximov, R. W. Short, S. X. Hu, J. F. Myatt, W. Seka, A. A. Solodov, B. Yaakobi, and D. H. Froula, Phys. Rev. Lett. **109**, 155007 (2012).

54. J. Zhang, J. F. Myatt, R. W. Short, A. V. Maximov, H. X. Vu, D. F. DuBois, and D. A. Russell, Phys. Rev. Lett. **113**, 105001 (2014).

55. R. W. Short, J. F. Myatt, and J. Zhang, Bull. Am. Phys. Soc. **58**, 27 (2013).

56. K. A. Brueckner, Phys. Rev. Lett. **36**, 677 (1976).

57. R. P. Drake *et al*., Phys. Rev. A **40**, 3219 (1989).

58. T. Döppner *et al*., Phys. Rev. Lett. **108**, 135006 (2012).

59. J. A. Delettrez, T. J. B. Collins, and C. Ye, Bull. Am. Phys. Soc. **59**, 150 (2014).

60. V. A. Smalyuk, R. Betti, J. A. Delettrez, V. Yu. Glebov, D. D. Meyerhofer, P. B. Radha, S. P. Regan, T. C. Sangster, J. Sanz, W. Seka, C. Stoeckl, B. Yaakobi, J. A. Frenje, C. K. Li, R. D. Petrasso, and F. H. Séguin, Phys. Rev. Lett. **104**, 165002 (2010).

61. J. F. Myatt, H. X. Vu, D. F. DuBois, D. A. Russell, J. Zhang, R. W. Short, and A. V. Maximov, Phys. Plasmas **20**, 052705 (2013).

62. D. T. Michel, A. V. Maximov, R. W. Short, J. A. Delettrez, D. Edgell, S. X. Hu, I. V. Igumenshchev, J. F. Myatt, A. A. Solodov, C. Stoeckl, B. Yaakobi, and D. H. Froula, Phys. Plasmas **20**, 055703 (2013).

63. V. N. Goncharov, T. C. Sangster, R. Betti, T. R. Boehly, M. J. Bonino, T. J. B. Collins, R. S. Craxton, J. A. Delettrez, D. H. Edgell, R. Epstein, R. K. Follet, C. J. Forrest, D. H. Froula, V. Yu. Glebov, D. R. Harding, R. J. Henchen, S. X. Hu, I. V. Igumenshchev, R. Janezic, J. H. Kelly, T. J. Kessler, T. Z. Kosc, S. J. Loucks, J. A. Marozas, F. J. Marshall, A. V. Maximov, R. L. McCrory, P. W. McKenty, D. D. Meyerhofer, D. T. Michel, J. F. Myatt, R. Nora, P. B. Radha, S. P. Regan, W. Seka, W. T. Shmayda, R. W. Short, A. Shvydky, S. Skupsky, C. Stoeckl, B. Yaakobi, J. A. Frenje, M. Gatu Johnson, R. D. Petrasso, and D. T. Casey, Phys. Plasmas **21**, 056315 (2014).

64. V. A. Smalyuk, M. Barrios, J. A. Caggiano, D. T. Casey, C. J. Cerjan, D. S. Clark, M. J. Edwards, J. A. Frenje, M. Gatu-Johnson, V. Yu. Glebov, G. Grim, S. W. Haan, B. A. Hammel, A. Hamza, D. E. Hoover, W. W. Hsing, O. Hurricane, J. D. Kilkenny, J. L. Kline, J. P. Knauer, J. Kroll, O. L. Landen, J. D. Lindl, T. Ma, J. M. McNaney, M. Mintz, A. Moore, A. Nikroo, T. Parham, J. L. Peterson, R. Petrasso, L. Pickworth, J. E. Pino, K. Raman, S. P. Regan, B. A. Remington, H. F. Robey, D. P. Rowley, D. B. Sayre, R. E. Tipton, S. V. Weber, K. Widmann, D. C. Wilson, and C. B. Yeamans, Phys. Plasmas **21**, 056301 (2014).

65. G. Fiksel, S. X. Hu, V. N. Goncharov, D. D. Meyerhofer, T. C. Sangster, V. A. Smalyuk, B. Yaakobi, M. J. Bonino, and R. Jungquist, Phys. Plasmas **19**, 062704 (2012).

66. I. V. Igumenshchev, W. Seka, D. H. Edgell, D. T. Michel, D. H. Froula, V. N. Goncharov, R. S. Craxton, L. Divol, R. Epstein, R. Follett, J. H. Kelly, T. Z. Kosc, A. V. Maximov, R. L. McCrory, D. D. Meyerhofer, P. Michel, J. F. Myatt, T. C. Sangster, A. Shvydky, S. Skupsky, and C. Stoeckl, Phys. Plasmas **19**, 056314 (2012).

67. J. A. Marozas, T. J. B. Collins, P. W. McKenty, J. D. Zuegel, P. B. Radha, F. J. Marshall, W. Seka, D. T. Michel, and M. Hohenberger, Bull. Am. Phys. Soc. **59**, 201 (2014).

68. J. A. Marozas, T. J. B. Collins, J. D. Zuegel, P. B. Radha, F. J. Marshall, and W. Seka, "Cross-Beam Energy Transfer Mitigation Strategy for NIF Polar Drive," presented at the 44th Annual Anomalous Absorption Conference, Estes Park, CO, 8–13 June 2014.

69. J. A. Marozas, J. D. Zuegel, and T. J. B. Collins, Bull. Am. Phys. Soc. **55**, 294 (2010).

70. T. R. Boehly, V. A. Smalyuk, D. D. Meyerhofer, J. P. Knauer, D. K. Bradley, R. S. Craxton, M. J. Guardalben, S. Skupsky, and T. J. Kessler, J. Appl. Phys. **85**, 3444 (1999).

71. S. P. Regan, J. A. Marozas, R. S. Craxton, J. H. Kelly, W. R. Donaldson, P. A. Jaanimagi, D. Jacobs-Perkins, R. L. Keck, T. J. Kessler, D. D. Meyerhofer, T. C. Sangster, W. Seka, V. A. Smalyuk, S. Skupsky, and J. D. Zuegel, J. Opt. Soc. Am. B **22**, 998 (2005).

72. J. B. Oliver, T. J. Kessler, C. Smith, B. Taylor, V. Gruschow, J. Hettrick, and B. Charles, Opt. Express **22**, 23883 (2014).

Impact of First-Principles Properties of Deuterium–Tritium on Inertial Confinement Fusion Target Designs

Introduction

Inertial confinement fusion (ICF) has been actively pursued in laboratories since the concept[1] was invented in 1972. In the conventional "hot-spot" ignition scheme, ICF capsules, consisting of a solid deuterium–tritium (DT) layer covered by an ablator, are driven to implode either by x rays in a hohlraum[2–4] or directly by lasers.[5,6] If properly designed, ICF targets can be compressed by shock waves and the spherical convergence to form an extremely dense (>1000× solid density) shell surrounding a high-temperature core (hot spot). A properly assembled core with an extremely high pressure (>100 ~ 300 Gbar) makes it possible not only to produce sufficient α particles from DT fusions but also to "bootstrap" the heat (α-particle stopping) in the hot spot.[7] If this occurs, a fusion burn wave could quickly propagate through the dense shell[8] and a net energy gain would be expected.

Designing and understanding ICF experiments rely on radiation–hydrodynamics simulations,[9–12] in which an accurate knowledge of properties of relevant materials (both DT fuel and ablators) under high-energy-density (HED) conditions is a prerequisite. To be specific, the equation of state (EOS) is needed to close the hydrodynamic equations.[13] The compressibility of material is determined by its EOS.[14] Besides the static EOS, an accurate knowledge of transport properties, such as thermal conductivity and viscosity, is also necessary for understanding the heat transport[15–17] and energy dissipation. In addition, the opacity of imploding capsules determines the radiation energy transport, which is also important in ICF simulations. Finally, the α-particle stopping power[18–20] of DT plasmas is also a prerequisite for ICF ignition simulations. The accuracy of these properties can affect the reliability of ICF target designs given that the margin for ignition to occur is usually quite small.

Studies of ICF ignition target designs[21–24] have revealed that the minimum laser energy scales as $E_L \propto \alpha^{1.9}$, with the adiabat α conventionally defined as the ratio of plasma pressure to the Fermi-degenerate pressure. This implies that to reduce the laser energy required for ignition, the imploding DT shell should be kept in a lower adiabat. Namely, maintaining a relatively lower temperature ($T \simeq 0.1$ to $0.2 \times T_F$, where T_F is the Fermi temperature) in the imploding DT capsule is key to obtaining higher compression and a larger energy gain for particular laser energy. As an example, the typical "path" of an imploding DT capsule on the temperature and density plane for a low-adiabat implosion (α = 1.5 to 3) is shown in Fig. 141.23. The in-flight DT shell in a low-adiabat implosion travels through a plasma region denoted as "warm dense matter" (WDM). Typically, the WDM regime for DT spans a density range from ρ = 1 to 200 g/cm^3 and temperatures of T = 1 to 200 eV, in which strong coupling and electron degeneracy are expected to be important. Warm dense plasmas are generally characterized by the Coulomb coupling parameter $\Gamma = q^2/(4\pi\epsilon_0 r_s k_B T)$ and the electron degeneracy parameter $\theta = T/T_F$, with the charge q, the Boltzmann constant k_B, and the interparticle distance $r_s = (3/4\,\pi n)^{1/3}$ for the particle density n. For WDM, $\Gamma \geq 1$ and $\theta \leq 1$. Even for the simplest element of hydrogen, accurate calculations of its properties in the WDM regime have been challenging in the past.

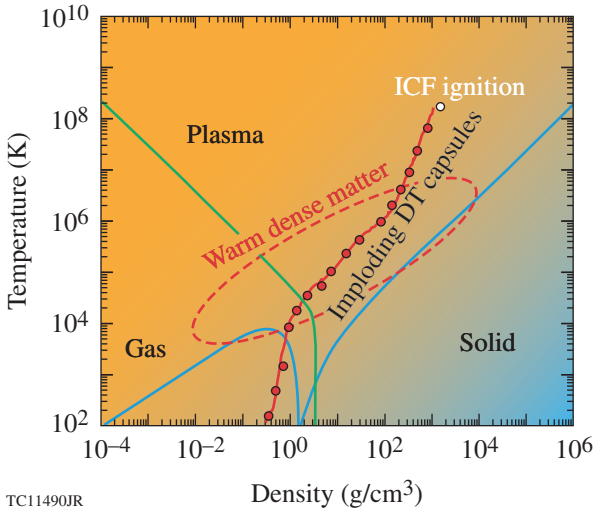

Figure 141.23
The density and temperature "path" of a low-adiabat imploding DT capsule to ICF ignition.

The many-body and quantum nature in such a complex system presents difficulties in handling WDM plasmas. Historically, approximate models were used to estimate the plasma properties in the WDM regime. For example, the extensively used *SESAME* EOS library[25] of DT and its updated version known as "*Kerley03*"[26] that is based on the chemical model of matter.[27] Although they have gained wide acceptance for a wide range of EOS parameters, such models may not be accurate enough to simulate WDM plasmas, especially for the old *SESAME* EOS that was widely used in hydrocodes. The thermal conductivity models, including the Lee–More model[28] and the *PURGATORIO* package,[29] are also extensively used in ICF simulations. These thermal conductivity models are based either on the first-order approximation to the Boltzmann equation or an average-atom scheme. They do not account fully for the many-body coupling and degeneracy effects in the WDM regime. Another example is the opacity of warm dense plasmas. The traditional astrophysics opacity table (AOT)[30] as well as the OPAL opacity project,[31] both of which were built for astrophysics applications, do not provide data in the WDM regime. Historically, the cold opacity of materials was patched for the WDM plasma condition in hydro simulations. Therefore, it is natural to ask how these approximated models may affect ICF simulations of low-adiabat implosions.

Taking advantage of the recent developments in first-principles (FP) methods, many studies on the properties of warm dense plasmas have been performed for both ICF applications and HED experiments in general. For instance, the EOS of deuterium/hydrogen has been investigated extensively using the path-integral Monte Carlo (PIMC) method,[32–37] the quantum-molecular dynamics (QMD) simulations,[38–49] and the coupled electron–ion Monte Carlo method.[50] These state-of-art calculations provided benchmarks for experimental measurements of the shock Hugoniot of hydrogen and deuterium.[51–58] In addition to the focus on the static EOS, the transport properties of warm dense hydrogen and its isotopes have also been revisited in recent years by FP simulations, especially the thermal/electric conductivities[59–65] and the viscosity.[64,66,67] Significant differences (by a factor of 3 to 10) in the WDM regime have been revealed between these models and the FP calculations of the thermal conductivity. In turn, these FP results have been used to improve the physics models[68] implemented in ICF hydrocodes. In addition, the electron–ion thermal equilibration has also been re-examined for ICF-relevant plasma conditions in recent years.[69–75] Most recently, the opacity of warm dense deuterium has been systematically investigated by QMD calculations[76] for the full range of ρ/T conditions covering the ICF implosion path. Again, orders-of-magnitude differences were identified when compared to the cold opacity that was patched to the AOT for ICF simulations. These FP calculations have been benchmarked with available experimental data of the principal Hugoniot and its optical reflectivity measurements.[77,78]

Besides the extensive studies of DT fuel, the FP methods have been applied to investigate the properties of ICF ablator materials such as plastic polystyrene (CH),[79–82] polyethylene,[83] beryllium and its mixture with CH,[63] as well as carbon.[84,85] The goal is either to systematically build complete tables of material properties under HED conditions or to perform FP calculations for a certain range of densities and temperatures to guide model improvements. Most importantly, these FP calculations can provide self-consistent properties of warm dense plasmas, while the self-consistency was often missing among the physics models adopted for ICF simulations. On the experimental side, ICF and HED experiments[86,87] equipped with accurate diagnostic tools such as x-ray Thomson scattering[88,89] have begun to provide detailed tests of various theoretical calculations.

Combining the FP methods of PIMC and QMD, we have systematically investigated the properties of deuterium over a wide range of densities and temperatures that fully cover the ICF implosion path. By mass scaling, the properties of DT can be derived from the deuterium properties. In previous publications, we have established the FP equation-of-state (FPEOS) table,[36,37] the thermal conductivity (κ_{QMD}),[65] and the FP opacity table (FPOT)[76] of the DT fuel for ICF applications. In this article we focus on their combined effects on the hydro predictions of ICF target designs by comparing them with the traditional model simulations. We found that the one-dimensional (1-D) predictions of ICF implosions, by comparing the FP-based properties of DT and traditional models, can change by up to a factor of ~2.5 in terms of neutron yield and energy gain; the lower the adiabat o f an imploding DT capsule, the more deviations expected. A reliable design of ICF ignition targets demands the use of the FP-based properties of DT.

This article is organized as follows: The next two sections (1) describe the two FP methods of PIMC and QMD and (2) the first-principles–based EOS, thermal conductivity, and opacity of warm dense deuterium compared with available experiments, other *ab initio* calculations, and the traditional model predictions. The significant discrepancies are also illustrated among these comparisons. The combined effects of these FP-based properties to ICF target designs are then presented by hydro-simulation comparisons of ICF implosions on both the OMEGA laser and the National Ignition Facility (NIF).

Finally, these results are summarized and future FP studies on ICF-relevant ablator materials are briefly mentioned.

The First-Principles Methods of PIMC and QMD for Warm Dense Plasmas

Understanding the properties of warm dense plasmas is challenging because of the many-body coupling and quantum degeneracy effects intrinsic to such complicated systems. It demands the full treatment of both effects using the fundamental principles governing a quantum many-body system. Among the various FP methods, PIMC and QMD have been extensively applied for studies of warm dense plasmas. Each of the two FP methods is briefly described in the following subsections.

1. Path-Integral Monte Carlo

A many-body quantum system in thermodynamic equilibrium can be described by the density matrix

$$\rho(\mathbf{R},\mathbf{R}';\beta)=\sum_n \phi_n(\mathbf{R})\phi_n(\mathbf{R}')e^{-E_n/k_\mathrm{B}T},$$

with $\beta = 1/k_\mathrm{B}T$, ϕ_n the eigenstates, and E_n the eigenenergy of the system. The eigenstates of an interacting quantum system are unknown, however, and no efficient numerical method exists to indirectly compute the density matrix. The fundamental idea of the path-integral approach is based on the convolution property of $\rho(\mathbf{R},\mathbf{R}';\beta)$. Namely, the density matrix at temperature T can be expressed as a convolution of density matrices at an M times higher temperature, $M \times T$:

$$\rho(\mathbf{R},\mathbf{R}';\beta)=\int \mathrm{d}\mathbf{R}_1\mathrm{d}\mathbf{R}_2\ldots\mathrm{d}\mathbf{R}_{M-1}\rho(\mathbf{R},\mathbf{R}_1;\Delta\beta)$$
$$\times\rho(\mathbf{R}_1,\mathbf{R}_2;\Delta\beta)\cdots\rho(\mathbf{R}_{M-1},\mathbf{R}';\Delta\beta). \quad (1)$$

At a high temperature, the correlation effects betwee n particles are small and a very good approximation for the density matrix exists.[90] The path integral is needed to recover the full correlation effects at a lower temperature. The integral on the right-hand side of Eq. (1) can be interpreted as a weighted average over all *paths* that connect the points $\mathbf{R}$ and $\mathbf{R}'$. $\mathbf{R}$ is a collective variable that denotes the positions of all particles $\mathbf{R} = \{\mathbf{r}_1,\ldots\mathbf{r}_N\}$. β represents the length of the path in "imaginary time," and $\Delta\beta = \beta/M$ is the size of each of the M time steps. In PIMC calculations, electrons and ions are treated on equal footing as paths, which means the quantum effects of both species are included consistently, although for the temperatures under consideration, the zero-point motion and exchange effects of the nuclei are negligible.

One can consequently interpret the positions $\mathbf{R}_1\ldots\mathbf{R}_{M-1}$ as intermediate points on a path from $\mathbf{R}$ and $\mathbf{R}'$. The multidimensional integration over all paths in Eq. (1) can be carried out efficiently by the Monte Carlo method.[91] Observables associated with an operator $\hat{O}$ can be derived from

$$\langle\hat{O}\rangle=\frac{\int \mathrm{d}\mathbf{R}\int \mathrm{d}\mathbf{R}'\langle\mathbf{R}|\,\hat{O}\,|\mathbf{R}'\rangle\rho(\mathbf{R}',\mathbf{R};\beta)}{\int \mathrm{d}\mathbf{R}\rho(\mathbf{R}',\mathbf{R};\beta)}. \quad (2)$$

For the kinetic and potential energies, E_K and E_P, as well as for pair correlation functions, only diagonal matrix elements $(\mathbf{R}' = \mathbf{R})$ are needed.

Since electrons are fermions, their fermionic character matters for the degenerate plasma conditions under consideration. This implies that one must construct an antisymmetric many-body density matrix, which can be derived by introducing a sum of all permutations $\mathcal{P}$ and then also include paths from $\mathbf{R}$ to $\mathcal{P}\mathbf{R}'$. While this approach works well for bosons,[91] for fermions each permutation must be weighted by a factor $(-1)^{\mathcal{P}}$. The partial cancellation of contributions with opposite signs leads to an inefficient algorithm when the combined position and permutation space are sampled directly.[91] This is known as the *Fermion sign problem*, and its severity increases as the plasma temperature decreases (becoming more degenerate). In our PIMC calculations, we deal with the Fermion sign problem by using the free-particle nodes,[92] although the nodes of a variational density matrix[93] have also been employed in other PIMC computations.[94,95] The details of our PIMC simulations of warm dense deuterium can be found in previous publications.[36,37]

In PIMC simulations, we approach the low-T density matrix from the known high-T ones through multidimensional integrations along the "temperature path." As the plasma temperatures decrease, the Fermi-sign problem prevents the efficient evaluation of the multidimensional integrations in the combined position and permutation space. Therefore, the lowest temperatures in our restricted PIMC calculations have only reached $T \simeq 0.1$ to $0.2 \times T_\mathrm{F}$. For even lower plasma temperatures, other FP methods should be used. The QMD method is one of the FP methods that can handle low-T plasmas.

2. Quantum-Molecular Dynamics

The QMD method is based on the finite-temperature density functional theory.[96–98] The many-electron system in a plasma can be described by a wave function $\Psi(\mathbf{r}_1,\mathbf{r}_2,\ldots\mathbf{r}_N)$, which satisfies the following Schrödinger equation (atomic units used throughout):

$$\left[-\frac{1}{2}\sum_i \Delta_i + \sum_i V(\mathbf{r}_i) + \sum_{i\neq j}\frac{1}{|\mathbf{r}_i-\mathbf{r}_j|}\right]\Psi = E\Psi. \quad (3)$$

The second term in Eq. (3) is the electron–ion interaction, while the third term describes the Coulomb repulsion among electrons. To solve the above Schrödinger equation, a tractable way is to map the many-electron wave function onto a one-electron basis, $\Psi(\mathbf{r}_1\mathbf{r}_2,\ldots,\mathbf{r}_N)\rightarrow\{\psi(\mathbf{r}_1),\psi(\mathbf{r}_2),\ldots,\psi_N(\mathbf{r}_N)\}$. The Kohn–Sham density functional theory[96,97] (DFT) is an efficient "mean-field" theory for many-electron systems, in which the total wave function takes a product form of individual one-electron "orbital," $\Psi_i(\mathbf{r})$. By doing so, Eq. (3) can be casted into the well-known Kohn–Sham equation for the orbital $\Psi_i(\mathbf{r})$:

$$\left\{-\frac{1}{2}\Delta + V_z(\mathbf{r}) + V_{\mathrm{H}}[\rho](\mathbf{r}) + V_{xc}[\rho](\mathbf{r})\right\}\psi_i(\mathbf{r}) = E_i\psi_i(\mathbf{r}), \quad (4)$$

with the electron density and the Hartree term defined as

$$\rho(\mathbf{r}) = \sum_{i=1}^{N}|\psi_i(\mathbf{r})|^2; \quad V_{\mathrm{H}}[\rho](\mathbf{r}) = \int\frac{\rho(\mathbf{r}')}{|\mathbf{r}-\mathbf{r}'|}\mathrm{d}\mathbf{r}'. \quad (5)$$

Since the exchange-correlation term V_{xc} and the Hartree term depend on the electron density $\rho(\mathbf{r})$, which is again a function of $\psi(\mathbf{r})$, the Kohn–Sham equation can be solved in a self-consistent way. Together with the ionic force, the resulting electronic force is then used to drive the classical ionic motion through Newton's equation under the Born–Oppenheimer approximation (in a QMD step).

Our QMD simulations have been performed within the Mermin's finite-temperature DFT,[98] which was implemented in the Vienna *ab initio* simulation package (VASP)[99,100] using a plane-wave basis. The generalized gradient approximation (GGA) with the Perdew–Burke–Ernzerhof (PBE) exchange-correlation function[101] is employed in our QMD simulations. The electron–ion interaction is modeled by either the projector augmented wave (PAW) pseudopotentials or the pure Coulomb potential. The system was assumed to be in local thermodynamic equilibrium with equal electron and ion temperatures ($T_{\mathrm{e}} = T_{\mathrm{i}}$). The isothermal ensemble was used for our QMD simulations in which the number of particles, volume, and temperature was kept constant. For periodic boundary conditions, the electron wave function can be described by Bloch waves, consisting of products of plane waves with different momenta $\hbar k$ and a periodic function of space. Each k point in the first Brillouin zone uniquely defines every Bloch state. For each QMD step, a set of electronic wave functions for each k point is self-consistently determined for a given ionic configuration. Then, the ions are moved classically with a velocity Verlet algorithm, according to the combined ionic and electronic forces. The ion temperature was kept constant through simple velocity scaling. Repeating these QMD steps, a set of self-consistent ion trajectories and electronic wave functions can be found. These trajectories provide a self-consistent set of static, dynamic, and optical properties of warm dense plasmas. The details of our QMD simulations of warm dense deuterium plasmas can be found in recent publications.[65,76]

3. Calculating Plasma Properties from PIMC and QMD Simulations

For PIMC simulations, only the EOS was derived. The total internal energy follows from $E = E_{\mathrm{K}} + E_{\mathrm{P}}$, where E_{K} and E_{P} are the kinetic and potential energies, respectively. The pressure P can be obtained from the virial theorem for Coulomb systems, $P = (2E_{\mathrm{K}} + E_{\mathrm{P}})/3V$ with the volume V. The tabulated FPEOS of deuterium from PIMC calculations can be found in Ref. 37. In QMD simulations, the EOS of warm dense deuterium was calculated in a straightforward fashion by evaluating the electron term, then adding the contribution from the classical ions. Using QMD simulations, we have extended the PIMC-derived FPEOS table from the PIMC's lowest temperature of $T = 15{,}625$ K down to a much lower temperature of $T = 1000$ K for most of the density points ($\rho_D \geq 0.1$ g/cm^3). Dynamical and optical properties are determined from the QMD trajectories by calculating the velocity dipole matrix elements. Namely, from the resulting QMD trajectories, we choose uncorrelated snapshots of these configurations to calculate the velocity dipole matrix elements D_{mn} using the wave functions. The quantity D_{mn} is then applied to compute the frequency-dependent Onsager coefficients within the Kubo–Greenwood formalism:[102]

$$L_{ij}(\omega) = \frac{2\pi(-e)^{4-i-j}}{3Vm_{\mathrm{e}}^2\omega}\sum_{mn}F_{mn}|D_{mn}|^2 \times\left(\frac{E_m+E_n}{2}-H\right)^{i+j-2}\delta(E_m-E_n-\hbar\omega), \quad (6)$$

where $V = 1/\rho$ is the atomic volume, $E_m(E_n)$ is the energy of the mth (nth) state, and H is the enthalpy per atom of the system. The quantity of F_{mn} is the difference between the Fermi–Dirac distributions for states m and n at temperature T. The Onsager coefficients essentially determine the transport and optical properties of the system.

To calculate the electron thermal conductivity of a plasma, the linear response of the plasma to an electric field **E** and a temperature gradient ∇T is considered. The resulting electric current $\mathbf{j}_e$ and the heat flux $\mathbf{j}_q$ can be expressed as

$$\mathbf{j}_e = \left(eL_{11}\mathbf{E} - \frac{L_{12}\nabla T}{T}\right)\Big/ e, \tag{7}$$

$$\mathbf{j}_q = \left(eL_{21}\mathbf{E} - \frac{L_{22}\nabla T}{T}\right)\Big/ e\,. \tag{8}$$

For plasmas having no electric current ($\mathbf{j}_e = 0$), the above equations in combination with the definition of $j_q = -\kappa\nabla T$ give the thermal conductivity (in atomic units of $\hbar = m_e = e = 1$):

$$\kappa = \frac{L_{22} - L_{12}^2 \big/ L_{11}}{T} \tag{9}$$

with the Onsager coefficients given by L_{ij} in Eq. (6). If there is no temperature gradient ($\nabla T = 0$), Eq. (7) reduces to the Ohm's law with the real electrical conductivity of $\sigma_1 = L_{11}$.

The opacity calculations rely on the evaluation of the frequency-dependent absorption coefficient $\alpha_K(\omega)$, which is related to the electrical conductivity and the index of refraction (n) of the plasma:

$$\alpha_K(\omega) = \frac{4\pi\sigma_1(\omega)}{cn(\omega)} \tag{10}$$

with the speed of light c. To calculate the refractive index n, we start from the real part of the electrical conductivity, $\sigma_1(\omega) = L_{11}(\omega)$, and determine the imaginary part from the principal value integral:

$$\sigma_2(\omega) = -\frac{2}{\pi}P\int \frac{\omega\sigma_1(\omega')}{\omega'^2 - \omega^2}\mathrm{d}\omega'. \tag{11}$$

The dielectric function $\epsilon(\omega) = \epsilon_1(\omega) + i\epsilon_2(\omega)$ can be calculated from the following expressions:

$$\epsilon_1(\omega) = 1 - \frac{4\pi}{\omega}\sigma_2(\omega),$$

$$\epsilon_2(\omega) = 1 - \frac{4\pi}{\omega}\sigma_1(\omega). \tag{12}$$

Using the dielectric function, we compute the real [$n(\omega)$] and imaginary [$k(\omega)$] parts of the refractive index:

$$n(\omega) = \sqrt{\frac{\left|\epsilon(\omega)\right| + \epsilon_1(\omega)}{2}},$$

$$k(\omega) = \sqrt{\frac{\left|\epsilon(\omega)\right| - \epsilon_1(\omega)}{2}}. \tag{13}$$

The frequency-dependent reflectivity is given by

$$R(\omega) = \frac{\left[n(\omega) - n_0\right]^2 + k(\omega)^2}{\left[n(\omega) + n_0\right]^2 + k(\omega)^2} \tag{14}$$

with the refraction index n_0 of the ambient environment ($n_0 = 1$ for vacuum). Finally, the mass absorption coefficient (α_m) is equal to the absorption coefficient (α_K) divided by the mass density:[103]

$$\alpha_m(\omega) = \frac{\alpha_K(\omega)}{\rho} = \frac{4\pi\bar{\sigma}_1(\omega)}{nc\bar{n}(\omega)} \times \frac{1}{\rho}. \tag{15}$$

The "bar" over σ_1 and n stands for averaging over the uncorrelated configuration snapshots being sampled. We found that five to ten snapshots generally give a good statistic with variation less than ~5%.

Under the multigroup diffusion approximation, the Rosseland (K_R) and Planck (K_P) mean opacities are used for the radiation transport and emission calculations in hydrodynamic simulations. The grouped Rosseland and Planck mean opacities are defined as

$$K_R(\omega_1{:}\omega_2) = \frac{\int_{\omega_1}^{\omega_2} n(\omega)^2 \dfrac{\partial B(\omega,T)}{\partial T}\mathrm{d}\omega}{\int_{\omega_1}^{\omega_2} n(\omega)^2 \dfrac{1}{\alpha_m}\dfrac{\partial B(\omega,T)}{\partial T}\mathrm{d}\omega}, \tag{16}$$

$$K_P(\omega_1{:}\omega_2) = \frac{\int_{\omega_1}^{\omega_2} n(\omega)^2 \alpha_m(\omega) B(\omega,T)\mathrm{d}\omega}{\int_{\omega_1}^{\omega_2} n(\omega)^2 B(\omega,T)\mathrm{d}\omega} \tag{17}$$

for a group of photon energies between $\hbar\omega_1$ and $\hbar\omega_2$. Here, the Planck function $B(\omega,T) = \left(\hbar\omega^3/4\pi^3c^2\right)/\left(e^{\hbar\omega/k_BT} - 1\right)$ depends on the emitting photon energy and the plasma temperature. Integrating the frequency from $\omega_1 = 0$ to $\omega_2 = \infty$, one obtains the total Rosseland and Planck mean opacities.

Comparisons of FP-Based Properties of Deuterium with Experiments and Models

With the PIMC and QMD methods, we have calculated the EOS, thermal conductivity κ, and opacity of deuterium for a wide range of densities and temperatures. From the combined PIMC/QMD calculations, the FPEOS table[36,37] covers the deuterium plasma conditions of $\rho = 0.002$ to 1596 g/cm^3 and $T = 0.086$ eV to 5.5 keV. While for QMD calculations of κ and opacity, we have considered the deuterium plasma ranges of $\rho = 0.1$ to 673.5 g/cm^3 and $T = 5000$ K up to the Fermi temperature T_F. These density and temperature points fully cover the typical shell conditions in low-adiabat ICF implosions. It is noted that DFT-based QMD and PIMC results have been combined in the past for the shock Hugoniot studies of hydrogen,[34] helium,[94,95] carbon,[84] and water.[81] In this section, we compare the FP-calculated properties of deuterium plasma with both model predictions and available experimental data.

In Fig. 141.24, our PIMC/QMD–predicted (a) pressure and (b) energy are plotted as a function of the plasma temperature for the case of $\rho_D \simeq 7.391$ g/cm^3. They are compared with a recent *ab initio* calculation,[48] using a different molecular-dynamics code (*ABINIT*[104]), which combines both the orbital-based and orbital-free density functional theories (QMD–OFMD). The solid red circles represent our QMD results, while the open blue squares represent the PIMC calculations and the open green diamonds are those given by Wang *et al.*[48] It is noted that all the internal energies shown are referenced to the ground-state energy ($E_0 = -15.886$ eV) of a D_2 molecule. Figure 141.24 shows that in the warm dense regime, where both PIMC and QMD are valid, the two calculations result in almost identical EOS values. The PIMC simulations, however, are applicable only to $T \sim 10$ eV for this density because as the plasma temperature decreases, the Fermi-sign problem in PIMC prevents the efficient evaluation of degeneracy effects. In the low-T regime ($T < 0.2 \times T_F$), the QMD results are complimentary to the PIMC results. Overall, our combined EOS results from PIMC/QMD simulations compare well with the values given by QMD–OFMD calculations.[48] As expected, Fig. 141.24(a) shows almost constant pressures at $T \ll T_F$. This is attributed to the dominant electron degeneracy pressure at plasma temperatures well below the Fermi temperature ($T_F \simeq 61.9$ eV for this density).

Figure 141.25 compares the FPEOS-predicted Hugoniot of deuterium with extensively used EOS models of *SESAME*[25] and the updated *Kerley03*,[26] as well as the laser-shock experiments by Hicks *et al.*[57] and by Boehly *et al.*;[105] the Z-machine data by Knudson *et al.*;[54,55] and that of Boriskov *et al.*[106] The pressure of shocked deuterium is plotted as a function of the compression (ρ/ρ_0). The Hugoniot temperatures are marked in Fig. 141.25(a). Figure 141.25(a) indicates that the FPEOS-predicted Hugoniot is softer than *SESAME* at $P < 2.5$ Mbar (1 Mbar = 100 GPa), while it is stiffer in the pressure range of $P = 2.5$ to 100 Mbar. The

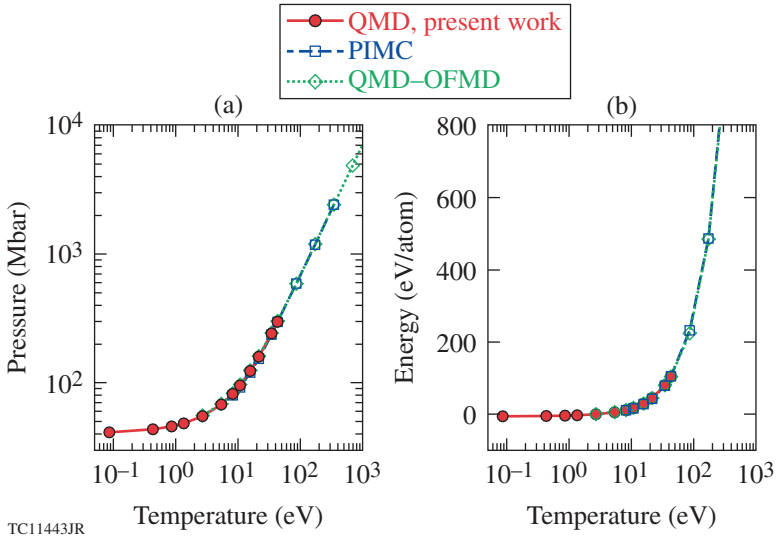

Figure 141.24
(a) The pressure and (b) energy as a function of temperature for $\rho_D = 7.391$ g/cm^3 are compared among different first-principles calculations: the current QMD calculations, the PIMC calculations,[37] and the QMD–OFMD calculations by Wang *et al.*[48]

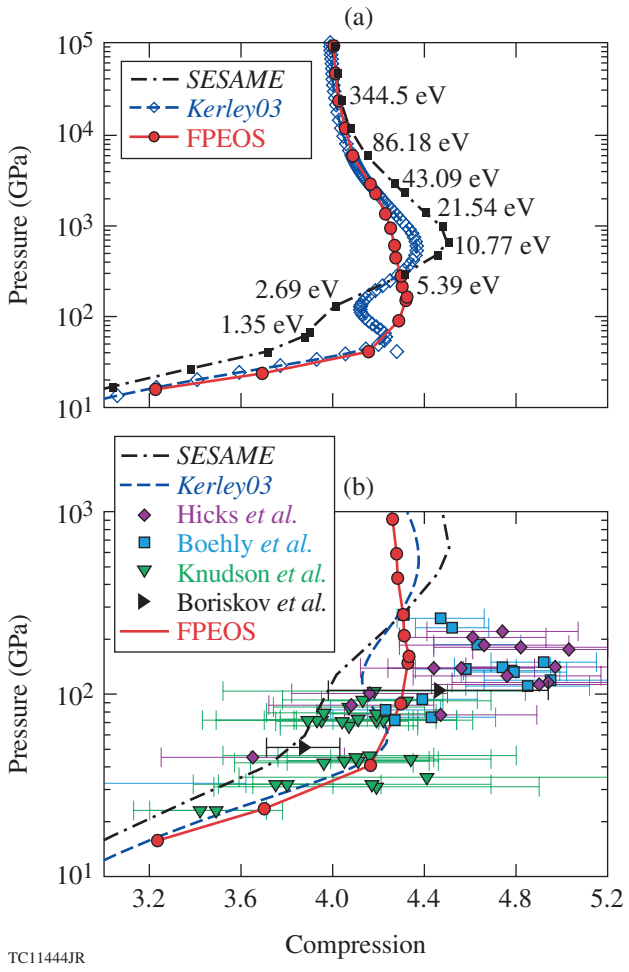

Figure 141.25
(a) The comparison of principal Hugoniot of deuterium among FPEOS, *SESAME*, and *Kerley03*; (b) their comparisons with available experimental data: the single-shock data published in Hicks *et al.*,[57] the OMEGA data derived from double-shock experiments by Boehly *et al.*,[105] the Z-machine data by Knudson *et al.*,[54,55] and the experiment by Boriskov *et al.*[106]

improved *Kerley03*, with including the molecular dissociation, quantum corrections, and a new ionization equilibrium model, gave Hugoniot values that were overall closer to the FPEOS. The slightly softer behavior is still seen, however, in *Kerley03* at pressures of $P \simeq 2.5$ to 10 Mbar, and the similar stiffer behavior at low pressure (P = 0.5 to 2 Mbar) is still less favorably compared with laser shock experiments than the FPEOS in this low-T range, as indicated by Fig. 141.25(b). The FPEOS Hugoniot is a bit closer to, but still not as soft as, what is indicated by the laser-shock experiments. To our best knowledge, this much-softer behavior[51,52,57,105] in these laser-shock experiments at $P \simeq 1$ to 2 Mbar has not yet been fully reproduced by *ab initio* calculations.

In Figs. 141.26 and 141.27, we compare the FPEOS with *SESAME*, *Kerley03*, and the classical Debye plasma model for a wide range of densities and temperatures. In these figures, we have normalized the pressure and energy of deuterium plasma by their *ideal* values, respectively. The *ideal* pressure (P_{id}) and energy (E_{id}) are the sum of contributions from the noninteracting Fermi electron gas together with classical ions. The deviations from these *ideal* values indicate the contribution from the Coulomb interactions. Figure 141.26 plots the normalized (a) pressure and (b) energy as a function of deuterium density for a plasma temperature of $T \simeq 10.77$ eV.

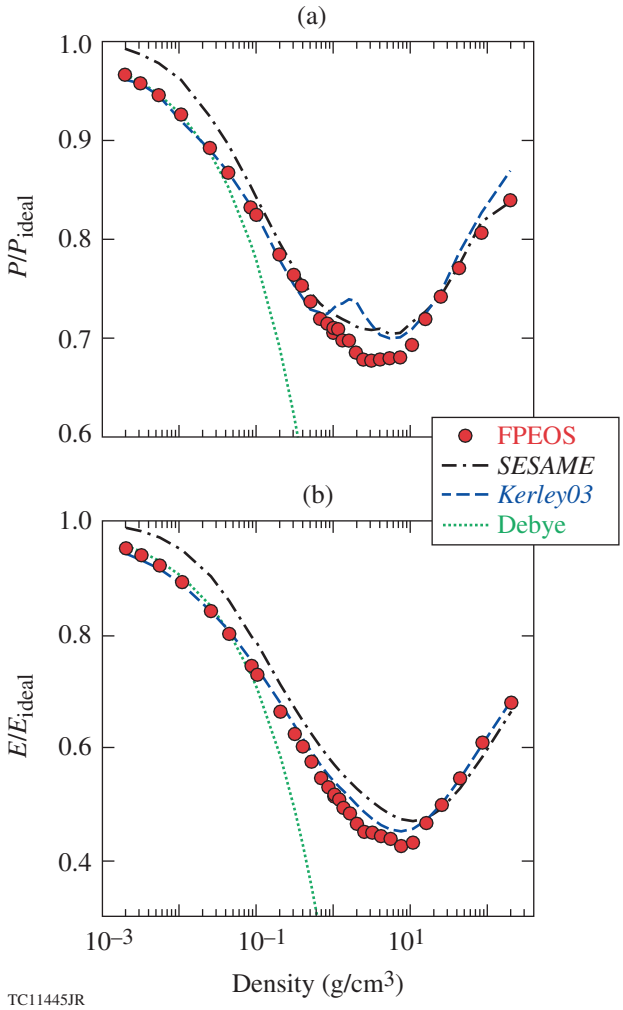

Figure 141.26
The normalized (a) pressure and (b) energy as a function of deuterium density for a plasma temperature at $T \simeq 10.77$ eV are compared among FPEOS, *SESAME*, *Kerley03*, and the classical Debye plasma model. The normalization is done with P_{id} and E_{id}, the total pressure and energy, respectively, for the ideal Fermi gas of electrons and the classical ions.

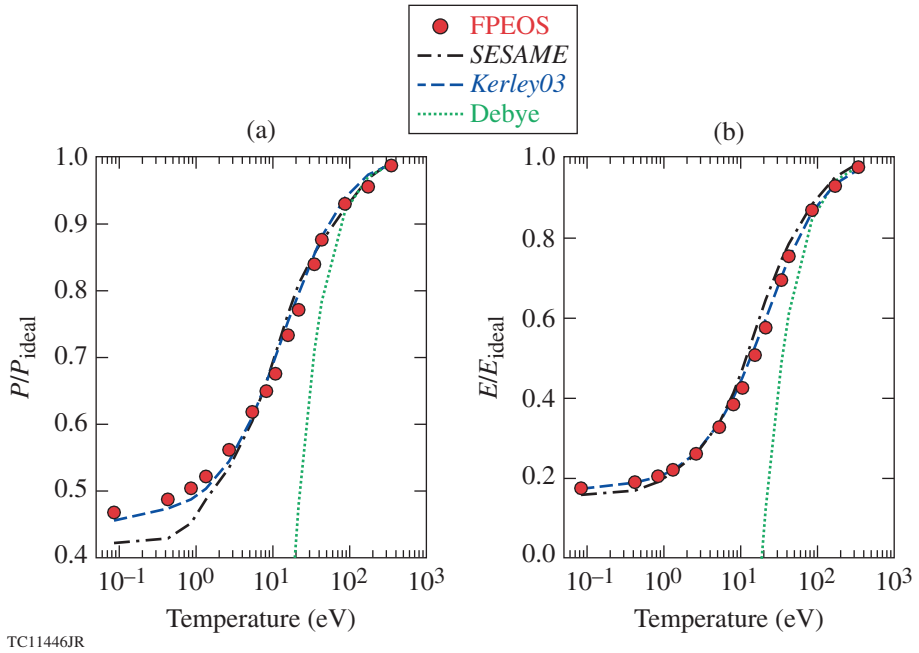

Figure 141.27
The normalized (a) pressure and (b) energy as a function of plasma temperature for the deuterium density of $\rho_D \simeq 7.391$ g/cm^3 are compared among FPEOS, *SESAME*, *Kerley03*, and the Debye model.

One sees that at very low densities the plasma is approaching a classical *ideal* gas; while as the density increases, both the pressure and energy decrease, which manifests the increasing Coulomb interactions among electrons and ions. Both reach a minimum at densities of several g/cm^3 for this temperature ($T \simeq 10.77$ eV), where the warm dense regime is located. As the density continues to increase, the Fermi degeneracy of electrons starts to become more dominant than electron–ion interactions so that the *ideal* Fermi gas is being approached. Namely, the ratios of both P/P_{id} and E/E_{id} gradually increase toward ~1 at high densities. As can be seen in Fig. 141.26, the *SESAME* model underestimates the electron–ion Coulomb interactions, even in the classical regime ($\rho_D < 0.1$ g/cm^3). The improved *Kerley03* and the classical Debye model better agree with the FPEOS in this low-density regime. The Debye model fails as plasma density increases to above 0.1 g/cm^3 because of its overestimated electron screening and the lack of electron degeneracy. In the warm dense regime of $\rho_D \simeq 1$ to 10 g/cm^3, both the *SESAME* and *Kerley03* models underestimated the Coulomb interactions between electrons and ions. In contrast to the FPEOS, both gave higher pressure and energy in this regime. The *Kerley03* model showed an unphysical pressure bump around $\rho_D = 1$ to 3 g/cm^3, which has also been noticed and modified in a recent EOS study at Livermore.[46] In Fig. 141.27, the normalized (a) pressure and (b) energy are plotted as a function of plasma temperature for the deuterium density of $\rho_D = 7.391$ g/cm^3. The *SESAME* model underestimates the pressure at low temperatures ($T < 1$ eV). As the plasma temperature increases to the high end, the system exhibits classical behavior as expected. In the warm dense regime ($T \simeq 10$ to 50 eV for this density), *SESAME* disagrees more with the FPEOS than the improved *Kerley03,* especially for the energies illustrated by Fig. 141.27(b).

For the transport and optical properties of warm dense deuterium, there were no direct measurements of thermal conductivity and opacity for the various densities and temperatures explored here. However, the optical reflectivity measurements[77,78] along the principal Hugoniot have been performed on both Nova and OMEGA, which enable us to make direct comparisons with our QMD calculations. In Figs. 141.28(a) and 141.28(b), the optical reflectivity versus the shock speed has been compared with both the recent OMEGA experiment[78] and an earlier Nova experiment[77] for different VISAR (velocity interferometer system for any reflector) wavelengths of $\lambda = 532$ nm and $\lambda = 808$ nm, respectively. The OMEGA experiments were taken from a decayed shock in deuterium for many shots. The experimental results are in good agreement with our QMD calculations. The early Nova experiment also compares well with other *ab initio* calculations.[41,43] This experimental confirmation lends credence to the L_{11} coefficients produced in our QMD studies of reflectivity and, in turn, to the other self-consistently calculated Onsager coefficients that determine thermal conductivity as well as the opacities.

Next, we compare the QMD-calculated κ with the Lee–More model prediction in Figs. 141.29(a) and 141.29(b) as a function of plasma temperature for densities of $\rho_D = 7.391$ g/cm^3 and

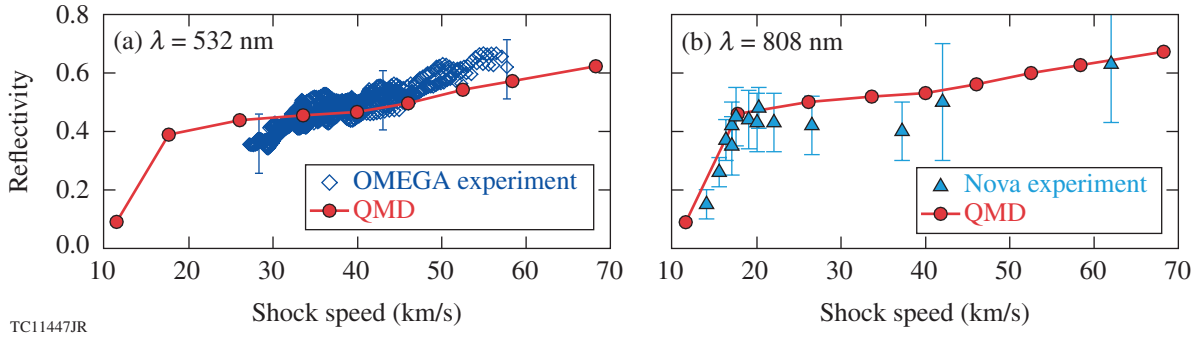

Figure 141.28
The comparison of reflectivity along the principal Hugoniot of deuterium between experiments and QMD calculations, for different VISAR wavelengths of (a) λ = 532 nm (OMEGA experiments) and (b) λ = 800 nm (Nova experiments).

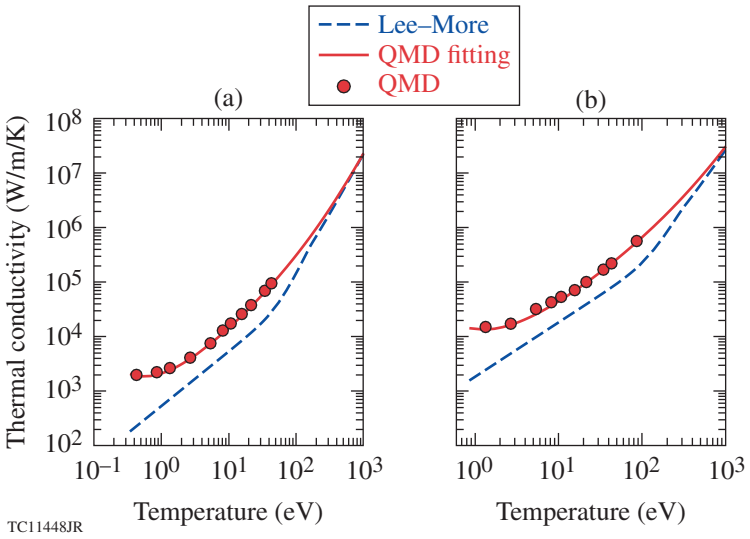

Figure 141.29
The QMD-predicted thermal conductivity κ of deuterium as a function of plasma temperature for densities of (a) $\rho_D \simeq 7.391$ g/cm^3 and (b) $\rho_D \simeq 24.945$ g/cm^3, which are compared with the Lee–More model and the fitting formula of Eqs. (19) and (20).

ρ_D = 24.945 g/cm^3, respectively. For each density point, the κ_{QMD} calculations have been performed to the highest temperature, approaching $T \simeq T_F$. The QMD results are represented by the solid red circles. Comparing with the Lee–More model (κ_{LM}) widely used in hydrocodes, we find κ_{QMD} is higher by a factor of 3 to 10 in the warm regime ($T < T_F$). Such κ enhancement in the WDM regime has also been observed in previous publications.[59–64] To apply these FP-based κ_{QMD} to ICF simulations, we have fit the κ_{QMD} results by the following formula:[65]

$$\kappa_{QMD} = \frac{20\times(2/\pi)^{3/2} k_B^{7/2} T^{5/2}}{\sqrt{m_e}\, Z_{eff}\, e^4} \times \frac{0.095\times(Z_{eff}+0.24)}{1+0.24\, Z_{eff}} \times \frac{1}{(\ln\Lambda)_{QMD}} \qquad (18)$$

with the same Spitzer prefactor as used in κ_{LM} and Z_{eff} = 1 for deuterium. The generalized QMD Coulomb logarithm has the following form:

$$(\ln\Lambda)_{QMD} = \exp\left\{\alpha_0 + \sum_{i=1}^{5}\left[\alpha_i(\ln\Gamma)^i + \beta_i(\ln\theta)^i\right]\right\}. \qquad (19)$$

This fifth-order polynomial function of coupling and degeneracy parameters (Γ,θ) has been fit with the κ_{QMD} data using multivariable least-square fit. To allow κ_{QMD} to converge to κ_{LM} at the ideal plasma conditions ($\Gamma \ll 1$ and $\theta \gg 1$), we have added high-temperature points from κ_{LM} into the data set for the global fitting. The resulting fitting parameters are expressed in Table141.II. Overall, the global fit with the above parameters, depicted by Fig. 141.29, gives only a small error of ~5%. The

Table 141.II: The fitting parameters for the $(\ln \Lambda)_{QMD}$.

i	α_i	β_i
0	−0.740148	
1	−0.181459	+0.861554
2	$+6.396443 \times 10^{-4}$	−0.105704
3	$+1.479543 \times 10^{-3}$	-6.757829×10^{-3}
4	-1.233616×10^{-4}	-1.69007×10^{-4}
5	-2.581072×10^{-5}	$+3.492008 \times 10^{-5}$

tabulated κ_{QMD} of deuterium can be found in the Supplementary Material of Ref. 65.

Finally, we examine the QMD-predicted opacities by comparing them to the cold-opacity-patched AOT in Figs. 141.30 and 141.31 for the deuterium density ρ_D = 7.391 g/cm^3. It is noted that the cold-opacity–patched AOT is currently used in our hydrocodes for radiation-transport simulations with the multigroup diffusion scheme. The total Rosseland opacity is plotted in Fig. 141.30 as a function of the plasma temperature. As the plasma temperature approaches T_F, the QMD opacity at T = 43.09 eV converges to the AOT value. Below ~30 eV, no data exist in the AOT for the warm dense regime. Historically, the cold opacity of solid deuterium had been patched into the AOT for ICF hydro simulations. Figure 141.30 illustrates that the QMD opacities in the WDM conditions are much higher than the cold opacities. Namely, the density-scaled cold opacities significantly underestimated the photon absorption of warm dense plasmas. This is understandable because as deuterium is compressed to this density (>35× compression) from solid D_2 and warms up to above ~10,000 K, energy gaps are filled and the density of states increases in such systems. As a result, photon absorptions become more probable than the cold solid case, leading to higher opacities. Figures 141.31(a) and 141.31(b) plot the corresponding grouped opacities as a function of the central photon energy in each group for plasma temperatures of T = 10.77 eV and T = 43.09 eV, respectively (48 photon-energy groups were used). Figure 141.31(a) shows that at the low plasma temperature of T = 10.77 eV, the grouped opaci-

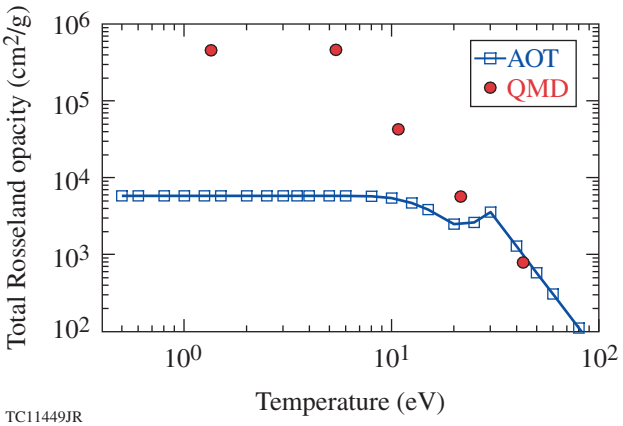

Figure 141.30
The total Rosseland opacity of deuterium as a function of the plasma temperature at a density of $\rho_D \simeq 7.391$ g/cm^3, which are compared between the cold-opacity–patched AOT and the QMD calculations.

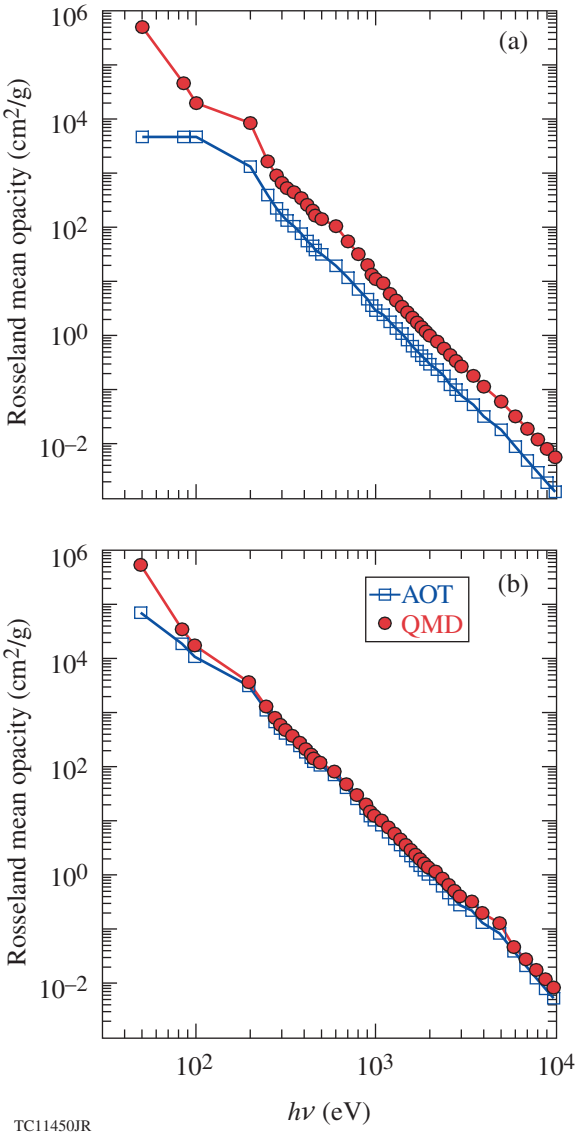

Figure 141.31
The grouped Rosseland mean opacity as a function of the photon energy $h\nu$, for the deuterium density of $\rho_D \simeq 7.391$ g/cm^3 at temperatures of (a) $T \simeq 10.77$ eV and (b) $T \simeq 43.09$ eV.

ties from QMD calculations become overall higher than the cold-opacity values. For photon-energy groups of $h\nu < 2$ keV (important to ICF), the QMD opacity is enhanced by a factor of 3 to 100, depending on $h\nu$. When the plasma temperature increases to $T = 43.09$ eV, Fig. 141.31(b) indicates that both the QMD and AOT opacities begin to agree with each other over a wide range of photon energies, except for the first two groups at $h\nu = 50$ eV and $h\nu = 85$ eV.

The first-principles opacity tables (FPOT) of deuterium and DT have been built from these QMD calculations for a wide range of densities ($\rho_D = 0.5$ to 673.518 g/cm^3) and temperatures (from $T = 5000$ K up to the Fermi temperature for each density point). For higher temperature points ($T > T_F$), we have incorporated the AOT data into the FPOT table since the FP calculations reproduced the AOT data at high-T plasma conditions, which are shown in Figs. 141.30 and 141.31. To make it compatible with our hydrocodes (*LILAC* and *DRACO*), we have created the FPOT in both the Rosseland and Planck mean opacities with 48 photon-energy groups for hydro simulations. The tabulated FPOT of deuterium can be found in the Supplementary Material of Ref. 76.

Impact of FP-Based Properties of DT on ICF Target Designs

With these FP-calculated tables of FPEOS, FPOT, and κ_{QMD} of DT (mass scaled from the deuterium properties) being implemented into our hydrocodes, we have investigated their combined effects on the 1-D prediction of ICF implosions through radiation–hydrodynamics simulations. The traditional physics models used in our 1-D hydrocode *LILAC*[107] were the *SESAME* for EOS, the Lee–More thermal conductivity (κ_{LM}), and the cold-opacity–patched AOT. We first examine a typical OMEGA implosion in Figs. 141.32 and 141.33. The cryogenic DT target with a diameter of $\phi = 865$ μm [shown in Fig. 141.32(a)] consists of a thin (7.5-μm) double-layer plastic ablator and a 40-μm layer of DT ice. The 3.7-μm outer layer of Si-doped CH is used to reduce laser imprints.[108,109] The OMEGA target is driven by a triple-picket laser pulse[12,110,111] with a total energy of ~26 kJ, illustrated by Fig. 141.32(b). The peak laser intensity is ~10^{15} W/cm^2. The properly timed pickets set up a low-adiabat capsule for the main pulse to implode.

In Fig. 141.33 the hydro simulation results using the FP-based properties of DT (FPEOS/FPOT/κ_{QMD}) are compared with the traditional models of *SESAME*/AOT/κ_{LM}. The solid red lines represent the FP simulations, while the dashed blue lines

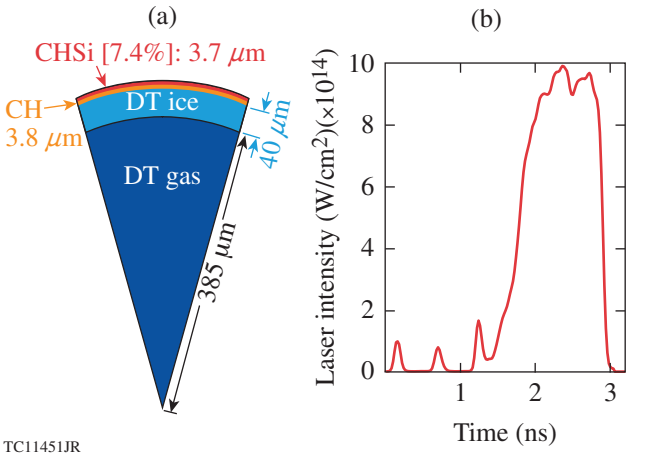

Figure 141.32
(a) A schematic diagram of cryogenic DT target on OMEGA; (b) the triple-picket pulse shape used for low-adiabat cryogenic DT implosions on OMEGA.

represent the "standard" model predictions. In Fig. 141.33(a), the density and electron temperature profiles of the imploding DT capsule, at the beginning of the deceleration phase ($t = 2.96$ ns), are plotted as a function of the target radius. We observe that the FP simulation gives a lower peak density of $\rho_D = 8.8$ g/cm^3 and a higher shell temperature of $T \simeq 38$ eV, in contrast to the standard model predictions of $\rho_D = 10.4$ g/cm^3 and $T \simeq 28$ eV, respectively. The major contributions to these changes come from EOS and opacity differences, while the thermal conductivity effect is relatively small at this stage. As previously discussed,[36,37,76] the stiffer behavior of DT in FPEOS at $P = 10$ to 100 Mbar causes part of the density drop; while the enhanced opacity from FPOT gives more radiation preheat in the warm dense DT shell, which increases the electron temperature and decreases the peak density inside the DT shell. Figure 141.33(b) displays the predicted minimum adiabat of the DT shell for the two simulations. It indicates that the FP-based simulation gives a higher adiabat of $\alpha \simeq 2.8$ in contrast to the model-predicted $\alpha \simeq 2$. These changes in plasma conditions of the DT shell can have a consequence in the overall target performance. Figure 141.33(c) illustrates the mass density and ion-temperature profiles at the peak compression ($t = 3.14$ ns). The peak density drops from $\rho = 354$ g/cm^3 in the *SESAME*/AOT/κ_{LM} model simulation to $\rho = 262$ g/cm^3 in the case of using FP-based DT properties (FPEOS/FPOT/κ_{QMD}). Also, the hot-spot pressure, ion temperature, and target convergence ratio are somewhat reduced in the FP simulation. These differences cause ~36% reduction in the 1-D neutron yield prediction for the FPEOS/FPOT/κ_{QMD} simulation, which is shown by Fig. 141.33(d). Finally, we compare the compression ρR history

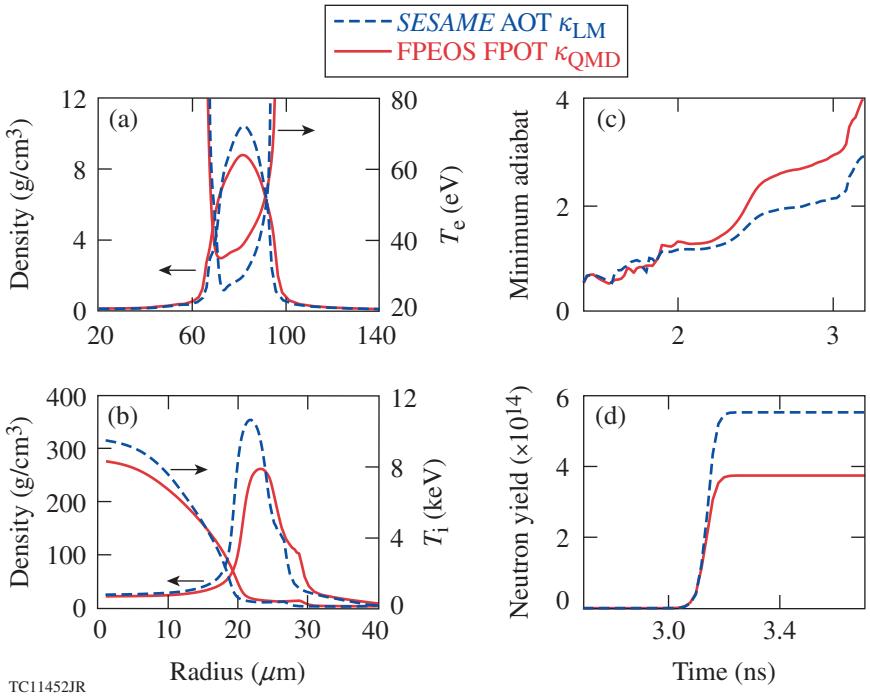

Figure 141.33
The hydro-simulation results using our first-principles–calculated properties of DT (solid red lines) are compared with the normal model simulation using *SESAME*-EOS, AOT, and the Lee–More thermal conductivity (dashed blue lines), for the OMEGA implosion shown in Fig. 141.32. The panels illustrate (a) the density and electron temperature profiles at t = 2.96 ns (the start of deceleration), (b) the minimum adiabat α as a function of time, (c) the density and ion temperature profile at peak compression (t = 3.14 ns), and (d) the neutron yield as a function of time.

in Fig. 141.34 for the two simulations. Consistent with the overall performance reduction, the FPEOS/FPOT/κ_{QMD} simulation gives a lower peak ρR than the model prediction. The neutron-averaged $\langle \rho R \rangle_n$ drops from 266 mg/cm^2 (*SESAME*-AOT-κ_{LM}) to 228 mg/cm^2 (FPOT/FPOT/κ_{QMD}). Namely, the compression ρR reduction is ~15% for this OMEGA implosion.

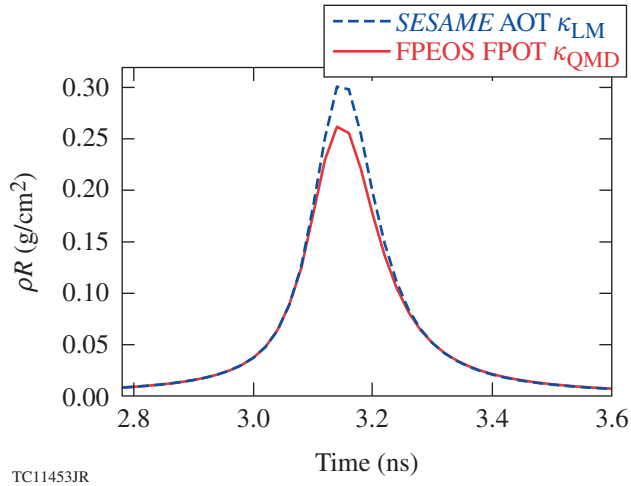

Figure 141.34
The predicted compression ρR's as a function of time are compared for the two simulations of the cryogenic DT implosion on OMEGA shown by Fig. 141.32. The neutron-averaged areal densities are $\langle \rho R \rangle_n$ = 266 mg/cm^2 (*SESAME*/AOT/κ_{LM}) and $\langle \rho R \rangle_n$ = 228 mg/cm^2 (FPOT/FPOT/κ_{QMD}), respectively.

Next, we study how the FP-based properties of DT affect the direct-drive–ignition target designs for the NIF. As a hydro-equivalent implosion to the OMEGA target discussed above, Fig. 141.35 shows the NIF target and the pulse shape, which are scaled from the hydro-equivalent OMEGA case shown in Fig. 141.32. The ϕ = 3452-μm target consists of a 36-μm CH/CHSi ablator layer and a 190-μm DT layer. The scaled laser pulse has a total energy of 1.5 MJ. According to the standard model prediction, this NIF ignition design should give a low-adiabat ($\alpha \simeq 2$) implosion. Again, we performed two 1-D hydro simulations using either the FP-based properties of DT or the standard plasma models. The simulation results are compared in Figs. 141.36 and 141.37. In Figs. 141.36(a) and 141.36(b), the density and temperature (T_e/T_i) profiles are plotted for the start of the deceleration stage (t = 13.0 ns) and the peak compression at t = 13.84 ns, respectively. Similar to what we have seen for the typical OMEGA implosion, the NIF results also show the reduced density and hot-spot ion temperature in the FPEOS/FPOT/κ_{QMD} simulation. The peak ion tem-

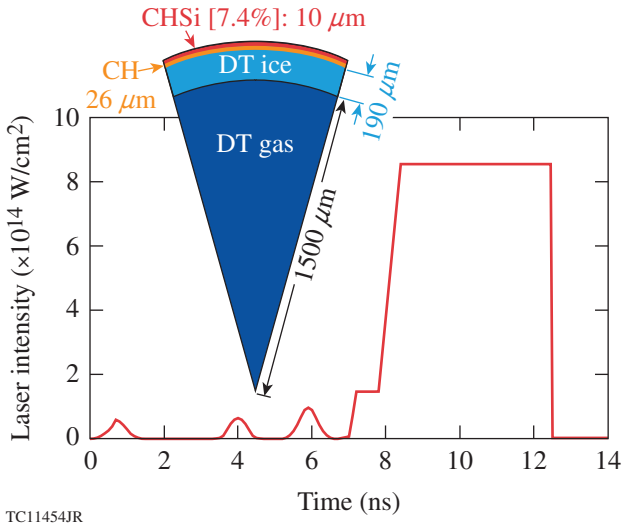

Figure 141.35
The model-predicted pulse shape for a direct-drive, low-adiabat ($\alpha \simeq 2$) ignition design for NIF, which is scaled from the OMEGA implosion shown in Fig. 141.32. The insert is a schematic diagram of a NIF target.

peratures inside the hot spot, illustrated by Fig. 141.36(b), are $T_i \simeq 10.9$ keV from the FP simulation, which is in contrast to the model-predicted $T_i \simeq 12.1$ keV. The peak density is also reduced to $\rho = 298$ g/cm^3 in the FPEOS/FPOT/κ_{QMD} simulation from the model-predicted $\rho = 371$ g/cm^3. These variations in ion temperature and peak compression can further affect the ignition burn-wave propagation. Figure 141.37(a) compares the FPEOS/FPOT/κ_{QMD} and SESAME/AOT/κ_{LM} simulations, at the start of burn-wave propagation (t = 13.86 ns). Now, the burn-wave–generated high pressure "reshocks" the shell and the resulting peak-density has a larger discrepancy: ρ = 532 g/cm^3 [*SESAME*/AOT/κ_{LM}] versus ρ = 366 g/cm^3 [FPEOS/FPOT/κ_{QMD}]; the temperature of burning plasmas in the hot spot varies from T_i = 17 keV to T_i = 13.4 keV, respectively. At the end, the total neutron yield changes from $Y = 2.1 \times 10^{19}$ [*SESAME*/AOT/κ_{LM}] to $Y = 1.2 \times 10^{19}$ [FPEOS/FPOT/κ_{QMD}], as indicated by Fig. 141.37(b). The energy gain varies accordingly by a factor of ~2, dropping from G = 40.0 to G = 23.4.

The degradation in target performance discussed above can be attributed to the plasma condition (ρ/T) changes in the in-flight DT shell. Namely, the model-predicted low adiabat ($\alpha \simeq 2$) is not reached in the imploding capsule. Instead, a higher adiabat is inferred from the FPEOS/FPOT/κ_{QMD} simulation. Therefore, to obtain a high-level gain (G = 40), we must use the FPEOS/FPOT/κ_{QMD} tables to retune the laser pulse so that the desired low-adiabat implosion can be recovered. As an

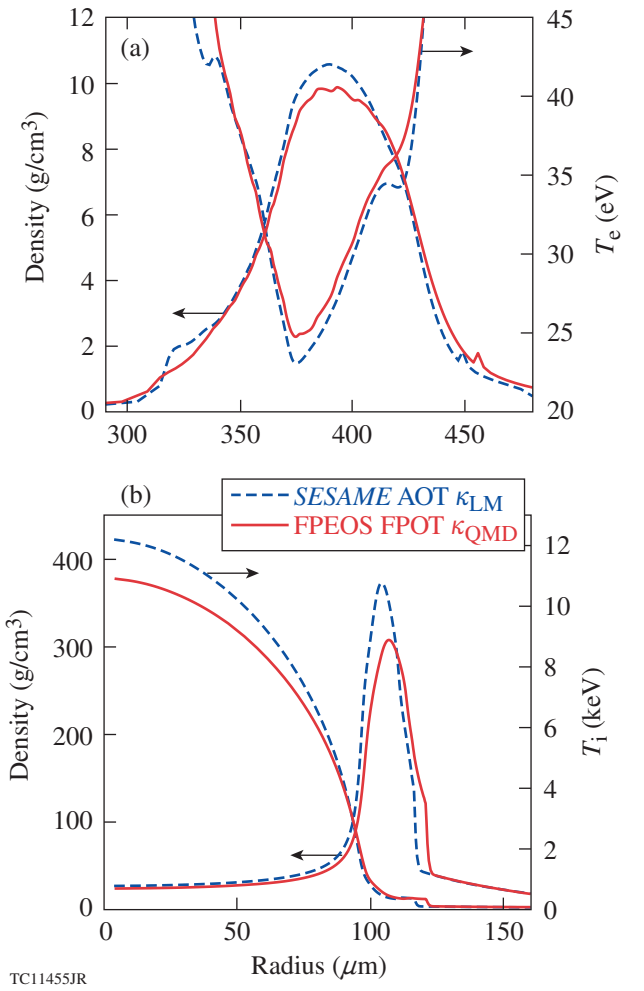

Figure 141.36
The hydro-simulation results using our first-principles–calculated properties of DT (solid red lines) are compared with the standard model simulation using *SESAME*-EOS, AOT, and the Lee–More thermal conductivity (dashed blue lines), for the NIF design shown in Fig. 141.35. The two panels indicate (a) the density and electron temperature profiles at t = 13.0 ns (the start of deceleration) and (b) the density and ion temperature as a function of radius at peak compression (t = 13.84 ns).

example, we show in Fig. 141.38(a) the fine-tuned pulse shape (solid red line) by using the FPEOS/FPOT/κ_{QMD} tables. The dashed blue line represents the original pulse shape predicted by the *SESAME*/AOT/κ_{LM} model. Compared to the original pulse, the retuned pulse has a slightly larger separation between the second and third pickets; also, the height of the main pulse's "step" is now both higher and longer than the original pulse. All these pulse changes place the target adiabat truly in the low level of $\alpha \simeq 2$, after the shock coalescence and enhanced radiation preheat are taken into account. Figure 141.38(b) indicates that the desired high-gain ($G \simeq 40$) implosion is now recovered with the retuned pulse using the FP-based properties of DT.

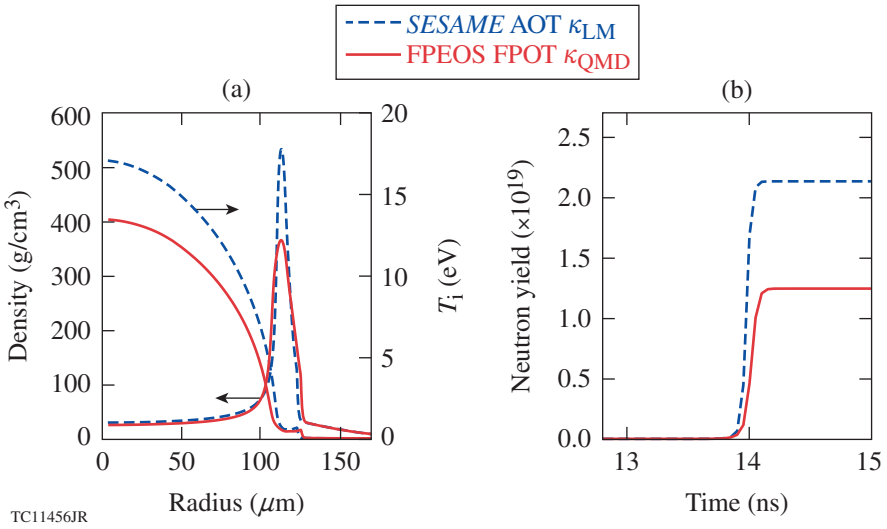

Figure 141.37
(a) Similar comparisons as shown in Fig. 141.36(b), but for a slightly later time (t = 13.86 ns) when the burn wave starts to propagate. The neutron production as a function of time is compared in (b) for the two simulations, in which the predicted energy gains are G = 40.0 (*SESAME*/AOT/κ_{LM}) and G = 23.4 (FPEOS/FPOT/κ_{QMD}), respectively.

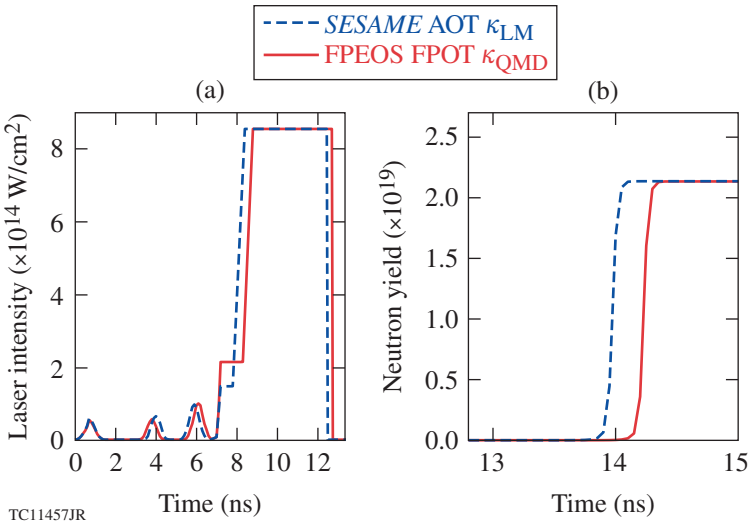

Figure 141.38
(a) The pulse shape (solid red line) was tuned by hydro-simulation using the first-principles properties of DT (FPEOS/FPOT/κ_{QMD}) to recover the high-gain level of $G \simeq 40$ for the same NIF target shown by the inset in Fig. 141.35. The dashed blue line indicates the original pulse shape predicted by the SESAME/AOT/κ_{LM} model for a similar gain level. The panel (b) shows the corresponding neutron yields predicted by hydro simulations using FPEOS/FPOT/κ_{QMD} and *SESAME*/AOT/κ_{LM}, for the same NIF target but different pulse shapes than illustrated in (a).

In Figs. 141.39 and 141.40, we further investigate a direct-drive NIF design with a very low adiabat ($\alpha \simeq 1.5$), which is the adiabat level often encountered in indirect-drive ICF implosions.[2–4] In such lower-adiabat implosions, the DT shells having higher ρ and lower T are in more strongly coupled and degenerate plasma conditions. Namely, the DT plasmas are readily in the WDM regime, and bigger differences between FPEOS/FPOT/κ_{QMD} and *SESAME*/AOT/κ_{LM} are expected. Here, the direct-drive NIF design uses a thin-layer (11-μm) HDC ablator. The HDC ablator has also been considered for indirect-drive target designs.[112] The thickness of DT ice is 180 μm with a target diameter of ϕ = 2982 μm. This relatively smaller target is intended to be driven by a low-intensity (~6 × 10^{14} W/cm^2), 1-MJ laser pulse (shown in Fig. 141.39). The implosion velocity is also relatively low: $v_{imp} \simeq 3 \times 10^7$ cm/s. The use of a mid-Z ablator and low-intensity pulse could avoid possible fast-electron preheat issues caused by the TPD instability.[113–116] The 1-D hydro-simulation results are presented in Fig. 141.40, where the peak density and T_i are compared for both FPEOS/FPOT/κ_{QMD} and *SESAME*/AOT/κ_{LM} simulations. Figure 141.40(a) shows the situation at the peak compression (t = 13.11 ns), while Fig. 141.40(b) illustrates the situation at the beginning of burn-wave propagation (t = 13.20 ns). Larger differences are seen in Fig. 141.40(b): ρ = 713 g/cm^3 versus ρ = 496 g/cm^3 and T_i = 20 keV versus T_i = 15.5 keV, respectively, from the *SESAME*/AOT/κ_{LM} and the FPEOS/FPOT/κ_{QMD} simulations. The final energy gain varies from the model-predicted G = 28.3 to G = 11.5 in the FP-based simulation. The variation is about a factor of ~2.5 between the two simulations, which is even larger than the α = 2 case discussed above.

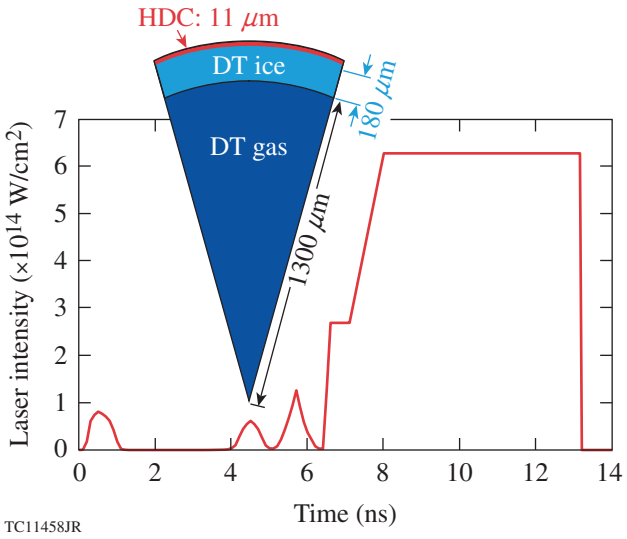

Figure 141.39
A very-low-adiabat ($\alpha \simeq 1.5$), low-implosion-velocity ($v_{imp} = 3.0 \times 10^7$ cm/s), direct-drive–ignition design for the NIF, which uses high-density carbon (HDC) as the thin-layer ablator. The target dimensions are illustrated in the inset. The mid-Z ablator and the lower peak intensity (~6×10^{14} W/cm^2) can help to reduce the TPD instability to avoid possible fast-electron preheat.

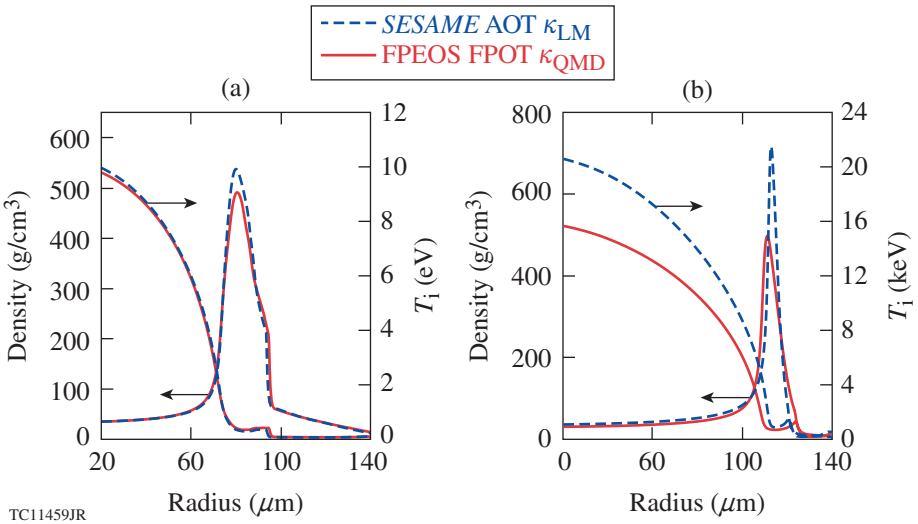

Figure 141.40
Simulation results for the thin HDC ablator target shown in Fig. 141.39: (a) the density and ion temperature profiles at the peak compression (t = 13.11 ns) and (b) the similar situation for a slightly later time (t = 13.20 ns) when the burn wave starts to propagate. The predicted energy gains are $G = 28.3$ (*SESAME*/AOT/κ_{LM}) and $G = 11.5$ (FPOT/FPOT/κ_{QMD}), respectively.

Summary

Combining the first-principles methods of PIMC and QMD, we have systematically derived accurate self-consistent properties of deuterium plasmas (or DT plasmas by mass scaling) over a wide range of densities and temperatures for ICF applications. They include the first-principles equation of state (FPEOS), the QMD-derived thermal conductivity (κ_{QMD}), and the first-principles opacity table (FPOT). Comparing these FP-based properties with the standard models adopted in hydrocodes, we found large discrepancies in the warm dense plasma regime. Implementing these FP-based tables into our hydrocodes, we have examined their combined effects on predicting ICF implosions, through hydro-simulations of both OMEGA targets and NIF ignition target designs. In predicting target performance between the FPEOS/FPOT/κ_{QMD} simulation and the usual models *SESAME*/AOT/κ_{LM}, changes of up to a factor of ~2.5 have been seen. The differences are caused by the adiabat increase, related to the stiffer behavior of DT in the pressure range of P = 10 to 100 Mbar, the enhanced opacity of the warm dense DT shell, and the higher thermal conductivity in the shell. The lower the adiabat of an ICF imploding capsule, the more variations expected. The desired high-gain target, which is truly a low-adiabat implosion, should be designed with the FP-based properties of DT fuel.

The stopping power of α particles in warm dense DT plasmas, recently attracting much attention in model studies and classical-MD calculations,[117,118] remains to be investigated by first-principles methods. We also noted that the ablator materials (CH, CHSi, and C) were still simulated with the standard

models in the current study. Whether or not that might change the prediction of the overall target performance remains to be investigated in future studies. But if we follow the same spirit of systematic work on DT, we could extend such first-principles studies to ICF-relevant ablator materials in the near future. Completely knowing the warm-dense–plasma properties of both DT and ablator materials would not only be beneficial for reliable ICF target designs but also improve our understanding of material behavior under HED conditions in general. We also hope that such first-principles studies will facilitate future experiments in the relevant plasma conditions.

ACKNOWLEDGMENT

This material is based upon work supported by the Department of Energy National Nuclear Security Administration under Award Number DE-NA0001944, the University of Rochester, and the New York State Energy Research and Development Authority. The support of DOE does not constitute an endorsement by DOE of the views expressed in this article. This work was also supported by Scientific Campaign 10 at the Los Alamos National Laboratory, operated by Los Alamos National Security, LLC for the National Nuclear Security Administration of the U.S. Department of Energy under Contract No. DE-AC52-06NA25396. B. Militzer acknowledges support from NSF and NASA.

REFERENCES

1. J. Nuckolls *et al*., Nature **239**, 139 (1972).
2. S. W. Haan, J. D. Lindl, D. A. Callahan, D. S. Clark, J. D. Salmonson, B. A. Hammel, L. J. Atherton, R. C. Cook, M. J. Edwards, S. Glenzer, A. V. Hamza, S. P. Hatchett, M. C. Herrmann, D. E. Hinkel, D. D. Ho, H. Huang, O. S. Jones, J. Kline, G. Kyrala, O. L. Landen, B. J. MacGowan, M. M. Marinak, D. D. Meyerhofer, J. L. Milovich, K. A. Moreno, E. I. Moses, D. H. Munro, A. Nikroo, R. E. Olson, K. Peterson, S. M. Pollaine, J. E. Ralph, H. F. Robey, B. K. Spears, P. T. Springer, L. J. Suter, C. A. Thomas, R. P. Town, R. Vesey, S. V. Weber, H. L. Wilkens, and D. C Wilson, Phys. Plasmas **18**, 051001 (2011).
3. M. J. Edwards, J. D. Lindl, B. K. Spears, S. V. Weber, L. J. Atherton, D. L. Bleuel, D. K. Bradley, D. A. Callahan, C. J. Cerjan, D. Clark, G. W. Collins, J. E. Fair, R. J. Fortner, S. H. Glenzer, S. W. Haan, B. A. Hammel, A. V. Hamza, S. P. Hatchett, N. Izumi, B. Jacoby, O. S. Jones, J. A. Koch, B. J. Kozioziemski, O. L. Landen, R. Lerche, B. J. MacGowan, A. J. MacKinnon, E. R. Mapoles, M. M. Marinak, M. Moran, E. I. Moses, D. H. Munro, D. H. Schneider, S. M. Sepke, D. A. Shaughnessy, P. T. Springer, R. Tommasini, L. Bernstein, W. Stoeffl, R. Betti, T. R. Boehly, T. C. Sangster, V. Yu. Glebov, P. W. McKenty, S. P. Regan, D. H. Edgell, J. P. Knauer, C. Stoeckl, D. R. Harding, S. Batha, G. Grim, H. W. Herrmann, G. Kyrala, M. Wilke, D. C. Wilson, J. Frenje, R. Petrasso, K. Moreno, H. Huang, K. C. Chen, E. Giraldez, J. D. Kilkenny, M. Mauldin, N. Hein, M. Hoppe, A. Nikroo, and R. J. Leeper, Phys. Plasmas **18**, 051003 (2011).
4. C. Cherfils-Clérouin *et al*., J. Phys.: Conf. Ser. **244**, 022009 (2010).
5. D. D. Meyerhofer, R. L. McCrory, R. Betti, T. R. Boehly, D. T. Casey, T. J. B. Collins, R. S. Craxton, J. A. Delettrez, D. H. Edgell, R. Epstein, K. A. Fletcher, J. A. Frenje, V. Yu. Glebov, V. N. Goncharov, D. R. Harding, S. X. Hu, I. V. Igumenshchev, J. P. Knauer, C. K. Li, J. A. Marozas, F. J. Marshall, P. W. McKenty, P. M. Nilson, S. P. Padalino, R. D. Petrasso, P. B. Radha, S. P. Regan, T. C. Sangster, F. H. Séguin, W. Seka, R. W. Short, D. Shvarts, S. Skupsky, J. M. Soures, C. Stoeckl, W. Theobald, and B. Yaakobi, Nucl. Fusion **51**, 053010 (2011).
6. R. L. McCrory, R. Betti, T. R. Boehly, D. T. Casey, T. J. B. Collins, R. S. Craxton, J. A. Delettrez, D. H. Edgell, R. Epstein, J. A. Frenje, D. H. Froula, M. Gatu-Johnson, V. Yu. Glebov, V. N. Goncharov, D. R. Harding, M. Hohenberger, S. X. Hu, I. V. Igumenshchev, T. J. Kessler, J. P. Knauer, C. K. Li, J. A. Marozas, F. J. Marshall, P. W. McKenty, D. D. Meyerhofer, D. T. Michel, J. F. Myatt, P. M. Nilson, S. J. Padalino, R. D. Petrasso, P. B. Radha, S. P. Regan, T. C. Sangster, F. H. Séguin, W. Seka, R. W. Short, A. Shvydky, S. Skupsky, J. M. Soures, C. Stoeckl, W. Theobald, B. Yaakobi, and J. D. Zuegel, Nucl. Fusion **53**, 113021 (2013).
7. O. A. Hurricane *et al*., Nature **506**, 343 (2014).
8. S. X. Hu, V. N. Goncharov, and S. Skupsky, Phys. Plasmas **19**, 072703 (2012).
9. D. S. Clark *et al*., Phys. Plasmas **18**, 082701 (2011).
10. T. R. Dittrich *et al*., Phys. Rev. Lett. **112**, 055002 (2014).
11. S. X. Hu, P. B. Radha, J. A. Marozas, R. Betti, T. J. B. Collins, R. S. Craxton, J. A. Delettrez, D. H. Edgell, R. Epstein, V. N. Goncharov, I. V. Igumenshchev, F. J. Marshall, R. L. McCrory, D. D. Meyerhofer, S. P. Regan, T. C. Sangster, S. Skupsky, V. A. Smalyuk, Y. Elbaz, and D. Shvarts, Phys. Plasmas **16**, 112706 (2009).
12. S. X. Hu, V. N. Goncharov, P. B. Radha, J. A. Marozas, S. Skupsky, T. R. Boehly, T. C. Sangster, D. D. Meyerhofer, and R. L. McCrory, Phys. Plasmas **17**, 102706 (2010).
13. S. Atzeni and J. Meyer-ter-Vehn, *The Physics of Inertial Fusion: Beam Plasma Interaction, Hydrodynamics, Hot Dense Matter*, International Series of Monographs on Physics (Clarendon Press, Oxford, 2004).
14. S. X. Hu, V. A. Smalyuk, V. N. Goncharov, J. P. Knauer, P. B. Radha, I. V. Igumenshchev, J. A. Marozas, C. Stoeckl, B. Yaakobi, D. Shvarts, T. C. Sangster, P. W. McKenty, D. D. Meyerhofer, S. Skupsky, and R. L. McCrory, Phys. Rev. Lett. **100**, 185003 (2008).
15. R. C. Malone, R. L. McCrory, and R. L. Morse, Phys. Rev. Lett. **34**, 721 (1975).
16. V. N. Goncharov, T. C. Sangster, P. B. Radha, R. Betti, T. R. Boehly, T. J. B. Collins, R. S. Craxton, J. A. Delettrez, R. Epstein, V. Yu. Glebov, S. X. Hu, I. V. Igumenshchev, J. P. Knauer, S. J. Loucks, J. A. Marozas, F. J. Marshall, R. L. McCrory, P. W. McKenty, D. D. Meyerhofer, S. P. Regan, W. Seka, S. Skupsky, V. A. Smalyuk, J. M. Soures, C. Stoeckl, D. Shvarts, J. A. Frenje, R. D. Petrasso, C. K. Li, F. Séguin, W. Manheimer, and D. G. Colombant, Phys. Plasmas **15**, 056310 (2008).
17. S. X. Hu, V. Smalyuk, V. N. Goncharov, S. Skupsky, T. C. Sangster, D. D. Meyerhofer, and D. Shvarts, Phys. Rev. Lett. **101**, 055002 (2008).
18. S. Skupsky, Phys. Rev. A **16**, 727 (1977).
19. C. K. Li and R. D. Petrasso, Phys. Rev. Lett. **70**, 3059 (1993).

20. L. S. Brown, D. L. Preston, and R. L. Singleton, Jr., Phys. Rep. **410**, 237 (2005).
21. M. C. Herrmann, M. Tabak, and J. D. Lindl, Nucl. Fusion **41**, 99 (2001).
22. C. D. Zhou and R. Betti, Phys. Plasmas **15**, 102707 (2008).
23. R. Nora, R. Betti, K. S. Anderson, A. Shvydky, A. Bose, K. M. Woo, A. R. Christopherson, J. A. Marozas, T. J. B. Collins, P. B. Radha, S. X. Hu, R. Epstein, F. J. Marshall, R. L. McCrory, T. C. Sangster, and D. D. Meyerhofer, Phys. Plasmas **21**, 056316 (2014).
24. V. N. Goncharov, T. C. Sangster, R. Betti, T. R. Boehly, M. J. Bonino, T. J. B. Collins, R. S. Craxton, J. A. Delettrez, D. H. Edgell, R. Epstein, R. K. Follet, C. J. Forrest, D. H. Froula, V. Yu. Glebov, D. R. Harding, R. J. Henchen, S. X. Hu, I. V. Igumenshchev, R. Janezic, J. H. Kelly, T. J. Kessler, T. Z. Kosc, S. J. Loucks, J. A. Marozas, F. J. Marshall, A. V. Maximov, R. L. McCrory, P. W. McKenty, D. D. Meyerhofer, D. T. Michel, J. F. Myatt, R. Nora, P. B. Radha, S. P. Regan, W. Seka, W. T. Shmayda, R. W. Short, A. Shvydky, S. Skupsky, C. Stoeckl, B. Yaakobi, J. A. Frenje, M. Gatu-Johnson, R. D. Petrasso, and D. T. Casey, Phys. Plasmas **21**, 056315 (2014).
25. B. I. Bennett *et al*., Los Alamos National Laboratory, Los Alamos, NM, Report LA-7130 (1978).
26. G. I. Kerley, Sandia National Laboratory, Albuquerque, NM, Report SAND2003-3613 (2003).
27. G. I. Kerley, Phys. Earth Planet. Inter. **6**, 78 (1972).
28. Y. T. Lee and R. M. More, Phys. Fluids **27**, 1273 (1984).
29. B. Wilson *et al*., J. Quant. Spectrosc. Radiat. Transf. **99**, 658 (2006).
30. W. F. Huebner *et al*., Los Alamos National Laboratory, Los Alamos, NM, Report LA-6760-M (1977).
31. C. A. Iglesias and F. J. Rogers, Astrophys. J. **464**, 943 (1996).
32. C. Pierleoni *et al*., Phys. Rev. Lett. **73**, 2145 (1994).
33. B. Militzer and D. M. Ceperley, Phys. Rev. Lett. **85**, 1890 (2000).
34. B. Militzer *et al*., Phys. Rev. Lett. **87**, 275502 (2001).
35. V. S. Filinov *et al*., Plasma Phys. Control. Fusion **43**, 743 (2001).
36. S. X. Hu, B. Militzer, V. N. Goncharov, and S. Skupsky, Phys. Rev. Lett. **104**, 235003 (2010).
37. S. X. Hu, B. Militzer, V. N. Goncharov, and S. Skupsky, Phys. Rev. B **84**, 224109 (2011).
38. L. Collins *et al*., Phys. Rev. E **52**, 6202 (1995).
39. J. G. Clérouin and S. Bernard, Phys. Rev. E **56**, 3534 (1997).
40. J. Clérouin and J.-F. Dufrêche, Phys. Rev. E **64**, 066406 (2001).
41. L. A. Collins *et al*., Phys. Rev. B **63**, 184110 (2001).
42. M. P. Desjarlais, Phys. Rev. B **68**, 064204 (2003).
43. B. Holst, R. Redmer, and M. P. Desjarlais, Phys. Rev. B **77**, 184201 (2008).
44. L. Caillabet, S. Mazevet, and P. Loubeyre, Phys. Rev. B **83**, 094101 (2011).
45. L. A. Collins, J. D. Kress, and D. E. Hanson, Phys. Rev. B **85**, 233101 (2012).
46. M. A. Morales *et al*., High Energy Density Phys. **8**, 5 (2012).
47. J. Vorberger, D. O. Gericke, and W. D. Kraeft, High Energy Density Phys. **9**, 448 (2013).
48. C. Wang and P. Zhang, Phys. Plasmas **20**, 092703 (2013).
49. V. V. Karasiev *et al*., Phys. Rev. B **88**, 161108(R) (2013).
50. J. M. McMahon *et al*., Rev. Mod. Phys. **84**, 1607 (2012).
51. L. B. Da Silva *et al*., Phys. Rev. Lett. **78**, 483 (1997).
52. G. W. Collins *et al*., Science **281**, 1178 (1998).
53. A. N. Mostovych *et al*., Phys. Rev. Lett. **85**, 3870 (2000); A. N. Mostovych *et al*., Phys. Plasmas **8**, 2281 (2001).
54. M. D. Knudson *et al*., Phys. Rev. Lett. **87**, 225501 (2001).
55. M. D. Knudson *et al*., Phys. Rev. Lett. **90**, 035505 (2003).
56. V. E. Fortov *et al*., Phys. Rev. Lett. **99**, 185001 (2007).
57. D. G. Hicks, T. R. Boehly, P. M. Celliers, J. H. Eggert, S. J. Moon, D. D. Meyerhofer, and G. W. Collins, Phys. Rev. B **79**, 014112 (2009).
58. P. Loubeyre, S. Brygoo, J. Eggert, P. M. Celliers, D. K. Spaulding, J. R. Rygg, T. R. Boehly, G. W. Collins, and R. Jeanloz, Phys. Rev. B **86**, 144115 (2012).
59. V. Recoules *et al*., Phys. Rev. Lett. **102**, 075002 (2009).
60. F. Lambert *et al*., Phys. Plasmas **18**, 056306 (2011).
61. D. E. Hanson *et al*., Phys. Plasmas **18**, 082704 (2011).
62. B. Holst, M. French, and R. Redmer, Phys. Rev. B **83**, 235120 (2011).
63. C. E. Starrett *et al*., Phys. Plasmas **19**, 102709 (2012).
64. C. Wang *et al*., Phys. Rev. E **88**, 013106 (2013).
65. S. X. Hu, L. A. Collins, T. R. Boehly, J. D. Kress, V. N. Goncharov, and S. Skupsky, Phys. Rev. E **89**, 043105 (2014).
66. J. D. Kress *et al*., High Energy Density Phys. **7**, 155 (2011).
67. J. D. Kress *et al*., Phys. Rev. E **82**, 036404 (2010).
68. G. Faussurier *et al*., Phys. Plasmas **21**, 092706 (2014).
69. G. Dimonte and J. Daligault, Phys. Rev. Lett. **101**, 135001 (2008).
70. B. Jeon *et al*., Phys. Rev. E **78**, 036403 (2008).

71. J. N. Glosli *et al*., Phys. Rev. E **78**, 025401 (R) (2008).

72. L. X. Benedict *et al*., Phys. Rev. Lett. **102**, 205004 (2009).

73. B. Xu and S. X. Hu, Phys. Rev. E **84**, 016408 (2011).

74. L. X. Benedict *et al*., Phys. Rev. E **86**, 046406 (2012).

75. C. Blancard, J. Clérouin, and G. Faussurier, High Energy Density Phys. **9**, 247 (2013).

76. S. X. Hu, L. A. Collins, V. N. Goncharov, T. R. Boehly, R. Epstein, R. L. McCrory, and S. Skupsky, Phys. Rev. E **90**, 033111 (2014).

77. P. M. Celliers *et al*., Phys. Rev. Lett. **84**, 5564 (2000).

78. T. R. Boehly, D. H. Munro, P. M. Celliers, R. E. Olson, D. G. Hicks, V. N. Goncharov, G. W. Collins, H. F. Robey, S. X. Hu, J. A. Marozas, T. C. Sangster, O. L. Landen, and D. D. Meyerhofer, Phys. Plasmas **16**, 056302 (2009); T. R. Boehly, V. N. Goncharov, W. Seka, S. X. Hu, J. A. Marozas, D. D. Meyerhofer, P. M. Celliers, D. G. Hicks, M. A. Barrios, D. Fratanduono, and G. W. Collins, Phys. Plasmas **18**, 092706 (2011); T. R. Boehly, V. N. Goncharov, W. Seka, M. A. Barrios, P. M. Celliers, D. G. Hicks, G. W. Collins, S. X. Hu, J. A. Marozas, and D. D. Meyerhofer, Phys. Rev. Lett. **106**, 195005 (2011).

79. C. Wang, X.-T. He, and P. Zhang, Phys. Plasmas **18**, 082707 (2011).

80. S. Hamel, L. X. Benedict, P. M. Celliers, M. A. Barrios, T. R. Boehly, G. W. Collins, T. Döppner, J. H. Eggert, D. R. Farley, D. G. Hicks, J. L. Kline, A. Lazicki, S. LePape, A. J. Mackinnon, J. D. Moody, H. F. Robey, E. Schwegler, and P. A. Sterne, Phys. Rev. B **86**, 094113 (2012).

81. K. P. Driver and B. Militzer, Phys. Rev. Lett. **108**, 115502 (2012).

82. S. X. Hu, T. R. Boehly, and L. A. Collins, Phys. Rev. E **89**, 063104 (2014).

83. T. R. Mattsson *et al*., Phys. Rev. B **81**, 054103 (2010).

84. L. X. Benedict *et al*., Phys. Rev. B **89**, 224109 (2014).

85. R. F. Smith *et al*., Nature **511**, 330 (2014).

86. S. H. Glenzer *et al*., Science **327**, 1228 (2010).

87. A. L. Kritcher *et al*., Phys. Rev. Lett. **107**, 015002 (2011).

88. S. H. Glenzer *et al*., Phys. Rev. Lett. **90**, 175002 (2003).

89. S. P. Regan, K. Falk, G. Gregori, P. B. Radha, S. X. Hu, T. R. Boehly, B. J. B. Crowley, S. H. Glenzer, O. L. Landen, D. O. Gericke, T. Döppner, D. D. Meyerhofer, C. D. Murphy, T. C. Sangster, and J. Vorberger, Phys. Rev. Lett. **109**, 265003 (2012).

90. E. L. Pollock, Comput. Phys. Commun. **52**, 49 (1988).

91. D. M. Ceperley, Rev. Mod. Phys. **67**, 279 (1995).

92. D. M. Ceperley, in *Monte Carlo and Molecular Dynamics of Condensed Matter Systems*, edited by K. Binder and G. Ciccotti (Italian Physical Society, Bologna, Italy, 1996).

93. B. Militzer and E. L. Pollock, Phys. Rev. E **61**, 3470 (2000).

94. B. Militzer, Phys. Rev. Lett. **97**, 175501 (2006).

95. B. Militzer, Phys. Rev. B **79**, 155105 (2009).

96. P. Hohenberg and W. Kohn, Phys. Rev. **136**, B864 (1964).

97. W. Kohn and L. J. Sham, Phys. Rev. **140**, A1133 (1965).

98. N. D. Mermin, Phys. Rev. **137**, A1441 (1965).

99. G. Kresse and J. Hafner, Phys. Rev. B **47**, 558 (1993).

100. G. Kresse and J. Hafner, Phys. Rev. B **49**, 14,251 (1994).

101. J. P. Perdew, K. Burke, and M. Ernzerhof, Phys. Rev. Lett. **77**, 3865 (1996); *ibid*. **78**, 1396(E) (1997).

102. R. Kubo, J. Phys. Soc. Jpn. **12**, 570 (1957); D. A. Greenwood, Proc. Phys. Soc. Lond. **71**, 585 (1958).

103. F. Perrot, Laser Part. Beams **14**, 731 (1996).

104. For details of the *ABINIT* code, please refer to http://www.abinit.org/.

105. T. R. Boehly, D. G. Hicks, P. M. Celliers, T. J. B. Collins, R. Earley, J. H. Eggert, D. Jacobs-Perkins, S. J. Moon, E. Vianello, D. D. Meyerhofer, and G. W. Collins, Phys. Plasmas **11**, L49 (2004).

106. G. V. Boriskov *et al*., Phys. **48**, 553 (2003).

107. J. Delettrez, R. Epstein, M. C. Richardson, P. A. Jaanimagi, and B. L. Henke, Phys. Rev. A **36**, 3926 (1987).

108. S. X. Hu, G. Fiksel, V. N. Goncharov, S. Skupsky, D. D. Meyerhofer, and V. A. Smalyuk, Phys. Rev. Lett. **108**, 195003 (2012).

109. G. Fiksel, S. X. Hu, V. N. Goncharov, D. D. Meyerhofer, T. C. Sangster, V. A. Smalyuk, B. Yaakobi, M. J. Bonino, and R. Jungquist, Phys. Plasmas **19**, 062704 (2012).

110. V. N. Goncharov, T. C. Sangster, T. R. Boehly, S. X. Hu, I. V. Igumenshchev, F. J. Marshall, R. L. McCrory, D. D. Meyerhofer, P. B. Radha, W. Seka, S. Skupsky, C. Stoeckl, D. T. Casey, J. A. Frenje, and R. D. Petrasso, Phys. Rev. Lett. **104**, 165001 (2010).

111. T. C. Sangster, V. N. Goncharov, R. Betti, P. B. Radha, T. R. Boehly, D. T. Casey, T. J. B. Collins, R. S. Craxton, J. A. Delettrez, D. H. Edgell, R. Epstein, C. J. Forrest, J. A. Frenje, D. H. Froula, M. Gatu-Johnson, V. Yu. Glebov, D. R. Harding, M. Hohenberger, S. X. Hu, I. V. Igumenshchev, R. Janezic, J. H. Kelly, T. J. Kessler, C. Kingsley, T. Z. Kosc, J. P. Knauer, S. J. Loucks, J. A. Marozas, F. J. Marshall, A. V. Maximov, R. L. McCrory, P. W. McKenty, D. D. Meyerhofer, D. T. Michel, J. F. Myatt, R. D. Petrasso, S. P. Regan, W. Seka, W. T. Shmayda, R. W. Short, A. Shvydky, S. Skupsky, J. M. Soures, C. Stoeckl, W. Theobald, V. Versteeg, B. Yaakobi, and J. D. Zuegel, Phys. Plasmas **20**, 056317 (2013).

112. O. L. Landen, D. K. Bradley, D. G. Braun, V. A. Smalyuk, D. G. Hicks, P. M. Celliers, S. Prisbrey, R. Page, T. R. Boehly, S. W. Haan, D. H. Munro, R. G. Wallace, A. Nikroo, A. Hamza, J. Biener, C. Wild, E. Woerner, R. E. Olson, G. A. Rochau, M. Knudson, D. C. Wilson, H. F. Robey, G. W. Collins, D. Ho, J. Edwards, M. M. Marinak, B. A. Hammel, D. D. Meyerhofer, and B. J. MacGowan, J. Phys.: Conf. Ser. **112**, 022004 (2008).

113. D. H. Froula, B. Yaakobi, S. X. Hu, P.-Y. Chang, R. S. Craxton, D. H. Edgell, R. Follett, D. T. Michel, J. F. Myatt, W. Seka, R. W. Short, A. Solodov, and C. Stoeckl, Phys. Rev. Lett. **108**, 165003 (2012).

114. D. T. Michel, A. V. Maximov, R. W. Short, S. X. Hu, J. F. Myatt, W. Seka, A. A. Solodov, B. Yaakobi, and D. H. Froula, Phys. Rev. Lett. **109**, 155007 (2012).

115. S. X. Hu, D. T. Michel, D. H. Edgell, D. H. Froula, R. K. Follett, V. N. Goncharov, J. F. Myatt, S. Skupsky, and B. Yaakobi, Phys. Plasmas **20**, 032704 (2013).

116. J. F. Myatt, H. X. Vu, D. F. DuBois, D. A. Russell, J. Zhang, R. W. Short, and A. V. Maximov, Phys. Plasmas **20**, 052705 (2013).

117. L. S. Brown and R. L. Singleton, Phys. Rev. E **79**, 066407 (2009).

118. P. E. Grabowski *et al*., Phys. Rev. Lett. **111**, 215002 (2013).

Spherical Strong-Shock Generation for Shock-Ignition Inertial Fusion

Introduction

Shock ignition (SI)[1–5] is an advanced concept in inertial confinement fusion (ICF)[6] that is very promising and has the potential to provide significantly higher gains than conventional hot-spot ignition.[7] SI is a two-step process where the fuel compression and ignition phases are separated by applying a highly shaped laser pulse with a duration of several nanoseconds. The concept of separating the compression and ignition phases has already been suggested by Shcherbakov,[8] but no detailed target design was presented. First, a cryogenic deuterium–tritium fuel shell is imploded to a high areal density with a low implosion velocity by a nanosecond laser driver; then a strong shock wave is launched at the end of the laser pulse that initiates ignition in the center of the compressed shell. A spherically converging shock wave is launched into the imploding shell by an abrupt increase in the power at the end of the laser pulse, producing an intensity spike of $>5 \times 10^{15}$ W/cm^2. The shock gains strength while propagating through the converging shell and is timed so that it meets the rebounded shock from the target center inside the shell close to the inner surface. This shock collision creates new shock waves; one of them propagates back to the capsule center, enhancing the piston action on the hot spot, and triggers ignition. Because SI implosions occur at a much lower velocity than in hot-spot ignition, significantly more mass can be assembled for the same laser energy, leading to higher gain if the fuel assembly can be ignited. The energy to achieve ignition is, according to simulations,[1,4] lower for SI than for hot-spot ignition. Two-dimensional (2-D) simulations[9] have also shown that SI targets are more resilient against hydrodynamic instabilities than hot-spot–ignition targets. The current status and the physics issues of the SI concept are reviewed in two articles that recently appeared in Nuclear Fusion.[5,10]

A critical component for SI is the strength of the ignitor shock, which depends on the energy coupling of the spike pulse. The laser-energy coupling into the target is not well understood at high-spike laser intensities. The inverse bremsstrahlung absorption, which is the main laser-energy absorption mechanism in ICF, significantly decreases in efficiency with higher intensities above 10^{15} W/cm^2 (Ref. 11). For laser intensities of up to 10^{15} W/cm^2, the absorption is in the regime of classical inverse bremsstrahlung absorption and the ablation pressure scales with the incident intensity according to $P_{\mathrm{abl}}(\mathrm{Mbar}) \approx 57\left(\eta_{\mathrm{abs}} I_{15} / \lambda_{\mu\mathrm{m}}\right)^{2/3}$ (Ref. 11), where η_{abs} is the laser-energy absorption fraction, I_{15} is the laser intensity in units of 10^{15} W/cm^2, and $\lambda_{\mu\mathrm{m}}$ is the laser wavelength in μm. One key issue for SI is to demonstrate that the spike pulse can generate a minimum ablation pressure of ~300 Mbar (Refs. 4 and 12). If the classical model is used for extrapolation, absorbed laser intensities of at least $\sim 4 \times 10^{15}$ W/cm^2 are required to launch sufficiently strong shocks on the target surface. Another critical issue is that laser–plasma instabilities play an important role in the high-intensity range. Laser–plasma instabilities[13] such as stimulated Brillouin scattering (SBS),[14,15] stimulated Raman scattering (SRS),[16] and the two-plasmon–decay (TPD) instability[17,18] are of concern in an ignition target design for two reasons: The instabilities generate energetic electrons that might preheat the shell, thereby reducing the final core compression; they also might increase the back-reflection of the laser light from the target, further degrading the laser–energy coupling to the capsule.

The physics of laser-spike absorption, ablation pressure generation, and hot-electron production are the major unknowns in the SI concept. Dedicated experiments must test the scaling of ablation pressure with spike intensity at SI-relevant laser intensities since there are currently insufficient experimental data at these high intensities. Only a few experiments have been performed to study laser-driven shocks in an intensity regime that is relevant for shock ignition.[19–21] These experiments utilized planar targets, however, that severely limit the attainable ablation pressure because of lateral heat losses from the laser spot. A spherical geometry is more relevant for SI and would minimize lateral heat losses, leading to higher pressures. Experiments on Laboratoire Pour L'Utilisation Des Lasers Intenses (LULI)[19] and OMEGA[20] used optical diagnostics to measure the shock-propagation velocity in a planar quartz witness sample layer. The shock breakout time at the target's rear surface was used as a metric to infer the peak ablation pressure on the laser-interaction side by comparing

the breakout time to predictions from 2-D radiation–hydrodynamic simulations. Peak ablation pressures of ~40 Mbar were reached on LULI with 0.53-μm-wavelength laser light at an intensity of ~1×10^{15} W/cm^2 and ~75 Mbar on OMEGA with 0.35-μm-wavelength laser light and an absorbed intensity of 1.2×10^{15} W/cm^2. Experiments at the Prague Asterix Laser Facility used the measured self-emission of the shock after breakout to infer shock pressures of up to 90 Mbar for intensities <10^{16} W/cm^2 and a 0.43-μm wavelength (Ref. 21). Recent OMEGA experiments have been more relevant to SI in terms of utilizing a spherical geometry and higher laser intensities. The experiments used solid plastic spheres that were irradiated by the OMEGA laser at intensities well above 10^{15} W/cm^2. An important finding was that the ablation pressure scales stronger than linearly with the laser intensity,[22] in contrast to what is expected from the classical model. Copious amounts of hot electrons are generated at incident laser intensities of >3×10^{15} W/cm^2 because of laser–plasma instabilities, which significantly enhance the pressure.

In this article we demonstrate the generation of ablation pressures of up to ~400 Mbar in spherical strong-shock (SSS) experiments on the OMEGA laser, which is an important milestone for the SI concept. The demonstration of ablation pressures exceeding 300 Mbar is crucial to developing a robust SI target design for the National Ignition Facility (NIF).[23] The SSS experiments investigate the strength of the ablation pressure and the hot-electron production with overlapping incident beam laser intensities of ~2 to 6×10^{15} W/cm^2. The primary observable from these experiments is the timing of the x-ray flash from shock convergence in the center of a solid plastic target. This information is used in radiation–hydrodynamic simulations that are constrained by the experimental results to infer the ablation and shock pressures. The convergent geometry causes a large enhancement of the shock strength in the center of the solid target,[24] achieving multi-Gbar levels. The results are therefore also relevant to the development of a direct-drive platform to study material properties at Gbar pressures. Similar experiments have been proposed in indirect drive on the NIF to measure the equation of state and opacities of matter at Gbar pressures.[25]

This article is organized as follows: (1) The experimental setup, which includes a description of the target, the laser conditions, and the diagnostics is presented. (2) The experimental results from the x-ray emission, the hot-electron characterization, and the laser backscattering are described. (3) Radiation–hydrodynamic simulations are used to infer the ablation and shock pressures. (4) Finally, we conclude with a discussion and an extrapolation of the ablation pressure for the NIF target design.

Experimental Setup

Figure 141.41 shows a schematic of the experimental strong-shock platform. The 60 UV beams (0.351-μm wavelength) from the OMEGA laser[26] are focused to a high intensity (at an overlapping beam intensity of ~6×10^{15} W/cm^2) on the surface of a solid target to launch a spherical shock wave that converges in the center, heating a small volume (<10-μm radius) to temperatures of several hundred electron volts (eV). At the time of shock convergence, a short burst of x rays emitted from the target is detected with an x-ray framing camera (XRFC)[27] and a streaked x-ray spectrometer (SXS).[28] The hot electrons are characterized from the measured hard x-ray bremsstrahlung emission. The absorbed laser power is measured and laser backscatter diagnostics characterize spectrally and temporally resolved optical emission generated by laser–plasma instabilities.

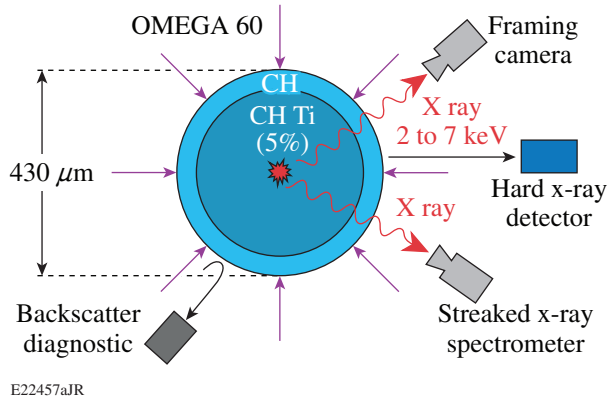

Figure 141.41
Schematic of the experimental OMEGA platform that is used to study the generation of strong shocks and the hot-electron production at shock-ignition–relevant laser intensities. A spherical shock wave is generated in solid targets, which converges in the center, producing a short burst of x rays that is detected with a framing camera and a streaked spectrometer. The hot electrons are characterized from the measured hard x-ray bremsstrahlung emission. The scattered laser light is measured temporally and spectrally resolved at different locations around the target to infer information on the laser–plasma instabilities and the total amount of absorbed laser energy.

1. Targets

The solid targets that were used comprised an outer 35- or 50-μm-thick pure plastic (CH) ablator and an inner CH core doped with titanium with an atomic concentration of 5%. These targets, fabricated and characterized by General Atomics, had an outer diameter of 415 to 600 μm. The sphericity ($\Delta r/r$) of the

targets was better than 0.5%. The heated plasma in the target center emitted continuum bremsstrahlung and line emission from the dopant material. Simulations were performed with different doping materials and doping concentrations to optimize the yield from ionic line emission. The strongest line emission was calculated for doping concentrations of ~0.1% atomic density with Ti. Because of manufacturing limitations, the doping concentration turned out to be 5% in the fabricated target, significantly higher than requested, which resulted in a considerable reabsorption of the emission from the center in the colder outer parts of the target. The opacity of the target might be an issue in interpreting the magnitude of the x-ray signal emitted by the central hot spot. Since the primary observable for determining the ablation pressure is the time of appearance of the x-ray flash, the opacity does not affect the data interpretation as long as the signal is strong enough to be measured, which was the case in our experiment. In addition, the 35- or 50-μm-thick undoped outer CH layer ensures that any detected line emission originates in the target interior rather than the hot corona since simulations predict that only ~12 μm of CH is ablated away during the laser interaction.

2. Laser Focus and Laser Pulse Shapes

The foci of the laser beams match the size of the smallest solid target. The 60 OMEGA beams were equipped with a mix of small-spot phase plates. Forty-three beams were equipped with IDI-300 phase plates developed for indirect-drive experiments,[29] 13 beams with ESG10-300, two beams with 100-μm, and two beams with 200-μm phase plates. The IDI-300 and ESG10-300 are elliptical phase plates, while the 100-μm and 200-μm phase plates provide small circular spots. While it is desirable to use a single type of phase plate, only 43 IDI-300's are available on the OMEGA Laser System. The complication of using a variety of small phase plates has a negligible effect on the primary observable. The elliptical phase plates were orientated such that the minor axis of the focus was aligned along the splitting direction of the birefringent optical wedges[30] to produce less-elliptical focal spots. Figure 141.42(a) shows a lineout through the minor axis of the elliptical focus of one of the laser beams equipped with an IDI-300 phase plate; Fig. 141.42(b) shows a lineout through the major axis. Polarization smoothing[30] and smoothing by spectral dispersion (SSD)[31] were applied to the beam. The far-field intensity distribution was measured using the ultraviolet (UV) equivalent-target-plane diagnostic.[32] Both lineouts are well fitted with super-Gaussian profiles having an order of $n = 2.15\pm0.05$ and radii of 218 ± 5 μm along the minor axis and 252 ± 7 μm along the major axis (see Fig. 141.42). The radii correspond to the 5% point of the maximum intensity. Similar measurements were performed with SSD turned off,

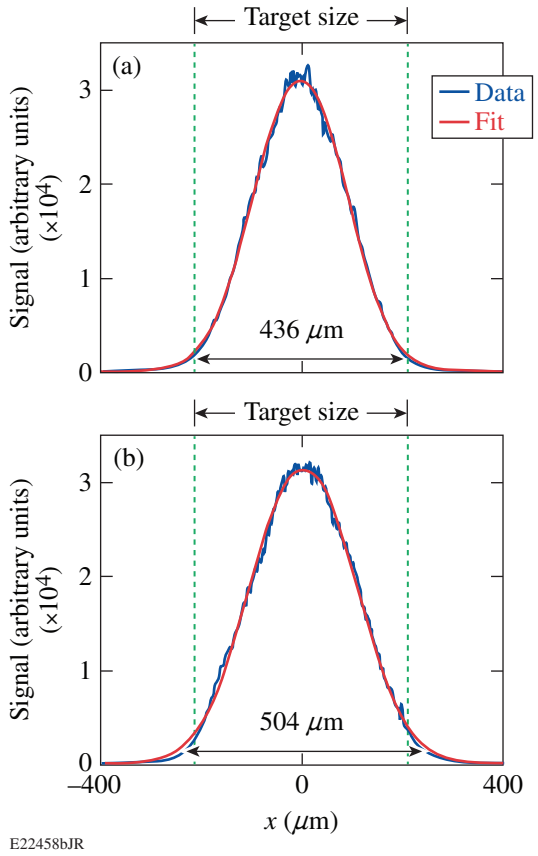

Figure 141.42
Lineouts through the (a) minor and (b) major axis of the elliptical focus of one of the laser beams. The beam was equipped with an IDI-300 phase plate and polarization rotator and used smoothing by spectral dispersion.

while retaining polarization smoothing, which resulted in a smaller spot. In this case, the fitting resulted in profiles with super-Gaussian orders and radii of $n = 1.9\pm0.1$ and 211 ± 10 μm along the major axis and $n = 4.0\pm0.3$ and 180 ± 5 μm along the minor axis, respectively. The spots are smaller when SSD is turned off, resulting in a higher single-beam intensity but similar average intensity when overlapping all 60 beams. Single beams without SSD contain significantly more nonuniformity, while turning on SSD reduces the single-beam uniformity σ_{rms} by a factor of ~8 (Ref. 30). The ESG10-300 phase plates produce slightly less elliptical and smaller spots compared to the IDI-300 phase plates with $n = 1.42\pm0.05$ and radii of 169 ± 5 μm and 179 ± 5 μm. The spot of the 200-μm phase plate is round with $n = 2.17\pm0.05$ and a radius of 125 ± 5 μm. No data are available for the 100-μm phase plate but it is expected that it produces a slightly smaller spot than the 200-μm phase plate. No data are available for the spots for the ESG10-300, 200-μm, and 100-μm phase plates when SSD is turned off. A summary of the fitting results can be found in Table 141.III.

Table 141.III: Summary of the fitting results through the major and minor axes of the elliptical focus profiles of the different phase plates used in the experiment. The super-Gaussian orders and radii along the major axis and the minor axis are provided.

	With SSD modulation				Without SSD modulation			
Phase plate	n_1	n_2	r_1 (μm)	r_2 (μm)	n_1	n_2	r_1 (μm)	r_2 (μm)
IDI-300	2.14	2.15	218	252	4.0	1.9	180	211
ESG10-300	1.43	1.40	169	179	No data			
100 μm	No data							
200 μm	2.13	2.20	123	126				

Various laser pulse shapes were applied in the experiments (see Fig. 141.43), including a 1-ns square pulse, a 1.4-ns shaped pulse consisting of a 0.5-ns, 3-TW power foot followed by a high-power (~22-TW) plateau [see Fig. 141.43(a)], and a longer 1.8-ns shaped pulse with a 1-ns, low-power (~2-TW) foot followed by a 0.8-ns, high-power square pulse [see Fig. 141.43(b)]. The low-intensity foot creates a plasma atmosphere around the target with which the high-intensity portion of the pulse interacts. This situation resembles the conditions of a shock-ignition target, where first a low-intensity pulse assembles the fuel and then at the end of the pulse, an intensity spike launches the ignitor shock wave into the shell. Figure 141.43(b) shows various versions of the 1.8-ns shaped pulse where the laser energy was varied between 13.6 to 27.1 kJ to irradiate targets with different on-target laser intensities, while keeping the intensity in the foot constant. The overlapping beam intensities in the peak reach up to ~6×10^{15} W/cm^2 for the smallest target.

3. Diagnostics

The x-ray emission from the center of the target was measured temporally and spatially resolved using an x-ray framing camera (XRFC)[27] and temporally and spectrally resolved with a streaked x-ray spectrometer (SXS),[28] while time-integrated measurements of the x-ray emission in the ~3- to ~7-keV range were made with an x-ray microscope imager.[33] The XRFC used a 4×4 array of 10-μm-diam pinholes to produce 16 enlarged images of the target on a microchannel-plate detector coupled to a charge-coupled–device camera. A 200-μm Be foil and a thin (12-μm) Ti foil were placed in front of the detector. Combined with the spectral response of the diagnostic, this restricted the range of recorded x rays to ~3 to 7 keV. An XRFC with a slow gating time of ~130-ps full width at half maximum (FWHM) was applied in the measurements. In some of the shots, a second faster (~60-ps) XRFC was also used. The SXS employs a flat Bragg crystal in front of an x-ray streak camera for time-resolved, x-ray spectroscopy of laser-produced plasmas in the 1.4- to 20-keV photon-energy range. The SXS relies on a pinned mechanical reference system to create a discrete set of Bragg reflection geometries for a variety of crystals. For these experiments, a rubidium acid phthalate (RbAP) crystal dispersed the x rays in an energy range of 3.8 to 6.5 keV onto a 28-mm-long, 250-μm-wide slit at the entrance of the streak camera, which was equipped with a photocathode comprised of a 12.5-μm-thick Be foil coated with a thin 200-nm layer of KBr. A 127-μm-thick Be blast filter protected the diagnostic from optical stray light and target debris.

The XRFC was absolutely timed with an accuracy of 50 ps through dedicated timing shots that used several laser beams to irradiate a 4-mm-diam plastic sphere coated with a thin layer of gold. The laser spots were spatially separated on target so that the generated x-ray emission was spatially separated and

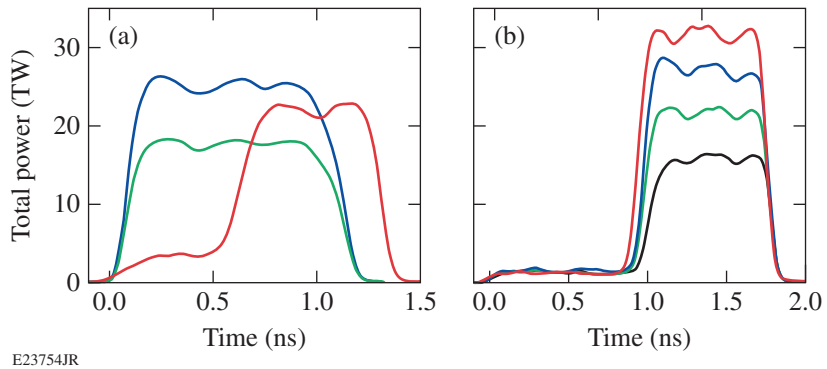

Figure 141.43
Total power of various laser pulse shapes that were used in the spherical strong-shock experiments. (a) Square pulse shapes (blue and green curves) with a pulse duration of 1 ns and shaped pulse (red curve) with a duration of 1.4 ns. (b) Shaped pulse with a 1-ns low-power foot followed by a 0.8-ns high-power square pulse. Various versions of this pulse form provide different laser energies on target while keeping the power in the foot constant.

unambiguously identified in the XRFC image. The timing of each laser beam was measured and cross-correlated with the measured time-resolved x-ray emission from each of the plasma spots. Details on the timing technique can be found in Ref. 34. In a similar way, the SXS diagnostic was also absolutely timed by using one laser beam interacting with a thin Ti foil and cross-correlating the x-ray emission with the laser pulse that generated the x-ray emission.

The hot electrons were characterized by measuring the hard x-ray emission in an energy range of 10 keV to ~700 keV using several diagnostics simultaneously. A time-resolved, four-channel hard x-ray detector (HXRD)[35] provided a measurement of the time history of the hard x-ray emission and hot-electron temperature in the low-intensity shots. The HXRD diagnostic was affected by signal saturation in the high-intensity shots. Each channel of the HXRD system consists of a fast scintillator coupled to a fast microchannel plate/photomultiplier tube and is filtered by a combination of Al and Cu foils of different thicknesses, giving various cutoff energies in a range from ~20 to 80 keV for the different channels. The time resolution of the HXRD system is ~100 ps. Two time-integrated imaging-plate diagnostics—high-energy radiography imager (HERIE)[36] and bremsstrahlung x-ray spectrometer (BMXS)[37]—provided temperature and hot-electron fraction measurements on all shots. The BMXS spectrometer contains 13 filters of increasing Z from Al to Pb and then increasing thicknesses of Pb for differential filtering and Fuji BAS-MS image plates sandwiched between the filters as detectors. The image plates and filters are contained in a thick Pb box that shields hard x rays with energy of up to 2 MeV. A 12.5-cm-long Pb collimator with a 1.2-cm-diam hole suppresses background radiation from the vacuum chamber walls and other diagnostics. Details on the BMXS diagnostic and the data analysis can be found in Ref. 37. The HERIE diagnostic contains a large image plate inside a thick Pb box. A mask with nine small windows is place d in front of the image plate. Different filter materials were mounted in the windows to obtain the differential filtering. BMXS and HERIE cover spectral ranges from ~10 to ~700 keV and ~20 to ~200 keV, respectively, which is sufficient for the expected hot-electron temperatures of up to 100 keV. Because of the large dynamic range of the image plates, the two time-integrated diagnostics provided reliable measurements even for the highest laser intensity.

The laser light that reflected back from the target was measured from two adjacent beam ports (30 and 25), which were equipped with a full-aperture backscatter station (FABS),[16,18] providing spectrally resolved measurements of the backscattered light. Time-resolved spectra were recorded by several streaked spectrometers covering the wavelength ranges of 351±3 nm for SBS, ~500 to ~700 nm for SRS, and 234±4 nm for $3\omega/2$ emission from the TPD instability. In addition, several scatter calorimeters and FABS's provided time-resolved measurements of the fraction of absorbed laser power.[16]

Experimental Results

1. X-Ray Emission Measurements

The SXS diagnostic provides a streaked x-ray spectrum showing, early in time, the x-ray emission from the interaction of the laser pulse with the plasma corona and, later in time, the x-ray flash from the shock convergence in the target center. Figure 141.44(a) shows an example of the SXS data from a target that was irradiated with a 1-ns square pulse; Fig.141.44(b) shows a lineout along the time axis at the Ti He_α-emission wavelength

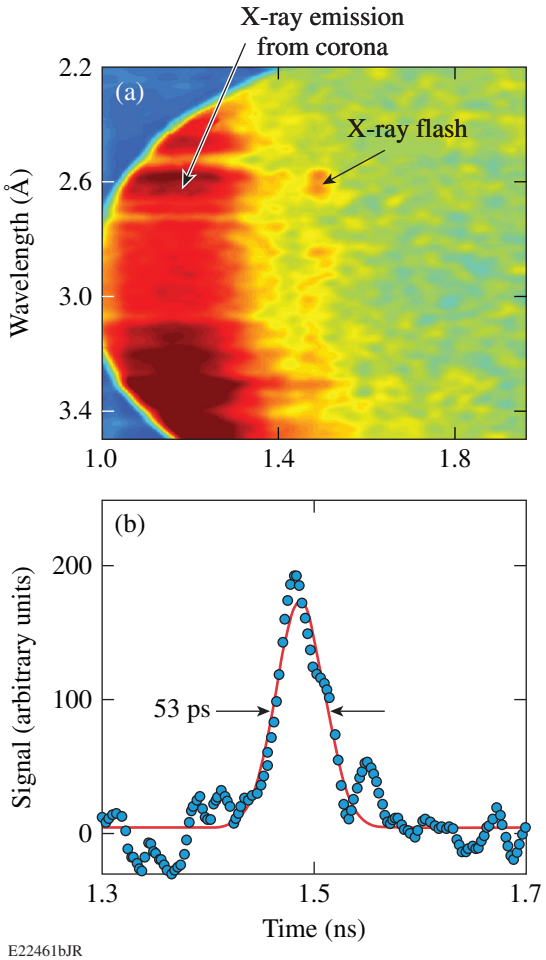

Figure 141.44
(a) Streaked x-ray spectrum showing, early in time, the x-ray emission from the plasma corona and, at 1.5 ns, the x-ray flash from the shock convergence. The target was irradiated with a 1-ns square pulse. (b) Time lineout at 2.6 Å of the x-ray flash with an emission time of 53 ps.

of ~2.6 Å. A short x-ray flash was measured with a FWHM emission time of 53 ps. By taking the temporal resolution of the instrument into account, this corresponds to a deconvolved emission time of ~35 ps.

Figure 141.45 shows a portion of the raw data collected with the XRFC for a shot with a 1-ns square pulse. At early times, the observed x-ray emission originated from the hot corona when the laser was still interacting with the target. Although the laser pulse is nominally 1 ns long, the first image at 1.13 ns (Fig. 141.45) was taken when the laser was still on, as can be seen from the measured pulse shape in Fig. 141.43(a). As time progressed and the laser shut off, the corona cooled and the x-ray emission from the target surface quickly disappeared. After a brief period where no x-ray emission was recorded, a small but bright source of x rays appeared at the target center, indicative of the shock convergence. Figure 141.46 renders a zoomed image of the emission from the center, demonstrating that the emission originated from a very small region. A diameter of 15 μm (FWHM) was measured, corresponding to a deconvolved size of ~9 μm when taking the 12-μm spatial resolution of the pinhole diagnostic into account. Measurements with the time-integrated x-ray microscope provided a higher spatial resolution (~5 μm) and resulted in emission sizes of ~7 μm.

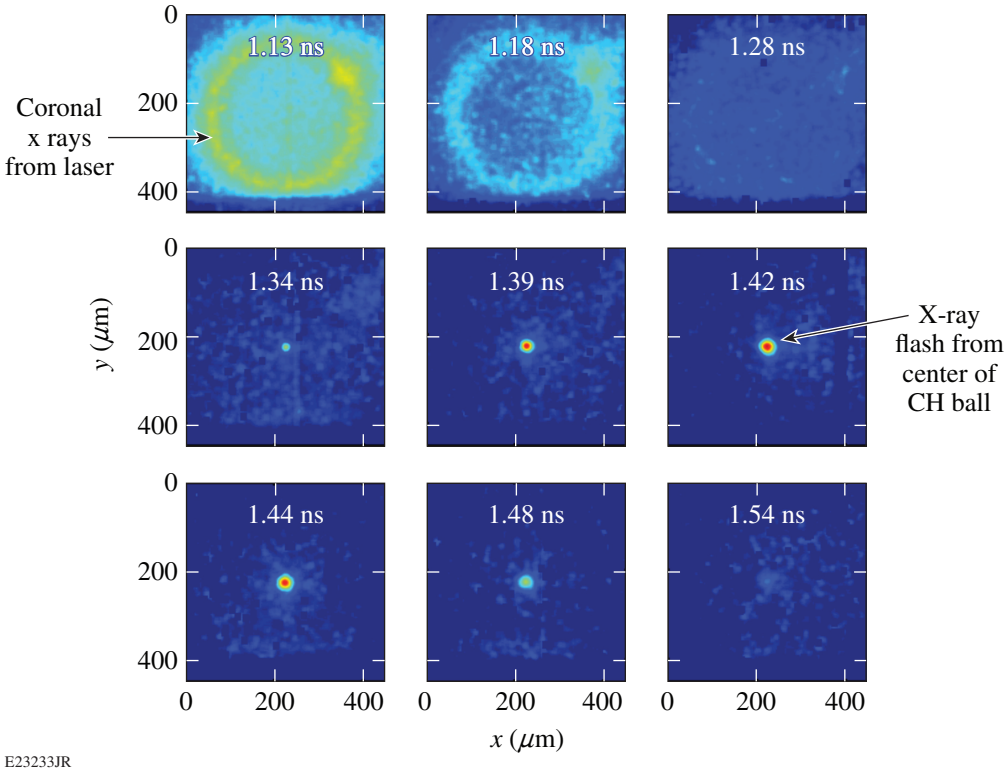

Figure 141.45
X-ray framing-camera images show the coronal x-ray emission from the target surface during the laser interaction and later the x-ray flash from the target center generated by the converged shock wave. The target was irradiated with a 1-ns square pulse.

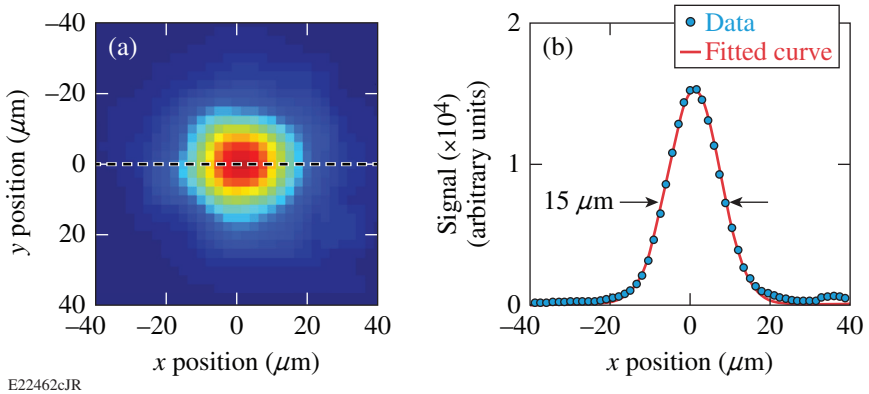

Figure 141.46
(a) Zoomed-in x-ray framing camera image of the emission from the target center at peak emission; (b) a horizontal lineout through the center of the emission, which is well fitted by a Gaussian profile with a width of 15 μm.

Figure 141.47 shows the measured x-ray flash time obtained from the XRFC and SXS diagnostics as a function of the absorbed laser intensity, which is defined as the maximum calculated absorbed power divided by the calculated critical density surface area. The absorbed laser power is obtained from 1-D radiation–hydrodynamic simulations, which are in good agreement with measurements as shown in **Simulations** (p. 58). The temporal occurrence of the x-ray flash between the two diagnostics is within the absolute timing error of each other. With increasing intensity, an earlier flash time was measured, indicative of a stronger shock.

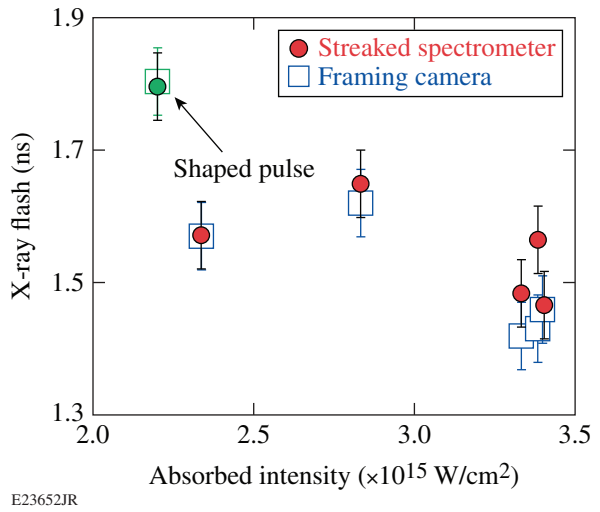

Figure 141.47
Measured x-ray flash time from the x-ray framing camera and streaked x-ray spectrometer versus absorbed laser intensity, which is defined as the maximum calculated absorbed power divided by the calculated critical-density surface area. The red symbols represent shots with the 1-ns square pulse, while the green symbol represents the 1.4-ns shaped pulse.

The strength of the measured x-ray signal from the target center depends on the laser intensity and, therefore, from the shock strength. Figure 141.48 shows the data from the time-integrating x-ray microscope using the 1.8-ns shaped pulse by varying the laser energy and the target diameter. The x-ray signal from the target center was integrated over the emission area and is shown as a function of the absorbed laser intensity. The open squares represent measurements with SSD and the solid dots are the results without SSD. The x-ray signal depends strongly on the laser intensity and SSD. The signal was measured at three different intensities without SSD and is seen to grow linearly with intensity, with the solid line being a linear fit through the no-SSD data. In addition, the signal increases significantly when switching SSD off,

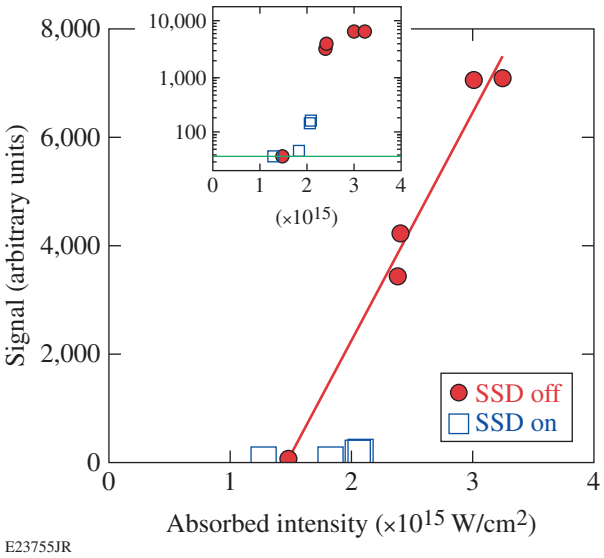

Figure 141.48
Measured time- and space-integrated x-ray emission from the target center as a function of the absorbed laser intensity. A time-integrating x-ray microscope[33] was used in this experiment. The square symbols represent measurements with smoothing by spectral dispersion (SSD) and the solid dots represent measurements without SSD. A shaped pulse with a pulse duration of 1.8 ns was used. The solid line is a linear fit to the dots. The inset shows the data in a semi-logarithmic plot with the noise floor given by the horizontal line.

with an ~25×-higher signal at 2.4×10^{15} W/cm^2 and no SSD, compared to the measurement at 2.1×10^{15} W/cm^2 with SSD. By switching SSD off, more than a factor-of-2 additional hot electrons are generated (see **Hot-Electron Measurements** on p. 55). Both an increased intensity and more hot electrons clearly enhance the shock strength and the magnitude of the x-ray signal from shock convergence. It was mentioned in the previous section that the higher-than-expected concentration of Ti doping in the target resulted in the reabsorption of x-ray emission from the target center. To avoid the complication arising from opacity effects, we solely infer the shock strength from the measured time of the x-ray flash and not from the strength of the x-ray signal.

Experiments were performed with different-sized targets with and without SSD. Figure 141.49 shows the measured x-ray flash time as a function of the target diameter using the 1.8-ns shaped pulse. The x-ray flash is later for larger targets with a linear increase in flash time with diameter. Fitting lines through separate data with and without SSD show that for a fixed diameter, the flash appears ~90 ps earlier when SSD is turned off. An earlier flash time indicates a stronger shock and is the result of the increased hot-electron production when SSD is turned off.

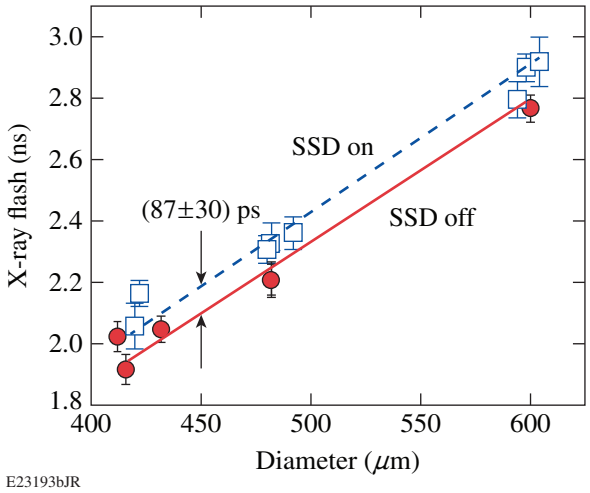

Figure 141.49
Measured x-ray flash time for different target sizes and shots with SSD (open squares) and without SSD (solid dots). The x-ray flash is later for larger targets and with SSD. An earlier flash time indicates a stronger shock. The 1.8-ns shaped pulse was used.

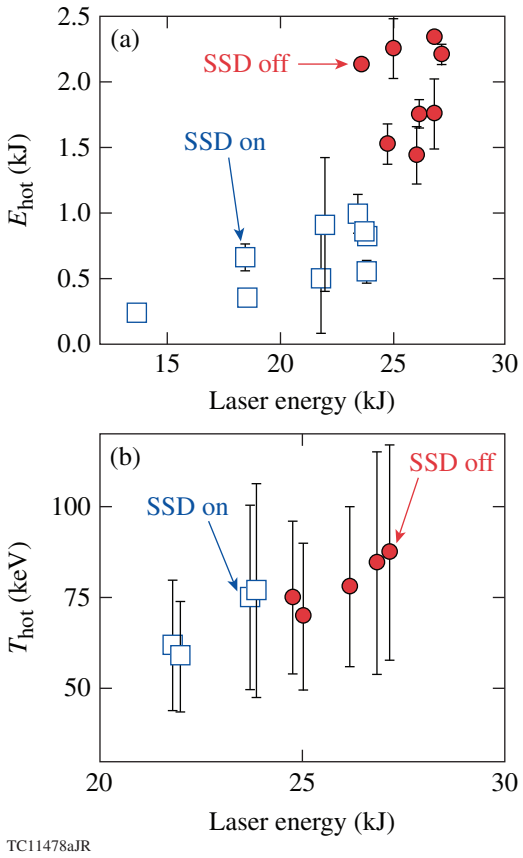

Figure 141.50
(a) Measured deposited hot-electron energy and (b) hot-electron temperature as a function of the incident laser energy. Measurements with and without SSD are represented by the squares and dots, respectively.

2. Hot-Electron Measurements

Laser–plasma instabilities can accelerate electrons to high energies, which can be detected via their hard x-ray bremsstrahlung emission when the electrons slow down in the target. The hard x-ray emission was measured with various diagnostics. Time-resolved measurements with HXRD at lower laser intensities show that most of the electrons are generated in the second half of the high-intensity plateau of the shaped pulses. Unfortunately, HXRD was driven into saturation at intensities above 2×10^{15} W/cm^2, so no reliable time-resolved measurements are available for most of the shots. The time-integrated hot-electron fraction and the temperature were well characterized with the two diagnostics HERIE and BMXS, which provided data on all shots. Figures 141.50(a) and 141.50(b) show the measured hot-electron energy and hot-electron temperature, respectively, as functions of the incident laser energy. The average values of the energy and temperature of both diagnostics are shown. Measurements with and without SSD are represented by the squares and dots, respectively. The reason why most of the shots without SSD obtained higher laser energy lies in the fact that switching off the SSD modulation reduces the spectral bandwidth, which results in a slightly higher efficiency in frequency tripling. An attempt was made to reduce this energy in some of the shots without SSD so that a direct comparison of hot-electron production can be made at 24 kJ. Beside the slight increase in hot-electron energy with laser energy, the hot-electron fraction was more than doubled when SSD was turned off, reaching hot-electron energies of up to 2300 J being deposited into the solid target, which is up to 9% of the total laser energy.

The hot-electron energy increases only slightly with laser energy, indicating that an almost constant fraction of laser energy is converted into hot electrons. This indicates that the instabilities were driven highly into saturation. Previous experiments at lower laser intensity and larger density scale lengths[38] showed that the fraction of laser energy converted into hot electrons scaled exponentially with intensity from 1.3 to 3×10^{14} W/cm^2 and continued to grow at a slower rate above 3×10^{14} W/cm^2, indicating the saturation of the instability. Other experiments[17] at shorter density scale lengths that extended up to ~2.5×10^{15} W/cm^2 reported a similar trend of strong exponential increase in hot-electron production below 1×10^{15} W/cm^2 and a leveling off above 1×10^{15} W/cm^2.

The measured bremsstrahlung emission was compared to Monte Carlo simulations assuming that the hot electrons were

generated isotropically within a 180° full divergence angle in the laser direction. The instantaneous conversion efficiency of laser power into hot-electron power reaches up to 15% in the second half of the high-intensity portion of the shaped laser pulse. The temperatures were inferred by fitting single-temperature Maxwellian distributions to the HERIE and BMXS data ranging from ~60 to ~80 keV, slightly increasing with higher laser energy. No significant difference in temperature was noted when SSD was turned off. The plotted temperatures are the average from both diagnostics with the error bars indicating the difference between both time-integrated diagnostics with BMXS measuring temperatures at the higher end and HERIE at the lower end.

3. Backscatter Measurements

Laser–plasma instabilities affect the laser-energy coupling and are sources for hot electrons and backscattered light. The optical signals from the laser backscatter diagnostics are compared for two laser shots: One shot with (shot 72676) and another without (shot 72678) SSD. Although shot 72678 had ~13% higher energy (26.8 kJ) and accordingly higher incident laser intensity (4.4×10^{15} W/cm^2) compared to shot 72676 (23.8 kJ, 3.9×10^{15} W/cm^2), the slight difference in laser intensity is an insignificant factor in explaining the difference in the LPI signatures. As a matter of fact, the optical emissions generated from SBS and TPD processes do not show any significant difference. Only the SRS-generated optical emission is very different and indicates a qualitative difference in the laser–plasma interaction when SSD is applied.

Figure 141.51 shows the reflected SBS spectra, for shots 72676 (SSD on) and 72678 (SSD off), which do not appear to be sensitive to the operation of SSD. The SBS signal exhibits a large spike as soon as the intensity spike is launched, which is caused by the local increase of the velocity gradient in the corona and a rapidly increasing ablation rate. During the short time interval of ~150 ps, up to 15% of the laser energy is back-reflected. The amount of laser light scattered by SBS during the remainder of the main drive, however, is lower and results, over the entire pulse duration, in up to ~7% of the laser energy. The near-backscattered light outside the FABS aperture was measured by the near-backscatter image (NBI) as well as by the scatter calorimeters (SCAL's). The overall laser-energy absorption was measured to be ~55%±5% for all of the shots.

SRS drives electron plasma waves by scattering laser photons and transferring some fraction of the photon energy to the plasma waves; therefore, the SRS-scattered photons possess a longer wavelength than the incident laser wavelength. SRS is excited in a plasma region with electron densities below the quarter-critical density. The TPD process operates close to the quarter-critical density and converts an incident laser photon into two electron plasma waves that each carry about half of the photon energy.

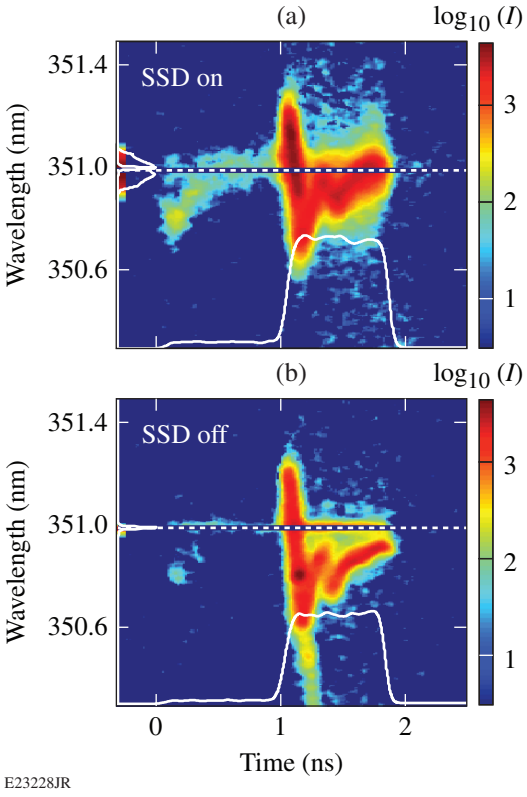

Figure 141.51
Streaked optical spectrographs measuring the stimulated Brillouin scattering (SBS) in one beam (Beam 30) (a) with SSD for shot 72676 and (b) without SSD for shot 72678. No significant difference in SBS is observed between SSD on and off. The intensity is rendered on a logarithmic scale. The *y* axis shows the wavelength of the reflected light and the *x* axis shows the time. The white curve represents the laser pulse shape.

The instabilities grow rapidly when a certain laser-intensity threshold is surpassed, which depends on the plasma density scale length and the electron temperature. This threshold from linear theory can be estimated for TPD with $I_{\mathrm{TPD}} \approx \left(8 \times T_{\mathrm{keV}} / L_\mu \lambda_\mu\right) \times 10^{15}\,\mathrm{W/cm^2}$ (Ref. 39), where T_{keV}, L_μ, and λ_μ are the electron temperature in keV, the density scale length in μm, and the laser wavelength in μm, respectively. For SRS, the threshold at $\sim n_c/4$ is estimated by $I_{\mathrm{SRS}} \approx \left(5 \times T_{\mathrm{keV}} / L_\mu^{4/3} \lambda_\mu^{2/3}\right) \times 10^{16}\,\mathrm{W/cm^2}$ (Ref. 40). *LILAC* simulations predict $T_{\mathrm{keV}} \approx 3.5$ and $L_\mu \approx 120$ during the high-intensity portion of the laser pulse at quarter-critical density, which results in a threshold of $\sim 7 \times 10^{14}$ W/cm^2 for both TPD and SRS. The threshold is exceeded during the rise of the high-intensity portion of the laser pulse.

Figure 141.52(a) shows a streaked optical spectrograph of the SRS back-reflected light when SSD was turned on, while Fig. 141.52(b) shows the result with no SSD. When the laser pulse (dashed curve) rises to its maximum intensity, SRS is excited ~100 ps after the strong shock is launched in a short burst of signal in the wavelength range of 540 to 600 nm, followed by a second burst at longer wavelengths (~600 to 660 nm) [see Fig. 141.52(a)]. The wavelength of the backscattered light correlates with the electron density of the plasma region from where the SRS signal was generated. A longer wavelength corresponds to a higher density as indicated by the white scale. The white curve is the spectrally integrated signal from ~540 to 660 nm and represents the temporal evolution of the SRS signal. The SRS signal is strongly quenched in the second half of the high-intensity plateau. The situation was completely different when SSD was turned off, which is shown in Fig. 141.52(b). The SRS signal was not quenched and persisted over the whole duration of the high-intensity plateau. The temporal integrations of the white curves show that with SSD off, a factor-of-5-more SRS-backscattered signal was produced compared to the case with SSD. This is accompanied with a significant increase in hot-electron production as discussed in **Hot-Electron Measurements** (p. 55).

The two emission lobes at ~700 nm that persisted over the whole duration of the high-intensity plateau were optical emission generated by electron plasma waves with half the laser frequency $(\omega_0/2)$ caused by TPD. Similarly, the $3\omega_0/2$ emission, which is also a signature optical emission from TPD,[17] carried on over the duration of the high-intensity plateau and was unaffected by SSD (see Fig. 141.53).

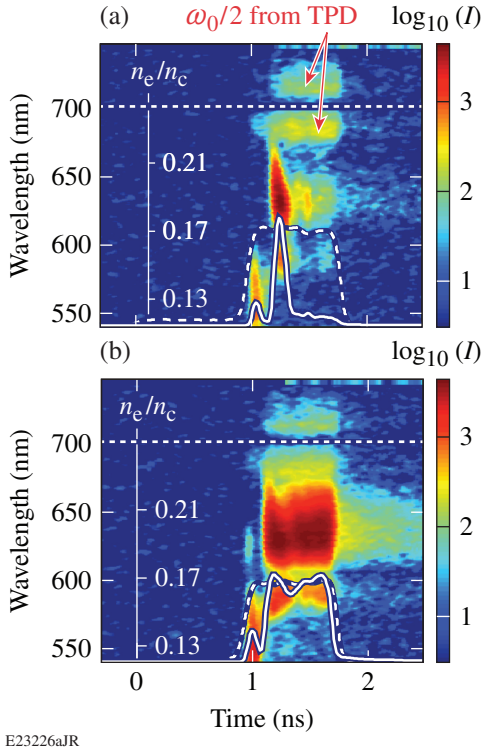

Figure 141.52
Streaked optical spectrographs measuring the stimulated Raman scattering (SRS) back-scattered signal in one beam (Beam 30) (a) with SSD for shot 72676 and (b) without SSD for shot 72678. The white dashed curve depicts the laser pulse shape and the white solid curve depicts the spectrally averaged SRS signal in arbitrary units. The white scale relates the wavelength to the electron density from where in the plasma the SRS signal was generated. A 5× higher SRS signal is generated without SSD.

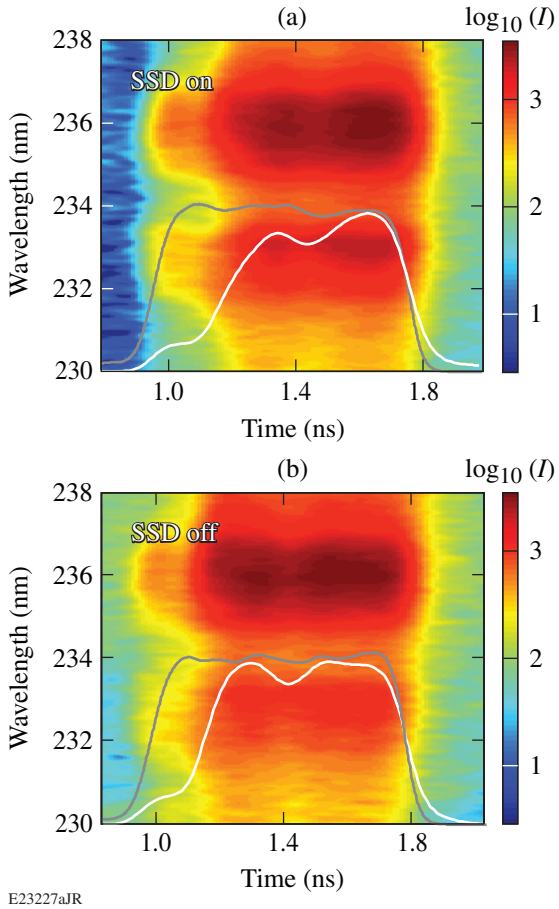

Figure 141.53
Streaked optical spectrographs measuring the $3\omega/2$ emission signal generated by the two-plasmon–decay (TPD) instability in one beam (Beam 30) (a) with SSD for shot 72676 and (b) without SSD for shot 72678. No significant difference in TPD activity is observed between the shots with and without SSD. The gray curve shows part of the laser pulse and the white curve represents the spectrally integrated $3\omega/2$ emission.

Previous experiments on the 24-beam OMEGA laser studied TPD and SRS with distributed phase plates (DPP's) and with and without SSD using laser intensities of up to ~1×10^{15} W/cm^2 but longer density scale length (~800 μm) and lower temperatures (~1 keV) (Ref. 41). A strong reduction (three orders of magnitude) of SRS was observed when SSD modulation was switched on, but SSD affected TPD only slightly. Quantitative differences remain, however, which are probably a consequence of the different plasma conditions; this is very similar to the observations made in our experiment. SSD reduced SRS backscatter by a factor of ~5 while hardly affecting TPD. The inverse growth rates of SRS and TPD are of the order of subpicoseconds and are much shorter than the smoothing time provided by SSD, which is ~25 to 50 ps for 1-THz bandwidth.[42] Therefore, it is not expected that SSD directly disrupts the growth of these laser–plasma instabilities. The suppression of beam filamentation with SSD might be one mechanism for the reduction in SRS. Previous experiments[43] reported a correlation between the onset of beam filamentation and the appearance of SBS and SRS emission in a laser beam that was not optically smoothed. When the laser beam was optically smoothed it did not break up in filaments and SRS and SBS were substantially suppressed.

Our data indicate that although the TPD instability is excited, SRS appears to be the primary generation mechanism of hot electrons. The observation of moderate hot-electron temperatures at these laser intensities has a significant impact on SI designs since they can enhance the ignitor shock[44] and improve the implosion performance.[12]

Simulations

The shock and ablation pressures, inferred from one-dimensional (1-D) radiation–hydrodynamic simulations with the code *LILAC*,[45] were constrained by the experimental observables. The timing of the x-ray emission from the center was the primary constraint. The measured hot-electron fraction and temperature were used as input in the simulations as well as the temporal dependence of the hot-electron production, which was assumed to be the same for all shots. Details on the simulations can be found in Ref. 22. As an example, Fig. 141.54 shows the observed (solid) and simulated (dashed) quantities for one shot. The gray curve represents the incident laser power and the blue curves represent the absorbed laser power, showing agreement between measurement and simulation. The red curves show the temporal evolution of the hard x-ray emission. The solid red curve represents the measurement and the dashed red curve represents the simulated hard x-ray emission, reflecting the time-dependent generation of the hot

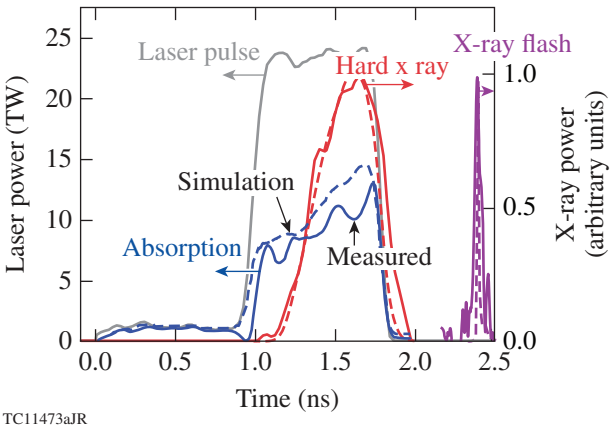

Figure 141.54
Comparison of measured (solid curves) and simulated (dashed curves) quantities for absorbed laser power (blue), hard x-ray emission >50 keV (red), and x-ray emission from the center of the target (magenta). The 1-D hydrodynamic simulations are constrained by the experimental observables.

electrons. The magenta lines show the x-ray flash from the target center. The simulations employed a multigroup radiation diffusion model, equation-of-state (EOS) models based on Thomas–Fermi[46] or *SESAME*[47,48] flux-limited thermal transport,[49] and a hot-electron transport package.[45,50] A fraction of the laser energy reaching the quarter-critical surface is converted into hot electrons, assuming a single-temperature Maxwellian distribution and an isotropic emission within a full 180° divergence angle in the forward direction. The hot electrons are transported in a straight line into the target. The transport of the thermal electrons is described by a flux limiter, which is the only free parameter in the simulations. It is adjusted to match the experimentally measured x-ray flash time and varies between 5% and 8%. The ablation pressure is the pressure in the shell at the position where the material velocity is zero in the lab frame. Although this is an approximate definition of the ablation surface, it is computationally the most accurate and is quite robust for targets that are converging with small fluid velocities (<10^7 cm/s) such as the solid spheres in our experiments.

Figure 141.55 shows the temporal evolution of the inferred shock and ablation pressures for one laser shot and two simulations with and without hot electrons. The black curve indicates the laser power in arbitrary units. The ablation pressure (blue curves) increases as a function of time and reaches up to ~220 Mbar at ~1.7 ns (solid blue curve) when hot electrons are included in the simulations. The pressure is built up from both thermal conduction of the absorbed laser energy and the energy deposition by hot electrons. The hot-electron contribution to

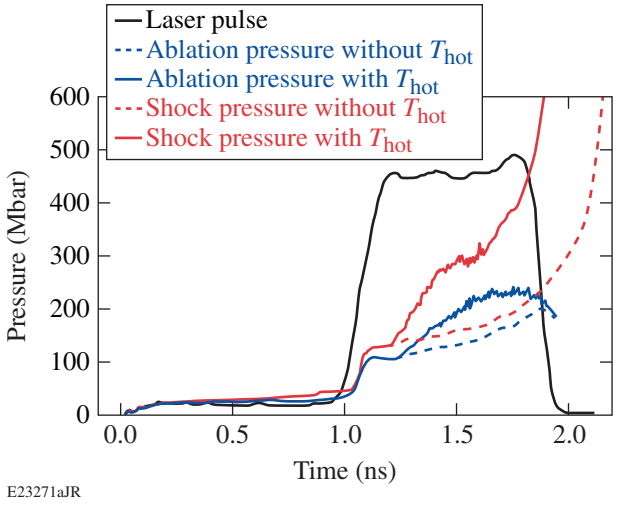

Figure 141.55
Temporal evolution of the simulated ablation (blue) and shock pressures (red) with (solid curves) and without (dashed curves) hot electrons.

the ablation pressure is ~30%, inferred by comparing it to a simulation that neglected the hot-electron contribution (dashed curve). It should be pointed out that the simulation without hot electrons calculates a later flash time than measured. The shock pressure without hot electrons (dashed red curve) closely follows the ablation pressure and rapidly increases in time because of convergence effects after the laser pulse is turned off.[24] The shock pressure including hot electrons exceeds 300 Mbar at 1.7 ns (solid red curve). The shock pressure is even more enhanced by hot electrons compared to the ablation pressure. The increase reaches ~50% when compared to the simulation without hot electrons. A higher fraction of the hot electrons is absorbed in the target volume behind the ablation surface, further augmenting the shock formation, while a smaller fraction is absorbed in front of the ablation surface. Similar conclusions were drawn from recent theoretical work showing that it should be possible to generate ~300-Mbar shock pressures resulting solely from hot electrons,[51,52] which might open a path to ignition based entirely on hot electrons.[53]

Discussion

The shock and ablation pressures are inferred by constraining radiation–hydrodynamic simulations to the experimental observables: the temporal occurrence of the x-ray emission, the hot-electron energy and temperature distribution, and the temporal evolution of the hard x-ray emission. In the SSS experiments, the distance from the quarter-critical density up to the ablation surface is typically ~120 μm during the later part of the intensity spike. The spatial integration of the density profile in this region results in areal densities of ~1 mg/cm^2, which provides only minimal stopping power for the hot electrons in the material before the ablation front compared to the areal density (~20 mg/cm^2) in the solid-density material behind the ablation front up to the shock front. Consequently, most of the hot electrons deposit their energy behind the ablation front, which affects the partition of the pressures at the ablation surface and the shock front. The hot electrons, therefore, enhance the shock strength beyond the applied ablation pressure, which explains why the hot electrons enhance the shock pressure more than the ablation pressure (see Fig. 141.55). For the shock it is subordinate how the energy was provided, whether from absorbed hot electrons or via thermal heat conduction between the critical density to the ablation surface or a combination of both mechanisms. Therefore, whether the shock is solely driven by the rocket effect or by a combination of ablation pressure and hot-electron energy, the pressure behind the shock must be independent of the mechanism driving the shock and even insensitive to many physics details. To support this point we applied different EOS models in the simulations. Thomas–Fermi or *SESAME* EOS models result in essentially the same shock pressure and reproduce the experimental observables although differences in the post-shock mass-density distribution are observed.

Figure 141.56 shows the scaling of the maximum ablation pressure versus the absorbed laser intensity. The error bars reflect the uncertainty in the simulated pressures and the calcu-

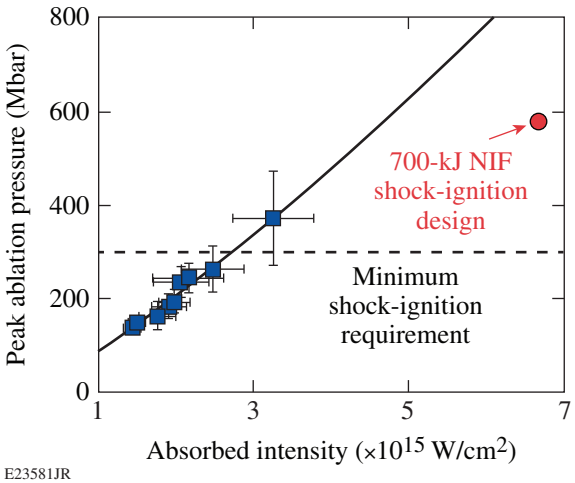

Figure 141.56
Scaling of the inferred maximum ablation pressure versus the absorbed laser intensity. The ablation pressures (solid squares) were inferred from simulations that match all the experimental observables. The solid line shows the extrapolation to higher intensities based on the OMEGA experiments, which is favorable for shock ignition. The solid red circle indicates the requirement for the 700-kJ NIF shock-ignition design.[12]

lated absorbed laser intensities based on the absolute measurement uncertainty in the x-ray flash time (±50 ps). Hot electrons significantly contribute to the shock formation and increase the ablation pressure by ~30%. At the highest absorbed intensity, the minimum required ablation pressure of 300 Mbar for shock-ignition designs is clearly surpassed. The solid line shows the extrapolation to higher intensities based on the OMEGA experiments, which is favorable for shock ignition. The solid red circle denotes the required ablation pressure for the 700-kJ NIF shock-ignition design presented in Ref. 12. Based on this extrapolation, ablation pressures exceeding 800 Mbar are expected at absorbed intensities of 6×10^{15} W/cm^2, which would exceed the required 600 Mbar by ~30%. The current OMEGA experiments were conducted, however, at a shorter density scale length—about a factor of 3 shorter than required for the 700-kJ NIF shock-ignition design. Further experiments on the NIF are required to study the ablation-pressure scaling for longer density scale length.

In summary, peak ablation pressures of close to ~400 Mbar have been produced on OMEGA using small solid spherical targets that were irradiated at high incident laser intensities (up to 6×10^{15} W/cm^2) in a regime that is relevant for shock ignition. The strength of the shocks was assessed using the timing of the x-ray flash produced from the shock convergence at the target center. Large amounts of hot electrons were produced that deposited their energy (up to 2.3 kJ) in the target and significantly enhanced (by up to ~50%) the shock strength. Measurements of the timing and magnitude of the x-ray flash and the hot-electron fraction demonstrate the enhancement of the shock strength from hot electrons. The extrapolation of the OMEGA results to the condition required for shock ignition on the NIF looks promising. The experiments also open the way to develop a platform to study material properties under extreme pressures by placing materials of interest at the center of the plastic sphere and compressing the sample material to Gbar pressures by the convergent shock.

ACKNOWLEDGMENT

This material is based upon work supported by the Department of Energy National Nuclear Security Administration under Award Number DE-NA0001944, the OFES Fusion Science Center grant No. DE-FC02-04ER54789, the DOE Laboratory Basic Science Program, the University of Rochester, and the New York State Energy Research and Development Authority. The support of DOE does not constitute an endorsement by DOE of the views expressed in this article.

REFERENCES

1. R. Betti, C. D. Zhou, K. S. Anderson, L. J. Perkins, W. Theobald, and A. A. Solodov, Phys. Rev. Lett. **98**, 155001 (2007).
2. W. Theobald, R. Betti, C. Stoeckl, K. S. Anderson, J. A. Delettrez, V. Yu. Glebov, V. N. Goncharov, F. J. Marshall, D. N. Maywar, R. L. McCrory, D. D. Meyerhofer, P. B. Radha, T. C. Sangster, W. Seka, D. Shvarts, V. A. Smalyuk, A. A. Solodov, B. Yaakobi, C. D. Zhou, J. A. Frenje, C. K. Li, F. H. Séguin, R. D. Petrasso, and L. J. Perkins, Phys. Plasmas **15**, 056306 (2008).
3. L. J. Perkins, R. Betti, K. N. LaFortune, and W. H. Williams, Phys. Rev. Lett. **103**, 045004 (2009).
4. X. Ribeyre, G. Schurtz, M. Lafon, S. Galera, and S. Weber, Plasma Phys. Control. Fusion **51**, 015013 (2009).
5. S. Atzeni, X. Ribeyre, G. Schurtz, A. J. Schmitt, B. Canaud, R. Betti, and L. J. Perkins, Nucl. Fusion **54**, 054008 (2014).
6. J. Nuckolls *et al*., Nature **239**, 139 (1972).
7. J. D. Lindl, *Inertial Confinement Fusion: The Quest for Ignition and Energy Gain Using Indirect Drive* (Springer-Verlag, New York, 1998).
8. V. A. Shcherbakov, Sov. J. Plasma Phys. **9**, 240 (1983).
9. A. J. Schmitt *et al*., Phys. Plasmas **17**, 042701 (2010).
10. D. Batani, S. Baton, A. Casner, S. Depierreux, M. Hohenberger, O. Klimo, M. Koenig, C. Labaune, X. Ribeyre, C. Rousseaux, G. Schurtz, W. Theobald, and V. T. Tikhonchuk, Nucl. Fusion **54**, 054009 (2014).
11. S. Atzeni and J. Meyer-ter-Vehn, *The Physics of Inertial Fusion: Beam Plasma Interaction, Hydrodynamics, Hot Dense Matter*, International Series of Monographs on Physics (Clarendon Press, Oxford, 2004).
12. K. S. Anderson, R. Betti, P. W. McKenty, T. J. B. Collins, M. Hohenberger, W. Theobald, R. S. Craxton, J. A. Delettrez, M. Lafon, J. A. Marozas, R. Nora, S. Skupsky, and A. Shvydky, Phys. Plasmas **20**, 056312 (2013).
13. W. L. Kruer, in *The Physics of Laser Plasma Interactions*, Frontiers in Physics, Vol. 73, edited by D. Pines (Addison-Wesley, Redwood City, CA, 1988).
14. A. A. Offenberger *et al*., J. Appl. Phys. **47**, 1451 (1976).
15. W. Seka, H. A. Baldis, J. Fuchs, S. P. Regan, D. D. Meyerhofer, C. Stoeckl, B. Yaakobi, R. S. Craxton, and R. W. Short, Phys. Rev. Lett. **89**, 175002 (2002).
16. S. P. Regan, D. K. Bradley, A. V. Chirokikh, R. S. Craxton, D. D. Meyerhofer, W. Seka, R. W. Short, A. Simon, R. P. J. Town, B. Yaakobi, J. J. Carroll III, and R. P. Drake, Phys. Plasmas **6**, 2072 (1999).
17. C. Stoeckl, R. E. Bahr, B. Yaakobi, W. Seka, S. P. Regan, R. S. Craxton, J. A. Delettrez, R. W. Short, J. Myatt, A. V. Maximov, and H. Baldis, Phys. Rev. Lett. **90**, 235002 (2003).
18. W. Seka, D. H. Edgell, J. F. Myatt, A. V. Maximov, R. W. Short, V. N. Goncharov, and H. A. Baldis, Phys. Plasmas **16**, 052701 (2009).
19. S. D. Baton *et al*., Phys. Rev. Lett. **108**, 195002 (2012).
20. M. Hohenberger, W. Theobald, S. X. Hu, K. S. Anderson, R. Betti, T. R. Boehly, A. Casner, D. E. Fratanduono, M. Lafon, D. D. Meyerhofer,

R. Nora, X. Ribeyre, T. C. Sangster, G. Schurtz, W. Seka, C. Stoeckl, and B. Yaakobi, Phys. Plasmas **21**, 022702 (2014).

21. D. Batani *et al*., Phys. Plasmas **21**, 032710 (2014).

22. R. Nora, W. Theobald, R. Betti, F. J. Marshall, D. T. Michel, W. Seka, B. Yaakobi, M. Lafon, C. Stoeckl, J. A. Delettrez, A. A. Solodov, A. Casner, C. Reverdin, X. Ribeyre, A. Vallet, J. Peebles, F. N. Beg, and M. S. Wei, Phys. Rev. Lett. **114**, 045001 (2015).

23. G. H. Miller, E. I. Moses, and C. R. Wuest, Opt. Eng. **43**, 2841 (2004).

24. G. Guderley, Luftfahrtforschung **19**, 302 (1942).

25. A. L. Kritcher *et al*., High Energy Density Phys. **10**, 27 (2014).

26. T. R. Boehly, D. L. Brown, R. S. Craxton, R. L. Keck, J. P. Knauer, J. H. Kelly, T. J. Kessler, S. A. Kumpan, S. J. Loucks, S. A. Letzring, F. J. Marshall, R. L. McCrory, S. F. B. Morse, W. Seka, J. M. Soures, and C. P. Verdon, Opt. Commun. **133**, 495 (1997).

27. D. K. Bradley, P. M. Bell, J. D. Kilkenny, R. Hanks, O. Landen, P. A. Jaanimagi, P. W. McKenty, and C. P. Verdon, Rev. Sci. Instrum. **63**, 4813 (1992).

28. M. Millecchia, S. P. Regan, R. E. Bahr, M. Romanofsky, and C. Sorce, Rev. Sci Instrum. **83**, 10E107 (2012).

29. S. P. Regan, T. C. Sangster, D. D. Meyerhofer, W. Seka, R. Epstein, S. J. Loucks, R. L. McCrory, C. Stoeckl, V. Yu. Glebov, O. S. Jones, D. A. Callahan, P. A. Amendt, N. B. Meezan, L. J. Suter, M. D. Rosen, O. L. Landen, E. L. DeWald, S. H. Glenzer, C. Sorce, S. Dixit, R. E. Turner, and B. MacGowan, J. Phys.: Conf. Ser. **112**, 022077 (2008).

30. T. R. Boehly, V. A. Smalyuk, D. D. Meyerhofer, J. P. Knauer, D. K. Bradley, R. S. Craxton, M. J. Guardalben, S. Skupsky, and T. J. Kessler, J. Appl. Phys. **85**, 3444 (1999).

31. S. Skupsky, R. W. Short, T. Kessler, R. S. Craxton, S. Letzring, and J. M. Soures, J. Appl. Phys. **66**, 3456 (1989).

32. S. P. Regan, J. A. Marozas, J. H. Kelly, T. R. Boehly, W. R. Donaldson, P. A. Jaanimagi, R. L. Keck, T. J. Kessler, D. D. Meyerhofer, W. Seka, S. Skupsky, and V. A. Smalyuk, J. Opt. Soc. Am. B **17**, 1483 (2000).

33. F. J. Marshall and J. A. Oertel, Rev. Sci. Instrum. **68**, 735 (1997).

34. D. T. Michel, V. N. Goncharov, I. V. Igumenshchev, R. Epstein, and D. H. Froula, Phys. Rev. Lett. **111**, 245005 (2013).

35. C. Stoeckl, V. Yu. Glebov, D. D. Meyerhofer, W. Seka, B. Yaakobi, R. P. J. Town, and J. D. Zuegel, Rev. Sci. Instrum. **72**, 1197 (2001).

36. R. Tommasini, J. A. Koch, N. Izumi, L. A. Welser, R. C. Mancini, J. Delettrez, S. Regan, and V. Smalyuk, Rev. Sci. Instrum. **77**, 10E303 (2006).

37. C. D. Chen *et al*., Rev. Sci. Instrum. **79**, 10E305 (2008).

38. D. H. Froula, B. Yaakobi, S. X. Hu, P.-Y. Chang, R. S. Craxton, D. H. Edgell, R. Follett, D. T. Michel, J. F. Myatt, W. Seka, R. W. Short, A. Solodov, and C. Stoeckl, Phys. Rev. Lett. **108**, 165003 (2012).

39. A. Simon, R. W. Short, E. A. Williams, and T. Dewandre, Phys. Fluids **26**, 3107 (1983).

40. H. A. Baldis, E. M. Campbell, and W. L. Kruer, in *Handbook of Plasma Physics*, edited by M. N. Rosenbluth and R. Z. Sagdeev, Vol. 3: Physics of Laser Plasma, edited by A. Rubenchik and S. Witkowski (North-Holland, Amsterdam, 1991).

41. W. Seka, R. E. Bahr, R. W. Short, A. Simon, R. S. Craxton, D. S. Montgomery, and A. E. Rubenchik, Phys. Fluids B **4**, 2232 (1992).

42. *LLE Review Quarterly Report* **36**, 158, Laboratory for Laser Energetics, University of Rochester, Rochester, NY, LLE Document No. DOE/DP/40200-79 (1988).

43. O. Willi *et al*., Phys. Fluids B **2**, 1318 (1990).

44. R. Betti, W. Theobald, C. D. Zhou, K. S. Anderson, P. W. McKenty, S. Skupsky, D. Shvarts, V. N. Goncharov, J. A. Delettrez, P. B. Radha, T. C. Sangster, C. Stoeckl, and D. D. Meyerhofer, J. Phys.: Conf. Ser. **112**, 022024 (2008).

45. J. Delettrez and E. B. Goldman, Laboratory for Laser Energetics, University of Rochester, Rochester, NY, LLE Report No. 36 (1976).

46. A. R. Bell, Rutherford Appleton Laboratory, Chilton, Didcot, Oxon, England, Report RL-80-091 (1980).

47. G. I. Kerley, Phys. Earth Planet. Inter. **6**, 78 (1972).

48. G. I. Kerley, Sandia National Laboratory, Albuquerque, NM, Report SAND2003-3613 (2003).

49. R. C. Malone, R. L. McCrory, and R. L. Morse, Phys. Rev. Lett. **34**, 721 (1975).

50. J. Delettrez, R. Epstein, M. C. Richardson, P. A. Jaanimagi, and B. L. Henke, Phys. Rev. A **36**, 3926 (1987); M. C. Richardson, P. W. McKenty, F. J. Marshall, C. P. Verdon, J. M. Soures, R. L. McCrory, O. Barnouin, R. S. Craxton, J. Delettrez, R. L. Hutchison, P. A. Jaanimagi, R. Keck, T. Kessler, H. Kim, S. A. Letzring, D. M. Roback, W. Seka, S. Skupsky, B. Yaakobi, S. M. Lane, and S. Prussin, in *Laser Interaction and Related Plasma Phenomena*, edited by H. Hora and G. H. Miley (Plenum Publishing, New York, 1986), Vol. 7, pp. 421–448.

51. S. Gus'kov *et al*., Phys. Rev. Lett. **109**, 255004 (2012).

52. X. Ribeyre *et al*., Phys. Plasmas **20**, 062705 (2013).

53. R. Betti, R. Nora, K. S. Anderson, M. Lafon, W. Theobald, R. Yan, and C. Ren, Bull. Am. Phys. Soc. **58**, 31 (2013).

Tritium Migration to the Surfaces of Aluminum 6061, Oxygen-Free, High-Conductivity Copper, and Stainless-Steel 316

Introduction

Tritium is a widely used hydrogen isotope with applications ranging from nuclear fusion to use as a radioactive label in the development of drugs.[1] When exposed to metal surfaces, tritium will undergo isotopic exchange with any hydrogen-containing species adsorbed on the surface, such as small organic molecules and water.[2] Because of this effect, the surface layer of an adsorbed material can contain large concentrations of tritium.[3] Tritium also dissolves in metal lattices,[4–6] where it occupies interstitial lattice sites, vacancies, etc. Tritium concentrations within the metal lattice are much lower than the corresponding surface concentrations.

Once removed from the tritium-gas environment, a contaminated metal will continue to outgas tritium for prolonged periods of time.[7] During this outgassing process, tritium first desorbs from the surface; then the tritium present in the metal lattice replenishes the depleted surface activity. Surface replenishment is diffusion limited and assumed to be much slower than tritium outgassing under ambient conditions.

The absorption of hydrogen isotopes by metals is preceded by adsorption onto the metal surface. While adsorption is a key step in the overall absorption of tritium, several fundamental aspects of the process remain unknown. A better understanding of the physical processes could lead to the development of effective tritium adsorption/absorption barriers, which is of particular interest for nuclear fusion reactors and a future hydrogen economy.

The present study has measured the replenishment of surface activity on stainless-steel 316, aluminum 6061, and oxygen-free, high-conductivity (OFHC) copper by selective removal of surface-bound tritium using an argon plasma. The migration of tritium to the surface is calculated with a diffusion model developed by the authors. This model calculates the solubility of tritium on the surface of each metal and the plasma-removal efficiency.

Experimental Setup and Procedures

Metal samples, with dimensions of $5.1 \times 1.8 \times 0.3$ cm, were charged with tritium by exposing them to ~1 atm of deuterium–tritium (DT) gas at 25°C. Table 141.IV details the exposure conditions. The loading apparatus contained multiple slots, which allowed for simultaneous loading of a set of samples while keeping each sample separate from its neighbors. Two different sets of samples were charged with tritium and then stored in a helium environment. The first set of samples contained only stainless steel; these samples were stored together in the same metallic container until each experiment. Individual samples were removed using a glove bag to retain the helium environment in the storage vessel. The second loading set contained stainless steel, copper, and aluminum samples. These samples were stored in individual containers until each experiment, which eliminated the use of a glove bag. Each sample was exposed to laboratory air briefly while loading it into the plasma chamber.

Several samples from each set were subjected to thermal desorption to determine the total activity.[8] Set #1 samples

Table 141.IV: Sample loading conditions. Samples were stored under helium. Set #1 samples were stored in the same container and removed using a glove bag; Set #2 samples were stored in separate containers.

Set	Time (h)	DT pressure (Torr)	T:D ratio	Storage time	Metal
1	3	686.8	45%	3.5 yrs	Stainless-steel 316
2	24	659.0	39%	≤36 days	Al, Cu, stainless-steel 316

contained ~200 μCi, whereas Set #2 samples contained 700 to 900 μCi, depending on the metal type.

Each sample was suspended inside a 2-L vacuum chamber that was purged with a flowing stream of argon at a pressure of 8 Pa (Fig. 141.57). A Tonks–Langmuir plasma[9] was ignited by passing a 13.56-MHz alternating current through a copper coil wrapped around the exterior of the glass vacuum chamber. Argon ions generated in the plasma were assumed to have a Maxwellian distribution with an average temperature of 298 K. These ions were accelerated toward the metal samples after crossing a sheath surrounding the sample to strike the surface with an energy of the order of 10 eV. The ion impact sputtered tritiated compounds from the surface. Tritium removed from the samples was monitored downstream of the vacuum chamber in real time by using an in-line tritium monitor (TM).[10]

The sample temperature was measured using an uncontaminated metal sample. The temperature increased by less than 1°C during 2-s plasma exposures. All samples were assumed to remain at room temperature throughout the decontamination sequence.

Between each plasma exposure, the sample was kept under the argon flow for various dwell periods. A layer of water redeposited on the metal surfaces during these dwell periods within 0.5 s because the base pressure of the vacuum system was of the order of 1 Pa.

The tritium diffusion rate in the three metals is low at room temperature. The mean distance that a triton will travel through the metal lattice is

$$\langle x \rangle = \sqrt{4 * D * t}\,, \tag{1}$$

where D is the bulk diffusion coefficient assumed to be constant during the plasma exposure time t. Using the best-fit values for solubility and diffusivity for each metal (discussed in the **Appendix**, p. 69), the maximum amount of activity from the bulk that could be released during a plasma exposure is calculated by

$$A = \langle x \rangle * SA * S * N_{\alpha} * \lambda\,, \tag{2}$$

where SA is the surface area of the sample, S is the molar tritium concentration in the bulk at the end of the storage period, λ is the decay constant for tritium, and N_{α} is Avogadro's number. The estimates are compared against the activity A_{data} removed during the first plasma exposure of each metal in Table 141.V and show that the triton contribution from the bulk to the total

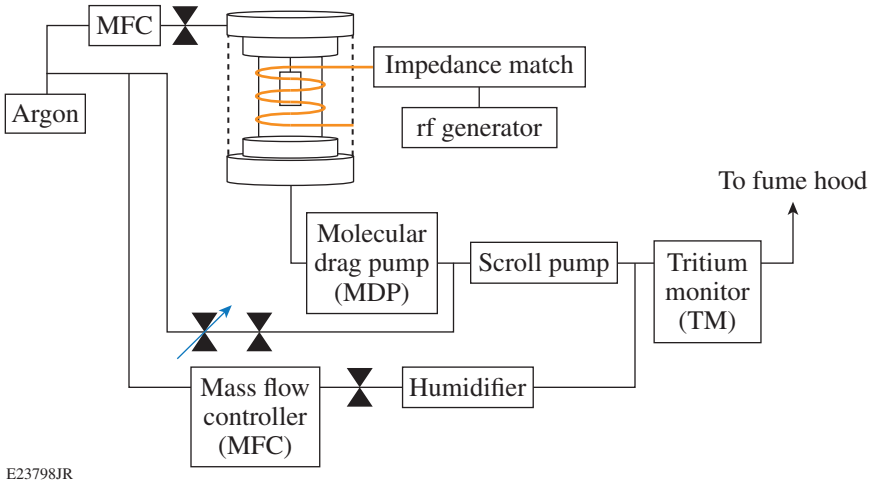

Figure 141.57
Diagram of the plasma system. Two gas lines are necessary for operating the tritium monitor (TM). A humid purge line reduces the memory effect of tritium in the TM. An additional dry purge line reduces the residence time of gas in the TM. rf: radio frequency.

Table 141.V: Calculated maximum activities A_{cal} that can be removed during a single plasma exposure, assuming the surface and bulk metal concentrations are in equilibrium.

Metal	$\langle x \rangle$ (μm)	A_{cal} (μCi)	A_{data} (μCi)
Aluminum	7.97	3.1	21±6
Copper	1.04	0.4	31±6
Stainless-steel 316	0.06	0.5	52±6

activity released in the first plasma exposure is 15%, 1%, and 1% for aluminum, copper, and stainless steel, respectively.

These 2-s exposures provided a controlled method for selective removal of surface-bound tritium without any significant contribution from the bulk. Table 141.V indicates that for all metal samples, the maximum activity released from the bulk during a 2-s plasma exposure is expected to be small compared to the activity present on the surface and is below the resolution of the experiment. Triton contributions from the bulk to the total activity released from a sample during a 2-s exposure are neglected in the analysis that follows.

Results

Tritium release from stainless-steel surfaces during a series of 2-s plasma exposures is shown in Fig. 141.58 on a log–log plot for both loading sets. The initial activity present on each surface determines the magnitude of the activity removed during each exposure series. Set #2 samples, which are loaded for a longer time and stored for a shorter time, have more surface activity than samples from Set #1. The trend in the quantity of activity removed with each successive plasma exposure appears similar for both sets, even though the initial activity removed from each sample differs.

To compare the activity-removal trends for each sample, the dependence on the initial activity was removed by normalizing the data to the initial activity removed in each series of plasma exposures. This was done by dividing each data series by the initial activity removed. The normalized data are replotted in Fig. 141.59. These data indicate that the trend in activity removed in sequential exposures does not depend on either the loading conditions or the storage time.

Figure 141.60 illustrates the dependence of the normalized amount removed on the dwell period between plasma shots. The dwell period between plasma exposures of stainless-steel samples was varied between 10 to 100 min for samples from the first loading set but was fixed at a constant 20 min for the second set of samples. This plot compares the response from two samples for clarity; it is representative of all the other data sets.

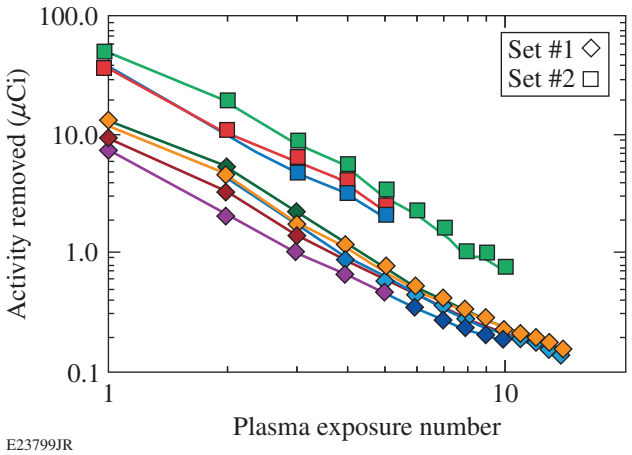

Figure 141.58
Activity removed from stainless-steel samples during a series of 2-s plasma exposures.

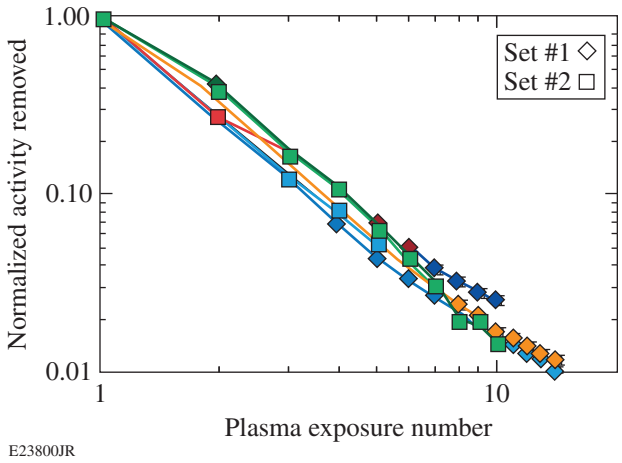

Figure 141.59
Activity removed from stainless steel in sequential exposures. The data were normalized to the initial activity removed for samples charged with DT under different conditions.

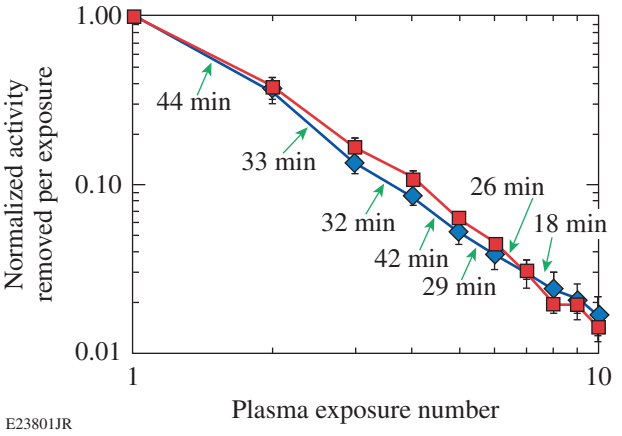

Figure 141.60
Dependence of activity removed from stainless-steel samples on variable dwell periods between plasma shots. A 20-min dwell period was used for the sample from Set #2 (red squares). The dwell period for the second sample (blue diamonds) varied between 18 and 44 min.

Decreasing the dwell period from 100 min to 10 min had no effect on the dependence of the normalized amount of activity removed with successive plasma exposures.

Normalized activities removed by sequential 2-s plasma exposures from aluminum and copper surfaces are compared to stainless steel in Fig. 141.61. Within experimental error, the same trend is observed in both aluminum and copper as in stainless steel.

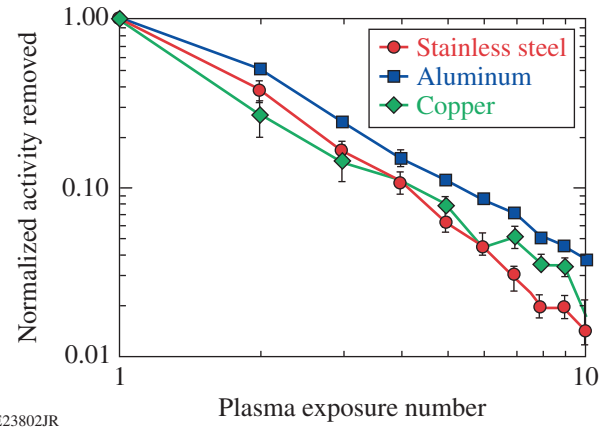

Figure 141.61
Comparison of the dependence of normalized activity removed from aluminum, copper, and stainless-steel samples on sequential plasma exposures for samples from Set #2

Discussion

Tritium dissolves in metals by dissociating into atoms and then occupying interstitial locations, defect sites, and grain boundaries within the bulk metal.[11,12] On the surface, tritium atoms isotopically exchange with protons present in adsorbed water layers. An illustration of the tritium-metal system is shown in Fig. 141.62. The metal-oxide layer, which forms between the hydroxyl layer and metal surface, has been omitted for simplicity. The hydroxyl groups bound to the bulk metal have spacing equal to the metal lattice parameter. This spacing arises because the oxygen atoms in the hydroxyl ion bind to a location directly on top of each metal center.[13]

The first layer of molecular water to adsorb is rigidly proton bonded to the hydroxyl layer.[14] This layer is not removable by purging with a dry gas alone.[15] Subsequent layers of adsorbed water become more mobile as the number of layers increases. The overall number of water layers on the metal surface is determined by an isotherm[16–18] that correlates with the water vapor pressure present over the metal surface, the metal in question, and the ambient temperature. The isotopic composition of

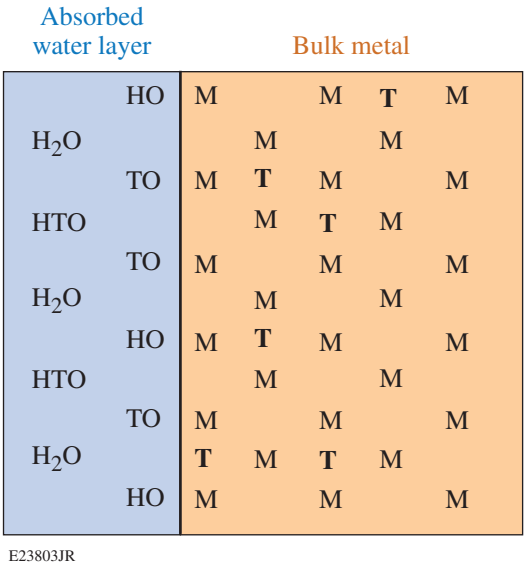

Figure 141.62
Illustration of the surface structure present on metals, including potential tritium locations within each media but excluding the native oxide layer between the base metal and the hydroxyl layer.

these outer layers of water is not expected to depend strongly on the substrate metal.

Short plasma exposures remove the tritium-rich water layers from the metal surface. Between plasma exposures, these water layers are quickly replaced by tritium-free water, as discussed above. During the dwell period, tritium is expected to migrate into the newly adsorbed water layers on the surface, driven by the tritium concentration gradient across the surface/bulk interface.

Three potential mechanisms may account for the tritium released during a series of plasma exposures:

1. The removable tritium inventory resides in the water/oxide layers and re-equilibrates within those layers during the dwell period.

2. Tritium migrates from the bulk into the surface layers at a constant rate.

3. The surface layers are replenished with tritium by Fickian diffusion from the bulk.

The predicted amount of activity removed in sequential plasma exposures based on each of these scenarios is compared against experimental data in Fig. 141.63.

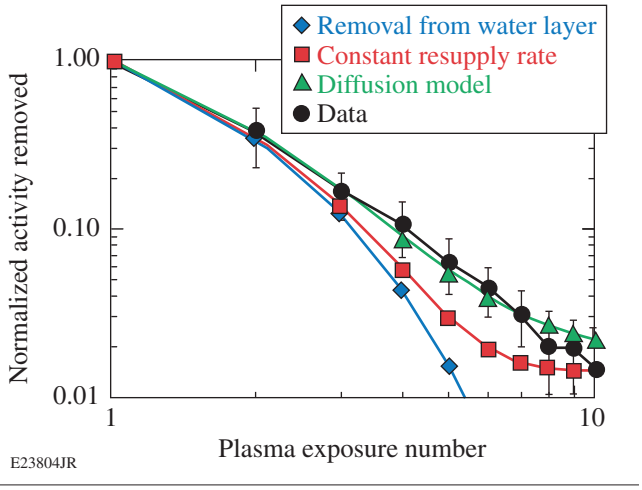

Figure 141.63
The plot compares different triton-accumulation scenarios in the water layer on a Set #2 stainless-steel sample. All calculations assumed a plasma efficiency of 65%. Error bars reflect the observed spread in the data.

If the entire tritium inventory released during the plasma-exposure sequence resides in the water layer on the metal surface, the amount of activity removed during a sequence should follow the relation

$$R_i = A_0 * (1 - \varepsilon)^{i-1} * \varepsilon, \tag{3}$$

where A_0 is the initial surface activity, i is the plasma-exposure number, and ε is the plasma-removal efficiency. The efficiency ε represents the fraction of tritium removed during a plasma exposure and is assumed to be constant throughout a series of exposures. This activity removal rate grossly underpredicts the experimental data shown in Fig. 141.63 and suggests that there is a replenishment of tritons from the bulk during the dwell period.

Including a constant rate of tritium migration from the bulk metal to the surface during the dwell period, the activity removed in the series of plasma exposures can be represented by

$$A_i = A_{i-1} * (1 - \varepsilon) + C, \tag{4}$$

$$r_i = A_{i-1} * \varepsilon, \tag{5}$$

where C is the amount of tritium migrating into the surface during a constant dwell period, A_i is the activity remaining after each plasma exposure, and r_i is the activity removed during exposure i.

Figure 141.63 shows that this calculation also underpredicts the activity removed during an exposure sequence, albeit to a lesser extent than that predicted by Eq. (3). In addition, after the eighth exposure, the calculated activity removed approaches a limiting value—a behavior that is not observed experimentally.

Figure 141.63 shows that the best fit to the data occurs for the third scenario, in which the surface is replenished with tritium by Fickian diffusion from the bulk. In this case, the quantity of activity removed during a plasma exposure is given by the residual surface activity and the quantity of activity that diffused into the surface layer during the dwell period:

$$A_i = \left[A_{i-1} * (1 - \varepsilon) - F * SA * \Delta t\right] * \varepsilon, \tag{6}$$

where A_i is the activity removed during exposure i, F is the diffusion flux $\left[\partial^2 c(x,t) \big/ \partial x^2\right]$ at the surface/bulk interface, SA is the sample surface area, Δt is the dwell period between plasma exposures, and ε is the plasma-removal efficiency.

In this case the tritium migration rate to the surface was estimated by calculating the concentration profiles throughout the metal. These profiles were calculated assuming Fickian diffusion[19] and take several factors into account:

1. There is a metallurgical bond between the surface layers and the bulk metal.

2. The rate at which the samples incorporate tritium during loading is also limited by diffusion into the metal.

3. Tritium equilibrates within the bulk during the storage time between loading the samples and exposing the plasma.

4. Tritium-concentration profiles beneath the water layer develop in the bulk metal as the tritons are transferred from the bulk to the water layer.

Triton diffusion from the bulk to the water layer must cross the surface/bulk interface. Assuming that there is a metallurgical bond between the metal substrate and the water layer closest to the metal surface, the tritium concentrations on either side of the surface/bulk interface are related through the ratio of their respective solubility as shown in Eq. (7):

$$C_{\text{surface}} = \frac{S_{\text{surface}}}{S_{\text{bulk}}} * C_{\text{bulk}} = S * C_{\text{bulk}}. \tag{7}$$

Simulating the model to predict the quantity of tritium removed involved three phases: sample loading, sample storage, and plasma exposures. The surface concentration was estimated using the tritium partial pressure over the metal samples assuming it to be saturated and fixed for the duration of the loading phase. Plasma exposures were assumed to remove a constant amount of water from the surface. However, the activity of the surface water depended on the tritium concentration in the bulk at the surface/bulk interface. Finally, no tritium was assumed to be lost during the dwell period between plasma exposures or during sample storage.

Typical calculated tritium-concentration profiles immediately following each exposure for a sequence of plasma exposures are shown in Fig. 141.64 on a semi-log plot. These particular profiles were calculated for an aluminum sample from Loading Set #2 (Table 141.VI). Only the profiles after plasma exposures 1, 3, 5, 7, and 9 are shown for clarity. Given the high diffusivity of aluminum at room temperature, the initial concentration profile in the bulk metal reached steady state during the storage period prior to the first plasma exposure. During the 20-min dwell period between each plasma exposure, the concentration gradient in the bulk relaxed over time as tritons migrated to the surface.

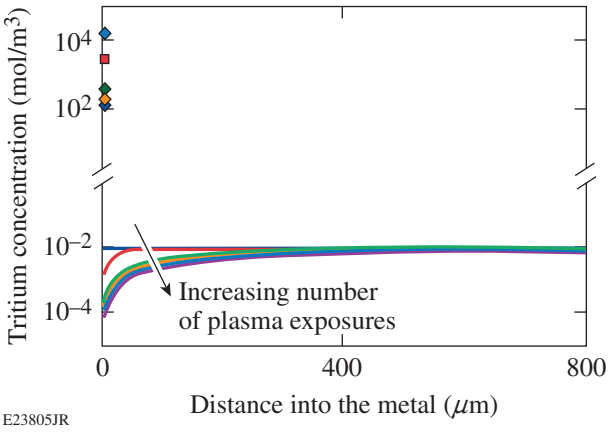

Figure 141.64
Calculated tritium-concentration profiles in aluminum after plasma exposures 1, 3, 5, 7, and 9. The initial profile prior to the first exposure is also shown.

Table 141.VI: Lattice diffusivity and solubilities calculated from a collection of literature references. Values reported here are for 25°C.

Metal	Diffusivity (m^2/s)	Solubility (mol $T/m^3/atm^{1/2}$)
Aluminum	7.95×10^{-12}	0.044
Copper	1.32×10^{-13}	0.220
Stainless-steel	3.76×10^{-16}	2.020

In the model, the sample recovers from each plasma exposure by repopulating the tritium-deficient water layer with tritons from the bulk near the interface, as illustrated in Fig. 141.65, in an effort to re-establish the surface concentration specified by Eq. (8). However, since the tritium migration rate is diffusion limited, the tritium concentration in the water layer cannot return to its original value within the dwell period. By the ninth exposure, the surface tritium concentration has dropped from its original value of 15.2 kmol T/m^3 to 0.6 kmol T/m^3. The corresponding bulk concentration at the

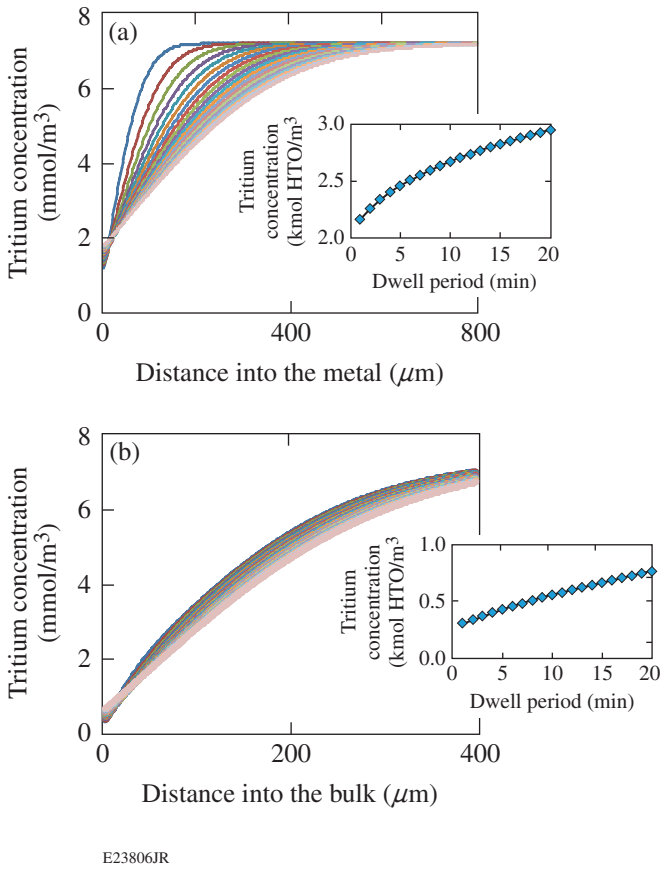

Figure 141.65
Evolution of tritium-concentration profiles during the dwell period after plasma exposures (a) #1 and (b) #3. The insets show the increase in surface concentration during each dwell period.

interface has dropped from 7.2 mmol T/m^3 to 0.3 mmol T/m^3, at which point the perturbed concentration depth profile extends ~75% to the center of the sample.

The diffusivity and solubility for each metal at 25°C are provided in Table 141.VI. These values represent the "best fit" computed from a compilation of literature references that are discussed in the **Appendix** (p. 69).

As an aside, extrapolating the lattice solubility of copper from high-temperature data (≥200°C) to room temperature underpredicts the effective hydrogen solubility in copper. The effective solubility is dominated by the significant number of shallow traps, defects, and vacancies present in copper.[20–22] Since the hydrogen binding energies in copper at defect sites and octahedral sites are similar,[23] the effective hydrogen diffusivity through copper at temperatures below 200°C does not deviate from the Arrhenius behavior extrapolated from higher temperatures.[24]

The model was fit to the data by varying both the plasma-removal efficiency and the surface-to-bulk solubility ratio. The results of the fits for the three metals are shown in Table 141.VII. Published isotherms were used to determine the water-layer thickness, but the values reported here include an additional proton-bonded monolayer, as discussed above. A graphical comparison between the model predictions and data is provided in Fig. 141.63.

Table 141.VII: Solubilities for tritium in the water layer on metal surfaces as derived from model fits to experimental data. Surface thicknesses of the water layers were calculated from the water isotherms published for these metals.

Metal	Surface thickness (nm)	Surface-layer solubility (kmol T/m^3)	Plasma-removal efficiency
Aluminum	0.54	53±2.0	0.85±0.05
Copper	0.54	50±1.0	0.56±0.05
Stainless-steel	0.92	17.5±0.3	0.66±0.05

The surface solubilities for each metal reported in Table 141.VII were calculated from the bulk metal solubility and the solubility ratio provided by Eq. (8). The surface solubilities for all three metals are similar, as expected. Additionally, they are less than the absolute maximum, which is estimated to be ≈100 kmol/m^3. The absolute maximum is calculated by counting the total number of protons on the surface for a given relative humidity:

$$S_{\text{surface}} = S * S_{\text{bulk}}. \quad (8)$$

Figure 141.66 shows the effect of varying the plasma-removal efficiency from 0.60 to 0.70 while holding the solubility ratio constant in the diffusion model. In this figure, the model is compared against a representative data set for a stainless-steel sample from Loading Set #2. The error bars reflect the observed spread in the data reported in Fig. 141.59 and do not include systematic errors in the data. This analysis suggests the removal efficiency is known to within ±5%. Tritium is removed from aluminum surfaces with the highest efficiency, while removal from copper surfaces is the lowest.

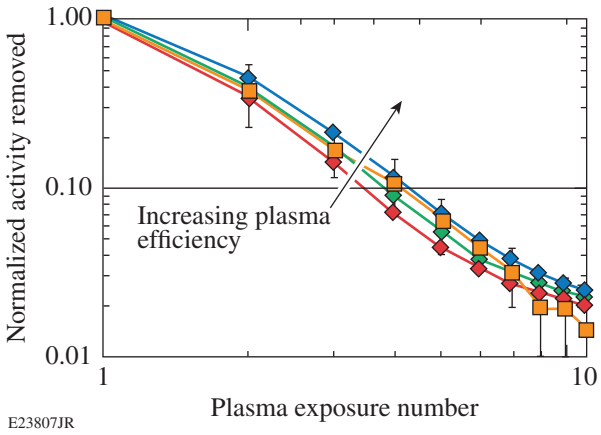

Figure 141.66
Comparison of the normalized activity removed from a Set #2 stainless-steel sample with the model for various plasma efficiencies. Data are shown as square points.

Conclusions

The experimental data show that low-pressure argon plasma is an effective tool in studying how tritium migrates from the bulk to the surface as tritium is removed from metal surfaces. Tritium is removed in decreasing quantities with successive plasma exposures, which suggests a depletion of the surface and near-surface tritium inventories. This trend in activity removed does not depend on dwell periods of less than 100 min, loading and storage conditions, or substrate metal.

The output of the diffusion model presented here confirms previous findings that the water layers on a metal surface provide a huge storage capacity for tritium. The concentration ratio across the water layer/bulk metal interface is uniquely determined by the solubility ratio across this interface. Perturbing the surface concentrations of tritons by replacing a tritium-rich water layer with a tritium-free water layer induces the tritium-

deficient water layer to "pump" tritium from the bulk to the surface in an effort to re-establish its previous equilibrium state. This process is driven by a concentration gradient that develops in the bulk because of the perturbation.

The model effectively describes triton transport into and out of stainless steel, aluminum, and oxygen-free, high-conductivity copper when these metals are exposed to a tritium partial pressure at room temperature:

1. The surface water layer rapidly saturates with tritium to values that are determined by the exposure conditions.

2. The bulk metal accepts tritium from the saturated tritium-rich water layer on the surface at a rate determined by the diffusivity of the base metal.

3. The surface tritium concentration equilibrates with the bulk concentration to a unique value determined by the metal solubility for hydrogen.

4. Tritium transport from the bulk can be encouraged via lattice diffusion or shallow traps by replacing the tritium-rich water layers on the surface with tritium-deficient water layers. This transport rate is determined by the diffusivity of the base metal.

Comparing the model predictions with data suggests that the tritium-concentration equilibration time constant within the water layers on the surface of these metals is significantly shorter than expected from the diffusivity in the bulk metal.

Appendix

The diffusivity and solubility have been measured for hydrogen isotopes in aluminum, copper, and stainless steel by a large number of investigators. Their data have been compiled in Tables 141.VIII–141.XIII below for each of the three metals of interest. The tables provide the pre-exponent, activation energy, and the temperature range over which the investigation was carried out. Additionally data have been plotted in Figs. 141.67–141.72 for each metal using the values in the tables in the following equation:

$$x(T) = x_0 * \exp\left(-\frac{E_\alpha}{R * T}\right),$$

where E_α is the activation energy in kJ/mol, x_0 is the frequency factor in m^2/s for diffusivity, and $mol/m^3 * \sqrt{atm}$ for solubility.

The "best-fit" values for diffusivity were determined by fitting the Arrhenius equation to the collection of data by varying the activation energy and frequency factor. The best-fit (average) values are presented in Tables 141.VIII–141.X. Best-fit curves using these values are plotted in Figs. 141.67–141.69.

The best-fit values for solubility were determined by computing the mean activation energy and frequency factors for each metal and are shown in Tables 141.XI–141.XIII. Best-fit curves using these values are plotted in Figs. 141.70–141.72. This approach yielded a better representation for the best-fit solubility curves for each metal than using a fitting routine as was done for determining the best-fit diffusivity values.

Several of the references in this collection were not included when the best fits were calculated because the data did not follow the same trend established by the remaining collection. The omitted references are highlighted in the tables and relevant figures. Three references were excluded from the collection of diffusivity values in aluminum. Two of these datasets were several orders of magnitude smaller than the rest of the collection. The third data set used an activation energy that differed considerably from other investigators. The higher activation energy suggests that trapping may have played an important role in the samples used by these investigators when measuring the hydrogen diffusivities in stainless steel.

The collection of solubility measurements for the three metals showed considerably more spread than the diffusivity measurements and points to the sensitivity between hydrogen solubility and the actual character of the bulk metal. While this spread is significant, the reported values for stainless steel and copper follow a similar trend. Although the frequency factor varies from study to study, the reported activation energies are similar. All references collected for stainless steel and copper were used to determine the best-fit values. Published measurements for hydrogen solubility in aluminum are considerably more sparse. Additionally, these studies use very different activation energies for hydrogen diffusion in aluminum. These best-fit values were computes with preference given to the most-recent studies.

Reiter *et al.*,[25] and more recently Causey *et al.*,[20] reviewed the tritium interactions with metals for fusion applications. There is good agreement between the Causey's best-fit datasets and the one presented here with exception to hydrogen diffusivities in copper and aluminum and the hydrogen solubility in aluminum. The differences are attributed to the size of the datasets used.

The hydrogen solubility values reported in Tables 141.XI–141.XIII below are calculated from measurements at elevated temperatures where hydrogen dissolution in the crystal lattice dominates. Contributions from vacancies, traps, and grain boundaries tend to be minor. Extrapolation from these temperatures, typically above 150°C, to room temperature can underpredict the actual hydrogen solubility, particularly in metals with low lattice solubilities like copper where the binding energies at the trap sites are similar to the binding energy within the lattice.[20,22,23] The effective hydrogen solubility in copper has been estimated to be of the order of 1000× the lattice solubility extrapolated from high temperatures to room temperature for the calculations used in this article.

Two observations suggest that the extrapolation of the hydrogen solubility at copper lattice sites from higher temperatures to room temperature underpredicts the actual solubility at room temperature. First, using a value based solely on lat-

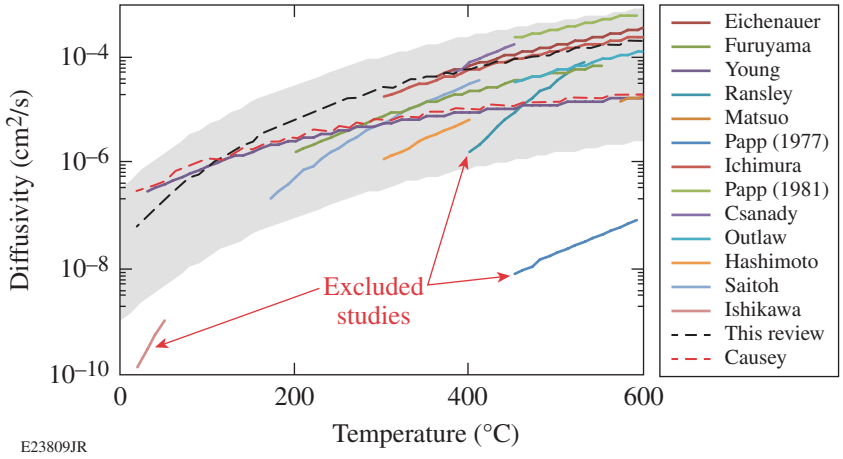

Figure 141.67
Collection of diffusivities for hydrogen isotopes in aluminum.

Table 141.VIII: Literature collection of diffusivities for aluminum.

Frequency factor (m^2/s)	Activation energy (kJ/mol)	Temperature range (°C)	Author (year)
1.1×10^{-5}	40.9	360 to 630	Eichenauer (1961)[26]
1.4×10^{-6}	35.7	200 to 560	Furuyama (1986)[27]
1.75×10^{-8}	16.2	30 to 600	Young (1998)[12]
12	140.0	400 to 530	Ransley (1955)[28]
2×10^{-6}	50.2	570 to 630	Matsuo (1967)[29]
2.5×10^{-6}	90.0	450 to 590	Papp (1977)[30]
4.58×10^{-6}	37.0	300 to 640	Ichimura (1979)[31]
1.9×10^{-5}	40.0	450 to 590	Papp (1981)[32]
1.30×10^{-3}	67.0	375 to 450	Csanady (1981)[33]
1.01×10^{-5}	47.7	450 to 625	Outlaw (1982)[6]
2.6×10^{-5}	58.7	300 to 400	Hashimoto (1983)[34]
6.1×10^{-5}	54.8	173 to 408	Saitoh (1994)[35]
9.2×10^{-5}	55.25	12 to 55	Ishikawa (1986)[36]
2×10^{-8}	16.0	—	Causey (2009)[20]
1.45×10^{-6}	30.0	—	Average

tice solubility suggests the total initial surface activity will be 0.39 μCi for the exposure conditions discussed here. However, the actual activity removed during the first plasma exposure of a copper sample was tenfold higher, 31.4±0.6 μCi. Secondly the total tritium inventory within the copper estimated from lattice solubility underpredicts the amount released when the metal is heated to high temperatures. The total activity in the bulk was calculated by integrating the concentration profile resulting from the semi-infinite solution to the diffusion equation. This solution used a fixed, saturated concentration at the surface/bulk interface, the mean diffusivity, and the mean lattice solubility. Summing the calculated bulk and surface activities yielded 109 μCi, which is 8× lower than the measured total activity of 810 μCi. Hydrogen storage in defect sites in the copper bulk dominates the amount stored within the lattice.

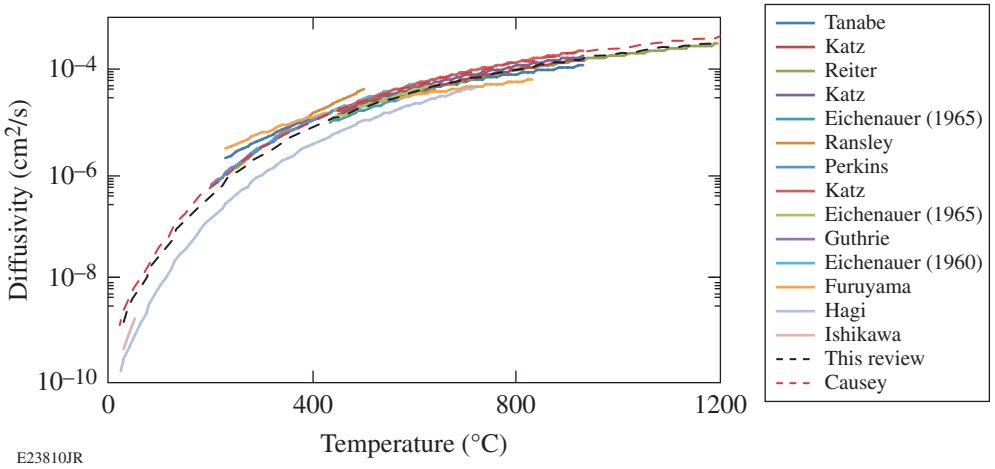

Figure 141.68
Collection of diffusivities for hydrogen isotopes in copper.

Table 141.IX: Literature collection of diffusivities for copper.

Frequency factor (m^2/s)	Activation energy (kJ/mol)	Temperature range (°C)	Author (year)
2.26×10^{-7}	29.3	227 to 927	Tanabe (1984)[4]
6.12×10^{-7}	36.5	450 to 925	Katz (1971)[37]
6.6×10^{-7}	37.4	470 to 1200	Reiter (1993)[25]
7.3×10^{-7}	36.8	450 to 925	Katz (1971)[37]
6.2×10^{-7}	37.8	430 to 640	Eichenauer (1965)[38]
6.8×10^{-6}	47.3	250 to 500	Ransley (1955)[28]
1.06×10^{-6}	38.5	200 to 440	Perkins (1973)[39]
1.13×10^{-6}	38.9	450 to 925	Katz (1971)[37]
1.15×10^{-6}	40.8	430 to 640	Eichenauer (1965)[38]
1.06×10^{-6}	38.4	200 to 440	Guthrie (1974)[5]
1.1×10^{-6}	38.5	270 to 650	Eichenauer (1960)[40]
8.2×10^{-8}	23.3	230 to 830	Furuyama (1986)[27]
9.0×10^{-7}	43.5	–13 to 727	Hagi (1986)[41]
2.74×10^{-4}	56.8	26 to 49.5	Ishikawa (1985)[24]
1×10^{-6}	38.5	—	Causey (2009)[20]
7.9×10^{-7}	38.6	—	Average

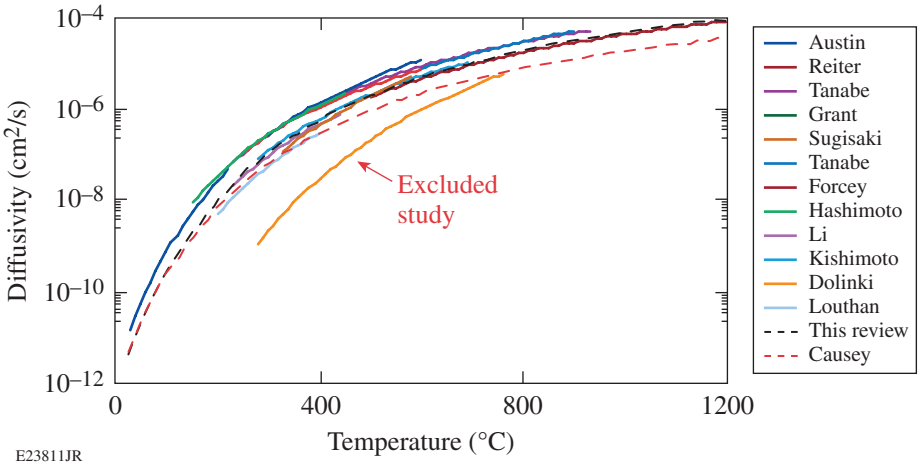

Figure 141.69
Collection of diffusivities for hydrogen isotopes in stainless steel.

Table 141.X: Literature collection of diffusivities for stainless-steel 316.

Frequency factor (m^2/s)	Activation energy (kJ/mol)	Temperature range (°C)	Author (year)
1.8×10^{-6}	52.7	25 to 222	Austin (1972)[42]
5.9×10^{-7}	51.9	500 to 1200	Reiter (1993)[25]
6.32×10^{-7}	47.8	227 to 927	Tanabe (1984)[4]
7.3×10^{-7}	52.4	276 to 692	Grant (1988)[43]
4.2×10^{-6}	64.0	330 to 580	Sugisaki (1985)[44]
1.74×10^{-6}	52.8	300 to 600	Tanabe (1979)[45]
3.82×10^{-7}	45.5	250 to 600	Forcey (1988)[46]
4.7×10^{-7}	46.3	150 to 450	Hashimoto (1985)[47]
4.79×10^{-7}	51.59	230 to 440	Li (1989)[48]
1.3×10^{-6}	54.0	600 to 900	Kishimoto (1985)[49]
1.2×10^{-5}	85.0	227 to 757	Dolinski (2000)[50]
4.7×10^{-7}	54.0	200 to 400	Louthan (1975)[51]
2×10^{-7}	49.3	—	Causey (2009)[20]
7.2×10^{-7}	52.9	—	Average

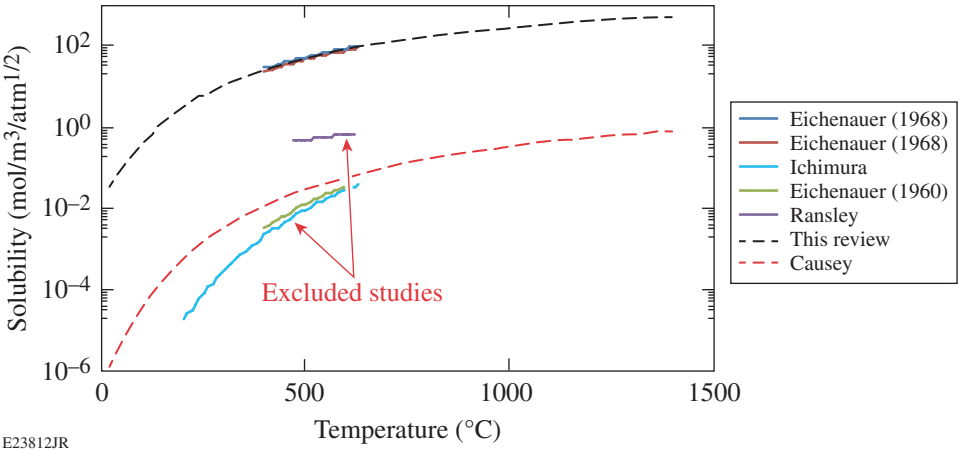

Figure 141.70
Collection of solubilities for hydrogen isotopes in aluminum.

Table 141.XI: Literature collection of solubilities for aluminum.

Frequency factor ($mol/m^3/atm^{1/2}$)	Activation energy (kJ/mol)	Temperature range (°C)	Author (year)
3954	27.4	400 to 630	Eichenauer (1968)[52]
4878	29.7	400 to 630	Eichenauer (1968)[52]
400	63.9	200 to 630	Ichimura (1979)[31]
111	58.2	400 to 600	Eichenauer (1960)[40]
7	17.3	465 to 620	Ransley (1948)[53]
15	39.7	—	Causey (2009)[20]
4416	28.5	—	Average

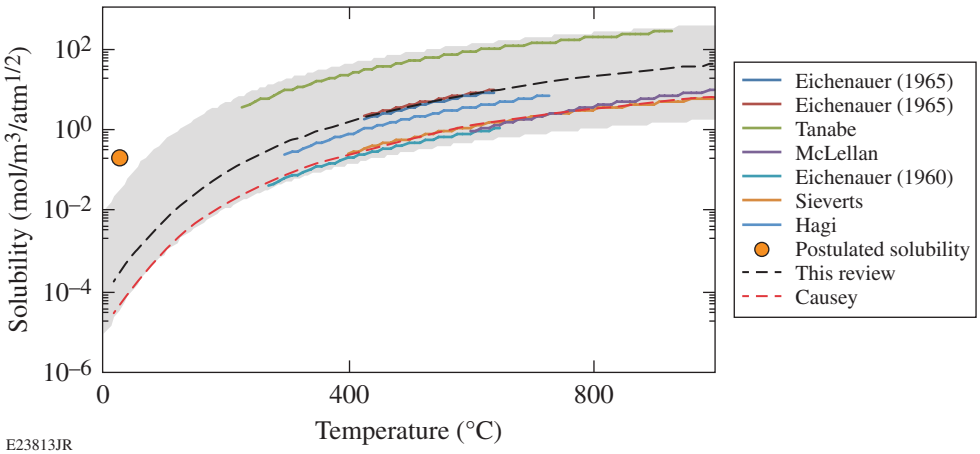

Figure 141.71
Collection of solubilities for hydrogen isotopes in copper.

Table 141.XII: Literature collection of solubilities for copper.

Frequency factor ($mol/m^3/atm^{1/2}$)	Activation energy (kJ/mol)	Temperature range (°C)	Author (year)
1674	40.0	430 to 635	Eichenauer (1965)[38]
1435	38.0	430 to 635	Eichenauer (1965)[38]
6116	31.2	227 to 927	Tanabe (1984)[4]
1657	54.7	600 to 1027	McLellan (1973)[54]
118	36.0	270 to 650	Eichenauer (1960)[40]
211	37.7	400 to 1000	Sieverts (1929)[55]
627	37.6	287 to 727	Hagi (1986)[41]
252	38.9	—	Causey (2009)[20]
1691	39.3	—	Average

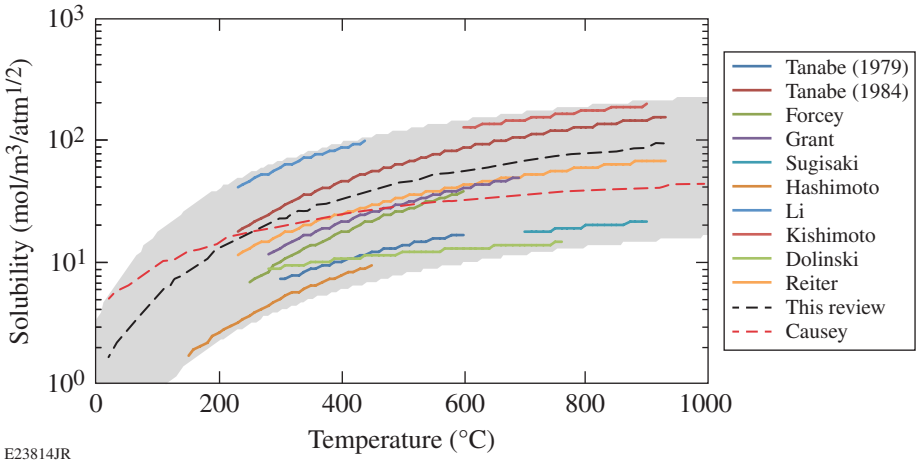

Figure 141.72
Collection of solubilities for hydrogen isotopes in stainless steel.

Table 141.XIII: Literature collection of solubilities for stainless steel.

Frequency factor ($mol/m^3/atm^{1/2}$)	Activation energy (kJ/mol)	Temperature range (°C)	Author (year)
89	12.1	300 to 600	Tanabe (1979)[45]
763	15.7	227 to 927	Tanabe (1984)[4]
477	18.5	250 to 600	Forcey (1988)[46]
353	15.7	276 to 692	Grant (1988)[43]
62	10.2	703 to 903	Sugisaki (1984)[56]
103	14.5	150 to 450	Hashimoto (1985)[47]
820	12.5	230 to 440	Li (1989)[48]
719	12.5	600 to 900	Kishimoto (1985)[49]
26	5	277 to 757	Dolinski (2000)[50]
262	13.1	227 to 927	Reiter (1993)[25]
85	6.9	—	Causey (2009)[20]
342	13.0	—	Average

REFERENCES

1. C. R. Shmayda, W. T. Shmayda, and N. P. Kherani, Fusion Sci. Technol. **41**, 500 (2002).
2. N. Nakashio *et al*., Fusion Sci. Technol. **39**, 189 (2001).
3. R.-D. Penzhorn *et al*., J. Nucl. Mater. **353**, 66 (2006).
4. T. Tanabe *et al*., J. Nucl. Mater. **123**, 1568 (1984).
5. J. W. Guthrie *et al*., J. Nucl. Mater. **53**, 313 (1974).
6. R. A. Outlaw, D. T. Peterson, and F. A. Schmidt, Scr. Metall. **16**, 287 (1982).
7. A. B. Antoniazzi, W. T. Shmayda, and T. Palma, in *Proceedings of the 15th IEEE/NPSS Symposium on Fusion Engineering, 1993* (IEEE, New York, 1993), Vol. 2, pp. 975–978; A. B. Antoniazzi, W. T. Shmayda, and T. Palma, in *Proceedings of the 15th IEEE/NPSS Symposium on Fusion Engineering, 1993* (IEEE, New York, 1993), Vol. 2, pp. 979–982.
8. M. J. Quinlan, W. T. Shmayda, S. Lim, S. Salnikov, Z. Chambers, E. Pollock, and W. U. Schröder, Fusion Sci. Technol. **54**, 519 (2008).
9. L. Tonks and I. Langmuir, Phys. Rev. **34**, 876 (1929).
10. N. P. Kherani and W. T. Shmayda, Fusion Sci. Technol. **21**, 340 (1992).
11. J. K. Nørskov *et al*., Phys. Rev. Lett. **49**, 1420 (1982).
12. G. A. Young, Jr. and J. R. Scully, Acta Mater. **46**, 6337 (1998).
13. J. Carrasco, A. Hodgson, and A. Michaelides, Nat. Mater. **11**, 667 (2012).
14. P. A. Thiel and T. E. Madey, Surf. Sci. Rep. **7**, 211 (1987).
15. M. Nishikawa *et al*., J. Nucl. Mater. **277**, 99 (2000).

16. T. Ohmi *et al*., Rev. Sci. Instrum. **64**, 2683 (1993).

17. S. P. Sharma, J. Vac. Sci. Technol. **16**, 1557 (1979).

18. H. A. Al-Abadleh and V. H. Grassian, Langmuir **19**, 341 (2003).

19. J. Crank, *The Mathematics of Diffusion* (Oxford University Press, Oxford, 1979), p. 189.

20. R. A. Causey, R. A. Karnesky, and C. San Marchi, in *Comprehensive Nuclear Materials*, 1st ed., edited by R. J. M. Konings *et al*. (Elsevier, Amsterdam, 2012), Vol. 4, pp. 511–549.

21. Å. Martinsson and R. Sandström, J. Mater. Sci. **47**, 6768 (2012).

22. M. G. Ganchenkova *et al*., Philos. Mag. **94**, 3522 (2014).

23. P. A. Korzhavyi and R. Sandström, Comput. Mater. Sci. **84**, 122 (2014).

24. T. Ishikawa and R. B. McLellan, J. Phys. Chem. Solids **46**, 445 (1985).

25. F. Reiter, K. S. Forcey, and G. Gervasini, *A Compilation of Tritium-Material Interaction Parameters* in *Fusion Reactor Materials* (Commission of the European Communities, Brussels, 1993).

26. W. Eichenauer, K. Hattenbach, and A. Pebler, Z. Metallkde. **52**, 682 (1961).

27. Y. Furuyama, T. Tanabe, and S. Imoto, J. Jpn. Inst. Met. **50**, 688 (1986).

28. C. E. Ransley and D. E. J. Talbot, Z. Metallkde. **46**, 328 (1955).

29. S. Matsuo and T. Hirata, J. Jpn. Inst. Met. **31**, 590 (1967).

30. K. Papp and E. Kovács-Csetényi, Scr. Metall. **11**, 921 (1977).

31. M. Ichimura, M. Imabayashi, and M. Hayakawa, J. Jpn. Inst. Met. **43**, 876 (1979).

32. K. Papp and E. Kovács-Csetényi, Scr. Metall. **15**, 161 (1981).

33. Á. Csanády, K. Papp, and E. Pásztor, Mater. Sci. Eng. **48**, 35 (1981).

34. E. Hashimoto and T. Kino, J. Phys. F: Met. Phys. **13**, 1157 (1983).

35. H. Saitoh, Y. Iijima, and H. Tanaka, Acta Metall. Mater. **42**, 2493 (1994).

36. T. Ishikawa and R. B. McLellan, Acta Metall. **34**, 1091 (1986).

37. L. Katz, M. Guinan, and R. J. Borg, Phys. Rev. B **4**, 330 (1971).

38. W. Eichenauer, W. Löser, and H. Witte, Z. Metallkde. **56**, 287 (1965).

39. W. G. Perkins, J. Vac. Sci. Technol. **10**, 543 (1973).

40. W. Eichenauer, Memoires Scientifiques Rev. Metallurg. **LVII**, 943 (1960).

41. H. Hagi, Trans. Jpn. Inst. Met. **27**, 233 (1986).

42. J. H. Austin and T. S. Elleman, J. Nucl. Mater. **43**, 119 (1972).

43. D. M. Grant, D. L. Cummings, and D. A. Blackburn, J. Nucl. Mater. **152**, 139 (1988).

44. M. Sugisaki *et al*., J. Nucl. Mater. **133–134**, 280 (1985).

45. T. Tanabe and S. Imoto, Trans. Jpn. Inst. Met. **21**, 109 (1980).

46. K. S. Forcey *et al*., J. Nucl. Mater. **160**, 117 (1988).

47. E. Hashimoto and T. Kino, J. Nucl. Mater. **133–134**, 289 (1985).

48. Y. Y. Li and Z. S. Xing, J. Nucl. Mater. **169**, 151 (1989).

49. N. Kishimoto *et al*., J. Nucl. Mater. **127**, 1 (1985).

50. Yu. Dolinski *et al*., J. Nucl. Mater. **283–287**, 854 (2000).

51. M. R. Louthan, Jr. and R. G. Derrick, Corros. Sci. **15**, 565 (1975).

52. W. Eichenauer, Z. Metallkde. **59**, 613 (1968).

53. C. E. Ransley and H. Neufeld, J. Inst. Met. **LXXIV**, 599 (1948).

54. R. B. McLellan, J. Phys. Chem. Solids **34**, 1137 (1973).

55. A. Sieverts, Z. Metallkde. **21**, 37 (1929).

56. M. Sugisaki *et al*., J. Nucl. Mater. **120**, 36 (1984).

Publications and Conference Presentations

Publications

R. Florido, R. C. Mancini, T. Nagayama, R. Tommasini, J. A. Delettrez and S. P. Regan, "Time-Resolved Characterization and Energy Balance Analysis of Implosion Core in Shock-Ignition Experiments at OMEGA," Phys. Plasmas **21**, 102709 (2014).

H. M. Johns, R. C. Mancini, P. Hakel, T. Nagayama, V. A. Smalyuk, S. P. Regan and J. Delettrez, "Compressed Shell Conditions Extracted from Spectroscopic Analysis of Ti K-Shell Absorption Spectra with Evaluation of Line Self-Emission," Phys. Plasmas **21**, 082711 (2014).

K. L. Marshall, O. Didovets, and D. Saulnier, "Contact-Angle Measurements as a Means of Probing the Surface Alignment Characteristics of Liquid Crystal Materials on Photoalignment Layers," in *Liquid Crystals XVIII*, edited by I. C. Khoo (SPIE, Bellingham, WA, 2014), Vol. 9182, Paper 91820J.

D. T. Michel, R. S. Craxton, A. K. Davis, R. Epstein, V. Yu. Glebov, V. N. Goncharov, S. X. Hu, I. V. Igumenshchev, D. D. Meyerhofer, P. B. Radha, T. C. Sangster, W. Seka, C. Stoeckl, and D. H. Froula, "Implosion Dynamics in Direct-Drive Experiments," Plasma Phys. Control. Fusion **57**, 014023 (2015).

T. Nagayama, R. C. Mancini, R. Florido, D. Mayes, R. Tommasini, J. A. Koch, J. A. Delettrez, S. P. Regan and V. A. Smalyuk, "Direct Asymmetry Measurement of Temperature and Density Spatial Distributions in Inertial Confinement Fusion Plasmas from Pinhole Space-Resolved Spectra," Phys. Plasmas **21**, 050702 (2014).

J. M. Ngoko Djiokap, N. L. Manakov, A. V. Meremianin, S. X. Hu, L. B. Madsen, and A. F. Starace, "Nonlinear Dichroism in Back-to-Back Double Ionization of He by an Intense Elliptically Polarized Few-Cycle Extreme Ultraviolet Pulse," Phys. Rev. Lett. **113**, 223002 (2014).

S. Papernov, "Defect-Induced Damage," in *Laser-Induced Damage in Optical Materials*, edited by D. Ristau (CRC Press, Boca Raton, FL, 2014), Chap. 3, pp. 25–74.

S. Papernov, A. A. Kozlov, and J. B. Oliver, "Interface Absorption Versus Film Absorption in HfO_2/SiO_2 Thin-Film Pairs in the Near-Ultraviolet and the Relation to Pulsed-Laser Damage," in *Laser-Induced Damage in Optical Materials: 2014*, edited by G. J. Exarhos, V. E. Gruzdev, J. A. Menapace, D. Ristau, and M. J. Soileau (SPIE, Bellingham, WA, 2014), Vol. 9237, Paper 92370Q.

M. J. Rosenberg, A. B. Zylstra, F. H. Séguin, H. G. Rinderknecht, J. A. Frenje, M. Gatu Johnson, H. Sio, C. J. Waugh, N. Sinenian, C. K. Li, R. D. Petrasso, P. W. McKenty, M. Hohenberger, P. B. Radha, J. A. Delettrez, V. Yu. Glebov, R. Betti, V. N. Goncharov, J. P. Knauer, T. C. Sangster, S. LePape, A. J. Mackinnon, J. Pino, J. M. McNaney, J. R. Rygg, P. A. Amendt, C. Bellei, L. R. Benedetti, L. Berzak Hopkins, R. M. Bionta, D. T. Casey, L. Divol, M. J. Edwards, S. Glenn, S. H. Glenzer, D. G. Hicks, J. R. Kimbrough, O. L. Landen, J. D. Lindl, T. Ma, A. MacPhee, N. B. Meezan, J. D. Moody, M. J. Moran, H.-S. Park, B. A. Remington, H. Robey, M. D. Rosen, S. C. Wilks, R. A. Zacharias, H. W. Herrmann, N. M. Hoffman, G. A. Kyrala, R. J. Leeper, R. E. Olson, J. D. Kilkenny and A. Nikroo, "Investigation of Ion Kinetic Effects in Direct-Drive Exploding-Pusher Implosions at the NIF," Phys. Plasmas **21**, 122712 (2014).

W. Theobald, A. A. Solodov, C. Stoeckl, K. S. Anderson, F. N. Beg, R. Epstein, G. Fiksel, E. M. Giraldez, V. Yu. Glebov, H. Habara, S. Ivancic, L. C. Jarrott, F. J. Marshall, G. McKiernan, H. S. McLean, C. Mileham, P. M. Nilson, P. K. Patel, F. Pérez, T. C. Sangster, J. J. Santos, H. Sawada, A. Shvydky, R. B. Stephens, and M. S. Wei, "Time-Resolved Compression of a Capsule with a Cone to High Density for Fast-Ignition Laser Fusion," Nat. Commun. **5**, 5785 (2014).

Forthcoming Publications

R. Arpaia, M. Ejrnaes, L. Parlato, F. Tafuri, R. Cristiano, D. Golubev, R. Sobolewski, T. Bauch, F. Lombardi, and G. P. Pepe, "High-Temperature Superconducting Nanowires for Photon Detection," to be published in Physica C.

R. Epstein, V. N. Goncharov, F. J. Marshall, R. Betti, R. Nora, A. R. Christopherson, I. E. Golovkin, and J. J. MacFarlane, "X-Ray Continuum as a Measure of Pressure and Fuel–Shell Mix in Compressed Isobaric Hydrogen Implosion Cores," to be published in Physics of Plasmas.

R. Epstein, S. P. Regan, B. A. Hammel, L. J. Suter, H. A. Scott, M. A. Barrios, D. K. Bradley, D. A. Callahan, C. Cerjan, G. W. Collins, S. N. Dixit, T. Doppner, M. J. Edwards, D. R. Farley, K. B. Fournier, S. Glenn, S. H. Glenzer, I. E. Golovkin, A. Hamza, D. G. Hicks, N. Izumi, O. S. Jones, M. H. Key, J. D. Kilkenny, J. L. Kline, G. A. Kyrala, O. L. Landen, T. Ma, J. J. MacFarlane, A. J. Mackinnon, R. C. Mancini, R. L. McCrory, D. D. Meyerhofer, N. B. Meezan, A. Nikroo, H.-S. Park, P. K. Patel, J. E. Ralph, B. A. Remington, T. C. Sangster, V. A. Smalyuk, P. T. Springer, R. P. J. Town, and J. L. Tucker, "Applications and Results of X-Ray Spectroscopy in Implosion Experiments on the National Ignition Facility," to be published in the Proceedings of Atomic Processes in Plasmas (invited).

G. Fiksel, A. Agliata, D. H. Barnak, G. Brent, P.-Y. Chang, L. Folnsbee, G. Gates, D. Hasset, D. Lonobile, J. Magoon, D. Mastrosimone, M. J. Shoup III, and R. Betti, "Note: Experimental Platform for Magnetized High-Energy-Density-Plasma Studies at the Omega Laser Facility," to be published in Review of Scientific Instruments.

M. Hohenberger, P. B. Radha, J. F. Myatt, S. LePape, J. A. Marozas, F. J. Marshall, D. T. Michel, S. P. Regan, W. Seka, A. Shvydky, T. C. Sangster, J. W. Bates, R. Betti, T. R. Boehly, M. J. Bonino, D. T. Casey, T. J. B. Collins, R. S. Craxton, J. A. Delettrez, D. H. Edgell, R. Epstein, G. Fiksel, P. Fitzsimmons, J. A. Frenje, D. H. Froula, V. N. Goncharov, D. R. Harding, D. H. Kalantar, M. Karasik, T. J. Kessler, J. D. Kilkenny, J. P. Knauer, C. Kurz, M. Lafon, K. N. LaFortune, B. J. MacGowan, A. J. Mackinnon, A. G. MacPhee, R. L. McCrory, P. W. McKenty, J. F. Meeker, D. D. Meyerhofer, S. R. Nagel, A. Nikroo, S. Obenschain, R. D. Petrasso, J. E. Ralph, H. G. Rinderknecht, M. J. Rosenberg, A. J. Schmitt, R. J. Wallace, J. Weaver, C. Widmayer, S. Skupsky, A. A. Solodov, C. Stoeckl, B. Yaakobi, and J. D. Zuegel, "Polar-Direct-Drive Experiments on the National Ignition Facility," to be published in Physics of Plasmas (invited).

C. M. Huntington, F. Fiuza, J. S. Ross, A. B. Zylstra, R. P. Drake, D. H. Froula, G. Gregori, N. L. Kugland, C. C. Kuranz, M. C. Levy, C. K. Li, J. Meinecke, T. Morita, R. Petrasso, C. Plechaty, B. A. Remington, D. D. Ryutov, Y. Sakawa, A. Spitkovsky, H. Takabe, H.-S. Park, "Observation of Magnetic Field Generation via the Weibel Instability in Interpenetrating Plasma Flows," to be published in Nature Physics.

S. X. Hu, V. N. Goncharov, T. R. Boehly, R. L. McCrory, S. Skupsky, L. A. Collins, J. D. Kress, and B. Militzer, "Impact of First-Principles Properties of Deuterium–Tritium on Inertial Confinement-Fusion Target Designs," to be published in Physics of Plasmas (invited).

P. M. Nilson, L. Gao, I. V. Igumenschev, G. Fiksel, R. Yan, J. R. Davies, D. Martinez, V. A. Smalyuk, M. G. Haines, E. G. Blackman, D. H. Froula, R. Betti, and D. D. Meyerhofer, "Magnetic-Field Generation by the Ablative Nonlinear Rayleigh–Taylor Instability," to be published in the Journal of Plasma Physics.

R. Nora, W. Theobald, F. J. Marshall, D. T. Michel, W. Seka, B. Yaakobi, M. Lafon, C. Stoeckl, J. A. Delettrez, A. A. Solodov, A. Casner, C. Reverdin, X. Ribeyre, A. Vallet, J. Peebles, F. N. Beg, M. S. Wei, and R. Betti, "Gigabar Spherical Shock Generation on the OMEGA Laser," to be published in Physical Review Letters.

W. Theobald, R. Nora, W. Seka, M. Lafon, K. S. Anderson, M. Hohenberger, F. J. Marshall, D. T. Michel, A. A. Solodov, C. Stoeckl, D. Edgell, B. Yaakobi, A. Casner, C. Reverdin, X. Ribeyre, O. Shvydky, A. Vallet, J. Peebles, F. N. Beg, M. S. Wei, and R. Betti, "Spherical Strong-Shock Generation for Shock-Ignition Inertial Fusion," submitted to Physics of Plasmas (invited).

F. Weilacher, P. B. Radha, T. J. B. Collins, and J. A. Marozas, "The Effect of Laser Spot Shapes on Polar-Direct-Drive Implosions on the National Ignition Facility," to be published in Physics of Plasmas.

Conference Presentations

D. D. Meyerhofer, S.-W. Bahk, J. Bromage, D. H. Froula, L. Gao, M. J. Guardalben, D. Haberberger, S. X. Hu, B. E. Kruschwitz, J. F. Myatt, P. M. Nilson, J. B. Oliver, C. Robillard, M. J. Shoup III, C. Stoeckl, W. Theobald, L. J. Waxer, B. Yaakobi, and J. D. Zuegel, "High-Energy-Density Physics with High-Energy and High-Intensity Lasers," Second High-Power Laser Workshop, Palo Alto, CA, 7–8 October 2014.

D. H. Froula, "An Overview of the Direct-Drive Program at the Laboratory for Laser Energetics," NRL Colloquium, Washington, DC, 8 October 2014.

The following presentations were made at ICUIL 2014, Goa, India, 12–17 October 2014:

J. Bromage, R. G. Roides, S.-W. Bahk, C. Mileham, J. B. Oliver, C. Dorrer, and J. D. Zuegel, "Technology Development for Ultra-Intense OPCPA."

C. Dorrer, R. G. Roides, J. Bromage, and J. D. Zuegel, "Self-Phase Modulation Compensation in a Regenerative Amplifier Using Cascaded Second-Order Nonlinearities."

D. Haberberger, J. Bromage, J. D. Zuegel, D. H. Froula, A. Cairns, R. Trines, R. Bingham, and P. A. Norreys, "Tunable Plasma-Wave Laser Amplifier."

B. W. Plansinis, "Spectral Changes Induced by a Phase Modulator Acting as a Time Lens," Frontiers in Optics, Tucson, AZ, 19–23 October 2014.

J. H. Kelly, "Laser-Driven Fusion at the University of Rochester and Parallels Between Laser/Optical and Radio-Frequency/Microwave Techniques," Microwave Update 2014, Rochester, NY, 24–25 October 2014.

The following presentations were made at the 56th Annual Meeting of the APS Division of Plasma Physics, New Orleans, LA, 27–31 October 2014:

K. S. Anderson, P. W. McKenty, T. J. B. Collins, J. A. Marozas, M. Lafon, and R. Betti, "An Implosion-Velocity Survey for Shock Ignition at the National Ignition Facility."

D. H. Barnak, G. Fiksel, H. Chen, P.-Y. Chang, D. D. Meyerhofer, G. J. Williams, S. Kerr, and J. Park, "Collimation of a Positron Beam Using an Externally Applied Axially Symmetric Magnetic Field."

R. Betti, A. R. Christopherson, J. Howard, A. Bose, and R. Nora, "Measurements of Alpha Heating in Inertial Confinement Fusion."

T. R. Boehly, G. Fiksel, S. X. Hu, V. N. Goncharov, T. C. Sangster, and P. M. Celliers, "Measurements of Laser Imprinting Using 2-D Velocity Interferometry."

A. Bose, R. Betti, K. Woo, R. Nora, R. Epstein, J. A. Delettrez, K. S. Anderson, and A. Shvydky, "Hydrodynamic Scaling of the Deceleration-Phase Rayleigh–Taylor Instability."

D. Cao, G. Moses, J. A. Delettrez, T. J. B. Collins, "Design Process for Applying the Nonlocal Thermal Transport iSNB Model to a Polar-Drive ICF Simulation."

P.-Y. Chang, J. R. Davies, D. H. Barnak, G. Fiksel, R. Betti, A. Harvey-Thompson, and D. Sinars, "Design of Scaled-Down Magnetized Liner Inertial Fusion on OMEGA."

A. R. Christopherson, R. Epstein, F. J. Marshall, R. Nora, C. Stoeckl, C. J. Forrest, J. A. Delettrez, P. B. Radha, and J. Howard, "Comprehensive Analysis of a High-Adiabat Cryogenic Implosion on OMEGA."

T. J. B. Collins, J. A. Marozas, J. A. Delettrez, P. W. McKenty, S. Skupsky, D. Cao, J. Chenhall, and G. Moses, "A Polar-Drive, Alpha-Heating Platform for the National Ignition Facility."

A. Davies, L. Ceurvorst, P. A. Norreys, D. Haberberger, D. H. Froula, R. Yan, and C. Ren, "Self-Generated Magnetic Fields in New Laser-Produced Plasma with High-Intensity Beams."

J. R. Davies, D. H. Barnak, R. Betti, A. Carreon, P.-Y. Chang, G. Fiksel, E. L. Campbell, and D. B. Sinars, "Instability Driven by a Self-Generated Magnetic Field: Relevance to Helical Structures in MagLIF Experiments."

A. K. Davis, D. T. Michel, I. V. Igumenshchev, R. S. Craxton, R. Epstein, V. N. Goncharov, S. X. Hu, M. Lafon, P. B. Radha, T. C. Sangster, and D. H. Froula, "Measurement of the Si Mass Ablation Rate in Direct-Drive Implosions on the OMEGA Laser System."

J. A. Delettrez, T. J. B. Collins, and C. Ye, "Limits on the Level of Fast-Electron Preheat in Direct-Drive–Igni tion Designs."

T. Eckert, L. Vincett, M. Yuly, S. Padalino, M. Russ, M. Bienstock, A. Simone, D. Ellison, H. Desmitt, T. C. Sangster, and S. P. Regan, "Coincidence Efficiency of Sodium Iodide Detectors for Positron Annihilation."

D. H. Edgell, I. V. Igumenshchev, D. T. Michel, J. F. Myatt, D. H. Froula, R. J. Henchen, and V. N. Goncharov, "Empirical Scaling of Hot Electrons with the Two-Plasmon–Decay Common-Wave Gain."

R. Epstein, F. J. Marshall, V. N. Goncharov, R. Betti, R. Nora, and A. R. Christopherson, "Fuel–Shell Mix Measurements Based on X-Ray Continuum Emission from Isobaric Implosion Cores on OMEGA."

G. Fiksel, D. H. Barnak, P.-Y. Chang, D. Haberberger, S. X. Hu, S. Ivancic, P. M. Nilson, W. Fox, A. Bhattacharjee, and K. Germaschewski, "Strongly Driven Magnetic Reconnection in a Magnetized High-Energy-Density Plasma."

T. M. Filkins, J. Steidle, D. M. Ellison, J. Steidle, C. G. Freeman, S. J. Padalino, G. Fiksel, S. P. Regan, and T. C. Sangster, "Measurements of Proton Energy Spectra Using a Radiochromic Film Stack."

R. K. Follett, D. H. Edgell, R. J. Henchen, S. X. Hu, J. Katz, D. T. Michel, J. F. Myatt, J. Shaw, and D. H. Froula, "Observation of Two-Plasmon–Decay Common Plasma Waves Using UV Thomson Scattering."

C. J. Forrest, C. Stoeckl, V. Yu. Glebov, T. C. Sangster, P. B. Radha, V. N. Goncharov, J. A. Frenje, and M. Gatu Johnson, "Measurements of Areal-Density Anisotropies Using Elastic Scattering in Cryogenic Direct-Drive Implosions."

W. Fox, G. Fiksel, D. Barnak, P. Nilson, S. X. Hu, A. Bhattacharjee, W. Deng, "Astrophysical Weibel Instability in Counter-Streaming Laser-Driven Plasmas" (invited).

J. Frenje, C. K. Li, F. Séguin, A. Zylstra, R. Petrasso, P. Grabowski, R. Mancini, S. Regan, J. Delettrez, V. Glebov, and T. Sangster, "Measurements of Charged-Particle Stopping Around the Bragg Peak in OMEGA ICF Plasmas."

D. H. Froula, G. Fiksel, V. N. Goncharov, S. X. Hu, H. Huang, I. V. Igumenshchev, T. J. Kessler, D. D. Meyerhofer, D. T. Michel, T. C. Sangster, A. Shvydky, and J. D. Zuegel, "A Pathway to Ignition-Hydrodynamic-Equivalent Implosions in OMEGA Direct Drive Through the Reduction of Cross-Beam Energy Transfer."

L. Gao, "Observation of Self-Similarity in the Magnetic Fields Generated by the Ablative Nonlinear Rayleigh–Taylor Instability."

M. Gatu Johnson, J. A. Frenje, A. Zylstra, R. D. Petrasso, C. Forrest, V. Yu. Glebov, J. P. Knauer, F. J. Marshall, D. T. Michel, T. C. Sangster, W. Seka, C. Stoeckl, D. Sayre, J. A. Caggiano, D. T. Casey, R. Hatarik, D. P. McNabb, J. E. Pino, A. Bacher, H. Herrmann, Y. Kim, J-. L. Bourgade, and O. Landoas, "Observation of Variations in the T + T Neutron Spectrum with Varying Center-of-Mass Energy."

V. Yu. Glebov, C. Stoeckl, T. C. Sangster, and C. Forrest, "Correlations of Multiple Ion-Temperature Measurements with Shot Parameters in DT Cryogenic Implosions on OMEGA."

V. N. Goncharov, T. C. Sangster, R. Epstein, S. X. Hu, I. V. Igumenshchev, C. J. Forrest, D. H. Froula, F. J. Marshall, D. T. Michel, P. B. Radha, W. Seka, C. Stoeckl, J. A. Frenje, and M. Gatu Johnson, "Understanding the Performance of Low-Adiabat Cryogenic Implosions on OMEGA."

M. C. Gregor, T. R. Boehly, C. A. McCoy, D. N. Polsin, D. D. Meyerhofer, D. E. Fratanduono, P. M. Celliers, and G. W. Collins, "The Release Behavior of Diamond Shocked to 15 Mbar."

D. Haberberger, P. M. Nilson, M. C. Gregor, T. R. Boehly, and D. H. Froula, "Studying the Equation of State of Isochorically Heated Al Using Streaked Optical Pyrometry."

R. J. Henchen, V. N. Goncharov, S. X. Hu, R. K. Follett, J. Katz, D. H. Froula, and W. Rozmus, "Heat Flux Measurements from Thomson-Scattered Electron Plasma Waves."

M. Hohenberger, P. B. Radha, J. W. Bates, R. Betti, T. R. Boehly, M. J. Bonino, D. T. Casey, T. J. B. Collins, R. S. Craxton, J. A. Delettrez, D. H. Edgell, R. Epstein, G. Fiksel, P. Fitzsimmons, J. A. Frenje, D. H. Froula, V. N. Goncharov, D. R. Harding, D. H. Kalantar, M. Karasik, T. J. Kessler, J. D. Kilkenny, J. P. Knauer, C. Kurz, M. Lafon, K. N. LaFortune, S. LePape, B. MacGowan, A. J. Mackinnon, A. MacPhee, J. A. Marozas, F. J. Marshall, R. L. McCrory, P. W. McKenty, J. Meeker, D. D. Meyerhofer, D. T. Michel, J. F. Myatt, S. R. Nagel, A. Nikroo, S. P. Obenschain, R. D. Petrasso, S. P. Regan, H. G. Rinderknecht, M. Rosenberg, T. C. Sangster, A. J. Schmitt, W. Seka, A. Shvydky, S. Skupsky, A. A. Solodov, C. Stoeckl, R. J. Wallace, J. Weaver, C. Widmeyer, B. Yaakobi, and J. D. Zuegel, "Polar-Direct-Drive Experiments on the National Ignition Facility" (invited).

S. X. Hu, V. N. Goncharov, T. R. Boehly, R. L. McCrory, S. Skupsky, L. A. Collins, J. D. Kress, and B. Militzer, "Impact of First-Principles Properties of Deuterium–Tritium on Inertial Confinement Fusion Target Designs" (invited).

I. V. Igumenshchev, "Effects of Self-Generated Magnetic Fields in Rayleigh–Taylor Unstable Laser-Irradiated Plastic Foils."

S. Ivancic, D. Haberberger, C. Stoeckl, K. S. Anderson, C. Ren, W. Theobald, D. H. Froula, D. D. Meyerhofer, T. Iwawaki, H. Habara, and K. Tanaka, "Optical Probing of Laser-Channeling Experiments on the OMEGA EP Laser System."

V. V. Ivanov, A. V. Maximov, A. A. Anderson, B. S. Bauer, and K. Yates, "Study of Strong Magnetic Fields Using Parametric Instability in a Magnetized Plasma."

J. P. Knauer, "Ion-Temperature Measurements for Cryogenic, High-Foot, Inertial Confinement Fusion Implosions at the National Ignition Facility."

M. Lafon, R. Betti, K. S. Anderson, T. J. B. Collins, P. W. McKenty, A. Shvydky, and S. Skupsky, "Benefits of Moderate-*Z* Ablators for Direct-Drive Inertial Confinement Fusion."

J. A. Marozas, T. J. B. Collins, J. D. Zuegel, P. B. Radha, F. J. Marshall, P. W. McKenty, W. Seka, D. T. Michel, and M. Hohenberger, "Cross-Beam Energy Transfer Mitigation Strategy for Polar Drive at the National Ignition Facility."

F. J. Marshall, J. A. Delettrez, R. Epstein, V. N. Goncharov, D. T. Michel, T. C. Sangster, and C. Stoeckl, "Time-Resolved Imaging of Cryogenic Target X-Ray Emission at Peak Compression on OMEGA."

A. V. Maximov, J. F. Myatt, R. W. Short, I. V. Igumenshchev, and W. Seka, "Cross-Beam Energy Transfer Driven by Incoherent Laser Beams with Colors."

C. A. McCoy, M. C. Gregor, D. N. Polsin, T. R. Boehly, D. D. Meyerhofer, D. E. Fratanduono, P. M. Celliers, and G. W. Collins, "Measurements of the Sound Speed and Grüneisen Parameter with a Nonsteady Wave Correction."

P. W. McKenty, J. A. Marozas, F. J. Marshall, J. Weaver, S. Obenschain, and A. Schmitt, "Evaluation of Wavelength Detuning to Mitigate Cross-Beam Energy Transfer Using the Nike Laser."

D. D. Meyerhofer, S.-W. Bahk, J. Bromage, D. H. Froula, M. J. Guardalben, D. Haberberger, S. X. Hu, B. E. Kruschwitz, J. F. Myatt, P. M. Nilson, J. B. Oliver, C. Robillard, M. J. Shoup III, C. Stoeckl, W. Theobald, L. J. Waxer, B. Yaakobi, and J. D. Zuegel, "OMEGA EP OPAL: A Path to a 75-PW Laser System."

D. T. Michel, T. C. Sangster, V. N. Goncharov, A. K. Davis, V. Yu. Glebov, R. Epstein, S. X. Hu, I. V. Igumenshchev, D. D. Meyerhofer, W. Seka, A. Shvydky, C. Stoeckl, and D. H. Froula, "Constraining the Hydrodynamic Efficiency in Hydrodynamic Simulations of Direct-Drive Cryogenic Implosions."

J. F. Myatt, J. Shaw, J. Zhang, A. V. Maximov, R. W. Short, W. Seka, D. H. Edgell, D. H. Froula, D. F. DuBois, D. A. Russell, and H. X. Vu, "An Investigation of Two-Plasmon–Decay Localization in Spherical Implosion Experiments on OMEGA."

P. M. Nilson, M. Lafon, C. R. Stillman, C. Mileham, R. Boni, T. R. Boehly, D. H. Froula, and D. D. Meyerhofer, "Direct Shock-Timing Measurements in CH Using Streaked X-Ray Radiography."

R. Nora, W. Theobald, F. J. Marshall, D. T. Michel, W. Seka, B. Yaakobi, M. Lafon, C. Stoeckl, J. A. Delettrez, A. A. Solodov, R. Betti, A. Casner, C. Reverdin, X. Ribeyre, A. Vallet, J. Peebles, F. N. Beg, and M. S. Wei, "Gigabar Spherical Shock Experiments on OMEGA."

S. Padalino, A. Simone, E. Turner, M. K. Ginnane, N. Dubois, T. C. Sangster, and S. P. Regan, "Time-Resolved Tandem Faraday Cup for High Energy TNSA Particles."

D. N. Polsin, M. C. Gregor, C. A. McCoy, T. R. Boehly, T. C. Sangster, D. E. Fratanduono, and P. M. Celliers, "Probing the Release of Shocked Material."

P. B. Radha, M. Hohenberger, F. J. Marshall, D. T. Michel, J. A. Delettrez, D. H. Edgell, D. H. Froula, V. N. Goncharov, J. P. Knauer, J. A. Marozas, R. L. McCrory, P. W. McKenty, D. D. Meyerhofer, S. P. Regan, T. C. Sangster, W. Seka, A. Shvydky, J. A. Frenje, M. Rosenberg, R. D. Petrasso, S. LePape, and A. J. Mckinnon, "Polar Drive on the National Ignition Facility."

S. P. Regan, M. J. May, M. B. Schneider, M. A. Barrios, J. D. Moody, K. L. Baker, G. V. Brown, D. Callahan, T. Doeppner, R. Epstein, K. B. Fournier, R. F. Heeter, D. E. Hinkel, O. S. Jones, R. Kauffman, J. D. Kilkenny, O. L. Landen, D. A. Liedahl, D. D. Meyerhofer, J. S. Ross, V. A. Smalyuk, and T. C. Sangster, "Hohlraum T_e Inferred from Au L-Shell Emission."

H. G. Rinderknecht, M. J. Rosenberg, C. K. Li, A. B. Zylstra, H. Sio, M. Gatu Johnson, J. A. Frenje, F. H. Séguin, R. D. Petrasso, P. A. Amendt, C. Bellei, S. C. Wilks, G. Zimmerman, N. M. Hoffman, G. Kagan, K. Molvig, V. Yu. Glebov, C. Stoeckl, F. J. Marshall, W. Seka, J. A. Delettrez, T. C. Sangster, R. Betti, V. N. Goncharov, and D. D. Meyerhofer, "Studies of Multi-Ion-Fluid Yield Anomaly in Shock-Driven Implosions."

M. J. Rosenberg, F. H. Séguin, H. G. Rinderknecht, H. Sio, A. B. Zylstra, M. Gatu Johnson, J. A. Frenje, C. K. Li, R. D. Petrasso, P. A. Amendt, C. Bellei, S. C. Wilks, G. Zimmerman, N. M. Hoffman, G. Kagan, K. Molvig, V. Yu. Glebov, C. Stoeckl, F. J. Marshall, W. Seka, J. A. Delettrez, T. C. Sangster, R. Betti, V. N. Goncharov, D. D. Meyerhofer, S. Atzeni, and A. Nikroo, "Studies of Ion Kinetic Effects in OMEGA Shock-Driven Implosions Using Fusion Burn Imaging."

T. C. Sangster, V. N. Goncharov, P. B. Radha, R. Betti, T. R. Boehly, C. J. Forrest, D. H. Froula, V. Yu. Glebov, S. X. Hu, I. V. Igumenshchev, J. Kwiatkowski, F. J. Marshall, R. L. McCrory, P. W. McKenty, D. D. Meyerhofer, D. T. Michel, J. F. Myatt, W. Seka, C. Stoeckl, J. A. Frenje, M. Gatu Johnson, W. T. Shmayda, S. Reid, N. Redden, R. Earley, R. T. Janezic, M. D. Wittman, J. H. Kelly, T. Z. Kosc, E. Hill, J. Puth, T. J. Kessler, and A. Shvydky, "Cryogenic Implosion Performance Using High-Purity Deuterium-Tritium Fuel."

W. Seka, W. Theobald, R. Nora, R. Betti, J. F. Myatt, R. W. Short, and R. E. Bahr, "Multibeam Laser–Plasma Interactions Lead to Localized Interaction Regions."

R. W. Short, J. F. Myatt, J. Zhang, and W. Seka, "Absolute and Convective Two-Plasmon Decay Driven by Multiple Laser Beams."

A. Shvydky, M. Hohenberger, P. B. Radha, R. S. Craxton, V. N. Goncharov, J. P. Knauer, J. A. Marozas, F. J. Marshall, P. W. McKenty, D. D. Meyerhofer, and T. C. Sangster, "Preparing for Polar-Drive Imprint Experiments at the National Ignition Facility."

A. Simone, S. Padalino, E. Turner, M. K. Ginnane, N. Dubois, K. Fletcher, M. Giordano, P. Lawson-Keister, H. Harrison, H. Visca, T. C. Sangster, and S. P. Regan, "Characterizing ICF Neutron Diagnostics on the nTOF Line at SUNY Geneseo."

H. Sio, H. G. Rinderknecht, J. A. Frenje, M. J. Rosenberg, A. B. Zylstra, F. H. Séguin, M. Gatu Johnson, C. K. Li, R. D. Petrasso, N. Hoffman, G. Kagan, K. Molvig, P. Amendt, C. Bellei, S. Wilks, C. Stoeckl, V. Yu. Glebov, R. Betti, and T. C. Sangster, "Exploration of Kinetic and Multiple-Ion-Fluids Effects in D^3He and T^3He Gas-Filled ICF Implosions Using Multiple Nuclear Burn Histories."

A. A. Solodov, B. Yaakobi, J. F. Myatt, C. Stoeckl, and D. H. Froula, "Fast-Electron Temperature Measurements in Laser Irradiation at 10^{14} W/cm^2."

C. R. Stillman, P. M. Nilson, M. Lafon, C. Mileham, R. Boni, T. R. Boehly, D. D. Meyerhofer, D. H. Froula, and D. E. Fratanduono, "Direct Measurements of Shock-Wave Propagation in CH Using Streaked X-Ray Radiography and VISAR."

C. Stoeckl, R. Epstein, G. Fiksel, V. N. Goncharov, S. X. Hu, D. W. Jacobs-Perkins, R. K. Jungquist, C. Mileham, P. M. Nilson, T. C. Sangster, and W. Theobald, "Measuring Mix in Direct-Drive Cryogenic DT Implosions Using Soft X-Ray Narrowband Backlighting."

D. Stutman, M. P. Valdivia, M. Finkenthal, S. P. Regan, C. Stoeckl, and B. Stoeckl, "Testing Talbot–Lau X-Ray Moiré Fringe Deflectometry with a Laser Backlighter."

W. Theobald, R. Nora, W. Seka, M. Lafon, K. S. Anderson, M. Hohenberger, F. J. Marshall, D. T. Michel, A. A. Solodov, C. Stoeckl, D. Edgell, B. Yaakobi, A. Casner, C. Reverdin, X. Ribeyre, O. Shvydky, A. Vallet, J. Peebles, F. N. Beg, M. S. Wei, and R. Betti, "Spherical Strong-Shock Generation for Shock-Ignition Inertial Fusion" (invited).

H. Wen, A. V. Maximov, R. Yan, J. Li, C. Ren, and J. F. Myatt, "Particle-in-Cell Modeling of Laser–Plasma Interactions in Three Dimensions."

K. M. Woo, A. Bose, R. Betti, J. A. Delettrez, K. S. Anderson, and R. Epstein, "A Three-Dimensional Hydrocode to Study the Deceleration Phase and Hot-Spot Formation in Inertial Confinement Fusion Implosions."

R. Yan, R. Betti, and J. Sanz, "Bubble Acceleration in Three-Dimensional Ablative Rayleigh–Taylor Instability."

J. Zhang, J. F. Myatt, R. W. Short, A. V. Maximov, H. X. Vu, D. A. Russell, and D. F. DuBois, "Calculation of Half-Harmonic Emission Generated by the Two-Plasmon–Decay Instability."

A. Zylstra, M. Gatu Johnson, J. A. Frenje, C. K. Li, F. H. Séguin, H. Sio, M. Rosenberg, H. Rinderknecht, R. D. Petrasso, H. W. Herrmann, Y. H. Kim, D. McNabb, D. Sayre, J. Pino, C. Brune, A. Bacher, C. Forrest, V. Yu. Glebov, C. Stoeckl, R. T. Janezic, and T. C. Sangster, "Studies of ^{3}He + ^{3}He, T + ^{3}He, and p + D Nuclear Reactions Relevant to Stellar or Big-Bang Nucleosynthesis Using ICF Plasmas at OMEGA."

J. P. Knauer, "OMEGA MIFEDS Magnetic-Field Generator," JOWOG-37, Los Alamos, NM, 3–7 November 2014.

W. R. Donaldson, B. Beeman, E. K. Miller, and R. G. Roides, "A 15-GHz Electro-Optic Measurement System for Noisy Environments," Avionics Fiber-Optics and Photonics Conference, Atlanta, GA, 11–13 November 2014.

The following presentations were made at the Fusion Power Associates 35th Annual Meeting, Washington DC, 16 December 2014.

R. L. McCrory, "Perspectives on Inertial Fusion."

T. C. Sangster, V. N. Goncharov, P. B. Radha, M. Hohenberger, R. Betti, T. R. Boehly, T. J. B. Collins, R. S. Craxton, D. H. Edgell, R. Epstein, C. J. Forrest, D. H. Froula, V. Yu. Glebov, D. R. Harding, S. X. Hu, I. V. Igumenshchev, T. J. Kessler, J. P. Knauer, J. A. Marozas, F. J. Marshall, R. L. McCrory, P. W. McKenty, D. D. Meyerhofer, D. T. Michel, J. F. Myatt, S. P. Regan, W. Seka, W. T. Shmayda, A. Shvydky, C. Stoeckl, J. A. Frenje, M. Gatu Johnson, R. D. Petrasso, H. G. Rinderknecht, M. Rosenberg, D. T. Casey, S. LePape, A. J. Mackinnon, R. J. Wallace, A. Nikroo, M. Farrell, S. P. Obenschain, M. Karasik, A. Schmitt, and J. Weaver, "OMEGA Recent Results and Plans."